# Thèse

Présentée à

**l'Université des Sciences et Technologies de Lille**

**Ecole Doctorale Sciences Pour l'Ingénieur**

Pour obtenir le titre de

**DOCTEUR DE L'UNIVERSITÉ**

Spécialité: Micro et Nanotechnologies,
Acoustique et Télécommunications

Par

**Adrián Díaz Álvarez**

# Surface characterization of III-V semiconductor nanowires: Morphological, structural and electronic properties

***Soutenue le 25 Novembre 2016***

Composition du Jury:

| | |
|---|---|
| Président | **Gilles DAMBRINE** |
| Rapporteurs | **Michel GENDRY** |
| | **Damien RIEDEL** |
| Examinateurs | **Sébastien PLISSARD** |
| | **Silvia RUBINI** |
| Directeur de thèse | **Bruno GRANDIDIER** |

**Abstract**

With the size reduction of optoelectronic devices, controlling the surface of semiconductor materials is becoming crucial to optimize their performances. This is particularly true for one-dimensional systems such as semiconductor nanowires that are subject to high surface-to-volume ratio. The aim of this thesis is therefore to perform a comprehensive study of the surface properties of III-V semiconductor nanowires and to determine to what extent they affect their overall properties. Starting with a description of the basic principles that govern their growth in order to obtain nanowire ensembles with a good uniformity, we then highlight a surface science tool, scanning tunneling microscopy, and a surface preparation technique, based on the use of a protective arsenic layer, that are key to further understand the structural and electronic properties of the surface of self-catalyzed GaAs and InAs semiconductor nanowires. In the fourth part of this work, we apply these techniques to analyze the structural and electronic properties of GaAs core-shell nanowires consisting of a thin shell grown at low temperature. We show the similarity of the shell properties with low-temperature grown GaAs thin film through the identification of their point defects and finally compare the THz properties of these nanowires with GaAs nanowires. The importance of the shell in the dynamics of the free charge carriers is demonstrated from the analysis of the THz waveforms.

---

Avec la miniaturisation des composants optoélectroniques, contrôler la surface de leur constituants actifs devient prépondérant. C'est en particulier vrai pour les nanofils semi-conducteurs dont la géométrie favorise un rapport surface sur volume élevé. L'objectif de cette thèse consiste donc à mener une étude précise de la structure cristallographique et électronique de leur surface et à déterminer à quel point cette surface affecte leurs propriétés physiques globales. Ce travail commence par une description détaillée de la croissance des nanofils III-V en insistant sur l'intérêt de fabriquer des ensembles de nanofils uniformes, condition nécessaire pour assurer une grande reproductibilité des résultats. Il se poursuit par un éclairage sur une technique de choix pour analyser la surface des nanofils, la microscopie à effet tunnel, et une technique d'encapsulation des nanofils pour préserver leur surface de toute contamination. L'intérêt de ces deux techniques est démontré au travers de l'étude de la surface de nanofils GaAs et InAs pour expliquer comment la désorption d'une couche protectrice d'arsenic conduit à des morphologies de surface différentes. L'expertise ainsi acquise est alors mise à profit pour caractériser des nanofils GaAs cœur-coquille, dont la coquille est fabriquée à basse température. Au travers de l'identification des défauts rencontrés dans la coquille, cette dernière se révèle posséder des propriétés similaires à celles de films GaAs fabriqués à basse-température. La durée de vie limitée des porteurs de charge photoexcités est alors exploitée pour étudier les effets induits par les défauts sur les propriétés d'émission THz de nanofils à base de GaAs.

# Contents


**Introduction** **6**

**1 Semiconductor Nanowires: Applications and growth** **9**

1.1 Introduction . . . 9
1.2 VLS Growth Mechanism . . . 16
1.2.1 Molecular Beam Epitaxy . . . 18
1.2.2 Metal-Organic Vapor Phase Epitaxy . . . 19
1.3 Modeling Semiconductor Nanowire Growth . . . 20
1.3.1 Supersaturation . . . 21
1.3.2 Crystal Phase . . . 23
1.3.3 Gibbs-Thomson effect . . . 32
1.3.4 Diffusion induced growth regime . . . 34
1.3.5 Self-Catalyzed III-V Nanowires . . . 37
1.3.6 Self-equilibration of the diameter of Ga-catalyzed GaAs Nanowires . . . 41
1.3.7 Conclusion . . . 46

**2 Characterization techniques** **48**

2.1 Scanning Tunneling Microscopy . . . 48
2.1.1 Introduction . . . 48
2.1.2 Theory of STM . . . 54
2.1.3 STM spectroscopy . . . 56
2.1.4 STM on semiconductor surfaces: Band Bending . . . 60
2.1.5 Omicron LT-STM . . . 64
2.2 THz-Time Domain Spectroscopy . . . 68
2.2.1 Introduction . . . 68
2.2.2 Experimental setup . . . 69
2.2.3 Modeling THZ-TDS curves . . . 73

**3 Preparation and Characterization of III-V Nanowires Surfaces** **77**

3.1 Introduction . . . 77
3.2 Surface preparation of Semiconductor Nanowires for STM . . . 80
3.3 Sidewall morphology of As decapped III-V semiconductor nanowires 82
3.3.1 Transfer of Nanowires in UHV . . . 82
3.3.2 Facets and Surface Morphology in III-V Nanowires . . . 84

3.4 Influence of As decapping in surface morphology . . . . . . . . . 91
3.4.1 Self-Catalyzed GaAs Nanowires . . . . . . . . . . . . . . . 91
3.4.2 Self-Catalyzed InAs Nanowires . . . . . . . . . . . . . . . 97
3.5 Conclusions . . . . . . . . . . . . . . . . . . . . . . . . . . . . 103

**4 Structural and electronic characterization of Low-temperature grown GaAs Nanowires 106**
4.1 Introduction . . . . . . . . . . . . . . . . . . . . . . . . . . . . 106
4.2 Low-Temperature Grown GaAs . . . . . . . . . . . . . . . . . . 108
4.2.1 Growth and structural properties . . . . . . . . . . . . . . 108
4.2.2 Transport models . . . . . . . . . . . . . . . . . . . . . . 114
4.2.3 Optical properties . . . . . . . . . . . . . . . . . . . . . . 116
4.2.4 Conclusions . . . . . . . . . . . . . . . . . . . . . . . . . 121
4.3 Synthesis of LT-GaAs Nanowires . . . . . . . . . . . . . . . . . 122
4.3.1 TEM characterization of LT-GaAs nanowires . . . . . . . 124
4.4 STM characterization of LT-GaAs Nanowires . . . . . . . . . . . 126
4.4.1 Structural properties . . . . . . . . . . . . . . . . . . . . . 127
4.4.2 Electronic properties . . . . . . . . . . . . . . . . . . . . . 132
4.4.3 Arsenic precipitates: Structural and electronic properties 135
4.5 Cathodoluminescence of LT-GaAs nanowires . . . . . . . . . . . 140
4.6 Free charge carrier lifetime in LT-GaAs nanowires . . . . . . . . 141
4.7 Conclusions . . . . . . . . . . . . . . . . . . . . . . . . . . . . 143

**5 Terahertz emission from GaAs core-shell nanowires 145**
5.1 Introduction . . . . . . . . . . . . . . . . . . . . . . . . . . . . 145
5.1.1 THz emission from semiconductor surfaces . . . . . . . . 149
5.1.2 Nanowires and THz: Detection and Emission . . . . . . . 152
5.2 Characteristic of terahertz emission from GaAs core-shell nanowires 157
5.2.1 GaAs core-shell nanowires: Growth and structural properties . . . . . . . . . . . . . . . . . . . . . . . . . . . . 157
5.2.2 Discussion of results . . . . . . . . . . . . . . . . . . . . . 160
5.3 Conclusions . . . . . . . . . . . . . . . . . . . . . . . . . . . . 168

**Conclusions 170**

**Bibliography 173**

**Publications 195**

**Acknowledgments 218**

*Le mystère des choses? Va-t'en savoir ce qu'est le mystère?*
*L'unique mystère est qu'il y en ait qui pensent au mystère.*
*Qui se tient au soleil et ferme les yeux,*
*Commence à ne plus savoir ce qu'est le soleil,*
*Et à penser maintes choses pleines de chaleur.*
*Mais il ouvre les yeux et voit le soleil,*
*Et voilà qu'l ne peut plus penser à rien.*

-Le gardeur de troupeaux.
*F.Pessoa sous l'Hétéronyme d'Alberto Caeiro.*

# Introduction

The world of nanotechnology is growing fast. As the shrinkage of 3D semiconductor compounds is reaching its limits in terms of device performance, mainly due to the larger interfacial effects arising as thousands of active compounds are interconnected together, pure 2D solids emerge as a new paradigm of materials. These materials are an excellent playground to explore new physical phenomena, as well as to develop new type of devices. However, regardless of their huge interest for fundamental research, they still lack the proper control and integration into working devices that can cover the fundamental needs of the modern world.

In this context, nanowires are a kind of hybrid quasi-1D materials, that naturally bridge the vast amount of knowledge acquired on 3D semiconductor compounds, which shapes all of our daily devices, with the world of nanotechnology. It is in this crossroad between nanometric geometry, controlled compound and shape, and crystal phase engineering, where the field of nanowire synthesis, based on the vapor-liquid-solid (VLS) growth mechanism, offers the flexibility and potential to hold this challenge.

The aim of this thesis is to explore the relation between the surface of the nanowires and their bulk properties. For this purpose, it is necessary to understand how the electronic and morphology of the surfaces of the nanowires can influence its performance as a device. This is summarized in the first part of chapter 1, that covers some of the main applications of semiconductor nanowires as active devices. Interestingly, due to their high surface-to-volume ratio, nanowire surfaces are very important to understand their performance as devices. Indeed, the main growth mechanism, VLS, is a growth regime in which many different fluxes of materials in three different states of matter -the solid, the liquid and the vapor- are exchanged within the growth chamber. In such a complex scenario, at the temperature and conditions in which nanowires are grown, kinetic effects, rather than thermodynamical ones, are responsible for the resulting nanowire crystal phase and structure. As a consequence, crystal phases that are not thermodynamically stable in bulk materials, such as the wurtzite phase for some III-V compounds, can appear along the crystalline structure of the nanowire. Furthermore, small changes in pressure, temperature, substrate and material fluxes during growth can result in a very disperse distribution of nanowire morphologies and crystal phases. Then, the first and foremost goal in the nanowire research field has to be focused in understanding the growth of the structures,

that is, in combining effective growth models with experimental results. The different growth regimes and subsequent modelings developed during the history of the field, as well as its importance regarding the crystal phase and nanowire morphology, will be the subject of the rest of chapter 1.

Chapters 3 and 4 will explore the relation between the surface of the nanowires and their electronic properties. In order to obtain a complete characterization of the nanowire surface, it is necessary to use a tool that is able to precisely give information about the type of crystalline structure and facet that is developed along the sidewalls of the nanowire, the morphology of the surface produced either during growth or after, and the resulting electronic state of the surface. Scanning Tunneling Microscope (STM) is the ideal tool to fulfill all these requirements at once, as it is possible to place the nanowires on flat substrates and scan the sidewalls with the STM tip. As STM has been the main characterization tool used in this work, chapter 2 will be devoted to explain its working mechanism, based on the quantum tunneling effect, and why it delivers such information about the samples. With this kind of tool, it is of paramount importance to understand very well its working principle, in order to get valuable physical information, as the analysis of the STM data can be a field itself. For example, the interaction of the metallic tip of the STM with semiconductor surfaces can influence them in such a way as to alter the tunneling current and the electronic properties of the surfaces, this is known as Tip Induced Band Bending, and will be covered in chapter 2. Finally, the STM machine, an Omicron UHV LT-STM, used to obtain all of the experimental results of chapter 3 and 4, will be described in detail.

To achieve a reliable characterization of the surface of the nanowires with STM, it is necessary to keep the surfaces as similar as possible, morphologically, structurally and electronically, as when the nanowires are grown. Thus, it is necessary to properly prepare the nanowire to be studied in UHV by STM. Chapter 3 will develop the different procedures used to prepare the nanowire for STM characterization: Atomic hydrogen cleaning and the arsenic capping layer method. After that, the procedure to transfer the nanowires to a suitable substrate in UHV will be described, followed by the main structural and morphological features encountered in the sidewalls of the nanowires. It is shown that the surfaces of the nanowires prepared by both methods exhibit very dissimilar morphologies. Their morphology also changes with the nature of the semiconductor compound. This will be further explored in the rest of the chapter, in which the origin of these morphologies is related to the interaction between the electronic structure of the nanowire as well as the different thermal processes governing the defect formation barriers on the nanowire when the arsenic layer is desorbed.

As evoked in chapter 1 and developed in chapter 3, the electronic state of the surface of a III-V semiconductor nanowire is largely influence by its morphology. Then, in chapter 4 and 5, this is further extended to intentionally growth a very defective shell covering the sidewalls of a nanowire. The material used to grow the shell is low-temperature grown GaAs, which is very well known for

its optoelectronic properties. The history and properties of thin-films of low-temperature GaAs will be detailed in chapter 4, followed by the description of the growth method used to incorporate such material as a nanowire shell. These nanowire will be characterized, using TEM, STM, cathodoluminescence and optical pump-probe characterization techniques, to further confirm that the intended shell shows indeed the properties of low-temperature grown GaAs thin films.

Finally, as with many other fields of semiconductor devices, nanowires offer interesting possibilities as terahertz (THz) emitters due to their reduced shape and inherent antenna geometry. In the first part of the chapter 5, an introduction to the field of THz optoelectronic as well as the state-of-the-art of THz devices using nanowires will be reviewed. In the second part of the chapter, the effect of the low-temperature grown shell on the THz emission from the nanowires is described and compared with the THz emission produced by similar nanowires but without any shell added. As it will be described, there are unexplored interaction mechanisms between the photoexcited carriers and the nanowires, when the former are produced within the structure of a nanowire, that influence the emission of radiation from nanowires, and particularly from nanowires with low-temperature grown shell. The challenges and opportunities of such devices are discussed in the final part of the chapter.

# Chapter 1

# Semiconductor Nanowires: Applications and growth

## 1.1 Introduction

A nanowire is a semiconductor compound that has adopted a one-dimensional wire-like shape as a consequence of the growth mechanism involved in its synthesis. Semiconductor nanowires are grown using the so-called VLS growth mechanism, that was for the first time described in 1964 in the work of Wagner and Ellis[1]. In VLS(Vapor-Liquid-Solid) growth, the vapor fluxes are directed to a metallic liquid droplet, which is usually gold, that drives the growth of the semiconductor material. It acts as a preferential nucleation spot and as a catalytic center, giving rise to an enhanced vertical growth of the material across the liquid droplet interface. The semiconductor nanowires grow following a crystalline bulk direction with faceted sidewalls. The resulting nanowires have a variable length, from several micrometers down to hundreds of nanometers, as well as variable diameter, from tens of micrometers down to few nanometers, depending on the growth conditions.

Semiconductor nanowires are synthesized in the same range of variability in material and complexity as their thin-film counterparts: they can be made of silicon or germanium as well as III-V, II-VI, III-N and metal-oxide compounds. They can be as well heterostructured and doped with equal level of versatility as the epitaxially grown semiconductors, and using the same kind of epitaxial systems: MBE, CVD or MOVPE reactors. Therefore, they inherit the well established understanding and vast span of applications that semiconductors compounds enjoy nowadays. The relevant novelty that nanowires add is the higher weight of the surface with respect to the bulk volume in the geometrical shape of semiconductor material, as they adopt wire-like geometries when grown with the VLS mechanism. In other words, they have a pronounced surface-to-volume ratio. This has an impact on the physical properties of the semiconductor material grown as a nanowire as it can enhance or even change completely the

integration with technological devices as well as its performance. For example: the growth of heterostructured and doped nanowires is achieved in the same way as with thin-film semiconductors, by changing relative pressure between the different precursors and/or atomic beams [2]. When the nanowire grows from the metallic liquid droplets involving the VLS mechanism, it adopts an almost perfect crystalline structure free from defects. This is a consequence of this high aspect-ratio that confers the nanowire a mechanism to accommodate stress without creating defects [3]. Then, the strain associated with heteroepitaxial growth is completely reduced as every monolayer of the nanowire can be radially extended to accommodate for the variation in bond length between two different types of semiconductor compounds. As nanowires are grown layer-by-layer in a direction dictated by the substrate plane orientation, when a new compound is added, it is perfectly incorporated along the length of the nanowire forming sharp interfaces. It is possible to synthesize novel nanowire heterostructures such as InAs/InSB, a compound combination which is not possible in thin-film epitaxy due to the large lattice mismatch between InSB compound and the rest of III-V semiconductors[4], such nanowires could perform notably as thermoelectric devices. Radial heterostructured nanowires can also be synthesized by changing the growth conditions (normally reducing the pressure of the vapor phase) to favor growth of the material in the sidewalls of the nanowire instead of inclusion through the liquid droplet, which promotes vertical growth.

Another novel feature of semiconductor nanowires is that they normally grow adopting crystalline phases that are not encountered on thin-film or bulk semiconductors. This phenomenon is known as polytypism. III-V materials, normally having zinc-blende(ZB) crystalline phase in bulk, can switch to wurtzite(WZ) crystalline phase when grown as a nanowire, as it was soon realized analyzing, by X-ray diffraction, the crystalline structure of GaAs or InAs nanowires grown by MOVPE [5]. The opposite is also true, materials normally crystallizing as WZ can present ZB inclusions along their structures, such as III-N nanowires [6]. This behaviour is related to the higher surface-to-volume ratio of the nanowires: as the surface energy of a WZ nanowire facet can be lower than their ZB counterpart, it potentially favours the formation of WZ crystallites The dynamics of the growing nanowires is very complex as there are several material fluxes and different physical mechanisms involved at the same time, and having that the energetic difference between the growth of WZ or ZB phases is very narrow, at the temperature in which nanowires are grown the two phases can be present in the body of the nanowire, normally intermixed. Polytypism needs to be controlled because in polytypic nanowires the intermixing of phases increases carrier scattering and diminishes the mobility along the nanowires, thus lowering its performance as electronic devices, as shown with InAs nanowire-FETs [7]. On the contrary, polytypism can improved some physical properties of a nanowire; as there is a small difference in band gap between the WZ and ZB phases of the same compound, semiconductor nanowires with different crystal phases along their structure can induce a change of their optical properties due to the formation of confined heterostructures with band stagger-

ing between WZ and ZB phases. The emitted wavelength in photo-luminescence measurements of GaAs nanowires with increasing WZ content has been found to be related to the formation of such heterostructures [8]. There is a large effort to understand and optimize the conditions whereby the occurrence of one crystal phase is favoured despite the other. Thus, some of the main physical mechanisms in play as well as the polytypic behaviour of different III-V nanowires will be further developed in section 1.3.2.

Nanowires have been proved to be suitable materials as a new archetype of nanostructures. Integrated into next-generation devices, overcoming miniaturization problems within thin-film technologies and adding new and promising features in electronic and optoelectronic circuits: Either as one single nanowire device or as a part of an ensemble of different nanowires. Here we review some examples to see how nanowires withstand against some of the devices for which semiconductors are vastly used in nowadays technological applications.

- **Nanowires as Field Effect Transistors(FET):** Field effect operation has been realized with semiconductor nanowires. There are several examples reported in the literature; from the first demonstration of a Silicon nanowire-FET [9] and a Germanium nanowire-FET[10] to high performance III-V devices such as InAs nanowire-FET [11]. In all cases, the nanowires are cleaved after growth by sonication and deposited on a suitable substrate that acts as a gate (normally highly doped $Si$ with $SiO_2$ layer on top). After deposition, Au/Ti or Al/Ti contacts are formed on top of the ends of the flat lying nanowires by electron beam lithography, to serve as drain and source electrodes. Good performance is reported in [9] and [10], but the measured carrier mobility is always lower than in planar MOSFET due to the detrimental effect that the surface scattering has on the free charge carriers. The mobility has been improved by passivating the surface of the nanowire to reduce charge trapping produced by surface dangling bonds or defects. Also, hysteresis effects (a change in the source-drain current with the direction of the sweeping voltage) are generally present in Nanowire-FET devices. This is a consequence of the small contact area between the nanowire sidewalls and the substrate, that affects the gate capacitance. To overcome this problem, a top-gate has been deposited conformal to the nanowire body in order to increase the contact area. Higher yield in mobility is found for InAs nanowires using this technique, as high as $6800cm^2/Vs$ [12], but still lower than bulk InAs $33000cm^2/Vs$. This is shown in figure 1.1, frame a), where the scheme of the proposed device is displayed (a1) along with a SEM picture (a2) and a characteristic curve of the $I_{DS}$ current as a function of the gate voltage ($V_{GS}$).

- **Nanowires as Optical Devices:** The optical and optoelectronic properties of the nanowires have become a very active area of research, as many interesting optical features arise when the nanowires interact with light. Nanowires have been proved to act as waveguides[13], antennas[14],

lasers[15][16] or LEDs with selective wavelength emission[17]. As a waveguide, the nanowire inherent geometry, as well as its small diameter and material variability, can effectively confine light into the nanowire body with guided wavelengths ranging from UV down to infrared. Light confinement and waveguiding was shown to operate in $SnO_2$ nanowires, in which a photo-luminescence (PL) pulse was activated in one end of the nanowire and the transmitted light reached the other end, showing spectral signatures proper of light confinement in longitudinal optical Fabry-Perot type modes [13]. The length of the nanowire and the type of semiconductor compound (which changes the refraction index) can be used to craft the number of Fabry-Perot modes in the nanowire. Lasing has also been achieved in CdS nanowires [15] due to the possibility to stand Fabry-Perot modes with sufficiently well cleaved nanowires. Onset of laser emission appears either by optically pumping the nanowire with a focused laser or by electrically pumping it by embedding the nanowire in a p-doped Si surface with a metallic layer on top (to selectively inject either electrons or holes in the p-n junction formed by the Si-CdS NW junction). In [17], nanowires were integrated as part of a multiwavelength photonic device by creating a cross-contacted network of p-n junctions between different II-VI or III-V nanowires and a p-doped Si nanowire as it is displayed in figure 1.1b1. The wavelength of the LED emission is tuned by selecting which p-n junction emits, as shown in figure 1.1b2. This shows the potential that nanowires can have as integrated components in nanophotonics devices. Also, advanced compounds with proved lasing capabilities such as multi quantum well(MQW) InGaN-GaN heterostructures have been successfully grown as nanowires in [16], where InGaN-GaN MQW heterostructured nanowires have been grown by MOVPE with a good control on the number of InGaN quantum wells embedded radially on the GaN nanowires. The schematics of these nanowires is depicted in figure 1.1b3. The InGaN-GaN MQW nanowires present WZ structures. In figure 1.1b4, it can be seen the PL emission from the nanowire ends as they are excited by a pumping laser. Furthermore, when increasing the power of the pumping laser there is a threshold for which lasing operation in the nanowire appears, detected as a prominent spectral signal with several fringes (figure 1.1b5, red curve), at a smaller wavelength than the PL emitted signal (figure 1.1b5, blue curve). Also, the wavelength at which laser operation onsets as well as the main PL emission peak of these nanowires has been proved to shift with the Indium content of InGaN quantum wells. Additionally, the power of the laser emission increases with the number of quantum wells.

- **Nanowires as Sensors:** Despite the detrimental effects that unpassivated nanowire surfaces can have for the performance of nanowire-FET devices, it can be also advantageous for the use of nanowires as sensors with very high sensitivity. The depletion or accumulation of charge carriers due to the interaction of surface defects or dangling bonds with exter-

nal gas particles affects the transport properties along the nanowire. The reason is that the extension of the depletion layer and the nanowire radius have the same order of magnitude. Therefore, changes in the charge state of the surface have a similar effect on the transport properties of the nanowires as if there was an external gate. It has been proved that a p-doped Si nanowire-FET can be used as a nanosensor of acidity (pH). This is achieved by coating the surface of the nanowire with PDMS [18]. Nanowire sensors are inserted into a solution. By decreasing the pH in the solution, the protonation of the surface depletes the valence band of the boron p-doped nanowire affecting the carrier transport along the length of the device. When the pH increases, the surface is deprotonated and the conductance increases accordingly. This concept is further extended when the surface of the Si NWs is functionalized with biomolecules to use them as biomolecular detectors of high precision. Also, n-doped $SnO_2$ nanowire-FETS have been used as oxygen and carbon monoxide detectors [19]. When oxygen content in the environment is increased, the oxygen molecules react with the vacancies of the nanowire surface, depleting it from electrons and reducing the conductivity along the nanowire. The reverse reaction is also produced if CO is inserted in the gas environment. As CO reacts with the oxygen vacancies converting $CO$ to $CO_2$, one electron is released to the nanowire conduction band, thus raising its conductivity. These two chemical reactions with the nanowire surface are schematized in figure 1.1c1, and the performance of the device as a function of time is seen in figure 1.1c2, where the variation of drain-source current is monitored as a function of time when the carbon monoxide content in the chamber is varied.

- **Nanowires as Solar Cells:**. It was shown by Kayes, Atwater and Lewis [20] that a nanowire having a radial core-shell structure forming a p(core)-n(shell) junction can be used as a photovoltaic device. In this geometry, the minority carrier diffusion length is comparable to the size of the shell of the nanowire. As the space charge region of the junction is directed radially all along the nanowire length, photoexcited-carriers can be separated well before they are recombined. This nanowire design has been realized for coaxial p-i-n Si NWs grown by CVD [21]. The nanowire photovoltaic device shows a 3.4% in efficiency, rather low compared to the values obtained in commercial Silicon solar cells based on thin-film technologies. One argued explanation is the polycrystalline nature of the outer shell and the role of the surface as recombination center. Furthermore, in order to contact the nanowires, they have to be disposed lying flat along the substrate, then, the light absorption on the nanowire is reduced as the effective area in which light impinges is smaller. However, optical absorption in the nanowires can be engineered, as they stand what are called leaky-mode resonances (LMRs) [22]. In these modes, light coupling with the cavity of the nanowire sustains resonance modes that are extended beyond the size of the nanowire diameter. As a result, the effective ab-

sorption on the nanowire can be enlarged by playing with its dimensions. In line with these results, it has been recently found that a single p-i-n GaAs nanowire solar cell can withstand remarkable light conversion efficiencies thanks to these leaky-modes, as their effective optical absorption increases [23]. In these devices, a single nanowire stands vertically, as shown in figure 1.1d1. It consists of a self-catalyzed GaAs nanowire with a coaxial p-i-n junction grown on top of a p-doped Si substrate with a thin oxide layer. After that, the nanowire device is embedded in SU-8 photoresist. In the top facet of the nanowire, a transparent ITO electrode is added. In 1.1d2, the doping profile of the nanowire is shown: the core is made of p-type Si doped GaAs, with an intermediate intrinsic GaAs layer and a n-type Be doped GaAs shell. When illuminated, it shows the characteristic behaviour of a p-i-n Solar cell device with apparent efficiencies up to 40%.

There are many additional topics in the broad field of nanowire devicing. Semiconductor nanowires have shown promising thermoelectronic capacities[24] or integration as anodes or cathodes into lithium-ion batteries [25]. They have excellent elastic properties which permit to fabricate electromechanical components with nanowires acting either as resonators[26] or piezoelectric actuators[27]. It is also possible to use nanowires networks as highly sensitive electrodes in functional nanoelectronic interfaces to biomolecules, cells and tissue [28]. Finally, nanowires are also being part of cutting-edge fundamental research such as the search for the Majorana fermions [29], with hybrid superconductor-semiconductor nanowire junctions or the realization of single-photon nanowire emitters [30].

There is a common concluding thread between all the different integration schemes in which nanowires take part in potential nanotechnological devices, it is the need to understand better and master the reproducibility in size and dimensions of the growing nanowires, to control its crystalline purity and the role that the surface plays on their transport, optical and chemical properties. In order to achieve this, large amount of research is devoted to resolve the fundamental aspects of VLS growth of semiconductor nanowires. The next section will develop some of these aspects explaining the interplay between the different physical mechanisms in VLS growth of nanowires that influence the aspect-ratio and structure of the resulting wires. Starting from the general description and historical context of VLS growth, in section 1.2, to the working principle of the main fabrication machines, MBE and MOVPE,in section 1.2.1 and 1.2.2. Later, reviewing the theoretical understanding and the modeling of VLS growth: supersaturation (section 1.3.1), the influence of nucleation on the crystal phase (section 1.3.2), the Gibbs-Thomsom effect (section 1.3.3), the diffusion-induced growth regime (section 1.3.4), the growth regime for self-catalyzed III-V nanowires (section 1.3.5) as well as the recently discovered self-equilibration regime (section 1.3.6) to finish with a brief account of some other advanced or complementary topics in modeling (section 1.3.7).

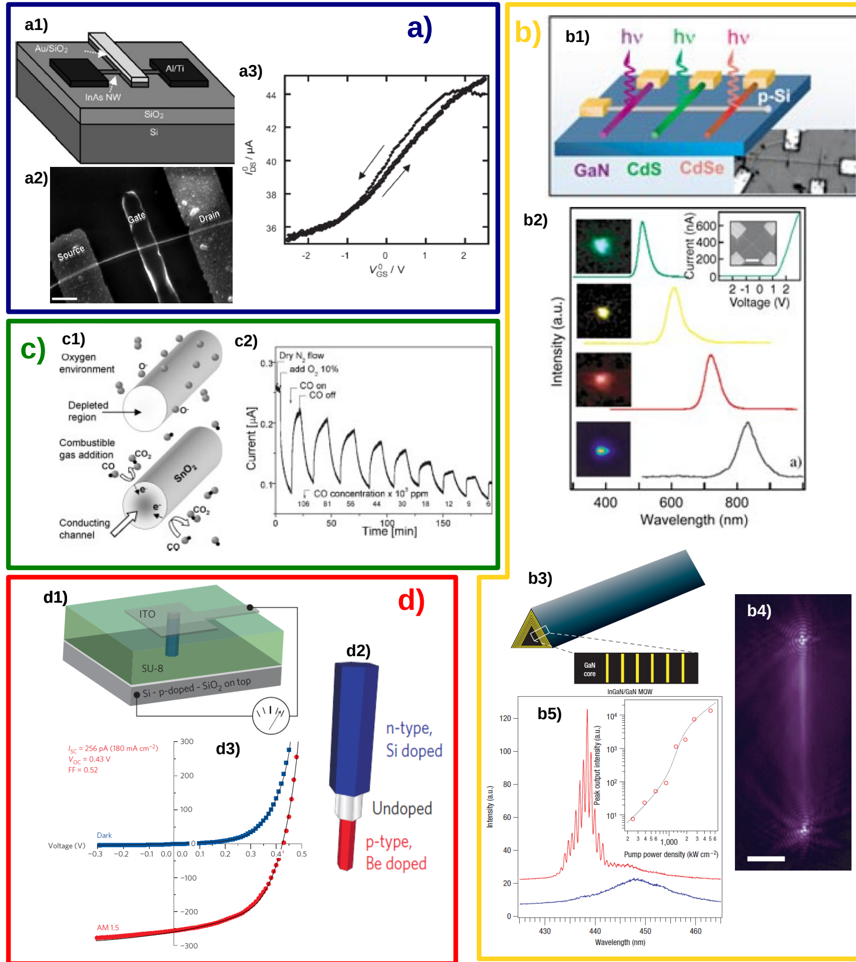


**Figure 1.1:** Frame a (blue): a1) Scheme of the InAs NW-FET device deposited on the oxidized Si substrate with the $Au/SiO_2$ top gate. a2) SEM image showing the final geometry of the proposed device (Scale bar: $1\mu$m.) a3) Graph showing the onset of drain-source current as a function of the gate voltage for different voltage sweep directions (black arrows). Extracted from [11] Frame b (yellow):b1) schematics and SEM image of a tricolor nanoLED array formed by the crossed p-n diodes of p-Si and GaN(pink), CdS(green) and CdSe(red), respectively. $5\mu$m of separation between the emitters. b2) EL spectra and images taken from different crossed p-n diodes between p-Si and n-CdS, CdS, CdSe, and InP, respectively (top to bottom). Inset shows I-V curve and SEM image for a p-Si/n-CdS crossed p-n junction (scale bar $1\mu$m). From [17]. b3) Schematic picture of the MQW nanowire with a magnified cross-sectional view of a nanowire face highlighting the InGaN/GaN MQW structure. InGaN layer is indicated in yellow. b4) Photoluminiscence image (False color) recorded from a GaN/In(0.05)Ga(0.95)N MQW structure. Scale bar is $5\mu$m. b5) Photoluminiscence spectra of a 26MQW nanowire recorded at excitation power densities of 250 (blue) and 1,300 $kWcm^{-2}$(red), respectively. Offset of spectra is set for clarity. In the inset: Log-log plot of output power versus pump power density. From [16]. Frame c(green): c1) Schematic representation of the $SnO_2$ nanowires with their surfaces reacting with the different gaseous environment, either with Oxygen molecules (up), taking out electrons from the nanowire , or with CO molecules (down) , adding electrons to it. c2) Current-time graph as a function of the different gas environment injected in the chamber. First, the current decreases when the oxygen is added, and then fluctuates whenever CO content in the chamber is changed. From [19]. Frame d(red): d1) Schematic of the vertical single-nanowire radial p-i-n device connected to a p-type doped silicon wafer by epitaxial growth. d2) Doping structure of the core-shell nanowire. d3) Current-voltage characteristics of the device in the dark and under AM 1.5G illumination, showing the figure-of-merit characteristic. Extracted from [23]

## 1.2 VLS Growth Mechanism

VLS(Vapor-Liquid-Solid) is a physical mechanism whereby growth of solids and nanomaterials from a liquid phase between a vapor and solid phase is realized. The liquid phase is a metallic droplet acting as a sink for vapor precursors and at the same time as a source for solid phase incorporation at the liquid-solid interface . It was described for the first time in 1964 by Wagner and Ellis in order to explain the predominance of silicon whiskers when using silicon tetrachloride ($SiCl_4$) as a precursor for chemical vapor deposition (CVD) growth of silicon in a (111) oriented substrate covered with micrometric sized gold droplets [1]. After $SiCl_4$ exposure at high temperatures (950 °C), they observed a dispersed array of whiskers of several micrometers of length and a few micrometers of diameter, regular flat lateral facets and a crystallized gold droplet on top. The whiskers where made of silicon that had grown axially in the <111> direction and presented (112) or (110) lateral facets. In order to explain these results, and given the temperature of the substrate during the $SiCl_4$ deposition, the VLS mechanism was proposed: At 950 °C, gold melts on top of the silicon substrate forming droplets of hemispherical shape. These droplets act as a catalyst center to promote the decomposition of the silicon tetrachloride ($SiCl_4$) precursors on its surface, followed by diffusions of Si atoms into the liquid droplet. As Si atoms are incorporated, alloying between silicon and gold starts to be developed. But as the temperature is above the eutectic temperature of Si-Au alloy, the droplet remains liquid and the supersaturation of Si on the Au droplet begins to increase, eventually leading to the precipitation of silicon at the interface between the liquid and the substrate. Precipitation starts with the formation of a small Si nucleus at the liquid-solid interface that is increased until completion of a monolayer above the (111) plane of the substrate. Silicon grows constrained in the dimensions of the hemispherical droplet at a higher rate than the rest of the substrate from where the vapor is directly in contact with the solid, thus forming a wire-like shape. In figures 1.2a and 1.2b the VLS mechanism is shown schematically: the liquid droplet promotes the growth of the Nanowhisker in the Vapor-Liquid-Solid environment, as the Si(111) oriented whisker grows, the liquid droplets remain wetting the top facet of the whisker, and effectively precipitating the growth of subsequent layers of Si below. A SEM image of the first whisker discovered by Wagner and Ellis is displayed in figure 1.2c. It can be seen the high aspect-ratio of the whiskers with a faceted structure on the lateral sidewalls, and a small crystal protrusion on top of the whisker, which is the crystallized gold droplet after growth.

Years after the discovery of VLS growth mechanism, as the refinement of the epitaxial growth and crystal characterization techniques was achieved, the size and distribution of the droplets have been reduced down to the nanometric scale, leading, by the same VLS mechanism, to the growth of nanometric thin and micro-metric long whiskers, now denominated nanowires. It has been found that the VLS mechanism could be extended to span the growth of not only Si nanowires, but also III-V, II-VI, III-N compounds [31][2][5], as well as oxide

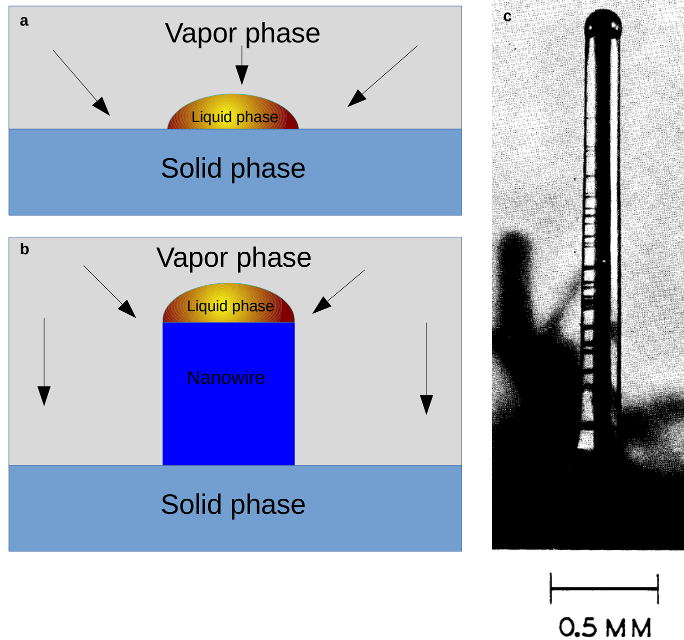


**Figure 1.2:** (a)Schematic view of VLS growth mechanism, involving the vapor, liquid and solid phases. Vapor interacts with the liquid and the substrate. Growth occurs at the interface between the liquid and the substrate where the whisker starts growing vertically (b). (c) SEM image of the micro-metrically sized silicon whisker after growth, the different contrast in the lateral sidewalls arise from the different facets occurring aside the <111> growth direction. In top of the whisker, the crystallized gold remains. Extracted from [1].

semiconductor [32] nanowires. Furthermore, the metallic liquid droplet driving the growth can be composed of other metals rather than gold [33], as long as the metal remains liquid when vapor precursors are incorporated, and catalytic decomposition and dilution of the vapor species is promoted without aggregation of the metal to the growing nanowire. Typically, noble and transition metals fit these requirements but still gold keeps being the most widely used metal to promote catalyzed growth.

Nowadays, frequently used techniques for nanowire growth are MBE (Molecular Beam Epitaxy) and MOVPE (Metal-Organic Vapor Phase Epitaxy), but also related epitaxial techniques (as laser-assisted catalytic growth or plasma-enhanced CVD), with growth promoted by the VLS mechanism. Gold is the most frequently used metal as the liquid droplet for Si, Ge, III-V and II-VI semiconductor nanowires, and gallium and indium liquid droplets to grow self-catalyzed III-V semiconductor nanowires. However, it should be noticed that the VLS mechanism is not restricted to the conditions herein proposed, as nanowire growth has been realized even when the droplet is solid [34], what is called Vapor-Solid-Solid(VSS) growth mode, and when the droplets are diluted in a solution, what it is called Solution-Liquid-Solid(SLS) growth mode [35]. The common feature is that an intermediate medium (usually but not

only, liquid) increase the rate of solid growth with respect to the normal interface between a supply and a solid (vapor-solid, solution-solid) and constrains it to its dimensions. The intermediate medium is at the same time a catalyst for the supply and a preferential nucleation environment for the solid.

Parallel to the experimental development of semiconductor nanowire growth, a large effort has been made to give a consistent physical explanation that fits in the frame of classical growth and nucleation theory. In this regard, research has been pioneered by Givargizov in the 70's [33], who underlined the importance of size effects and supersaturation in the growth rate of the whiskers and predicted the important role that adatom diffusion along the solid phase can have in the kinetics of growth. As the diameter of the nanowires has been shrinked, the interplay between nanowire diameter, crystal orientation, polytypism and growth rate in gold catalyzed or self-catalyzed schemes requires refined models [36][37][38][39][40]. An overview of the main growth models of semiconductor nanowires is developed in section (1.3), putting the focus on III-V semiconductor nanowires.

### 1.2.1 Molecular Beam Epitaxy

Molecular Beam Epitaxy (MBE) is a technique used to grow solids, thin-films or nanostructures epitaxially [41]. This is achieved by inserting the atomic species as vapor beams in a low pressure (high vacuum) chamber where the substrate lies. The different atomic species are evaporated by heating solid sources of the different materials in effusion cells that are placed surrounding the main chamber. The atomic beams are incorporated into the main chamber by opening or closing shutter doors connecting the effusion cells (at a higher pressure) with the main chamber. As the pressure in the main chamber is very low, the beam travels ballistically to the substrate to arrive sequentially or simultaneously as the user decides. Controlling the atomic fluxes (through Equivalent Beam Pressures(EBP) in the different effusion cells) and the temperature of the substrate, complex heterostructures, doped semiconductor nanostructures and thin-films can be grown with great control in thickness and purity. Also, as there is high vacuum in the main chamber, MBE reactors can be equipped with a RHEED (Reflection-High Energy Electron Diffraction) system that allows to monitor the thickness and structure of the material at the same time as it is being grown, through the diffraction pattern and intensity of a reflected electron beam on the surface. In the figure 1.3a, a sketch of a MBE reactor is displayed, with the different effusion cells placed around the main chamber where the substrate and RHEED system are. For the context of semiconductor nanowires, two important features of MBE growth are the high diffusivity of the adsorbed atomic species on the substrate and the ballistic nature of the beam that changes the effective section of collection of atomic species by the catalyst droplet [42], although the whole substrate stage is usually rotating to homogenize deposition.

### 1.2.2 Metal-Organic Vapor Phase Epitaxy

Metal-Organic Vapor Phase Epitaxy (MOVPE) is a technique to grow solids, thin-films or nanostructures epitaxially in a high vapor pressure environment. The vapor contains Metal-Organic precursors that are decomposed on the surface of the substrate or in the liquid droplet through catalytic reactions, leaving the atomic species free to diffuse along the surface to promote the growth of the material [43]. Metal-Organic precursors arrive at the main chamber sequentially or simultaneously through several separated pipelines, where the different metal-organic species are kept in liquid form in special vessels called bubblers until they are introduced to the main chamber. A carrier gas, such as hydrogen, is fluxed through the bubblers, picking up the complexes and transporting them to the main chamber. The amount of metal-organic species transported in the vapor depends on the rate of carrier gas flow and on the temperature in the bubbler. Additionally, other atomic species, such as arsenic or phosphor are transported directly to the main chamber in a vapor phase, as they form gaseous species called tryhydrides. Figure 1.3b illustrates the main elements of a MOVPE chamber. Important features for nanowire growth are the higher pressure of the vapor phase keeping growth closer to thermodynamical equilibrium and the collection of the atomic species. Indeed, they are collected from the surrounding vapor at all angles. Also, diffusion of atomic species on the substrate is more influenced by the vapor supersaturation than in MBE systems [42]. Typical organometallic complexes for the growth of III-V semiconductors are Trimethylgallium (TMGa), Trimethyl antimony (TMSb), Trimethyl Indium (TMIn) and the tryhydrides Arsine(AsH3) and Phosphine(PH3).

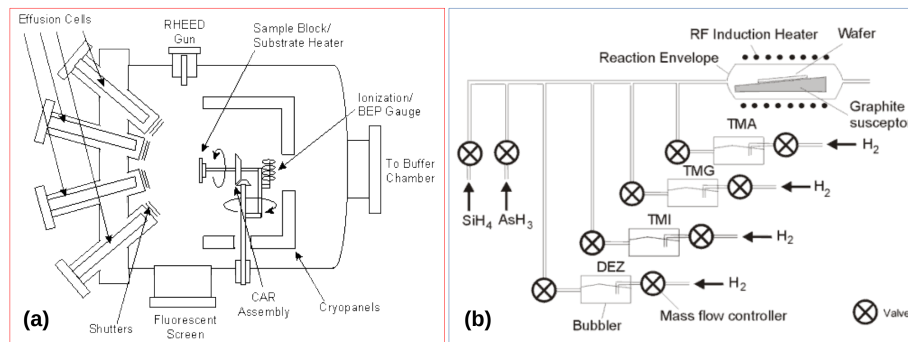


**Figure 1.3:** (a) Schematic view of a MBE growth chamber. Several effusion cells with the different solid sources pointing to the stage where the substrate lies, the stage can be heated and rotated. An electron gun and fluorescent screen are placed aside the chamber to track growth (RHEED). (b) Schematic view of a MOVPE growth chamber. The metallorganic complexes are kept in bubblers in separated chambers connected to the main reactor environment through valves and hydrogen pipelines.

## 1.3 Modeling Semiconductor Nanowire Growth

Modeling nanowire growth when the VLS mode is involved takes into account primarily the physical conditions whereby a solid nucleus precipitates at the liquid solid interface of the growing nanowire. It has been proved [37] [44] that growth of a nanowire proceeds one semiconductor monolayer at a time, and each monolayer starts with a single nucleus formation that rapidly spreads to form a monolayer whose area equals the nanowire section. In nucleation theory, the probability to form a stable solid nucleus depends exponentially on its free energy of formation, the latter being proportional to the degree of supersaturation. Then, the growth rate of the nanowire (length changes with time: $dL/dt$) can be expressed as:

$$dL/dt \propto \exp(\Delta G/k_B T) \tag{1.1}$$

Supersaturation in the liquid droplet is not exactly known and cannot be measured *in-situ* while the nanowires are growing. It is dependent on the concentration of the atomic species in the alloy formed at the liquid phase. In general, this concentration varies according to the material balance on the droplet, which depends on the different atomic fluxes exchanging matter with it. Figure 1.4 shows the main ways from which material balance in the droplet changes, they can be listed as:

- **Absorption from the vapor phase:** The rate at which atomic species are adsorbed at the liquid droplet interface and incorporated into it varies with the pressure of the gas phase and the catalytic efficiency, as well as the shape of the droplet. In MBE, the atomic fluxes arrive ballistically to the growth chamber with a fixed angle and momentum. Its magnitude is estimated with the equivalent beam pressure measured on the effusion cells and with the equivalent planar growth rate of the semiconductor material. In this case, the droplet operates as a physical catalyst whose collection efficiency depends on its capture area (effective cross-section). For MOVPE, the pressure on the growth chamber is higher and the vapor fluxes arrive to the droplet from all directions. The droplet acts as a chemical catalyst, the absorption rates depends on the efficiency of decomposition of the metallorganic species as well as on the droplet capture area.

- **Desorption from the liquid phase:** The rate at which atomic species leave the liquid droplet depends on the supersaturation difference between the liquid droplet and the vapor phase. Size effects such as Gibbs-Thomsom can be important to enhance this contribution. It also varies with the area of the droplet.

- **Diffusion:** Depending on the position at which the atomic species are deposited from the vapor, up to two diffusion fluxes have to be considered. First, the diffusion flux from the substrate to the nanowire base, and from

there to the liquid droplet. Second, the diffusion flux coming from the atomic species deposited directly on the lateral facets of the nanowire during growth. For III-V nanowires, only group III atomic species diffuse, as it is known that group V atoms are highly volatile and do not diffuse. The diffusion current has to be resolved obtaining, normally numerically, the gradient concentration profile either on the substrate or on the nanowire sidewall and the diffusivity, which depends on the diffusion length of a particular adatom and its lifetime before being desorbed or recombined.

- **Nanowire growth:** The rate at which a nanowire monolayer grows depends on the probability to form a critical nucleus and on the section of the nanowire from where it extends.

The different flux-rates between absorption/desorption, diffusion and nanowire growth at the nanowire upper facet determine the rate at which the nanowire grows. The reason is that nucleation is an stochastic process whose probability depends on the varying concentration of species in the liquid droplet and the interfacial forces between the nucleus and the environment. So, as long as it is considered that the concentration in the droplet is high enough so that a nucleus can be formed with similar probability at all times and that the time between nucleations is much larger than the time to grow a monolayer, the limiting factor on the growth rate of the nanowire will be the balance between the different rates at which particles are incorporated or leave the liquid droplet when steady-state conditions are reached. The main models accounting for the different growth-regimes encountered in nanowire growth will be developed in sections 1.3.1, 1.3.4, 1.3.5 and 1.3.6 .

Furthermore, it is needed a physical explanation for the appearance of several polytypes along the axial length of the nanowire. This is explained considering what is the probability to form a given nucleus, WZ or ZB in the environment of the liquid droplet. This assumption will be further extended in section 1.3.2.

Either by MBE or MOVPE, post-growth analysis of the nanowires relies on characterization techniques using electron microscopy techniques such as SEM or HR-TEM to analyze the shape, volume and crystal structure of the nanowires or scanning probe microscopes, such as STM or AFM in order to determine the structural and electronic properties of the nanowire surfaces. Any growth model has to be able to explain the interplay between the parameters that the user can change when the growth takes place and the resulting structural changes on the nanowires.

### 1.3.1 Supersaturation

In the frame of crystal growth, supersaturation is defined as the difference in chemical potential between the supply phase (vapor or liquid) and the growing phase (substrate or nanowire).

$$\Delta\mu_{vs} \equiv \mu_{vapor} - \mu_{solid} \tag{1.2}$$

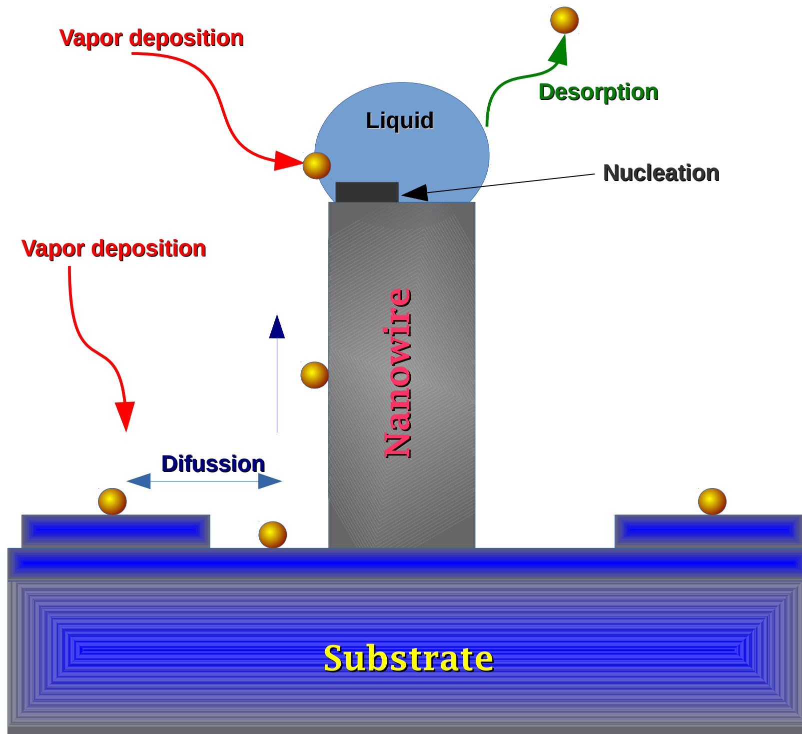


**Figure 1.4:** Sketch showing the different material fluxes involved in VLS growth of semiconductor nanowires.

To have solid growth, the chemical potential of the supplying phase has to be larger than the chemical potential of the solid phase. In this way, there is a net transfer of material from the vapor to the solid in such a way that the equilibrium concentration of the growing phase increases and becomes supersaturated [45]. Otherwise, when the chemical potential of the vapor phase equals the chemical potential of the solid phase, there is no net material transfer and the supersaturation is zero, the system is at equilibrium. Finally, if the chemical potential of the solid phase gets larger than the one of the vapor phase, supersaturation becomes negative (as defined before) and there is desorption from the solid rather than incorporation to it. The system acts against the imbalance in chemical potential to reach equilibrium between phases. Therefore, the thermodynamic driving force for growing solids or nanowires is the difference in chemical potential, that is, the supersaturation.

In VLS growth, three phases intervene : Vapor, Liquid and Solid. The differences in chemical potentials between all the phases has to be considered to understand the growth of a nanowire. As stated in reference [45], the chemical potential of the vapor phase has to be larger than the one of the solid phase to have epitaxial growth of any sort. Also, the chemical potential of the liquid droplet has to be larger than the one of the solid phase in order to precipitate a solid nucleus from which the nanowire layer is formed. Finally, in order to have a

net transfer of atomic species from the vapor to the liquid droplet, the chemical potential of the vapor phase should be larger than the chemical potential of the liquid phase. Schematically put:

$$\mu_{vapor} \geq \mu_{liquid} \geq \mu_{solid} \tag{1.3}$$

Or, viewed as supersaturation differences:

$$\Delta\mu_{vapor-solid} \geq \Delta\mu_{vapor-liquid} \tag{1.4}$$

$$\Delta\mu_{vapor-solid} \geq \Delta\mu_{liquid-solid} \tag{1.5}$$

In view of equation 1.5, nanowire growth is thermodynamically allowed but still the growth rate of the solid substrate around the liquid droplets should be larger than in the nanowire, considering that growth rate is related to the degree of supersaturation. But as showed in [45], it is necessary to consider that the droplet is not a large, sparse liquid but a small, hemispherically shaped one which holds a triple-phase line (TPL) between the solid, the liquid and the vapor phase. Under these conditions, the probability to form a stable nucleus gets increased at the triple-phase line of the droplet as it is a preferential nucleation spot wherefrom a nanowire layer grows. Also, in [38], it was proved that there is a net diffusion flux of adatoms from the substrate to the liquid droplet, which has to be included in the balance of chemical potentials and increases the liquid droplet supersaturation, enhancing the growth rate of the nanowires with respect to the substrate.

### 1.3.2 Crystal Phase

Compound semiconductors present two different types of crystal phases: the zinc-blende(ZB) crystalline structure, and the wurtzite crystalline structure (WZ). The Zinc-Blende is a cubic structure characterized by the arrange of the two types of atoms of the binary compound as a Face Centered Cubic (FCC) crystalline lattice with double basis. This is equivalent to two single-atomic FCC lattices of the different elements shifted to each other in such a way that their covalent interaction has tetrahedral symmetry, every atom is bonded covalently with four atoms of the other element. This is represented in figure 1.5a where the atomic species are modeled as small spheres of different colors. It is seen that every atom of one group (III or II) is coordinated with four adjacent atoms belonging to the other group(V or VI) of the compound. Similarly, the wurtzite crystalline structure is an hexagonal structure characterized by the formation of a Hexagonal Closed-Packed (HCP) structure with double basis composed of the two atomic elements that bond together to form the semiconductor, or equivalently, two HCP lattices intertwined to give a covalent interaction with tetrahedral symmetry, as seen in figure 1.5b, only this time the orientation between adjacent tetrahedrons has a different symmetry than in the ZB lattice. The difference between ZB or WZ structures can be further understood by sequentially extending the lattice as a series of stacked

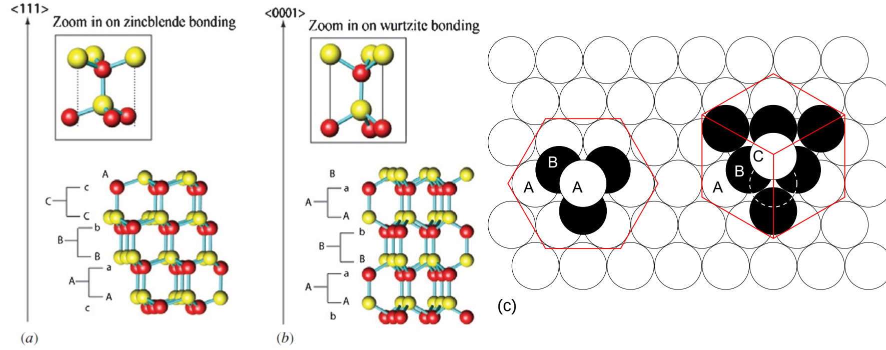


**Figure 1.5:** Bonding configuration in the Zinc-Blende(a) and Wurtzite(b) structures. The lower part of the figure represents the stacking sequences when the material is grown in the equivalent <111> (ZB) (a) or <0001> (WZ) (b) directions as viewed from the side, or <110> direction. In (c) the stacking sequence is represented in the cubic (right) and hexagonal(left) lattices as viewed from above (<111> or <0001> directions).

layers of the different compounds in such a way as to minimize the close packing between atomic elements, as it is presented in figure 1.5c. The first layer of a plane of the (111)FCC or (0001)HCP lattice (labeled as stacking sequence A) is a triangular lattice, the second layer is build up adding atoms in the intersection of the atoms on the previous layer in such a way that a new triangular lattice is formed (stacking sequence B). In order to add another layer on top of the second one, there are two possibilities to keep packing up in a similar fashion (minimizing packing and forming tetrahedral interaction with the previous layer). Either, the atoms are deposited in the intersection of the three atoms of the previous layer but with the same orientation as atoms in the first layer. Then, the stacking sequence is again A and the solid grows with hexagonal symmetry if the layers are piled up repeating the sequence ABABAB (or equivalently, the <0001> direction with respect to an HCP lattice). Or else, the atoms are deposited at the intersection of three atoms of the previous layer but their orientation is rotated in relation with the orientation of the first layer. Then, a new stacking sequence, C, arises, and the lattice is extended by piling up layers following the stacking sequences ABCABC (or <111> direction with respect to a FCC lattice) with cubic symmetry. It is straightforward to extend this construction of layered growth to binary semiconductors, only considering that each new layer forming a stacking sequence is composed of the two atomic species involved in the compound (labeled as Aa, or Bb, or Cc for each layer), as shown in figures 1.5a and b, with a side view of the crystalline structure of the ZB and WZ structures along the <111>(ZB) and <0001>WZ directions. Labeling the stacking sequences accordingly: AaBbCcAaBbCc for ZB and AaBbAaBbAa for WZ.

For semiconductor nanowires, this way of label its crystalline structure is convenient for several reasons:

- Semiconductor nanowires are usually grown along the <111> or <0001>

directions [46], constituting the most synthesized and modeled nanowire system. As growth has been proved to proceed in a layer-by-layer fashion [44][38] along this direction, it is natural to use this labeling to structurally characterize the nanowires.

- The formation of twins along the length of the nanowire. A twin is a defect in the ZB structure characterized by the appearance of a mirrored plane with respect to the previous one, inverting the stacking sequence. Twins are known to appear frequently in nanowires grown along the <111> direction [47][48]. They can be labeled as ABC**A**CBA, where the stacking plane A is the defect plane.

- The inclusions of stacking faults along the length of the nanowire. A stacking fault is a defect in the WZ structure characterized by the interruption of its stacking sequence by a C type plane, therefore giving locally a ZB structure: ABAB**C**AB. [49][46].

III-V bulk semiconductors adopt the ZB structure when they are grown, but III-N semiconductors have WZ structure. This is due to the energetic difference between WZ and ZB arising from the difference between the third-nearest-neighbour atom spacing, which is shorter for WZ structure (as seen in 1.5b). The ionic character of the chemical bond (ionicity) affect its bond-length. Compounds with lower ionicity such as the III-V tend to favour a ZB configuration because the steric hindrance between atomic elements acts against the distance between third-nearest-neighbour and prevents shorter bond-length. Other compounds, as III-N, with higher ionicity, can sustain shorter bond lengths and adopt preferably a WZ phase [46].

A striking difference when growing III-V semiconductor nanowires is that they can adopt the WZ structure as well as the ZB structure, without a clear trend between growing techniques and compound. When growing nanowires using gold as a liquid medium, the formation of WZ structure along the length of the nanowire tends to be the rule rather than the exception, for which is normally seen an apparently random intermixing between ZB sections along the nanowire with WZ intersections and twinning as well as WZ sections with several stacking faults. By controlling the experimental accessible growth conditions -temperature, V/III ratio- in MBE or MOVPE, it is possible to access growth regimes in which the nanowires that showed primarily ZB structure with several twins or WZ inclusions can change its structure to be almost completely WZ with a few stacking faults [50][46]. This is exemplified in figure 1.6a-d for a Au-catalyzed GaAs nanowire.

Also, Johansson *et.al* [47] have achieved the formation of twinning superlattices in MOVPE growth of Au-Catalyzed GaP Nanowires on top of a (111)B GaP substrate. As seen in figure 1.6e-g, they observe a periodic change in the orientation between the lateral facets of the growing nanowire after a new twin plane appears. The shape of the nanowires is the one of a truncated octahedron composed of (111)A, or (111)B planes at their facets, schematized in figure 1.6e-g. When a twin plane is formed, the orientation of the octahedron changes

because the facets growing inwards start to grow outwards and vice-versa, thus giving the nanofaceting pattern shown in the figure. It was also proved that the statistical distribution of twin planes along the length of the nanowires is correlated with the small difference in formation energy between a ZB nucleus and its twin. At the growth temperature of (500°C), thermal energy is enough to overcome energy barrier between both types of nucleus.

Furthermore, Caroff *et.al* [49] have been able to control polytypism in Au-catalyzed InP Nanowires growth by MOVPE. They discuss the possibility to tune the twin distribution and the stacking fault inclusion by changing the radius of the nanowire, which is dictated by the size of the liquid gold particle, as well as by increasing the temperature. They have shown that, by increasing the radius of the nanowire from 10 up to 140 nm, or by raising the substrate temperature from 400°C up to 480°C, a transition between nanowires showing mainly WZ structures with some stacking faults to nanowires with larger stacking fault density appears. Finally, nanowires with a single coherent ZB phase are formed. Also, they have been able to see the formation of coherent twinning superlattices at a given nanowire radius in which the formation of ZB starts to be predominant. This work opens the possibility to engineer coherent WZ-ZB superlattices by changing droplet diameter and temperature at a fixed V/III ratio.

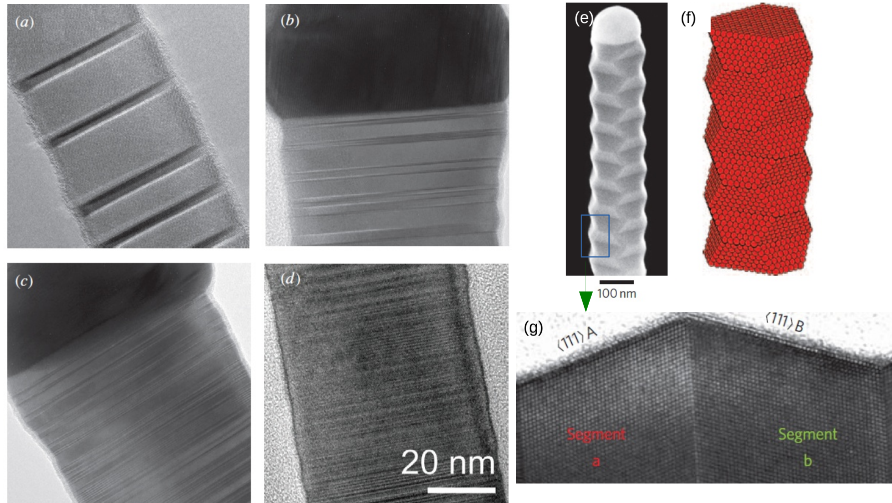


**Figure 1.6:** a) to d), series of TEM images of the crystalline stacking of Au-catalyzed GaAs nanowires as viewed from the $<\bar{1}10>$ direction and grown at different temperatures a) 350 °C, b) 400 °C, c) 500 °C, d) 550 °C. In a) the nanowire exhibits a ZB structure with some twin planes (dark contrast) interlaced along its length. When increasing the temperature, WZ segments (c) and twin density (b-d) start to increase and be intermixed to the ZB structure up to the point in which WZ and ZB are densely mixed in equal proportion (d). Extracted from [46]. e) SEM image of Au-catalyzed GaP nanowires showing the coherent twin-plane superlattice. The contrast of the image periodically changes as a coherent twin plane appears during growth, inverting the growing direction of the lateral {111}A,B facets, as depicted in f) and g). Extracted from [47]

To understand polytypism, it is necessary to consider that nanowires are

structures of nanometric diameter with a high surface-to-volume ratio. The formation of WZ sections can be energetically favorable due to the lower surface energy of its facets with respect to the ZB structure. As the growth of a nanowire layer starts with the formation of a single nucleus, Glas *et.al* [37] have developed a model to explain polytypism in semiconductor nanowires by looking at the conditions by which a WZ nucleus is formed in the liquid droplet. They have shown that nucleation is normally favoured at the triple phase line of the liquid droplet (TPL) in VLS growth for both WZ and ZB nucleus. Furthermore, if supersaturation is sufficiently high, the WZ nucleus has a reduced formation energy on the TPL. To support their arguments: First, they have observed that, during MBE growth of Au-catalyzed GaAs Nanowires over (111)B GaAs substrates, ZB phases appear systematically at the initial and final stages of growth, that is, at the beginning and at the end of the nanowire length. These two moments are characterized to be out of steady-state conditions when the concentrations (so therefore supersaturation) of chemical species in the gold droplet are lower.

Then, the following model is proposed considering the formation energy (free enthalpy) of a single nucleus in the center of the liquid droplet, which is modeled as a monolayered 2D island of length L, area A, perimeter P and height h (as sketched in figure 1.7a) to be:

$$\Delta G = -Ah\Delta\mu + Ph\gamma_{lL} + A(\gamma_{NL} - \gamma_{SL} + \gamma_{SN}) \tag{1.6}$$

In this equation, standard in classical nucleation theory, the first term accounts for the energy reduction with respect to liquid phase when a solid nucleus is formed. That is, the atoms constituting the nucleus have less energy forming part of a solid condensate than being sparse in the liquid. The second two terms refer to the energy cost to form the interfaces of the solid nucleus. Either as the lateral interfaces between the nucleus and the liquid with a given area (Ph) and interfacial energy $\gamma_{lL}$, or the upper and lower interfaces of the nucleus, which hold an equilibrium of interfacial forces between the upper facet of the nucleus and the liquid (NL), the lower facet of the nucleus and the substrate (SN) and the liquid and the substrate (SL), whenever the nucleus with area A is formed, as depicted in figure 1.7a. There is a critical nucleus size for which the energetic reduction of forming a bulky nucleus overbalances the cost of creating new surfaces and a stable nucleus is formed, which subsequently expands to grow the monolayer. In the liquid droplet, a careful attention to this balance has to be considered looking at the interplay of forces between the interfaces while the nucleus is being formed. In equation 1.6, the second term accounting for the surface energy of the lateral facets of the nucleus and the liquid droplet is equivalent between WZ and ZB structures if we consider that the nucleus is monolayered and the surrounding liquid is the same for both nucleus. In the last term, the interfacial energy between substrate and liquid, and nucleus and liquid is considered to be similar as they are both (111) planes, $\gamma_{NL} = \gamma_{SL}$. It is at the interface between the substrate and the newly formed nucleus where

the difference in energy between ZB and WZ nucleation takes place. There, the formation of a ZB is favoured because the formation of a new WZ on top of the ZB substrate requires and additional energy in order to rotate the nucleus to the WZ orientation. Therefore, if nucleation occurs away from the triple phase line, in the center or close to the center of the liquid-solid interface area, ZB nuclei are formed preferentially, and the nanowire will grow adopting ZB crystalline structure.

If, on the contrary, a nucleus is formed at the triple line phase, some fraction of the nucleus is in contact with the vapor and a new energetic contribution from the new nucleus-vapor interface influences the free enthalpy of formation of the critical nucleus. Considering that a fraction $\alpha$ of the nucleus is in contact with the vapor (figure 1.7b) and substitutes some area $\tau$ of the liquid vapor interface , the balance now reads:

$$\Delta G(\alpha) = -Ah\Delta\mu + Ph[(1-\alpha)\gamma_{lL} + (\gamma_{lV} - \tau\gamma_{LV})] + A\gamma_{SN} \tag{1.7}$$

Nucleation at the TPL becomes favorable when the difference $\Delta G(\alpha) - \Delta G(0) = \alpha Ph(\gamma_{lV} - \gamma_{lL} - \tau\gamma_{LV})$ is negative, and approximating $\tau = sin\beta$ ($\beta$ being the contact angle), this happens when $\gamma_{lV} - \gamma_{lL} - sin\beta\gamma_{LV} \leq 0$. Some of these parameters are not experimentally accessible and *ex-situ* characterization with SEM or TEM of the contact angle of the nanowire has to be performed by looking at the crystallized droplet on the tip. Although it gives only an approximate value, as the droplet is crystallized after growth, it has been approximated to be in the range $90° \leq \beta \leq 125°$. Also, $\gamma_{lL} \approx \gamma_{lV}$ is considered, as there is a 90° contact angle between the liquid droplet and the substrate before the nanowires are grown (which stands for an equilibrium of forces between the solid-liquid and the solid-vapor interface in a (111)B GaAs substrate and therefore similar interfacial energies). Finally, if $\gamma_{LV}$ approximately takes a value in between those of pure liquid gold ($1.15J \cdot m^{-2}$) and pure liquid Ga ($0.72J \cdot m^{-2}$(ref 19 of [37]), the condition $\gamma_{lV} - \gamma_{lL} - sin\beta\gamma_{LV} \leq 0$ is satisfied and nucleation is thermodynamically favorable at the TPL of the liquid droplet for ZB as well as for WZ nuclei.

Once proved that the conditions for favorable nucleation at the TPL of the liquid droplet are likely to be developed in VLS growth mode, it is necessary to see which kind of nuclei, WZ or ZB has a lower formation energy. At the TPL, one lateral facet of the nucleus is now in contact with the vapor, then the interfacial energy between the nucleus lateral surface and the vapor, $\gamma_{lV}$, can have different values between the two types of nuclei. As a ZB nucleus is grown, the order of stacking sequences is different from the WZ nucleus, and if grow proceeds along (111)B direction, as in fig.1.5a, the ZB stacking can grow forming either (111)A or (111)B lateral facets, which are not parallel to the growth direction but slightly tilted. On the other hand, a WZ nucleus stacks forming $\{10\bar{1}0\}$ facets in which the facet is oriented parallel to the growth direction. Other ZB and WZ facets can be formed, as {110} or the polar {112} for ZB nanowires, as well as $\{11\bar{2}0\}$ WZ facets [46]. In the model of [37], the

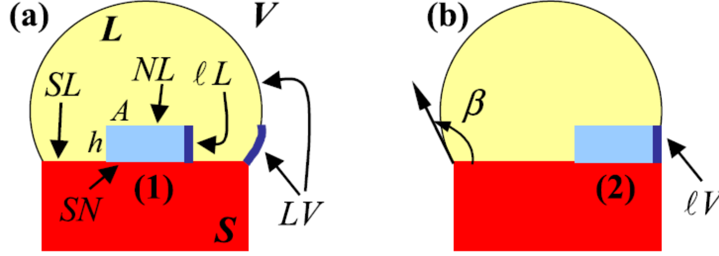


**Figure 1.7:** Representation of the liquid droplet when a nucleus is formed at the center of the liquid-solid interface (a), or at the triple phase line (b), where the nucleus substitutes part of the liquid vapor interface by creating a new interfacial between the sidewall of the nucleus and the vapor. The symbols represent the different interfaces, and are explained in the text.

(111) type microfacets are considered for the ZB structure, and the $\{10\bar{1}0\}$ for the WZ. As shown in [51], for III-V nanowires, both WZ facets have generally less energy in III-V nanowires than ZB phases, so the conclusions of this model remain valid.

The interfacial energy between the vapor and the lateral facet of the nucleus can be expressed as: $\tilde{\gamma_j} = \gamma_j/cos\theta_j + (\gamma_{LS} + \gamma_{LV}cos\beta)sin\theta_j$, with j=A,B,W being, respectively, (111)A (when a Ga atom is in the edge), (111)B (when an As atom is in the edge) or wurtzite, and $\theta_j$ the tilting angle of the nucleus with respect to the growth direction. The position-dependent formation enthalpy now reads:

$$\Delta G_j = -Ah\Delta\mu + Ph\Gamma_j + A\gamma_{SN} \tag{1.8}$$

$\Gamma_j$ is a term including the energy of the lateral interface as well as its fraction in contact with the TPL. Considering a triangularly shaped nucleus with one of its sides in contact with the TPL ($\alpha = 1/3$), the formation enthalpy is minimized to obtain the critical size of the nucleus and the critical nucleation barrier:

$$\Delta G^*_W = \frac{3\sqrt{3}}{2}\frac{h\Gamma_W^2}{\Delta\mu - \gamma_{SN}^{WZ}} \qquad \Delta G^*_{j=A,B} = \frac{3\sqrt{3}}{2}\frac{h\Gamma_j^2}{\Delta\mu} \tag{1.9}$$

For WZ to be formed preferentially, $\Delta G^*_W \leq \Delta G^*_{j=A,B}$ , which requires two conditions: One is material related, $\tilde{\gamma_W} \leq \tilde{\gamma_j}$, and can be fulfilled if there is nucleation at the TPL, as in the nanowires grown in [37], even though interface energies are not well known and estimates have to be made counting the density of dangling bonds in ZB and WZ lateral facets. The second is a supersaturation driven condition: if the supersaturation is high enough to overcome the barrier to grow a stacking fault (which is to start growing WZ nucleus on top of ZB substrate or top facet): $\Delta^*_\mu = max_{j=A,B}(\frac{\Gamma_j^2}{\Gamma_j^2 - \Gamma_j^2}\frac{\gamma_{SN}^{WZ}}{h})$.

According to this model, nanowire growth is kinetically driven by the formation of a small nucleus that rapidly expand to complete the monolayer. There is a complex dynamical environment that subsist during nanowire growth. However, intermixing between WZ and ZB phases could be tuned by changing the supersaturation or the interfacial energies with careful control of various experi-

mental parameters: III/V ratio, droplet diameter, dopants, type of substrate or temperature. The model has been successively applied and adapted to explain polytypism for several nanowire growth schemes from Au-catalyzed nanowires to self-catalyzed III-V nanowires either in MBE or MOVPE conditions.

For Au-catalyzed growth of III-V semiconductor nanowires, it has been used to qualitatively explain the onset between ZB and WZ phases in various works [49][46]. Also, Algra. *et al* [48] have been able to explain polytypism and twinning superlattices in the frame of MOVPE growth of doped Au-assisted InP nanowires. They observed that polytypic nanowires with a majority of WZ sections were progressively changed to have more ZB sections by p-doping the nanowires with zinc through the incorporation of diethylzinc at the vapor phase (DEZn). Increasing the DEZn concentration, all the nanowires tend to have ZB in the whole axial structure. This was explained to be due to the interaction between zinc atoms and the solid liquid interface, which makes nucleation favourable away from the TPL, promoting the formation of a ZB nucleus. Same effects have been seen by J. Wallentin *et.al* [52], but they propose, studying post-growth HR-TEM images of the contact angle, that increasing Zn concentration promotes the change of contact angle of the liquid droplet, and this is what drives nucleation away from the TPL. The latter idea is used to expand Glas model in [53], considering not only the interfacial energies when a nucleus is formed at the TPL but also how the volume of the droplet changes as V/III ratio varies and how it affects the ZB/WZ formation probabilities integrated all along the liquid-solid interface. They show that during the growth of Au-catalyzed nanowires the droplet is wetting the top facet. As the volume of the droplet increases (by tuning V/III flux ratio), more of the TPL is in contact with the edge of the top facet, thus changing the nucleation probabilities between ZB or WZ nuclei.

Lately, with the realization of self-catalyzed nanowires (mainly GaAs nanowires assisted by liquid Ga droplet), it has been observed the prevalence of ZB structure along the axis of the nanowire rather than WZ, despite some WZ inclusions at the beginning and at the end of the growth, as well as when the V/III ratio or temperature are intentionally varied. Several groups have adapted Glas model to explain this behaviour [54][55]. Particularly, Cirlin and collaborators [56] have grown pure ZB self-catalyzed GaAs nanowires in a MBE reactor at $560-630°C$ with diameters ranging from 70-80 nm. They have proposed that the purity of ZB phase arises as a consequence of a reduced interfacial interaction between the gallium liquid droplet and the vapor, promoting the wetting of the lateral facets of the nanowire during growth. Thus, increasing the probability of nucleation at the center of the liquid droplet and favoring the grow of ZB phases. This same idea has been applied to explain the WZ/ZB intermixing in self-catalyzed GaAs nanowires [55] when the growth conditions are suddenly varied, as in the beginning or end of the growth. It was proposed that the intermixing behaviour is related with the TPL shift of the liquid droplet that promotes ZB nucleation if the droplet wets the lateral facets and WZ/ZB transition when the liquid droplet shift its position to the top facet. The typical

intermixing of phases observed at the end of growth is explained due to the TPL shift effect as the Ga droplet shrinks in volume when the Ga shutter is switched off and the remaining Ga in the droplet is incorporated to the growing nanowire. Also, the role that the concentration of group V species has on the nucleation probabilities has been analyzed, with the same ideas of droplet volume shrinkage and TPL shift, to attain control over the structure of the growing nanowire to be ZB, WZ or and intermixed superlattice [54].

### 1.3.3 Gibbs-Thomson effect

The Gibbs-Thomson effect is a manifestation of the discrete size of the liquid medium in VLS growth mode. If the liquid particle reduces his size, the surface-to-volume ratio of the liquid droplet increases, magnifying the curvature of the surface and reducing the supersaturation between the two phases. This is a consequence of the elevation of the liquid chemical potential with the curvature of the liquid droplet that raises the internal pressure of the diluted phase in the liquid, thus reducing the incorporation of atomic species from the gas phase and increasing desorption of diluted species in the liquid phase. Givargizov [33] was the first to realize that the finite size of the gold droplets during the VLS growth of Si whiskers (same conditions as [1]) could have a detrimental effect on the length of the whiskers as the smallest liquid droplets can influence the growth rate of the whiskers due to the Gibbs-Thomsom effect.
In particular, the Gibbs-Thomson effect changes the vapor-solid(whisker) supersaturation as:

$$\Delta\mu_{vs} = \Delta\mu_{vs}^{\infty} - 4\alpha\Omega/d \tag{1.10}$$

In equation 1.10, the vapor-solid supersaturation decreases with respect to that of an infinite planar liquid-solid interface $\Delta\mu_{vs}^{\infty}$ through the term $-4\alpha\Omega/d$, which is proportional to the whisker surface energy ($\alpha$), the atomic volume of silicon ($\Omega$) and inversely proportional to the diameter of the whisker (d). If the diameter of the whisker tends to very large values, the supersaturation value equalizes to that of the infinite planar interface, whereas if the diameter decreases, the supersaturation is reduced with respect to the planar interface down to the point in which is equal to zero.

Givargizov proposed that the growth rate (defined as V on his publication) of the whiskers had to be proportional to the supersaturation at some unknown asymptotical dependence as:

$$V = dL/dt \approx (\Delta\mu/k_BT)^n \tag{1.11}$$

As a consequence, the Gibbs-Thomson effect has a limiting influence on the growth rate of the whisker as a function of its diameter and thin whiskers should grow slower than thicker ones. There is a critical diameter for which growth stops. Experimentally, the growth rate was measured as a function of the whisker diameter at different supersaturations for Au catalyzed Si whisker grown by CVD at 950 °C. In figure 1.8a, at all the different supersaturations, the growth rate gets larger as the diameter of the whisker increases, but for all the curves, there is a minimum diameter for which growth does not occur. The growth rate was fitted to equation 1.11 to clear the order of n. It was shown to be properly fitted at n=2 because the square root of the growth rate as a function of the inverse of the diameter (1/d) was linear, $V^{1/2} = b^{1/2}(\Delta\mu_{vs}^{\infty} - 4\alpha\Omega/d)$ as shown in figure 1.8b. The critical diameter is: $d_c = 4\alpha\Omega/\Delta\mu_{vs}^{\infty}$

The critical diameters for Si whiskers proposed in the work of Givargizov were of the order of $\approx$ 100nm, but much more smaller Si or III-V nanowires, with nanometric diameters, have been grown several years later using CVD,

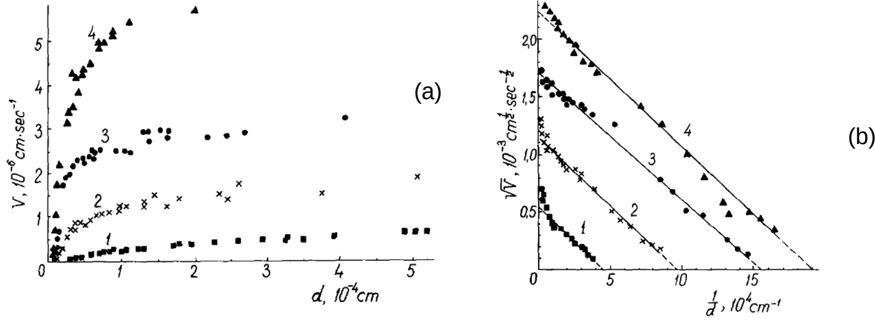


**Figure 1.8:** a) Growth rate (V) as a function of the whisker diameter (d) at different supersaturations for Au-Catalyzed Si whisker grow by CVD. There is a critical diameter limiting the size at which nanowire grow occur, as predicted by the Gibbs-Thomson effect. b) Fitting of the data for $V^{1/2}$ versus $1/d$. Extracted from [33].

MOVPE and MBE techniques [5][2][57][58]. Also, as well as the nanowire diameter, the growth temperature has been further decreased and the proposed kinetic dependence of the growth-rate as $V \propto (A-B/d)^2$ holds no longer true, as it is normally seen that thinner nanowires grow faster than thicker ones[57][58]. The latter is explained as a growth regime in which the rate limiting factor is the diffusion of adatoms from the substrate or nanowire sidewalls to the liquid droplet of the growing nanowire, as will be further developed in section 1.3.4. The possibility to grow much more smaller nanowires without any critical diameter is to be found, as developed by Johansson [36], in the different environment provided at modern MOVPE and MBE reactors, in which the growth temperature of III-V semiconductor nanowires is much more reduced than in the CVD chambers used to grow in [33][1](from $\approx 1000°$C to $400 - 700°$C ). Then, following Johansson, for their MOVPE Au-catalyzed GaP nanowires, the vapor pressure of III species on the liquid at the growth temperature of 470°C is lower and therefore supersaturation is larger. They estimate that the minimum critical radius in their nanowires for which Gibbs-Thomsom effect should be taken into account is as small as $R \approx 0.34$nm and that the vapor pressure of Ga on the liquid gold droplet is approximately $P^* = 2.48 \times 10^{-9} Pa$ at 470°C, while the vapor pressure on the chamber has the value $P = 2.76 \times 10^{-3} Pa$,much larger than in the liquid droplet. Then, they estimate that in Givargizov experiment the vapor pressure of Si on the liquid droplet had to be of the order of $P^* \approx 10^{-5} Pa$ at 1050°C and the vapor pressure of the chamber of the order of $P \approx 10^{-4} Pa$. Both pressures having similar magnitudes,the internal pressure on the liquid droplet is important and supersaturation is reduced by the Gibbs-Thomsom effect and becomes a limiting process in growth kinetics. Also, Dubrovskii has studied in detail the interplay between Gibbs-Thomsom effect and other kinetic mechanisms for the growth rate of Si and III-V nanowires in MOVPE and MBE [59][60], finding that a growth rate following equation 1.11 is an asymptotic case of a more general expression. It only affects the growth rate when the vapor-liquid supersaturation and nanowire diameter are very low.

Furthermore, it has been shown by Dubrovskii and Glas [38] that, to properly take into account the Gibbs-Thomsom effect for small nanowires, in which the growth is mononuclear, it is necessary to carefully analyze the supersaturation of the liquid with respect to the nanowire, and to be aware that the effective surface and volume of the liquid droplet changes instantaneously as a critical nucleus is formed. In a latter paper, the Dubrovskii-Glas model has been fit to experimental growth-rate versus diameter curves of nanowires grown either by MBE or MOVPE [42]. They propose values of nanowire diameter for which Gibbs-Thomsom effect is important to be (for Si, GaAs and InAs nanowires), respectively, $2.44 - 4.66$nm, $2.24 - 4.1$nm and $3.08 - 4.46$nm. Two orders of magnitude smaller than the ones of Si whiskers on CVD grown at 1050 °C.

### 1.3.4 Diffusion induced growth regime

As seen in the previous section, if the growth rate of the nanowire is dictated by the influence of the Gibbs-Thomson effect, the nanowires with a smaller radius grow at a slower pace than the nanowires with larger radius. This is not the case when the nanowires are grown in MOVPE or MBE chambers, for which it is normally measured that thinner nanowires grow at a faster rate than thicker ones as experimentally corroborated in several works [36][57][60]. For example, in figure 1.9a, extracted from [57], the inverse dependence between length and diameter of nanowires is observed for MBE grown Au-catalyzed Si nanowires at 550°C [57], as well as, in figure 1.9b, for MOVPE grown Au-catalyzed GaP nanowires grown at different temperatures (extracted from [36]).

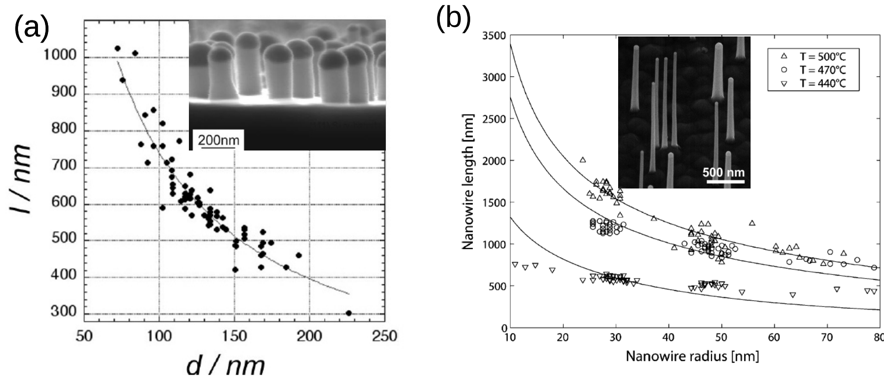


**Figure 1.9:** a) Nanowire length versus nanowire diameter for MBE grown Au-catalyzed Si nanowires at 550 °C, the inset shows a SEM image of the resulting nanowires. b) Same as a), with MOVPE grown Au-catalyzed GaP nanowires at several temperatures, the inset also showing SEM image of the resulting nanowires. In both cases, experimental data fits good with the proposed Diffusion-Induced growth regime model developed in refs[36].

To study how diffusion influences the growth rate, the material balance in the droplet has to be considered: When the nanowire is growing, atomic species reach the liquid droplet from the vapor phase at a flux ($J_a$), as well as desorb from the liquid surface with flux ($J_{des}$). Both of these atomic fluxes have

an effective section that scales proportionally to the surface area of the liquid droplet, which is, in a first approximation, of the order of the squared radius of the nanowires, $R^2$. The real surface of the droplet is corrected multiplying it by a factor that takes into account the contact angle of the hemispherical droplet, but can be disregarded in this approximation as it does not change substantially the magnitude of the contact area. The nanowire growth rate ($dL/dt$) scales as the area of the liquid-nanowire interface, which is also of the order of $R^2$. If both of these contributions were counterbalanced, growth rate would not have a kinetic dependence on the radius of the nanowire, and only very small nanowires should be affected by the Gibbs-Thomson effect. But diffusion of group III species on the substrate and nanowire sidewalls during MBE growth and on the nanowire sidewall during MOVPE growth gives also a net atomic flux directed to the liquid droplet[60][38], ($j_{dif}$). This flux scales in magnitude with the perimeter of the contact interface between the nanowire sidewall and the liquid droplet, $R$. Following [36] and [38], for Au-catalyzed III-V semiconductor nanowires (although similar conclusions can be extracted with silicon nanowires), the following simplifications are assumed:

- Small concentration of group V species into the liquid droplet. Group V flux incomes mainly through the vapor phase directly to the droplet.
- Diffusion of group V atoms through the substrate or nanowire sidewalls is negligible as the group V species are highly volatile at the growth temperatures.
- Sufficient concentration (although small) of group V species in the liquid droplet to guarantee the material supply for growing a nanowire monolayer.
- Time between nucleation events sufficiently large to refill the droplet with enough group V species after completion of a nanowire monolayer.

Then, material balance for group III species in the droplet is expressed as:

$$\frac{dN_{III}}{dt} = \chi_{III} J_{A-D} \pi R^2 + 2\pi R j_{dif,III} - \frac{\pi R^2}{\Omega_s} \frac{dL}{dt} \tag{1.12}$$

With $\chi_{III}$ being a geometrical parameter that accounts; either for the angle of impingement of the flux for MEB beams, or the catalytic efficiency for the decomposition of organometallic species on the liquid droplet for MOVPE growth. $\Omega_s$ the atomic volume of a III-V dimer, and $J_{A-D}$ the net flux between adsorption and desorption currents from the vapor phase. If steady-state conditions are reached, ($dN_{III}/dt = 0$), the growth rate($dL/dt$) takes the form:

$$\frac{dL}{dt} = \chi_{III} \Omega_s J_{A-D,III} + \frac{1}{R} 2\Omega_s j_{dif,III} \tag{1.13}$$

It is readily seen that the growth rate is inversely proportional to the nanowire radius. The section of the nanowire scales with the droplet area but the diffusion

current scales with the perimetral length of the nanowire. Then, the material needed to grow a nanowire monolayer increases quadratically with the radius. For sufficiently thick nanowires, the incorporation of group III species through diffusion cannot supply enough material and growth rate is reduced.

The complex dependence of the nanowire growth rate to supersaturation, pressure, temperature and time are not developed in the previous expressions and have to be taken into account to model growth. Generally, the diffusion flux is obtained from the concentration gradient on the edge of the nanowire top face: $j_{dif} = 2\pi RD\frac{dn}{dr}|_{r=R}$, where D is the diffusivity of the atoms on the sidewall or substrate, related to the diffusion length through: $\lambda_{s,w} = \sqrt{D_{s,w}\tau_{s,w}}$, for which $\lambda$ is the diffusion length and $\tau$ is the lifetime of atomic species on the sidewall or substrate.

The concentration gradient has to be obtained by solving the diffusion equation (Fick's second law) with appropriate boundary conditions. Depending on the model, several approaches have been followed; in some cases solving the diffusion equation in the substrate and in the nanowire sidewall separately and matching the boundaries at the nanowire bottom [42][36], or solving the equation only through the substrate and considering that there is no impingement or desorption from the sidewalls, as in [38]. The former method is more relevant to MOVPE growth when diffusion of group III species through the substrate is negligible but not through the nanowire sidewalls. As well as to model latter stages of growth (in both MOVPE and MBE), when the nanowires are longer than the diffusion length, and diffusion through adsorbed particles at the sidewalls becomes dominant. The latter method fits for the modeling of MBE growth (in which group III atomic species have larger diffusion lengths through the substrate) when the nanowire is not very long, so that there is negligible desorption or absorption of atomic species at the nanowire sidewalls. Whatever the solving scheme applied, similar dependence are encountered, in the form of hyperbolic trigonometric functions, that scale with the effective diffusion length $\lambda_s/L$. With an appropriate parameter optimization, a good reproduction of the diffusion current can be obtained using this expressions.

Additionally, the contribution of the absorption-desorption flux $J_{A-D}$ to the growth rate has to be modeled. It takes into account the supersaturation difference between the liquid and the vapor phase, the catalytic efficiency of the liquid droplet to capture material and the desorption probability. These effects have been considered with different degrees of detail. For example: in [36], they do not consider the Gibbs-Thomson contribution to the supersaturation of the liquid droplet. In [38][42], not only this contribution is considered, but also the nature of the interaction between the vapor and the droplet, that varies with the growth method (physical and geometrical in MBE or based on chemical reactions in MOVPE).

Finally, when both diffusion and absorption-desorption fluxes are obtained, the growth rate dependency with nanowire diameter can be fitted to the experimental curves. The resulting growth-rate is a non-monotonic function which, for very small nanowires, is regulated by the small size of the droplet. Thin-

ner nanowires grow slower than the thicker ones giving a rising slope in the $dL/dt - R$ curve. When the diameter increases, growth rate increases up to a maximum, after which diffusion current competes with the Gibbs-Thomsom effect and growth becomes diffusion limited with the falling slope in the $dL/dt - R$ curve depending on the inverse of the radius of the nanowire. The position of the maxima is regulated by all the parameters that interplay during growth: supersaturations, temperature, III/V ratio,droplet size and type of material. Unfortunately, not all of these parameters are exactly known and estimations of concentrations in the liquid droplet, vapor fluxes and interfacial energies have to be made in order to fit the experimental curves to the model. In figure 1.10, extracted from[42], the experimental growth rate was fitted with respect to these model giving a good agreement at all diameters for Si, InP and GaAs nanowires, the first two grown with MOVPE and the last with MBE.

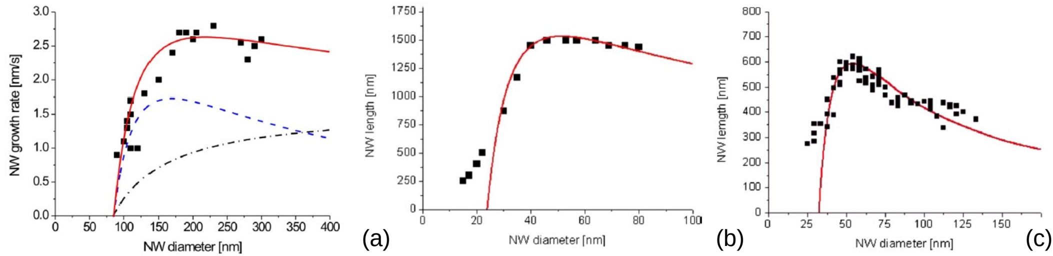


**Figure 1.10:** a) Experimental and modeled growth rate versus diameter dependence in MOVPE grown Si nanowires with: Squared scattered points represent the experimental data, a dashed-dotted line represents the contribution from direct impingement to the growth rate and the dashed line is the diffusion-induced contribution to growth rate. The red line is the fit to the experimental data taking into account both contributions. b) Length-diameter dependence (squares) and theoretical fit to the model (red line) for MOVPE grown InP nanowires. c) Length-diameter dependence (squares) and theoretical fit to the model (red line) for MBE grown GaAs nanowires.

### 1.3.5 Self-Catalyzed III-V Nanowires

In VLS growth of Au-catalyzed semiconductor nanowires, it has been found that gold diffuses into the sidewalls of the growing nanowire being aggregated into the crystalline surface of the semiconductor [61][62]. This is considered as a nuisance for the performance of several semiconductor devices, such as solar cells or FETs, as the gold atoms enhance recombination of the semiconductor charge carriers. It is possible to grow III-V semiconductor nanowires using a liquid droplet entirely composed of group III element atoms, which is a metallic liquid in the range of growth temperatures. When this is the case, the nanowires are considered to be grown self-catalyzed, as the liquid droplet is also part of the growing semiconductor compound. The group III liquid droplet plays the same role as gold in VLS growth, acting as a catalytic attractor as well as a nucleation center holding a triple phase line equilibrium between the nanowire, the liquid and the vapor.

For self-catalyzed III-V semiconductor nanowires, the most extensively material studied is GaAs. Gallium is a metal that presents a very low melting point (29.77°C). At the nanowire growth temperature, adsorption of gallium onto a substrate leads to Ga diffusion and Ga atoms can be pinned at special craters or pinholes situated on the substrate to start forming liquid droplets. This leads subsequently to the growth of nanowires in VLS mode, with the same epitaxial orientation as the substrate. In particular, self-assisted GaAs nanowires using Ga as a liquid medium were initially grown in a MBE reactor in which a GaAs(111) or GaAs(001) substrates were covered by a oxidized silicon layer of varying thicknesses [63]. The $SiO_2$ layer was sputtered into the GaAs substrates, after which the substrates were dipped in HF aqueous solution in order to passivate the surface and freed it from contamination. After HF treatment, they were heated in the vacuum chamber at high temperature, $600-700$°C during 30 minutes. The thickness variation ranged from 6 to 90 nm. It was seen, with SEM and AFM, that the post-treated surface presented small craters or pinholes randomly placed. Those pinholes act as nucleation points for the diffusive gallium species up to the moment in which the liquid droplet starts capturing arsenic from the vapor and VLS growth of the nanowires begins. There is an epitaxial relation between the thickness of the oxide layer and the growth direction of the nanowires for thin $SiO_2$ epilayers, as the pinholes open up small sections of the underlying GaAs (111) or (001) substrate and the nanowires grow following the same direction of the surface. For larger thicknesses, the oxide layer is rough and still has several pinholes, but the nanowires grow in different directions with no epitaxial relation to the substrate. Instead of GaAs, silicon, for which oxide occurs naturally, can be used as a substrate [8][56][54][64]. Moreover, the growth of self-catalyzed nanowires by lithographically patterning a $SiO_2$ layer with ordered arrays of holes has been realized [65]. Gallium is trapped in the holes and the growth of the nanowires starts from there. Even though GaAs is the most studied system for self-catalyzed growth, several examples of other self-catalyzed III-V nanowires with gallium and indium liquid droplets are reported in the literature, including GaP [66][67], InAs [68] or InP [69] nanowires.

The substrate plays an important role in the realization of self-catalyzed nanowires. In this regard, recent research has focused on explaining the impact of the interaction between gallium and oxidized silicon on the yield of GaAs nanowire growth[70][71]. Some degree of engineering of the oxide layer as well as optimization of the proper growth temperature are necessary in order to achieve higher yields. This is due to the different surface interaction between the gallium atoms and the substrate, that changes the contact angles of the gallium droplet. The most optimal conditions (higher density of vertical nanowires) are found to appear for an approximate thickness of $\approx 0.9$nm, giving a contact angle of the gallium droplet of 90°.

The binary nature of the liquid alloy that is developed in self-catalyzed growth has major consequences for the growth rate and the crystal phase of the nanowires. In section 1.3.2, it has been shown how the tuning of V/III-ratio and

temperature during growth can lead to changes in the volume and the contact angle of the droplet, and thus to a controllable growth of ZB/WZ sections along the structure of the nanowire. For GaAs nanowires: having a high V/III ratio leads to a decrease in the volume of the droplet, followed by a reduction of the nanowire radius that grows tapered in the vertical direction, as the droplet does not balance the incorporation of gallium with the consumption of it by the nanowire growth, and it is finally crystallized. On the contrary, if the ratio is small, the gallium droplet increases its volume and the nanowire evolves towards larger radius and contact angles, probably creating a dense intermixing between WZ and ZB phases, or even unstabilizing the droplet (which produces kinks and changes in the growth direction [64]).

Despite the notorious effect of the V/III imbalance on the morphology and crystal phase of the nanowire, it oftenly does not change the growth rate as it has been shown that it is the amount of arsenic reaching the liquid droplet alone that influences the rate at which self-catalyzed nanowires grow[55][72]. In

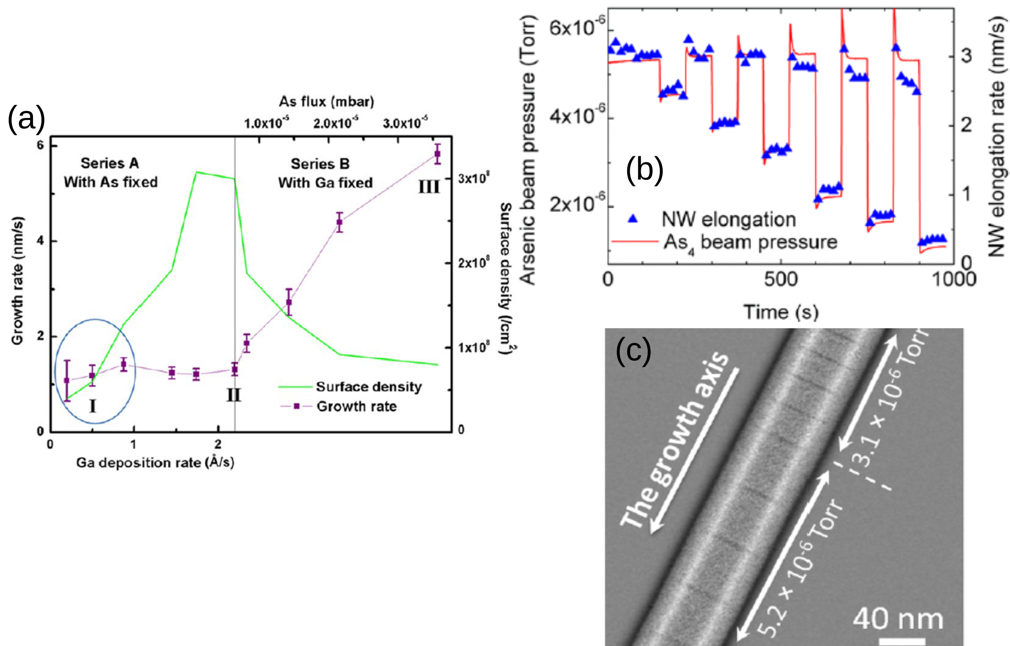


**Figure 1.11:** a) Surface density and growth rate of self-catalyzed GaAs nanowires grown by MBE as a function of the Ga flux (left panel) and As flux (right panel). In the left panel the As flux is fixed to $6 \times 10^{-6} mbar$ and in the right panel the Ga flux is fixed to $2.2 Å/s$ [55]. b) Correlation between the arsenic beam pressure and the elongation rate of the nanowire. It is seen that the elongation rate follows the changes on arsenic flux as it is changed periodically. c) HAADF image of a single GaAs NW with thin AlGaAs markers (dark contrast). Distance between markers changes when arsenic beam pressure is changed. b) and c) from [72]

figure 1.11a [55], it can be seen how the growth rate and density of nanowires changes for MBE grown self-catalyzed GaAs nanowires when switching between two series of parameters: Series I (left panel of the figure), in which the As flux is fixed and the Ga deposition rate is ramped up showing no effect on the

growth rate, only an increase in the nanowire density. In Series II, when the As flux is changed (through equivalent beam pressure changes) for a fixed Ga deposition rate, it is seen how the growth rate increases almost linearly as the arsenic pressure is increased, while the surface density of nanowires is decreased as the excessive amount of arsenic in the chamber probably impedes diffusion of gallium, precluding crystallization of solid GaAs around the nanowires. This growth regime, in which the arsenic flux limits the growth rate, has been studied in detail by Ramdani *et al.* using a marker method [72]. In their work, the growth of the GaAs nanowires is periodically marked by including Aluminum in the MBE chamber at regularly spaced intervals for short periods of time. When aluminum is included, ternary semiconductor AlGaAs is grown directly on top of the GaAs nanowire as long as the aluminum shutter is switched on. After switching off the aluminum shutter, if the arsenic pressure is paralelly ramped up, it is seen how the distance between the AlGaAs markers increases due to the increased growth rate of the GaAs nanowires, as depicted in figure 1.11b,c.

As long as the influx of gallium to the droplet is sufficient to keep its volume approximately constant, the growth rate can be modeled considering arsenic material balance, which can be expressed with the arsenic effective flux into the liquid droplet($J_{As,eff}$:Absorption-Desorption-Crystallization of the nanowire) as:

$$\frac{dN_{As}}{dt} = J_{As,A-D}\pi R^2 - \frac{\pi R^2}{\Omega_{GaAs}}\frac{dL}{dT} \tag{1.14}$$

From which follows a growth rate, in steady state conditions, $(dL/dt)$ equal to:

$$\frac{dL}{dt} = \Omega_{GaAs}J_{As,A-D} \tag{1.15}$$

Where $\Omega_{GaAs}$ is the atomic volume of a GaAs dimer. Equation 1.15 is straightforwardly integrated to give a linear relationship between nanowire length and flux with time: $L = \Omega_{GaAs}J_{As,A-D}t$. However, as proved in [72]. The As-limiting regime only fits to the observed growth rate as long as it is considered that arsenic reaches the liquid droplet not only from the direct beam but also from the re-emitted arsenic coming from the surrounding nanowires or substrate.

As explained in the last section for Au-catalyzed III-V nanowires, standard modeling proceeds assuming that the limiting effect on the growth rate comes from the diffusion of group III species to the gold droplet through the substrate or sidewall of the nanowire, while the droplet is a ternary alloy between gold and the atoms of group III and V. For GaAs self-catalyzed nanowires, the situation is simplified as the liquid droplet is made of gallium with a small concentration of arsenic. Therefore, the number of parameters to fit to a model is reduced to: Interfacial energy of the critical nucleus, concentration of arsenic in the droplet, interfacial energy of the critical nucleus and prefactor of the nucleation growth rate. These parameters can be extracted interplaying experimental curves to a model as recently proposed by Glas [39]. The model takes into account the material balance of group V in the droplet (as in equation 1.15) considering

separate processes: Arsenic incorporation from the vapor through the beam or through re-emission from the substrate or surrounding nanowires, arsenic desorption from the droplet, and arsenic aggregation with gallium to nucleate the GaAs nanowire. It has opened the way to precisely determine the unknown physical parameters that can be used later to control the length and quality of growing nanowires in similar systems.

### 1.3.6 Self-equilibration of the diameter of Ga-catalyzed GaAs Nanowires

In the previous section, it was shown how, under a given set of assumptions for the growth of Ga-catalyzed GaAs Nanowires, it was possible to model growth rate as a linear function of the effective arsenic flux feeding the gallium droplet. This model assumes steady-state conditions that are only valid as long as the gallium flux into the liquid droplet is sufficiently well balanced with the loss of gallium given up by the droplet to grow the nanowire, so that the influence of gallium on the growth rate is minimal. This can be achieved growing with larger than unity V/III ratios [53][55]. Plissard *et.al* [64][65] studied in detail the influence of this ratio for a given temperature and substrate thickness, as previously mentioned. When the ratio is much larger than unity, the growth of GaAs is suppressed, as the liquid droplet is readily consumed by the high imbalance between the two materials. In the opposite case, very low V/III ratio, the droplets grows uncontrollably, leading to an increase of the wire diameter and a further destabilization of the growth rate due to the higher wetting of gallium on the sidewalls of the nanowire. Eventually, it can even suppress vertical growth in favour of two-dimensional crystalline growth. This is in stark contrast with Au-catalyzed GaAs nanowires, even though the V/III ratio has major consequences on the polytypism of the wires, the range of ratios for which vertical nanowires can still growth (even tough there is tapering) is broader [73]. According to these results, the Au droplet preserves the growth regime close to steady-state conditions at all times, thus stabilizing growth. In this sense, growth of Ga-catalyzed GaAs nanowires should not be that stable, as gallium not only drives nucleation but also takes part on it. The fact that several groups have reported high yield of long vertical self-catalyzed GaAs nanowires using an optimized set of parameters[53][55], with almost perfect crystallinity, suggests that a growth regime in which the gallium droplet balance remains stable is achieved.

Recently, a relation between the distribution of the gallium droplet size on a patterned $SiO_2$ surface, and the resulting diameter of the MBE growth self-catalyzed GaAs nanowires after 300 s of growth[74], has been encountered. The substrate is a thin layer of $SiO_2$ in which a regular array of holes has been deposited using electron lithography. Prior to growth, a predeposition step of gallium is set by switching on the Ga beam, in order to nucleate droplets inside the patterned holes. After that, an arsenic beam is introduced to the chamber and nanowire growth begins. The growth temperature is 630°C with a V/III

equivalent growth ratio of 1.8 and a 2D equivalent GaAs growth rate of one monolayer per second. The diameter of the regular array of holes on the $SiO_2$ layer is 60 nm and the pitch between holes is 100 nm. Figures 1.12a,b and c show various stages of growth: figure 1.12a shows the distribution of gallium droplets on the array of holes prior to growth. The droplets present a sparse distribution of sizes which ranges, from 20 nm, to complete filling of the hole. In figures 1.12b and c, a top and 30 °tilted SEM images of the GaAs nanowires after growth are displayed. The nanowires present a homogeneous distribution in size and diameter with a very minimal amount of tapering. Thus, the large distribution of sizes between gallium droplets (that should lead to the growth of nanowires with a broad distribution of diameters) seems to be homogenized during the growth. This implies that, under the growth conditions for these nanowires, some dynamical mechanism at the droplet constrains the diameter distribution to a narrow range of values. This is easily seen on figure 1.12d, in which a histogram of the diameter distribution of the nanowires after 300s of growth is superimposed to the size distribution of the gallium droplets. It can be seen how the initial sparse distribution of gallium droplets narrows down to a very stretched diameter distribution centered around 50 nm.

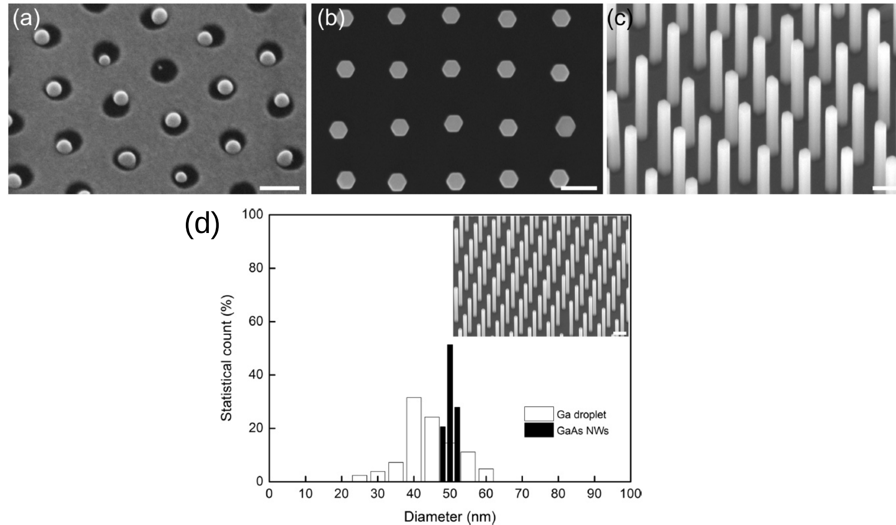


**Figure 1.12:** a)30 °tilted SEM image of the Ga droplets crystallized on the pinholes during the Ga predeposition step prior to growth . b) A top SEM view of the resulting nanowire array showing the projection of the hexagonal [111]B top facet, all the nanowires present similar diameters, and a 30 °tilted SEM image of the nanowire array showing the homogeneity between adjacent nanowires, c). For this array, hole size is 60 nm and pitch between holes 100 nm, the scale bar is equal to 100 nm. In d), a histogram showing the distribution of nanowire diameter (black bars) is overlayed to the larger diameter distribution of the gallium droplets before growth (white bars).

To further investigated this effect, a model of the droplet radius evolution during growth is developed. The evolution of the droplet size with time can be

modeled considering material balance of gallium in the droplet:

$$\frac{dN}{dt} = \eta I \pi R^2 + 2I\lambda R sin\alpha - \frac{\pi R^2}{\Omega_{GaAs}}\frac{dL}{dt} \tag{1.16}$$

The total amount of gallium is the balance between the impinging vapor flux (I) on the droplet, corrected by a geometrical factor for the incidence of the beam ($\eta$), which, for contact angle ($\beta$) larger than 90 °is equal to $sin^2(\beta)$. The gallium flux is deposited at the nanowire sidewalls at an angle $\alpha$ and reaches the droplet through sidewall diffusion with diffusion length $\lambda$. The last term is the gallium incorporated to the nanowire. Considering that the volume is proportional to the amount of gallium in the droplet: $V = \Omega_{Ga}N = (\pi R^3/3)f(\beta)$, where $f(\beta)$ is a geometrical function relating the volume of a spherical cap and the radius of its base, and assuming $\beta$ as being independent of the radius, equation leads to:

$$\frac{dR}{dt} = -A + \frac{B}{R} \tag{1.17}$$

Where $A = \frac{\Omega_{Ga}}{\Omega_{GaAs}f(\beta)}\left(\frac{dL}{dt} - \eta\nu\right)$, with $\nu = I\Omega_{GaAs}$, this term stands for the net balance between growth rate and gallium deposited on the liquid droplet directly from the vapor phase. And $B = \frac{2\Omega_{Ga}}{\pi\Omega_{GaAs}f(\beta)}\nu\lambda sin\alpha$, accounts for the diffusion influx. The sign of $A$ influences the asymptotical behaviour of the radius with time. If A<0, meaning a high Ga influx to the droplet not compensated by the nanowire growth, the radius of the droplet will increase. On the contrary, if A>0, the Ga influx is lower and growth can be compensated with a sufficiently high arsenic concentration. Furthermore, the radius can evolve towards a steady-state value due to a focusing effect produced by the Ga diffusion flux that balances, through the contrary sign of the term $B$, the size of the droplet. That is, if the radius of the nanowire is smaller than a critical value $R_c$, the droplet will increase its volume up to the steady-state radius and if the radius is bigger than $R_c$, the droplet will shrink down to it, being $R_c = B/A$. Thus, under appropriate V/III ratio, the imbalance between nanowire growth and gallium incorporation from the vapor to the droplet is self-regulated to a steady-state value by means of the gallium diffused through the sidewalls.

Considering a constant flux and growth rate, equation 1.17 has the following solution:

$$\frac{t}{\tau} = \frac{R_o - R}{R_c} + ln\left(\frac{R_o - R_c}{R - R_c}\right) \tag{1.18}$$

Where $R_0$ is the initial radius of the droplet. The parameters in equation 1.18 can be extracted from the experimental results. First, the diameter of the nanowires narrows down to 50 nm, thus $R_c = 25$ nm. Then, considering that the length of the nanowires is $\approx 1\mu$m after 300 s of growth, gives an equivalent growth rate of $dL/dt \approx 3.33$ nm/s. The equivalent two dimensional growth rate, $\nu cos\alpha$, equals 0.326 nm/s, thus giving $v = 0.360$ nm/s and $\alpha = 25°$. Taking the contact angle as $\beta = 115°$ and injecting all the parameters to extract the value of A, it results on $A = 0.300$ nm/s. Therefore, the conditions for self-equilibration regime are fulfilled. B can be extracted from $R_c$, giving a value of: $B = R_cA =$

7.50 nm$^2$/s. The diffusion length is estimated after B with a value of: $\lambda = 750$ nm, which is indeed an approximate value, as diffusion on the sidewalls has been considered to be constant at the initial stages of growth, and this is not reflected in the model. Finally, $\tau = R_c/A = 83$ s, shorter than the growth time (300 s) , thus the narrowing of diameters can be considered to be homogenized in the system when growth is stopped. In figure 1.13, the dependence of the droplet diameter with time in equation 1.18 has been plotted for several initial diameters ($2R_0$), with the parameters extracted from the experiments. It is seen that the initial sparse diameter distribution is narrowed to the critical radius as the system evolves. For t=300 s, the distribution of diameter is almost homogeneous and equal to the critical diameter found in figure 1.12d.

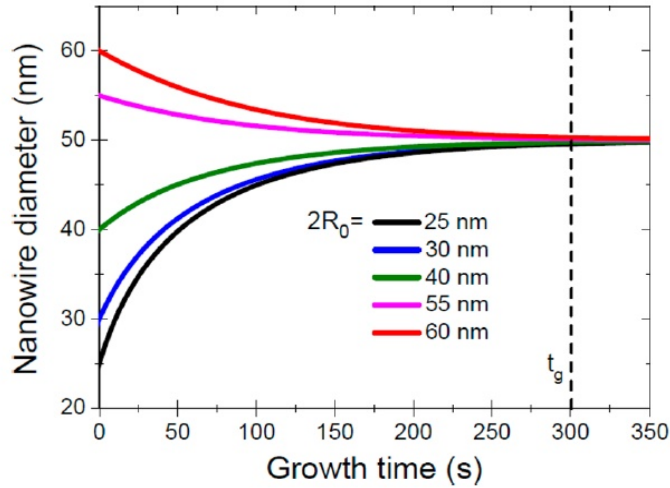


**Figure 1.13:** Representation of the nanowire diameter evolution with time for different initial diameters as obtained from equation 1.18, under the experimental conditions described in [74]. The vertical dashed line marks the total growth time of 300 s.

As a final remark; in [74], self-equilibration mechanism for Ga-catalyzed GaAs nanowires is observed and described for the first time, as well as predicted theoretically. Shortly after the publication of this work, the self-equilibration regime has been also described theoretically by Tersoff in [75]. The model of [75] follows similar considerations as the ones herein developed, only considering MOVPE growth and a slightly more developed expression for the diffusion current through the sidewalls, but still leading to the same functional dependence for the evolution of the system towards a critical radius. Additionally, Tersoff has quantified the conditions for self-equilibration regime to occur to be:

$$1 < \frac{F_5}{F_3} < 1 + \frac{\lambda}{R} \tag{1.19}$$

Where $\frac{F_5}{F_3}$ is the V/III ratio. Taking the MBE diffusion length here obtained of $\lambda = 750$ nm, the critical radius of 50 nm and the V/III ratio of 1.5, the conditions

for self-equilibration regime proposed by Tersoff are likely to be achieved in [74] for the initial droplet size distributions. But it is necessary to be aware that the correct inequality to be at work for MBE growth can be different as the term $\lambda/R$ should be corrected by some geometrical factor accounting for the different nature of the vapor flux, that changes the effective capture section of the nanowire sidewalls and of the liquid droplet.

To conclude: A growth regime in which the nanowire diameter tends to a critical value has been achieved. It has been proved that it is possible to reach a growth regime in which the different material fluxes (nanowire growth, adsorption-desorption and diffusion) interact in a self-equilibrating regime. The key point is that the volume of the droplet evolves as the system does. Thus, for liquid droplets with small initial diameter, the diffusion contribution (which scales as 1/R) to the growth rate will be much larger than the absorption-desorption flux and than the rate at which the nanowire monolayers are grown. Thus, the droplet will start to increase its volume, followed by an increase of the diameter of the nanowire. As the diameter of the nanowire gets larger, the weight of the diffusion term, 1/R, will be reduced, eventually leading to a stabilization of the droplet size, as the diffusion current can be counterbalanced by absorption-desorption and growth. In the opposite way, if the liquid droplet size is initially large, the diffusion contribution is small and the droplet shrinks in volume, as there is no sufficient incorporation of gallium from the vapor phase. But as its size gets reduced, the diffusion term (scaling as 1/R) dominates again and the system is stabilized, by increasing the droplet volume, against complete consumption of the droplet.

The observed self-stabilization regime for Ga-catalyzed GaAs nanowires is not only an indication for the more homogeneous diameter distribution that it is normally observed when growing self-catalyzed nanowires [53][65]. It also suggests new methods to interact between the growth parameters and the growth dynamics in order to attain a total control of the nanowire aspect ratio. This, in conjunction with the crystal phase control that it has been already achieved in self-catalyzed GaAs nanowires, could lead to a precise engineering of such nanowires.

### 1.3.7 Conclusion

In this chapter, the VLS growth mechanism, which is the physical mechanism involved in the majority of semiconductor nanowires grown either by MBE or MOVPE reactors, has been described. An up-to-date review of growth models has been developed. Nanowire modeling fits in the frame of the nucleation theory of growth for semiconductor crystals, but adapted to the special environment provided by the liquid droplet from which the nanowires grow. First, the relation between supersaturation and growth rate and how it enters in the probability to form a given nucleus has been briefed. Then, the origin of the polytypism on the growing nanowires has been explained with a nucleation model that accounts for the different nature of the critical nucleus between the ZB and WZ phases and the probability to form such nuclei depending on the nucleation spot at the interface between the liquid droplet and the solid. In III-V semiconductor nanowires, if nucleation takes places at the center of the interface, the ZB phase is favoured. Otherwise, both phases can appear, with higher probability to form WZ nuclei at higher supersaturations. Following that, a review of the kinetic models accounting for the growth rate of gold catalyzed semiconductor nanowires has been carried out. Starting from the initial models, the influence of the Gibbs-Thomsom effect was found to limit the growth of smaller nanowires despite larger ones. More recent models explain the experimentally observed opposite behaviour, smaller nanowires tend to grow faster and this is a consequences of the larger diffusion fluxes from the substrate to the nanowire. Finally, it has been shown for self-catalyzed semiconductor nanowires that there is a different limiting factor for the growth rate, which is related to the incorporation of group V species into the liquid droplet. As the liquid droplet is made entirely of group III species, the growth rate is linearly dependent on the amount of group V species that reaches it, considering that the droplet supplies enough group III material to grow the nanowire. In the last section, it has been proved that, for self-catalyzed nanowires, it is possible to reach a dynamical regime during growth in which the balance between the absorption-desorption fluxes and diffusion fluxes tends to stabilize the volume of the droplet to a fixed, critical value, so that all nanowires finally show the same morphological aspect-ratio. This has been termed as self-equilibration regime and could have far reaching consequences for the absolute control of the dimension and crystal shape of an ensemble of nanowires.

Even though the nucleation and kinetic models have successfully explained the main observed trends between nanowire morphology, crystal structure and growth conditions such as V/III ratio or temperature, they usually stand on many uncertainties, as they depend on several unknown parameters such as the concentration of atomic species in ternary alloys or the interfacial energies between the nucleus and the growing nanowire. Also, the interface between the liquid and the growing nanowires can hardly considered to be ideally flat, with the liquid droplet pinned at the TPL on the top facet of the nanowire. The more general case has to consider the situation for which the droplet wets the lateral facets and the growth regime is developed in several steps with the formation

of truncated facets in the edge of the nanowire-liquid interface prior to the formation of the top-facet of the nanowire [76]. There are two additional modeling schemes accounting for these factors: First, Tersoff and Schwarz have developed a continuum model that simulates the dynamical evolution of the nanowire morphology, considering the dependence of the growth rate on supersaturation and how it changes with the balance of forces at the TPL when the nanowire is growing[77][78]. Second, Krogstrup *et.al* have developed an advanced model based on kinetic transition-state theory [40]. Additionally, nanowire growth is considered to proceed in a steady-state regime in which the nanowire material supply is always guaranteed by the sufficiently large time between nucleation events, so that, whenever a nucleation takes place, it is not affected by the previously grown monolayers. This is also an ideal-case assumption, as nucleation events hold anti-correlation between them, so the formation of a new nucleus affects the delay time for the formation of the next one, as studied in [79] and [80].

For the following chapters, several aspects relating the surfaces of III-V nanowires will be studied, using STM and optical spectroscopy. It is therefore necessary to understand what growth related mechanisms might influence the nanowire surfaces, which can, ultimately, delimit what is the observed morphology, atomic structure and underlying electronic state on the sidewalls of the nanowires.

# Chapter 2

# Characterization techniques

## 2.1 Scanning Tunneling Microscopy

### 2.1.1 Introduction

In the first part of this section, the mechanism responsible for tunneling transport of electrons between different materials will be discussed, illustrated by the main physical parameters governing the tunneling effect as well as how they are used to create a scanning tunneling microscope (STM).
**- Tunneling.**
The energy necessary to extract an electron from a metallic surface is the difference between the Fermi energy level of the metal in which the electron is bounded and the energy of the vacuum level, in which the electron is considered a free particle. This energy difference is called the work-function of the metal, and it is represented as: $\phi$. Its magnitude is of the order of a few electron-volts, for example, around 5.2 eV for gold and 4.5 eV for silver (The exact work-function depends on the crystalline structure of the surface). When two metals are faced in very close proximity, in the sub-nanometric range, the difference between the work-functions of the two metals acts as an energy barrier. Classically, electrons with an energy less than the barrier should not pass, and thus no electrical current can be produced, unless the work necessary to cross the barrier is provided by an external source ; for example, a battery creating a large voltage difference between the metals to force the thermoionic emission of electrons from one metal to another. Nonetheless, it is found experimentally that when two metals are put together at nanometric distances and very low voltage difference between them, a small but detectable electron current is produced. The origin of this current is a purely quantum phenomena which is called tunneling effect. The tunneling effect is a consequence of the wave nature of electrons at the atomic scale. In a STM, a metallic tip is brought at nanometric distances to the surface of a metal or of a highly conductive sample. Even though the energy barrier is larger than the energy of the electrons (the Fermi energy), the wavefunction of the electrons does not completely vanish at the interface be-

tween the surface of the tip and the vacuum, as there is a small probability that the electron can be outside the metal, or equivalently, the wavefunction tails into the vacuum. This way, for a given distance d, and a voltage V, between the tip and the surface, the electron wavefunction of the tip can overlap with the electron wavefunctions of the surface, opening a transmission channel if the quantum transition rules for electrons are fulfilled. As found in many quantum physics and STM textbooks [81][82][83], the transmission probability for tunneling can be obtained in a 1D geometry by solving Schrödinger's equation for a free electron in a constant potential. The tunneling junction is approximated by a square barrier (vacuum) with an energy higher than the electron energy at the tip/sample, such as the one depicted in figure 2.1. The zero of energies is the Fermi level of the sample, the electrons in the tip are at an energy $eV$ higher than the sample. The magnitude of the barrier is then approximated by an effective barrier height given by $\bar{\phi} = (\phi_{tip} + \phi_{sample})/2 - eV/2$. The width of the barrier is the distance d between the tip and the sample. Solving 1D-Schrödinger's

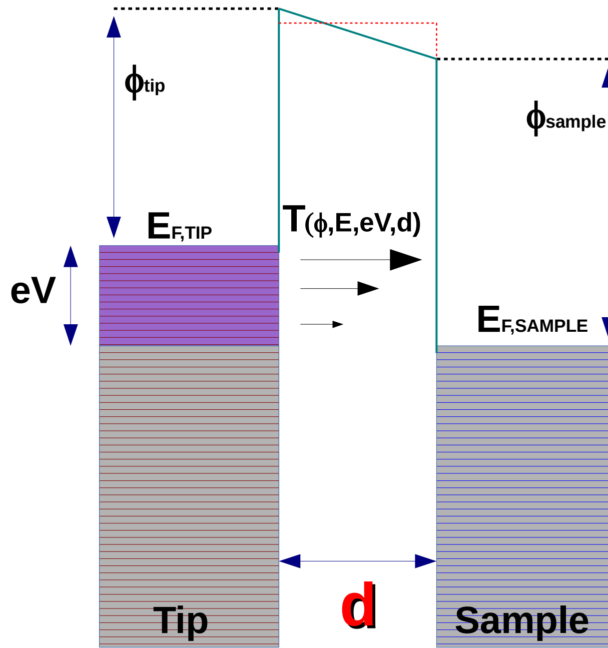


**Figure 2.1:** Sketch of the energy diagram of a tunneling junction. The main parameters and energy scales involved in the process of tunneling of an electron from the filled energy levels of the tip at a larger energy potential (eV) to the empty level of the sample are outlined in the figure. The transmission probability depends on the tunneling distance, d, as well as on the tunneling barrier height, which depends on the effective barrier height formed by the vacuum energy levels of tip and sample, approximated by a square barrier (in dashed red line in the figure).

equation in the three regions (tip, vacuum and sample) and matching the wavefunction continuity at the boundaries, the transmission probability for electrons having an energy (E) in the range $E = [E_{F,sample}, E_{F,sample} + eV]$ is given by

the following expression:

$$T(E,V,d) \propto exp\left[-2d\sqrt{\frac{2m}{\hbar^2}\left[(\phi_{tip}+\phi_{sample})/2+eV/2-E\right]}\right] \tag{2.1}$$

In equation 2.1, $m$ is the mass of the electron and $\hbar$ is the reduced Planck's constant. There is a direct exponential dependency between the transmission probability for tunneling and the distance between the tip and the sample,d. The tunneling current between tip and sample is directly proportional to this transmission factor. Thus, changes as small as few picometers in distance will result in exponentially amplified or decreased tunneling currents. This is the most important factor determining the applicability of the STM as an ultrasensitive surface corrugation probe, as will be explained in the next paragraph. It is also important to note that the transmission probability depends on the applied voltage between the sample and the tip. Looking at figure 2.1, all the electronic states at the tip in the bias window (range of energies between $E_{F,sample}$ and $E_{F,tip}$) can take part in the tunneling current, but the electrons closer to the Fermi level of the tip have a reduced barrier height, and thus can tunnel with higher probability. Furthermore, this approximation for the transmission probability considers that the energy is conserved, corresponding to elastic tunneling. There are also inelastic tunneling processes, which are important to track interactions between electrons and phonons. But they are observable only at very low temperatures. These processes are not studied in this work and will not be further explained.

**- Scanning.**

As seen in the previous paragraph, the transmission probability for electrons to tunnel between the tip and the sample is exponentially dependent on the distance between them. Then, if the tip is brought in proximity to the sample and moved laterally along its surface at a constant distance and voltage from it, nanometric changes in the morphology of the surface, as for example the presence of terraces in a given crystalline surface, will change this distance between the tip and the sample, resulting in a exponential change of the tunneling current. The tunneling current variations, in the nanoampere range, are amplified and converted to voltage (with a current-voltage converter). Tunneling current images are composed by recording all the changes in current when the tip scans a portion of the surface. The changes in tunneling current are transformed to changes in height with equation 2.1, allowing to reconstruct the topology of the surface, that is, scanning the surface. This method of scanning is called constant height mode. The tip is moved by coupling it to a piezoelectric material, which are non-centrosymmetric crystals with oriented electric dipoles along a given crystalline direction. If such a material is polarized with a large voltage, the electric dipoles rotate, inducing strain in the atomic structure, which finally results in nanometric elongations or contractions of the whole piezoceramic piece. For STM, the piezoceramic materials used are ceramics of the family of the PZT (lead zirconate titanate ceramics) [84]. To achieve a fine

tuning on the movement of the tip, a tube shaped PZT is coupled to the tip, as shown in figure 2.2. If the material is properly calibrated, it is possible to precisely move the tip in the XYZ directions by applying voltage differences between four separated metallic pads conformally sticked to the outer ring of the tube and an inner metallic pad in the inner ring of the tube. The different voltage combinations between the metallic pads allow to induce nanometric deformations in the piezoceramic and thus to extend/shorten the tube and as such the distance between the tip and the sample as well as to deflect/elongate one side of the tube with respect to the other to be able to move laterally the tip along the surface. The problem with the constant height scanning mode is

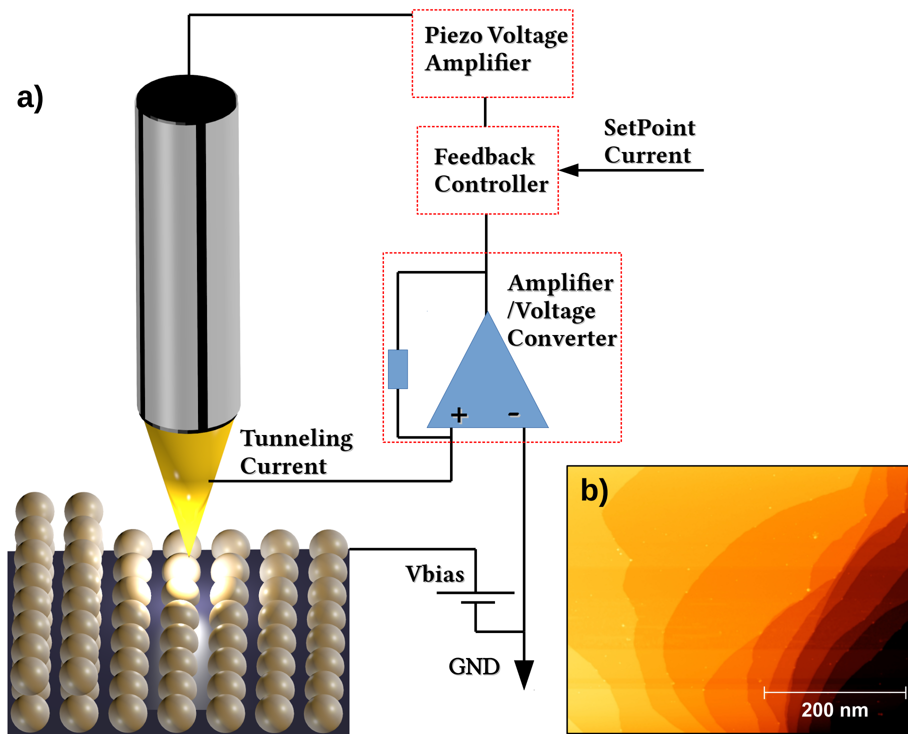


**Figure 2.2:** a) Sketch of the tunneling junction and feedback controlling circuit in a scanning tunneling microscope. The sample is represented as a series of two atomic planes in a square lattice. The metallic tip scanning the sample is represented ideally with a conical shape, and a sharp, needle-like end pointing towards the sample. The piezo-electric tube is coupled to the tip. The electric circuit set a bias voltage between the tip and the sample. Then it collects the tunneling current from the tip and amplifies it. After the current is compared in the feedback controller circuit, a voltage is fed to the piezo-tube in order to change the tip-sample separation and maintain the current constant. b) STM image of a clean Ag(111) surface taken in the constant current scanning mode. The surface is composed by a series of stacked terraces with irregular shapes. The color scale represents the height. $Vbias = -1V$,$I_{tunnel} = 10pA$

that the surface is normally sloped with respect to the tip and the morphology of the surface is not known, which can result in crashes of the tip against the sample when the scanning is performed at distances larger than few nanometers or in rough samples. It is then necessary to use a feedback mechanism in order

to control the distance between the tip and the sample. This is done with the constant current scanning mode, which is the basis of the use of a STM as a surface scanning device. The working principle is depicted in figure 2.2 a. A bias voltage is set between the tip and the sample, a tunneling current in the nanoampere range is detected, amplified and converted to voltage. This tunnel current is compared to a fixed reference set by the STM user, which is called setpoint current. The difference between the reference and the detected current is fed to high-voltage amplifiers controlling the elongation of the piezo-tube and thus the distance between the tip and the sample. When the tunneling current is compared to the reference, a digital or analog (depending on the model of STM) PID controller (proportional integrator derivator controller) tries to maintain the current constant at the reference value. This way, if the tip scans along the sample and the distance between both electrodes is reduced as a result of a morphology change such as an atomic step, the tunneling current increases, but the feedback controller reacts by increasing the voltage in the piezo in order to separate the tip until the detected current is similar to the reference. Then, the changes in the voltage applied to the piezoceramic tube to shorten/extend it in order to keep a fixed current follow the topography changes encountered by the tip scanning the surface, reproducing a topographical image of it. As an example, in figure 2.2 b, the topography of the (111) crystallographic surface of silver was acquired in the constant current mode. The changes in height applied to the piezoelectric tube in order to keep the current constant are transformed to a false-color scale in which the darkest colors reproduce the deepest point of the images while the brightest color, the highest point. The image represents a series of steps, or step bunching along the surface of silver.

**- Microscope.**

The feature that makes STM such a powerful characterization tool is the ability to discriminate not only the morphology of a surface but also, when the scan is performed under stable enough conditions on flat, clean and conductive surfaces, the atomic structure of the surface. To be able to understand what produces the tunneling current while scanning a crystalline surface and what information is obtained, it is useful to depict a more complete expression for the tunneling current in a general case, extracted from Bardeen's tunneling theory[82], in the approximation of zero temperature:

$$I = \frac{4\pi e}{\hbar} \int_0^{eV} \rho_{tip}(E - eV)\rho_{sample}(E)T(E, V, d)dE \tag{2.2}$$

In equation 2.2, $\rho$ is the density of states of the tip or sample at a given energy E, while T is the transmission factor of equation 2.1. The tunneling current flowing between the tip and the sample at a fixed distance d and voltage V arises from the product of the density of states between the tip and the sample weighted by the transmission probability at any given energy and integrated along the available energy states opened by the polarizing bias. The factor $(E - eV)$ appearing in the density of states of the tip means that when the polarizing voltage (bias) is positive (negative), the Fermi level of the tip is

shifted above (below) the Fermi level of the sample, and the integration range is then from 0 (($E = E_{F,sample} = 0$) to eV ($E = E_{F,tip} = E_{F,sample} + eV = eV$), as depicted in figure 2.1. In general, the three factors taking part on the magnitude of the tunneling current have to be considered for every surface that is scanned in order to interpret the images. On the surface of materials, there are electrons bounded to the adatoms at different states. If these states are localized approximately at the same position as the atom, as the tip is moved along the surface, the tunneling current increases when the overlap between the states of the tip and the sample is maximum (that is, when the tip is right on top of the atom) and decrease otherwise. As the tip is moved along a chain of atoms, the tunneling current increases at the atomic positions, the feedback mechanism operates on the transmission factor by increasing or decreasing the distance through the piezo-tube elongations. If the density of states of the tip is considered approximately constant, the changes of tunneling current are then directly ascribed to the spatial changes in the density of states of the sample at a given bias. Thus the STM image of a crystalline surface reproduces, rather than the atomic positions, the positions at which the density of electronic states of the sample is larger, in the energy range allowed by the bias voltage and with a transmission factor set by the voltage, distance and barrier height.

An example of the atomic contrast observed in the STM image of a crystalline surface, relevant to this work, is found when scanning the (110) surface of GaAs, as showed in [85]. GaAs is a III-V semiconductor with a ZB structure. If a GaAs film is grown along the <100> direction, it is possible to mechanically cleave the film in UHV, accessing the non-polar (110) surfaces with STM. In this surface, the topmost Ga and As atoms are stacked in zig-zag rows forming an almost ideal truncated bulk (110) ZB plane (figure 2.3 c). But as the Ga and As atoms have different electronegativity, there is a small charge transfer from the Ga atom to the As atom, producing a small buckling of the As surface atoms with respect to the Ga surface atoms. As a consequence, the spatial distribution of the electronic states occupied by the electrons in the (110) surface is centered around the As atoms while the empty states are centered on the Ga atoms. Then, when scanning the (110) surface of GaAs with a STM tip at negative voltage (thus probing the occupied states of the sample, which are the valence band states and the surface occupied states), the maximum contribution to the tunneling current will arise from the As surface states and thus the contrast in the image will give the information about the position of the As atoms (figure 2.3 a). When the scan is performed at positive voltages (thus probing the empty states of the sample, or conduction band states and surface empty states), the maximum contribution to the tunneling current arises from electrons of the tip transferred into empty states of the Ga atoms, and thus at different positions with respect to the As atoms (figure 2.3 b). Is is only when combining the STM images taken at positive and negative voltages that a complete structural image of the surface can be composed. Finally, it is noticed that in equation 2.2 the temperature is not considered, in order to account for this factor, it is necessary to include the occupation probability for electrons via the inclusion of a factor

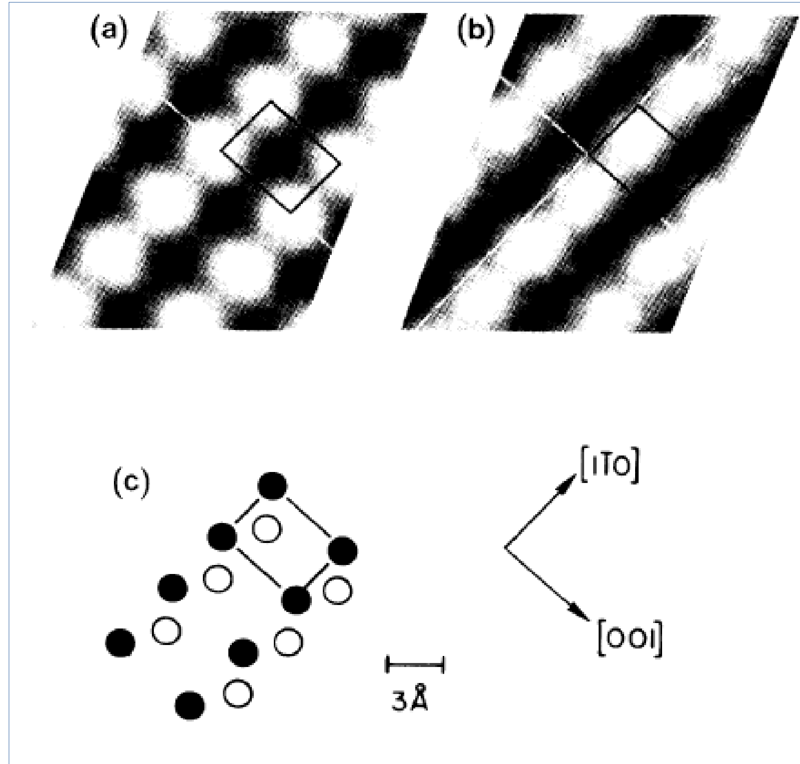


**Figure 2.3:** Cross Sectional STM image of the (110) surface of GaAs acquired at positive sample voltages of 1.9V (a) and negative sample voltages of -1.9V (b). c) Schematic top view of the atomic structure of the GaAs(110) surface, with the gallium atoms represented by solid circles and the arsenic atoms by open circles. The square line on figures a),b) and c) represents the surface unit cell. It is seen that at positive voltages the tunneling current arises mainly from the gallium surface atoms while at negative voltages it is produced by the arsenic surface atoms. Extracted from [85]

in the integrand, accounting for the difference in the Fermi-Dirac distribution function between the tip and the sample, which has the effect of broadening the distribution of electronic states available for tunneling.

### 2.1.2 Theory of STM

In the last section, equations 2.1 and 2.2 have been used to illustrate the working principles of a STM, and to intuitively understand the important parameters in play when STM imaging is performed. Both expressions are approximations of a more general case involving three systems: the sample, the vacuum and the tip, whose wavefunctions have to be known precisely at all positions in space in the range of energies of interest to interpret the STM results. To simplify the problem, several approximations have to be considered to be able to obtain a good understanding of the STM imaging without having to simulate the full system. It is the purpose of this section to show the two most used models to interpret and simulate STM images and spectroscopy measurements.

**- Bardeen's Tunneling Theory.**
Equation 2.2 was obtained prior to the invention of STM to analyze the experiments of tunneling spectroscopy between metals by Bardeen. Obtaining the full solution for the wavefunction of the system composed by the tip, the sample and the vacuum is very complex. Bardeen's approach divides the problem in two regions split by the vacuum, with a solution of the Schrödinger's equation independently obtained in this two subsystems: sample+vacuum ($\psi_{sample}$) and tip+vacuum ($\psi_{tip}$). Then, applying perturbation theory, the transfer rate($w$) of an electron from an energy level of one subsystem ($E_{tip,i}$) to the other ($E_{sample,f}$) is given by Fermi's golden rule [81]:

$$w_{tip,i\rightarrow sample,f} = \frac{2\pi}{\hbar} \left|M_{fi}\right|^2 \delta(E_{sample,f} - E_{tip,i}) \tag{2.3}$$

Where $\delta$ is the Dirac delta-function and $M_{fi}$ is the transition matrix element between states f and i, given by:

$$M_{fi} = \frac{h^2}{2m} \int_S \left[\psi_{tip,i}(r) \nabla \psi^*_{sample,f}(r) - \psi^*_{sample,f} \nabla \psi_{tip,i}(r)\right] dS \tag{2.4}$$

In the last equation, the integral is performed at an arbitrary surface at the separation region between the tip and the sample. Summing-up the transition rates between the wavefunctions of the different energy levels of the tip and the sample and multiplying by the charge of the electron and the spin degeneracy ($\times 2e$), the tunneling current is obtained as:

$$I = \frac{4\pi e}{\hbar} \sum_{i,f} \left|M_{fi}\right|^2 \delta(E_{sample,f} - E_{tip,i}) \tag{2.5}$$

Finally, considering the properties of Dirac's delta-functions and the formal expression for the density of states as a function of energy :

$$\rho(E) = \sum_n \delta(E - E_n) \tag{2.6}$$

The expression 2.5 (counting only the states in the bias window and at 0K), leads to the equation 2.2. Details of this derivation can be found elsewhere [82][83].

**- Tersoff-Hamann Approximation.**
While equation 2.2 and its implication for STM have been explained in the introduction. It is not straightforward to understand the different role played between the sample and the tip in a STM that makes possible the interpretation of an STM image contrast as arising mostly from the electronic distribution on the sample. In principle, the wavefunctions of the tip and the sample enter symmetrically in equation 2.4. But in STM, the sample is a crystalline surface with the atoms periodically arranged while the tip is a sharp conical metal, ideally with a point-like end in which all the interactions are produced, in principle, between the sample and the closest atom to the tip. This asymmetry was used

by Tersoff and Hamann to simplify Bardeen's Model as well as to gain a more intuitive picture of the tunneling process [86].

Starting from equation 2.5, the sample wavefunctions are expanded as surface periodic Bloch functions with the z-component of the wavevector being complex and tailing into the vacuum. The apex of the tip is approximated by a metallic sphere with center of curvature $r_o$ and radius $R$ at a fixed potential, whose wavefunction is the groundstate solution of Schrödinger's equation in a spherical well of constant potential (s-like solution):

$$\psi_{tip,i} \propto \kappa R e^{\kappa R}(\kappa|\vec{r} - \vec{r_o}|)^{-1} e^{-\kappa|\vec{r}-\vec{r_o}|} \tag{2.7}$$

In equation 2.7, $\kappa$ is the inverse of the decay length of the wavefunction in vacuum, which depends on the barrier height set by the different work-functions between the tip and the sample.

Inserting equation 2.7 as well as the surface Bloch wavefunctions in equation 2.5, it is then possible to evaluate the matrix element to obtain a final expression for the tunneling current proportional to [86]:

$$I \propto \sum_f |\psi_{sample,f}(\vec{r_o})|^2 \delta(E_f - E_i) \tag{2.8}$$

This equation implies that the tunneling current is directly proportional to the sum of the sample wavefunctions evaluated at the center of curvature of the spherically-symmetric point-like metallic tip. In other words, the tunneling current at each position of the tip with respect to the sample is proportional to the density of states of the sample evaluated at the center of curvature of the tip and sample at the energy of the tip $E_i$. Using the Tersoff-Hamann approach it is then natural to interpret the role of the tip in STM imaging as a point-like probe of the wavefunctions of the surface evaluated at its apex, and thus, at a given distance between the tip and the sample.

This approach is one of the most used approximation to interpret and understand STM images at various polarizing voltages. As long as the tip wavefunction is considered to be a s-like solution of Schrödinger's equation, it is only necessary to calculate the distribution of states on the surface (using any suitable simulation method) to be able to reproduce the experimental STM image. However, not always the tip can be approximated by s-like spherical wavefunctions, and the total wavefunction has to be expanded with higher order solutions of the Schrödinger equation on the tip (p-like or d-like) to obtain a more accurate description of the tunneling current. Details of this expansion can be found in the book of Chen [82].

### 2.1.3 STM spectroscopy

So far, it has been shown how the STM is used to probe the topography as well as the atomic structure of the surface by scanning the metallic tip over it. It is also possible to perform spectroscopy. The STM user can control the

tunneling current, the distance and the voltage between the tip and the sample. Inspecting equations 2.1 and 2.2, it is seen that the unknowns are then the densities of states of the sample and the tip and the barrier height. Then, varying one of the user accessible STM parameters while keeping the others fixed or free to change, can give access to the unknown parameters in equation 2.2. This is the basis of the STM spectroscopies.

For example, the transmission factor of equation 2.1 entering in the expression for the tunneling current varies exponentially with the distance between the tip and sample multiplied by a square root factor including the voltage and the effective barrier height. If the tip-sample distance is ramped up with the piezo-tube and the tunneling current is stored as a function of the distance while keeping the voltage constant, the curve of the tunneling current as a function of distance will vary exponentially. By plotting the logarithm of this current with respect to the distance, it is possible to extract the square root factor entering in equation 2.1 to obtain the effective barrier height. The work-function of the sample can be obtained if the work-function of the tip is known. This is called current versus distance spectroscopy or I(Z) spectroscopy, this kind of experiment was used as a proof of concept in the first published paper describing the possibility of building a STM, published by Binnig and Rohrer in 1982 [87].

**-I(V) spectroscopy.**

Inspecting equation 2.2, if the tip is kept at a given distance from the sample (without applying a height controlling feedback) and the voltage is ramped from negative to positive values, the Fermi level of the tip will be shifted up or down with respect to the Fermi level of the sample. The tunneling current is measured at each voltage. Looking at figure 2.2, at positive voltage, electrons can tunnel from the tip in a range of energies within the bias window giving a current proportional to the empty density of states of the sample, while at negative voltages, electrons occupying the filled states of the sample within the bias window can tunnel to the tip giving a current proportional to the filled density of states of the sample. This is the basis of the current versus bias spectroscopy or I(V) spectroscopy, which is a powerful spectroscopy method to obtain information about the density of states of the sample to be studied. This approximation is valid as long as it is considered that the density of states of the tip is almost constant (and thus only contributes to the current with a proportional factor). Also, the transmission factor depends on the voltage and its effect has to be taken into account in order to get a meaningful signal.

To numerically show the information obtained performing I(V) spectroscopy is useful to start from equation 2.2 and check how the tunneling current changes when the voltage is varied:

$$\begin{aligned}&\tfrac{dI}{dV} = \tfrac{4\pi e}{\hbar}\tfrac{d}{dV}\int_0^{eV}\rho_{tip}(E-eV)\rho_{sample}(E)T(E,V,d)dE\\&= \tfrac{4\pi e}{\hbar}\left[e\rho_{tip}(0)\rho_{sample}(eV)T(eV,V,d)\right] + \int_0^{eV}\tfrac{\partial\rho_{tip}(E-eV)}{\partial V}\rho_{sample}(E)T(E,V,d)dE\\&+\int_0^{eV}\rho_{tip}(E-eV)\rho_{sample}(E)\tfrac{\partial T(E,V,d)}{\partial V}dE\end{aligned} \tag{2.9}$$

The right-hand side of equation 2.9 is composed of three terms: the first one is

proportional to the density of states of the sample at the energy $eV$ multiplied by the constant factor $e\rho_{tip}(0)$ and by the transmission factor $T(eV, V, d)$. The second one varies as the derivative of the density of states of the tip with the voltage. So in the approximation of constant density of states of the tip it can be considered to be very small. The third term is equal to the tunneling current multiplied by a constant factor resulting from the derivative of the transmission factor with the voltage.
As the transmission factor changes when the voltage is varied, one useful normalization of the $dI/dV$ signal to get values related with the density of states is to divide the derivative by the current over voltage, in order to get the following expression, after arranging terms, from equation 2.9:

$$\frac{\frac{dI}{dV}}{\frac{I}{V}} \propto \frac{\rho_{sample}(eV) + \int_0^{eV} \frac{1}{T(eV,eV)} \frac{\partial}{\partial eV} T(E, eV)\rho_{sample}(E)}{\frac{1}{eV} \int_0^{eV} \frac{1}{T(eV,eV)} T(E, eV)\rho_{sample}(E)dE} \tag{2.10}$$

The second term of the numerator divided by the denominator is a slowly varying function acting as a constant background that can be discriminated from the voltage varying density of states. The signal obtained with this normalization is directly proportional to the density of states of the sample, which is used in current versus voltage spectroscopy to analyze the electronic properties of surfaces.

The utility of this spectroscopy is that it gives information about the density of states locally. As the tip can be moved along the surface with very high precision, it has an enormous variety of uses in surface science and nanotechnology. As for example: to characterize the atomic structure of the surface and the different role played by the dangling bonds in the reconstruction of semiconductor surfaces [88], or to study the electronic properties of defects as well as the position of the charge transition levels with respect to the Fermi level of the sample [89], to study surface states of metals forming standing waves as in silver [90] or to tunnel resonantly trough the discrete states of adsorbed molecules on the surface of metals [91], to select just a few.

However, when the sample is a semiconductor with a large band-gap, additional features need to be considered. For example, when the voltage window lies within the band-gap there are no states to tunnel into and the tunneling current goes to zero. In this case, the derivative of the current $dI/dV$ will be null as well, but it will go to zero slower than the current, so that the normalized signal, equation 2.10, can contain singularities in the band-gap edges. This effect is softened, with a different normalization, by convoluting the tunneling current signal at every voltage with a voltage dependent exponential function, such as $exp(-(V' - V)/\Delta V)$ [92]. This way, the steep change in tunneling current close to the band gap is smoothed and there are no singularities in the normalized curve. However, if there are resonant peaks from electronic states in the spectroscopy curve, they will be also smeared out and appear less sharp in the normalized curve, but not shifted in position. The factor $\Delta V$ in the exponential has to be optimized to find a good compromise between obtaining

a sharp curve with well defined spectroscopic features but without artificial singularities close to the band edges. A good compromise value is to use a $\Delta V$ equal to the band-gap of the material.

Also, when the sample is a semiconductor with a large bandgap and a low conductivity, the distance at which the tip is set with respect to the sample when performing the spectroscopy is important. In order to gain sensitivity to tunnel into/out of states close to the band edges, it is necessary to approach the tip closer to the sample to increase the transmission factor. But at very short distances, and when the voltage increases beyond the band-gap window, the number of states available for tunneling current can increase in such a way that it overpasses the amplification range of the current converter, saturating the electrical signal. To overcome this problem and increase the dynamical range of the measurement, a varying voltage is applied to the piezoceramic tube while performing the spectroscopy. This is done in such a way that the distance between the sample and the tip decreases at lower voltage where high sensitivity is required while it increases when the voltage increases again, as described in [92].

**-Lock-In Technique**

When performing I(V) spectroscopy, the tunneling current signal is obtained as a function of the varying voltage. The current has to be amplified by a current-voltage converter that amplifies as well the electrical noise during the experiment. If the numerical derivative of the I(V) curve is performed, the density of states of the sample is recovered. However, the signal-to-noise ratio can be very poor and masked by the noise and therefore the spectroscopic features hard to distinguish. A solution is to use the Lock-In Technique, that is a technique in which the derivative of the tunneling signal, $dI/dV$, is obtained directly at the same time as the current, and with a very high signal-to-noise ratio.

The working principle of the Lock-In Technique is based on the properties of the harmonic functions. For example, taking two arbitrary cosine signals, $S_{ref} = Acos(\omega_{ref}t + \vartheta)$ and $S_{mod} = Bcos(\omega_{mod}t)$ oscillating at the frequencies $\omega_{mod}$ and $\omega_{ref}$ and with the phase difference $\vartheta$, and multiplying them, the following product is obtained:

$$S_{ref} \times S_{mod} = \frac{1}{2}AB(cos((\omega_{ref} - \omega_{mod}) + \vartheta) + cos((\omega_{ref} + \omega_{mod}) + \vartheta))$$

If the frequency of both signals is equal $\omega_{ref} = \omega_{mod}$, the product transforms to a constant, phase-dependent term, $1/2ABcos(\vartheta)$, plus a term oscillating at the sum of frequencies, $1/2ABcos(2\omega_{ref} + \vartheta)$. Then, if a low-pass filter with a threshold frequency lower than $\omega_{ref}$ is applied to the signal, the remaining signal is only the constant term, containing information about the phase and the amplitude of both signals.

In the case of STM, the Lock-In Technique is implemented with an electronic circuit that does exactly what has been described in the previous paragraph. The tunneling current has to be modulated periodically, this is done when performing STM spectroscopy by adding a small harmonic signal to the

bias voltage, at a given frequency ($\omega_{mod}$) and with a very slow amplitude($V_{mod}$), such that the voltage applied between the tip and the sample is $V = V_{bias} + V_{mod}cos(\omega_{mod}t + \vartheta)$, and the tunneling current (in first-order approximation):

$$I_{mod}(V_{bias} + V_{mod}cos(\omega_{mod}t + \vartheta)) \approx I(V_{bias}) + \frac{dI}{dV_{bias}}V_{mod}cos(\omega_{mod}t + \vartheta)) + \ldots$$

A reference signal with the same frequency as the modulated signal is generated in the Lock-In circuit, $R = Acos(w_{mod}t + \vartheta_r)$. Both signals, the reference and the modulated current, are passed through a multiplier circuit. The multiplied signal is composed of several periodic harmonic terms varying as multiples of the reference frequency as well as a constant term directly proportional to the derivative of the current with respect to the voltage and the phase difference: $\frac{1}{2}A\frac{dI}{dV_{bias}}V_{mod}cos(\vartheta - \vartheta_r))$. If the multiplied signal is passed trough a low-pass frequency filter, this term can be sorted out from the frequency varying terms to directly obtain the $dI/dV$ signal. A phase shifter is also added to the Lock-In circuit to change the phase of the reference signal and optimize the phase difference with respect to the modulated signal to obtain a higher amplitude.

The modulated tunneling current signal is computed as a sum of harmonic functions containing not only the current signal, but all the noise contributions to the signal oscillating at various frequencies (generally different from $\omega_{mod}$). All these terms are amplified by the current-voltage converter, but the reference signal “locks” the term containing only the first-derivative response, which can be sorted out by low-pass filtering, thus leaving out all the noise signals with harmonic response different than $\omega_{mod}$.

### 2.1.4 STM on semiconductor surfaces: Band Bending

When a polarized metallic tip is brought at tunneling distances from a metallic sample, a strong electric field is developed across the junction. Inside the volume of a metal, there is no net charge and the voltage is held constant. As the metallic tip approaches the sample, there is a redistribution of charge in the surface which screens the electric field so that the sample is kept at zero potential. The tip reacts as well screening the surface charges in order to keep the tip at the polarizing voltage. Then, the voltage between the tip and the sample is well defined. This is not the case when the metallic tip is facing the surface of a semiconductor material. Depending on the sign of the voltage and type of doping, there might be not enough free charges in the semiconductor to screen the voltage and part of it is dropped inside the semiconductor, thus shifting in energy the position of the surface states. This effect is known as tip-induced band bending (TIBB) and can have a significant effect on the shape and energetic profile of the spectroscopic curves obtained with STM.

In general, even when the tip is close to the semiconductor at zero voltage, there will be a difference in electrostatic potential due to the different work-functions, which is called contact potential. This effect already creates a band bending at the surface whose sign depends on the magnitude of the

work-functions. The contact potential can be expressed as:

$$\Delta V_c = \phi_{m,tip} - \chi - (E_c - E_{F,sample}) \tag{2.11}$$

In which, $\phi_{tip}$ is the work-function of the tip and $\chi$ the electron affinity of the semiconductor. Then, the electrostatic potential of a polarized tip-sample junction ($V$), with the origin of potential at a point far deep inside the bulk semiconductor, is:

$$\Delta\phi_{tip} = eV + \Delta V_c \tag{2.12}$$

To estimate the magnitude of the Tip Induced Band Bending is necessary to solve Poisson's equation in the 3D geometry formed by the tip and the sample. In the calculation, the boundaries of the potential are the value of the electrostatic potential of equation 2.12 at the tip, and the position of the Fermi level (the zero energy reference) in a point inside the semiconductor not influenced by the band bending. A very complete solution to this problem is treated by Feenstra in [93], in which the Tip Induced Band Bending of a tip-semiconductor junction is exactly solved for a 1D case. In general, however, knowing the three-dimensional potential distribution in the tip-sample junction is necessary to correctly describe the band bending. The approach proposed in [93] is to integrate the three-dimensional Poisson's equation using a finite-differences discretization scheme in a system of coordinates appropriate to the problem. Furthermore, it requires to take into account that the Fermi-level of the semiconductor at the surface is not well defined as it changes with the band-bending, thus it is necessary to solve the equation using a self-consistency algorithm.

This approximate solution of Poisson's equation is obtained in [93], allowing to represent maps of the distribution of voltage between the tip and the semiconductor. In figure 2.4d, equipotential lines of the voltage between the tip and the surface are depicted, where it can be seen that the potential penetrates into the semiconductor region, with a maximum at the closest point from the apex of the tip. The potential at this point is denoted $\phi_0$. Once the potential problem is solved, the effect of the band bending on the position of the electronic states of the sample can be approximated as a shift in the position of the levels by:

$$E - E_{F,sample} = eV - \phi_0 \tag{2.13}$$

A band diagram sketching this effect is depicted in figure 2.4a, where the potential of the tip is higher than in the sample and the semiconductor band bends upwards. As the voltage increases, the magnitude of $\phi_0$ increases as well. For example, on a n-type semiconductor as the one shown in figure 2.4a, if the band bends upwards, the surface becomes depleted of electrons. The tunneling electrons from the tip encounter a positively charged surface and no current is produced unless the voltage is further increased to overcome this barrier. Then, the apparent band-gap measured by the spectroscopic experiment is larger than the real band-gap of the material.

More considerations rather than solving Poisson's equation have to be taken

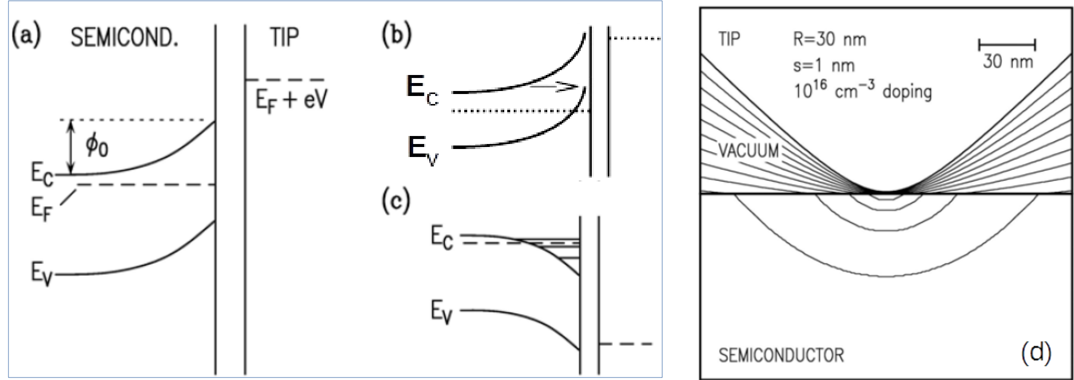


**Figure 2.4:** a) Schematic diagram of energy bands of a tunnel junction between a metallic tip and a semiconductor sample. The conduction and valence bands are denoted as $E_C$ and $E_V$. The tip-induced band bending produces and upward bend of the semiconductor band at the surface, the amount of band bending is characterized by the difference in electrostatic potential energy between the surface and the bulk of the semiconductor ($\phi_0$). The tip is at an applied potential $eV$ with respect to the semiconductor. b) and c) show quantum effects that affect the tunneling current as a result of tip induced band bending. In b), an inversion current of electrons is produced as the Fermi level of the semiconductor crosses the conduction band. In c), localized quantum states in the surface can be produced as a result of the accumulation layer on the surface. d) Simulation of the electrostatic potential distribution (lines defining constant potential regions across the junction) produced by a metallic tip on a semiconductor surface. The TIBB is calculated by discretization of Poisson's equation as in [93], with an hyperbolically shaped tip with radius (R) of 30 nm, distance to the sample (s) of 1nm and a n-type doping concentration of $1 \times 10^{16} cm^{-3}$. Extracted from [93][94].

into account to properly characterize tip-induced band bending: First, in a semiconductor, the atomic plane exposed to the surface generally suffers a reconstruction to reduce its surface energy. A distribution of surface states arises in the surface as a consequence of the arrangement of unsaturated atomic bonds, or dangling bonds. The energy distribution of states depends on the type of material and surface reconstruction. It is generally dispersed through a range of energies in the band-gap (close or resonant to the band-edges or deep in the band-gap). Furthermore, when the semiconductor is doped, there is a charge transfer between the free electron/holes in the bulk material and the empty/filled surface states which leads to the creation of a surface accumulation/depletion region producing a band bending at the surface as a consequence of the rearrangement of charges. This effect is known as surface induced band-bending. Nonetheless, when the metallic tip of the STM is approached to any of such surfaces and a potential difference is applied between the tip and the sample, the distribution of potential that is already on the surface added to the potential drop produced by the tip can affect the spectroscopic curve, the degree of which is dictated by the distribution and charge of surface states. The effect of surface states has to be considered and simulated for each semiconductor to be studied, and extends not only to intrinsic surface states but also to extrinsic states (as the boundaries between domains in (2x8) reconstructed p-type Ge(111) surface [95] or the step states of GaAs(110) [96]). In [95], the effect of such surface states is

included on the finite-differences algorithm that simulates the tip induced band bending. The surface states are modeled as a thin, charged 2D sheet limiting the vacuum and the surface, with a charge distribution that depends on the position of the charge-transition levels. One important consequence of having a large concentration of surface states is that they can screen the electric field of the tip, thus reducing the amount of band bending. In such a situation, it is said that the Fermi level of the surface is pinned by the defect states, while when the material is semi-insulating and no surface states screen the electric field of the tip, the tip induced band-bending can be large enough so that the depletion region enters far into the semiconductor and no tunneling current is detected [97], corresponding to a surface with the Fermi level unpinned.
Second, quantum effects derived from the tip-induced band bending can alter the tunneling current detected in the spectroscopic measurements. Two of these effects are presented in figure 2.4b and c. If the voltage of the tip produces a very large band bending, it is possible that the the minority carrier band crosses the Fermi level of the semiconductor, such that a tunneling electron current is produced between the majority carrier band and the minority carrier band and from there to the tip (figure 2.4b). This effect is known as inversion, and its magnitude have to be considered in order to interpret its impact on the shape of spectroscopic curves at large voltages. For example, it has been studied in [95] at the (111) surface of p-type Ge. Also, when there is a surface accumulation layer, as in figure 2.4c, the electrons might be confined in localized states between the surface and the conduction band of the semiconductor. Resonances with these states can appear when the voltage along the tip varies in a spectroscopic curve. Their energy depends not only on the properties of the semiconductor but also on the shape of the tip and magnitude of TIBB. To properly account for this effect in the simulation of an I(V) curve, it is necessary to solve self-consistently the Poisson and Schrödinger equations taking into account the contribution of these states to the tunneling current. As the solution of the Schrödinger equation in the system involves advanced simulation techniques, sometimes it is suitable to separate the semiconductor states in the effective mass approximation for spatial directions parallel to the surface and then solve the one dimensional Schrödinger equation in the perpendicular direction to the surface. In this direction, there is a complex voltage profile induced by the tip, which requires the use of numerical techniques to obtain an exact solution, such as the shooting method, as described by Feenstra in [98]. Additionally, there can be quantization also along the surface of the semiconductor, as on small heterostructures or quantum dots. Both cases has been treated, with the appropriate solution of the Schrödinger equation in a confined potential, in order to reproduce the spectra obtained in [99] to calculate the band offsets in the presence of InGaP/GaAs heterojunctions or to measure the electronic impact of InAs quantum dots in GaAs[100].

### 2.1.5 Omicron LT-STM

The STM used to explore the samples studied in this work is an UHV low-temperature STM fabricated by the company Omicron, now Scienta-Omicron [101]. In figure 2.5, a picture of the Omicron LT-STM is presented. The STM

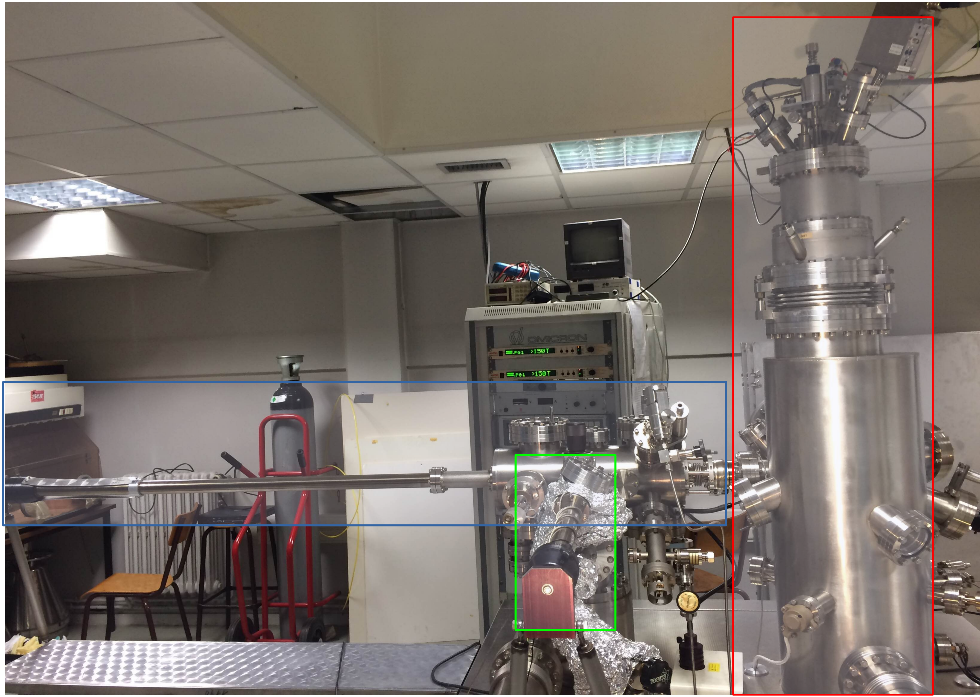

**Figure 2.5:** Picture of the Omicron LT-STM located in the basement of ISEN, at Lille. Three square boxes with different colors surround the three main elements of which the STM is composed: Analysis chamber (Red Line), Preparation chamber(blue line) and Fast entry lock chamber (green line). The tower behind the STM holds the power supplies and controllers for the different pumps, detectors and heaters installed in the STM.

is composed of three main stainless steel vacuum chambers, highlighted in the figure by colored square boxes: the green square box surrounds the fast-entry lock chamber (centered on the picture), while the sample preparation chamber is highlighted by a blue square box (left side of the picture) and the red square box corresponds to the analysis chamber in which the STM main stage is set (right side of the picture).

The two main chambers, preparation and analysis, are pumped by the combination of a turbo-molecular pump, an ion-getter pump as well as a titanium sublimation pump (TSP). Each chamber holds three of these pumps in order to achieve ultra high vacuum (UHV) independently. The fast-entry lock chamber is pumped with the turbo-pump of the preparation chamber. Once high vacuum is achieved with the turbo-pumps, the combination of ion-getter pumps and TSP's allows the system to maintain a base pressure of the order of $P \approx 10^{-10}$ Torr. The functions of each chamber can be summarized as:

- **Fast entry lock chamber:** It serves as an auxiliary chamber to take samples or tips in or out of the preparation chamber. The magnetically fixed transfer rod contains three slots so that three samples/tips can be transferred at each time. It is pumped by the combination of a rotary pump as well as a turbo-pump. A mechanical gate valve connects it with the preparation chamber.

- **Preparation chamber:** In this chamber the samples/tips are prepared so that they are suitable to perform STM imaging/spectroscopy. The preparation chamber contains a storage compartment with the capacity to hold five tips/samples. Depending on the kind of samples, different preparation routines are necessary. The main element of the chamber is a XYZ manipulator, which contains a 3D movable heating stage in which samples are placed. Just below the sample mounting slot of the heating stage there is a resistive heating module composed of a tungsten filament that is heated to increase the temperature of the samples by thermal contact (max.heat power:60W). In the base of the stage, a type K (NiCr/Ni) thermocouple controls the temperature on the stage. Furthermore, there is a top contact in the upper part of the heating stage which can be coupled with the Omicron sample holders in order to heat the samples by applying a direct DC current through them (max.current 5A). The temperature of the sample is controlled through an external pyrometer placed on a viewport just on top of the heating stage. Also, there is an additional fixed sample stage at the bottom of the chamber, just below the XYZ manipulator. Finally, and ion-mass spectrometer is set on the preparation chamber to gain control over the chemical environment of the chamber and also to track different desorption processes occurring during the preparation of the samples.
  Semiconductor samples are annealed in the heating stage at high temperatures in order to clean the surface from pollution and oxide aggregates as well as to induce surface reconstructions. For metallic surfaces, a combination of cycles of annealing and ion sputtering is performed in order to achieve a clean surface. For this, an ion-gun is placed at the bottom of the chamber facing the heating stage at a fixed angle. The heating stage can be turned upside down with the XYZ manipulator.
  Sometimes it is necessary to perform sample preparations involving a mechanical contact between different substrates in UHV: For example, when transferring vertically oriented nanowires from the as-grown samples to a clean semiconductor surface on which they are deposited horizontally with respect to the surface, or when the preparation of cross-sectional STM surfaces by UHV cleaving is necessary. In these cases, the fixed sample stage is used. This secondary stage allows for direct current heating of the samples and can be put to face samples at the main heating stage in order to perform the mechanical operations such as nanowire cleaving. Furthermore, it serves as an auxiliary stage to evaporate materials form this stage to the surface of the samples placed on the main heating stage. In this

LT-STM, there have been synthesized 2D solids such as Silicene[102] by evaporating silicon from a Silicon (111) surface on a clean Ag(111) surface in a controllable way as well as self-assembled molecular monolayers, by heating a specially prepared sample with molecular powder to evaporate different molecules on top of p-type Si(111)-B surfaces[103].
The preparation chamber is connected with the analysis chamber by a mechanical gate valve.

- **Analysis chamber:** In figure 2.5, it can be seen that the analysis chamber is somewhat larger than the other chambers, with a vertical tube-like shape. This geometry serves to place the cryostats surrounding the STM stage in the center in order to cool down the chamber, as well as to suspend the whole stage with metallic strings to increase the mechanical stability. Additionally, an eddy current damping system just below the STM stage further assists in the stabilization against external vibrations. The cooling system is composed of two cryostats. One outer cryostat, conformally covering the STM stage in order to shield it thermally, and a smaller inner one directly in contact with the STM stage to cool it down. The outer cryostat is filled with liquid nitrogen, and the inner cryostat can be filled with liquid nitrogen (to achieve 77K operation) as well as with liquid helium (to go down to 4K). A heating resistor placed inside the STM can be used to access intermediate temperatures in the range 4K-Room temperature. The temperature is read with an inner diode glued to the base of the stage.
  Outside the outer cryostat, a carousel stage with seven slots serves to transfer samples from the preparation chamber as well as a reservoir of samples/tips. A wooblestick is used to introduce the samples/tips from the carousel into the STM stage.
  In the STM stage, the tip is mounted magnetically just on top of the piezo-ceramic tube and below the sample. The coarse approach of the tip is achieved with slip-stick inertial sliders, with traveling distances of 5 mm in the XY direction and 10 mm in the Z direction. The fine approach is performed with a piezo-ceramic tube that supports the tip, with sensitivities of 16 nm/V in the XY directions and 6 nm/V in the Z direction for room-temperature operation and 2.8 nm/V in the XY direction and 1 nm/V in the Z direction for 4.2K operating temperature. The maximum allowed voltage on the piezoelectric is $\pm 140V$. Just on top of the analysis chamber, the SPM pre-amplifier (small metallic box on top-right of figure 2.5) is externally connected to the tip-sample circuit.

Finally, the tips used to characterize all the materials of this work are tungsten tips, which were prepared in two steps: First, electrochemical etching outside the STM with a procedure discussed in [104], and then annealing in UHV. Briefing: A small tungsten wire is cut and placed into the Omicron tip holder. The tungsten wire is immersed in a NaOH solution in which a DC voltage is applied between the tip and the solution to create an ionic current. This current

etches the immersed part of the tip, and the etching rate is higher close to the triple phase contact point than to the end of the wire in such a way that it forms a very thin neck. This neck is eventually broken by the weight of the remaining immersed tip, leaving a very sharp tip with a crystalline apex. After the tip is transferred to the preparation chamber of the LT-STM, it is annealed in UHV in order to remove the oxide layer as well as residues of the electrochemical etching.

## 2.2 THz-Time Domain Spectroscopy

### 2.2.1 Introduction

The measurement of the physical processes occurring in the picosecond and sub-picosecond time range on a semiconductor nanostructure relies on the use of an ultrafast excitation source such as a femtosecond-laser. When a semiconductor material is excited by a very short focused laser pulse in the femtosecond time scale and with the main wavelength of the pulse at an energy equal or higher than the semiconductor bandgap, a distribution of electrons will be excited to the conduction band as well as holes in the valence band. Depending on the type of material and geometry of the nanostructure, the distribution of electron-hole pairs can be split and decay to equilibrium following different paths as a result of radiative or non-radiative recombination inside the material having a variable duration in the range of the picoseconds up to the nanoseconds. Also, a fraction of the laser beam is separated spatially before arriving to the target sample. This fraction of the beam, which depending on the experiment can be called probe beam or sampling beam is then delayed with respect to the pump beam by altering the optical path mechanically and subsequently targeted to the sample or detector. Changing the delay between the pump and probe beams and measuring the change of some physical properties of the sample as a function of this delay, as for example the transmissivity or reflectivity of the probe beam, it is possible to track the decay processes at the sample and infer physical properties such as the lifetime of the photogenerated carriers. This is the base of the optical pump-probe technique with sub-picosecond resolution. The probe signal can be detected and converted to an electrical signal (e.g.: change of reflectivity of the probe beam directed to a photodiode current), despite the fact that the bandwidth of electronic equipment is limited up to the GHz range. The realization of this technique relies then on the possibility to apply periodical and similar optical pulses to the target sample at a given repetition rate. In this way, if the period between pulses is larger than the time it takes for the material to recover its equilibrium properties and the pump-probe optical path difference remains fixed at a given delay, it is possible to retrieve the averaged response of the material at that fixed delay between pump and probe pulses. By scanning the delay and measuring the material response for each delay, the response of the material as a function of time is recovered. Such a detection technique is called Equivalent Time Sampling (ETS) and is the basis of the detection setup used when working with ultrafast signals in the time domain such as the terahertz emitted from optically excited semiconductors and nanostructures.

There are different ultrafast spectroscopies. When the optical pump beam is targeted to a sample, it excites a distribution of photoexcited carriers. The decay processes followed in the next picoseconds by this distribution of carriers are tracked by measuring the changes in reflectivity or transmissivity across the sample with an optical probe beam, which is targeted to the sample at different delays with respect to the pump beam. This technique is called Optical Pump-Probe spectroscopy and it is used to measure the lifetime of the core-shell

GaAs-(LT-GaAs) nanowires described in chapter 4. To probe if a semiconductor sample emits THz radiation after photoexcitation, a different detection scheme must be used: the pump beam impacts the target sample and a THz pulse is generated, this pulse is focused onto a THz radiation detector, which captures the amplitude and phase of the THz waveform in the time domain. The sampling beam is targeted to the detection system at different delays in order to probe the emitted THz pulse. This technique is called THz-emission spectroscopy and it has been used to explore the emission properties of photoexcited semiconductors in the THz range [105][106]. Furthermore, it has been used to investigate the emission properties of semiconductor nanowires in the THz range and the results are presented in chapter 5. Additionally, it is also possible to set a more complex scheme in which the ultrafast laser beam is split into three different beams. One beam goes to an auxiliary sample to induce a THz pulse with a known intensity and power, this THz pulse (THz probe beam) is then directed to the target sample. The second portion of the ultrafast laser pulse acts as a pump beam for the target sample, so that it excites a distribution of electrons and holes in the material, which then are probed by the THz probe beam at different delays between both beams. The transmitted THz probe beam, interacting with the target sample, is focused onto a THz detector in a time delay set by the third fraction of the initial laser beam (THz detection beam). This setup is called Optical Pump-THz probe spectroscopy and is a very powerful technique to study the transport properties of semiconductor nanostructures in the picosecond range without using contacts. One advantage of this technique is the use of two differential delay lines, which makes possible to probe the transmitted beam at different frequencies, from where it can be extracted the dielectric function of the material in the THz range (and then the complex refractive index or conductivity). More details are provided in [105][107]. This technique has been successfully applied to study the conductivity, mobility, and scattering rates as well as the plasma resonances of several semiconductor nanowires in a contactless fashion: GaAs Nanowires[108][109], GaN nanowires[110], InAs nanowires[111], InP nanowires[111] and doped GaAs nanowires[112].

### 2.2.2 Experimental setup

In chapter 5, THz-emission spectroscopy has been used to characterize the THz radiation emitted from semiconductor nanowires in the time domain. A photoconductive antenna has been used as the detection media. A detailed review of the experimental scheme will be developed in the rest of the section, followed by a discussion of the main features encountered in THz curves measured with time domain spectroscopy (THz-TDS) using photoconductive antennas as detectors, which can give more insight into the fundamental physical parameters determining the emission profile detected from the nanowire samples.

A sketch of the optical measurement setup used to perform THz spectroscopy in the time domain is displayed in the figure 2.6:

In the upper part of the figure the femtosecond laser is depicted as a square

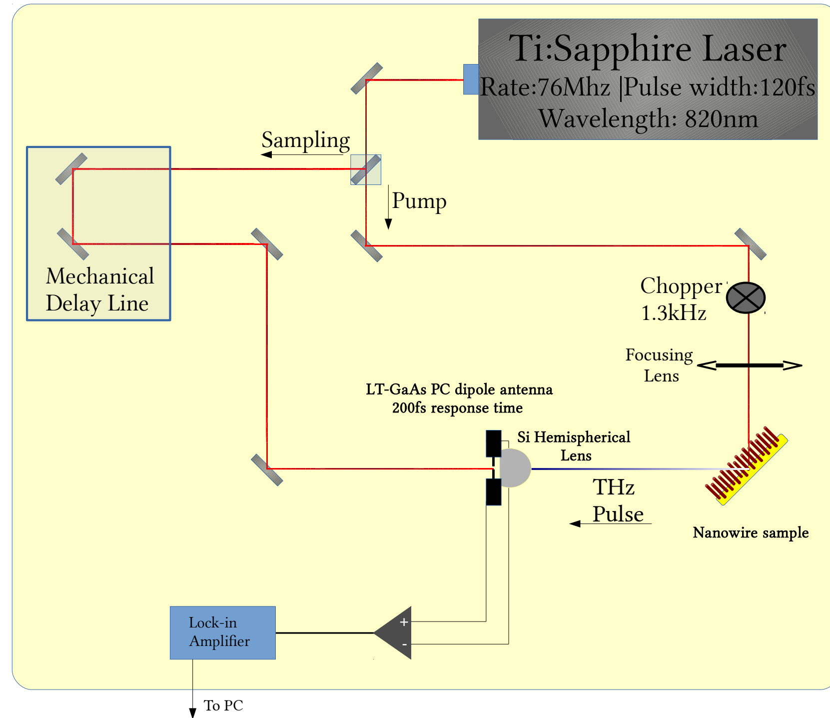


**Figure 2.6:** Schematic representation of the THz-time domain spectroscopy used to capture the THz emission spectra of the samples with nanowires. Upper part box sketches the position of the laser. The red line represents the femtosecond-pulse laser beam, which is split into sampling and pump beam. In the bottom of the figure, the nanowire sample is displayed in the right lower part, with the THz pulse represented by a blue line and the LT-GaAs PCA antenna in the lower part of the figure. Details of the experimental setup are described in text.

box. It is a Ti:Sapphire Laser (MAI-TAI), which in these measurements have been operating at a repetition rate of 76MHz, a wavelength of 820 nm and a pulse width of 120fs. The experiment can be schematized with the following elements:

- The femtosecond pulse exiting the laser is placed onto an optical circuit. In the first part of the circuit, the beam is separated by a beam splitter and divided into a sampling beam and a pump beam.

- The pump beam is passed through an optical chopper wheel spinning at 1.3kHz, which serves to modulate the signal in the Lock-In amplifier at the same frequency as the periodic reference.

- The pump beam is focused to the target sample with a convergent lens with a focal distance of 50 mm. The distance between the target sample and the lens is adjusted so that the sample lies on the focal plane of the lens.

- A distribution of photoexcited electron-hole pairs is created along the target sample, which in the case of this study has been either a semiconductor reference (InAs) or substrates with the vertically oriented core-shell GaAs nanowires. Ultrafast dynamical processes inside the sample lead to the radiation of an electromagnetic pulse whose main frequency components lie within the THz range.

- An additional focusing lens with a focal distance of 25 mm is placed at a given distance and angle after the target sample, in order to collimate the THz radiation. The collimated THz pulse is subsequently passed through a film of black polyethylene, which is transparent in the THz range but absorbs light in the wavelength of the laser in order to avoid parasitic signals from the reflected part of the pump beam on the target sample.

- The THz pulse is directed to a Silicon hemispherical lens that focus the beam into the detector. The detector is a LT-GaAs photoconductive dipole antenna (PCA) with a response time of approximately 200fs. The THz beam has to be focused, using the Si lens, onto the LT-GaAs photoswitch, which is placed in a gap of 30 $\mu$m between two metallic pads of the antenna. Such an antenna geometry is optimized to yield resonances of the impinging electromagnetic field in the THz range. When the pulse is properly focused into the photoconductive material, the electric field of the THz pulse resonates with the antenna and polarizes it depending on its phase. Then, the voltage between the pads of the photoconductive antenna will vary as the waveform change its phase with time.

- The sampling beam is directed to a mechanical delay line formed by two moving mirrors facing each other at an angle of 90 °, the stage formed by the mirrors is moved and controlled by a stepping motor with a step resolution of 40 fs in order to increase or decrease the optical path and as such scan the delay between the two beams.

- The sampling beam is further directed towards the LT-GaAs PCA from the opposite side on which the Si lens is placed. The beam impacts the LT-GaAs material and creates a distribution of electron-hole pairs in it that effectively short-circuit the gap between the pads of the antenna. If the THz beam arrives at the same time, the THz electric field polarizes the antenna giving the e-h pair distribution a net direction from which an electrical current in the nanoampere scale will flow between the pads. The direction of this current will depend on the phase of the THz field.

- The current between the two electrodes of the antenna is collected and further amplified and converted into voltage by a current-voltage converter with an amplification factor of $10^7 V/A$.

- The electrical signal is further fed to the Lock-In amplifier in order to increase the signal-noise ratio and finally collected by a computer or an oscilloscope.

Using the presented scheme, the THz emission characteristic in the time domain from the semiconductor nanowires samples as well as from a InAs (n-type) reference have been measured. Each time a new sample is placed on the pump beam line, a careful optimization of the laser spot focus as well as the directionality of the emitted THz pulse onto the LT-GaAs PCA has to be performed.

In the figure 2.7a, an example of a time domain curve obtained using this setup to detect the THz emission waveform from an InAs (n-type) sample is displayed. The physical mechanism involved in the generation of a THz pulse from an InAs surface is related to the great difference in mobility between the electrons and holes in this material. This THz waveform has been studied in several works [113][114][115] and it is produced by a mixture of physical effects in which the dominant one seems to be the so-called photo-Dember effect. The electron-hole distribution behaves as an oscillating dipole as a consequence of these effects, generating a dipole radiation pattern.

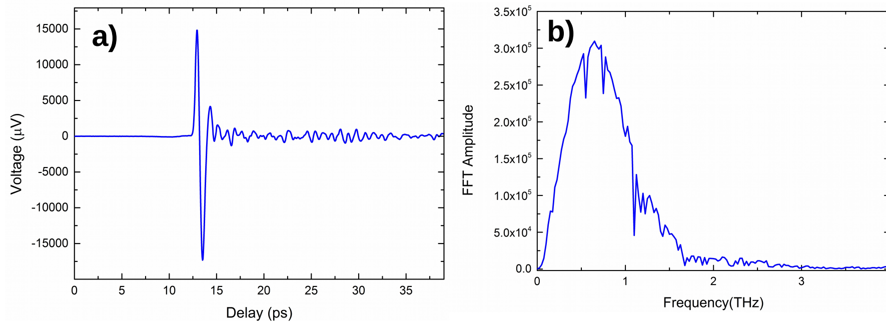


**Figure 2.7:** a) Time-domain waveform capturing the THz pulse emitted from a n-InAs bulk sample using the optical setup described in this section. The excitation wavelength was 820 nm and the average power of the pump beam 12 mW. b) FFT spectra of the THZ-TDS spectra of figure a), the multiple dips present along the curve represent the water absorption lines of the THz beam.

Following the THz waveform of 2.7a, when the delay is 0 no signal is detected because the sampling beam and the THz beam do not overlap in time at the PCA. By scanning the delay up to 120 picoseconds difference, one peak with positive voltage appears. It is followed in the next few picoseconds by another similar peak of negative voltage. The signal with increasing delays contains a train of small and noisy peaks. The amplitude of the voltage captured by the detector is proportional to the amplitude of the THz electric field and the voltage sign to the orientation of the radiative dipole. To gain further insight into the emission profile it is convenient to perform the Fast Fourier Transform of the time domain curve. As displayed in figure 2.7b, the FFT gives information about the bandwidth of the emitted pulse as well as the radiated power. Several dips can be detected interlaced along the FFT peak. They correspond to absorption resonances of the THz pulse with the water molecules present in the air, since the THz radiations are highly absorbed by water molecules [116]. One way to avoid

such spectral dips is to cover the space in which the THz beam is transmitted with a cage and purge the air with some THz inert gas such as nitrogen.

### 2.2.3 Modeling THZ-TDS curves

Performing THz-emission spectroscopy experiments on a semiconductor nanostructure allows to access the waveform of the THz radiation emitted by the sample with respect to time, which is a consequence of the ultrafast dynamics followed by the photoexcited electron-hole pair distribution within the nanostructure. In a THz-TDS curve, the waveform of the radiated THz radiation in the far field will be translated to a time dependent voltage curve with information about the magnitude and phase of the radiated electric field in the sub-picosecond timescale. The shape of the waveform can yield information about the lifetime of the photoexcited carriers inside the semiconductor nanostructure as well as the physical mechanism involved in the charge separation and the recombination. However, extracting physical information from these curves requires careful consideration of the excitation setup (femtosecond laser) as well as the detection setup.
The aim of the rest of the section is to reproduce the keypoints of a physical model for the THz-emission spectroscopy experiment developed by Jean-Louis Coutaz and collaborators and fully detailed in [117][118]. Coutaz's model considers a THz pulsed radiation produced from a LT-GaAs photoswitch coupled to a dipolar antenna. But the main physical consequences influencing the shape of the curves can yield valuable information to the case of pulsed emission from semiconductor surfaces (chapter 5, section 5.1.1). As explained before, a femtosecond laser pulse is targeted onto a semiconductor THz emitter at a given wavelength to create electron-hole pairs. If the emitter is GaAs grown at low temperature (LT-GaAS) embedded in some biased antenna geometry, the electron-hole pairs will be split by applying an external bias between the electrodes of the antenna and accelerated towards them. The amplitude of the electric field of the radiation emitted by the current transient will be proportional in the far field to:

$$E_{THz} \propto \frac{dj_{em}(t)}{dt} \tag{2.14}$$

The photocurrent transient which generates the pulse is formed by a initial fast rise in which the photocarriers are generated and split, followed by a generally slower decay. The rise is triggered by the femtosecond laser pulse. The decay is a consequence of the collision and recombination of the accelerated electron-hole pairs. The time resolved photocurrent is approximated by the convolution operator between the temporal profiles of the optical pulse power and the current density generated inside the photoconductor by:

$$j_{em}(t) = P_{opt}(t) \otimes [n_{em}(t) q v_{em}(t)] \tag{2.15}$$

In equation 2.15, $P_{opt}(t)$ can be modeled by a Gaussian curve with a FWHM set by the femtosecond pulse duration ($\tau_{las}$). The current density depends on the

density of photoexcited carriers, $n_{em}(t)$, which generally involves the dynamics of recombination of holes and electrons, but in this model is approximated by the change in electron population with a single exponential decay time ($\tau_{em}$), as holes are less mobile in LT-GaAs and have less influence in the photocurrent transient. The velocity of the carriers ($v_{em}$) is obtained by integrating the dynamical equation in the Drude model approximation, in which the acceleration is produced by the electric field $E_{DC}$ (external bias in the case of LT-GaAs antenna), and there is a damping term associated with scattering between carriers (collision time, $\delta\tau$):

$$\frac{dv(t)}{dt} = -\frac{v(t)}{\delta\tau_{em}} + \frac{qE_{DC}}{m_{eff}} \tag{2.16}$$

If equation 2.16 is solved and inserted into equation 2.15 along with the carrier density and optical temporal profile, the following expression is obtained:

$$\begin{gathered} j_{em}(t) \propto \int_0^\infty \left[\frac{P_{em}}{\tau_{las}} exp(-\frac{4ln2(t-t')^2}{\tau_{las}^2})\right] \times \\ \left[exp(-\frac{t'}{\tau_{em}})\right] \times q \left[q\frac{\delta\tau em}{m_{eff}}(1 - exp(-\frac{t'}{\delta\tau_{em}}))E_{DC}\right] dt' \end{gathered} \tag{2.17}$$

In which $P_{em}$ is the averaged laser power, the first bracketed term represents the Gaussian laser pulse, the second term is the temporal dependence of the electron density and the last term is the solution to equation 2.16. The solution of the integral gives the following expression:

$$\begin{gathered} j_{em}(t) \propto [exp(\frac{\tilde{\tau}_{las}^2}{4\tau_{em}^2} - \frac{t}{\tau_{em}})erfc(\frac{\tilde{\tau}_{las}}{2\tau_{em}} - \frac{t}{\tilde{\tau}_{las}}) \\ -exp(\frac{\tilde{\tau}_{las}^2}{4\tilde{\tau}_{em}^2} - \frac{t}{\tau_{em}})erfc(\frac{\tilde{\tau}_{las}}{2\tilde{\tau}_{em}} - \frac{t}{\tilde{\tau}_{las}})] \times \frac{q^2 P_{em} E_{DC} \delta\tau_{em}}{m_{eff}} \end{gathered} \tag{2.18}$$

In this equation, $\tilde{\tau}_{las} = \frac{\tau_{las}}{2\sqrt{ln2}}$ and $\frac{1}{\tilde{\tau}_{em}} = \frac{1}{\tau_{em}} + \frac{1}{\delta\tau_{em}}$. Only considering one type of carriers (electrons) and a simplified version of the Drude model, the equation reproducing the photocurrent is already a complex expressions with a mixture of constants terms, exponential and error functions. A more detailed expression can be obtained considering light and heavy holes acceleration by adding the respective equation of dynamics to the photocurrent density. Also, when the THz emitter is not a biased photoconductive antenna, but a semiconductor surface, it is needed to solve the respective equations of dynamics of photoexcited carriers, considering that the electric field separating the carriers could arise from a different origin (as a built-in electric field in the surface of the semiconductor or the photo-Dember field, as explained in chapter 5, section 5.1.1).

Finally, the emitted THz radiation in the far field is obtained by considering the classical Hertzian dipole approximation, that is, by deriving the photocurrent expression as in equation 2.14, then, the spectrum of the THz pulses can be obtained by the Fourier transform of equation 2.14, giving the following expression:

$$E_{THz}(f) \propto \frac{q^2 P_{em} E_{DC} f \times (\tau_{em} - \tilde{\tau}_{em}) exp(-(\pi f \tilde{\tau}_{las})^2)}{m_{eff}(1 - 2i\pi f \tau_{em})(1 - 2i\pi f \tilde{\tau}_{em})} \tag{2.19}$$

In equation 2.19, f is the frequency of the spectra. By inspecting equations 2.14, 2.18 and 2.19, very important aspects determining the shape of the THz radiation emitted in the far field as well as the characteristic of materials that can be good THz emitters are deduced. First; the proportional dependencies, the emitted THz amplitude will increase linearly with the power of the laser pulse as well as with the magnitude of the bias electric field accelerating the electrons and holes. In figure 2.8a, the temporal profiles of the laser pulse, the photocurrent in the material as well as the THz radiated in the far field are displayed overlay. It is seen that the laser pulse, which has a Gaussian shape in

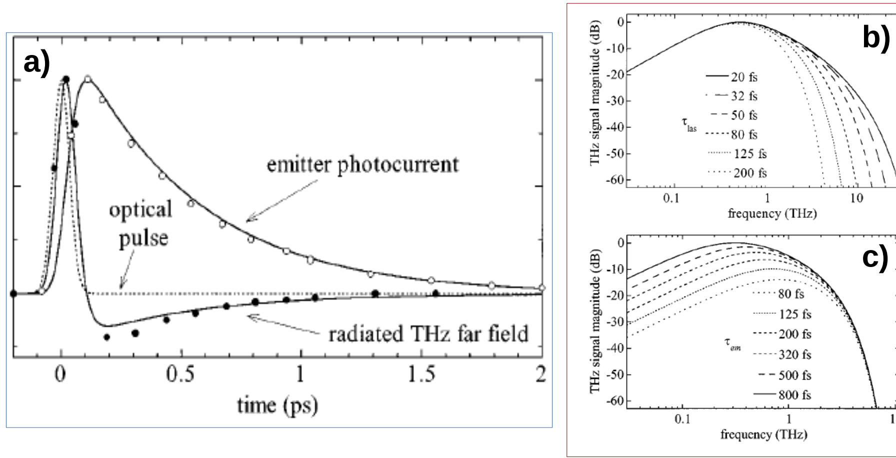


**Figure 2.8:** a) Calculated photocurrent in the emitter overlay to the amplitude of the radiated field versus time, the temporal shape of the laser pulse is drawn as a dotted line. Results obtained for fittings using the model of [117]. In the curves: $\delta\tau_{em} = 30fs$ and $\tau_{las} = 120fs$. b) Calculated frequency spectra for the THz emitted field for different laser pulses durations. c) Calculated frequency spectra for the THz emitted field for different carrier lifetimes in the emitter. Curves extracted from [117].

the femtosecond range, gives rises to a fast increase in the photocurrent along the emitter. When the pulse finishes, the photocurrent reach its peak value, and starts decreasing in a slower fashion as long as there is recombination of photocarriers within the material. Then, the radiated THz field in the dipole approximation has two peaks, a short first peak whose width is determined by the rise time of the photocurrent with the laser excitation, and a second one, of opposite sign, as a consequence of the decay of the photocurrent whose width will be determined by the lifetime of carriers. The sharpness of this second peak will be enhanced if the material is a good photoconductor as LT-GaAs[119], and the peak will be more blunt and undefined if the material has slow lifetimes and low mobilities[120]. Also, the sign of the electric field in the antenna is conserved, the relative sign of the first peak with respect to the second one will be flipped if the electric field separating the carriers changes its orientation, as it is also seen in equation 2.18.

In figures 2.8b and 2.8c , the Fourier transform of the THz radiation in the

far field is represented (equation 2.19) as a function of the pulse width ($\tau_{las}$)and lifetime of the material ($\tau_{em}$), respectively. It is seen in figure 2.8b that the bandwidth of the emitted signal is determined by the width of the laser pulse, increasing with shorter pulses. This is a consequence of the first fast transient in the photocurrent of equation 2.18 and figure 2.8a, whose sharpness depends on the width of the laser pulse. As the laser pulse gets shorter, the photocurrent rise is more step-like and higher frequencies are contained in the spectrum. As seen in figure 2.8c, shortening the lifetime of the material does not change the bandwidth of the emitted field but decreases the amplitude of the spectrum at low frequencies influencing the emitted power (which is proportional to the square of the THz electric field) as well as the signal-to-noise ratio of the signal.

This model is further extended in [117] to obtain the response in the detector. As the detector is a LT-GaAs photoconductive antenna, the equations of dynamics of the carriers will be very similar. The optical pulse modeling the sampling beam has similar temporal profile but less power, and the accelerating field in the antenna is the THz radiated field that reaches it. In general, the amplitude of the current depends on the amplitude of the THz field for a given laser pulse power. The bandwidth of detection is also determined by the duration of the laser pulse and the resonant frequencies of the antenna. Also, as with the emitter, the lifetime of carriers in the antenna determines the signal-to-noise ratio of the signal. The antenna response has been studied in [121]. The working regime is different depending on the lifetime of the photoconductor. First, the detector samples the THz signal at each time if the carrier lifetime of the antenna is shorter than 1 picosecond, giving a Dirac impulse photocurrent response, whereas if the lifetime of the antenna is much larger than 1 picosecond, the antenna will integrate the signal at each point, giving a more broadened and undefined photocurrent transient in the detector. In the case of our experiments, the lifetime of the LT-GaAs antenna is approximately 200fs, so that it can be considered to be in the regime of point to point photo-sampling.

Detection of radiation with photoconductive antennas was pioneered more than thirty years ago by Auston[122]. Since then, the materials performing as photoswitches (from RD-SOS (Radiation Damaged-Silicon on Sapphire) to LT-GaAs) have been improved to obtain better response and the detection bandwidth can be as high as 30THz when using very short femtosecond-pulses of 30fs [123]. Another very popular kind of detectors, offering higher detection bandwidth but a less simple setup are the electro-optical crystal. Details can be found in [105]. These two detection methods are the most oftenly used in the literature to measure THz radiation emitted from nanowires.

In chapter 5, the THz-emission spectroscopy setup described in this section, using a LT-GaAs photoconductor antenna as the receiver, has been used to detect the THz radiation emitted from an ensemble of core-shell GaAs nanowires.

# Chapter 3

# Preparation and Characterization of III-V Nanowires Surfaces

## 3.1 Introduction

Nanowire surfaces are as important as the bulk in determining the nanowire electrical properties due to their high surface-to-volume ratio. In the previous chapter, the influence of the surface on the resultant properties of nanowire field effect transistors was reviewed (Section 1.1). The mobility in semiconductor nanowires can be largely influenced by the surface crystalline structure and morphology, normally dampening its performance. Different passivation techniques have been followed in order to enhance this property. For example, the adsorption of different molecules at the sidewalls of the nanowires produces a large band bending along the radius of the nanowire, this changes the conductivity of the wires. Such effect is used to build very precise gas sensors. Furthermore, the research in thermoelectric nanostructures pursues the synthesis of nanowires with larger figures of merit (ZT). The figure of merit is a parameter indicating how efficient a thermoelectric actuator is. It is defined, at a temperature T, as: $ZT = \frac{S^2\sigma}{\kappa_e+\kappa_{th}}T$, where $S$ is the Seebeck coefficient, $\sigma$ the electrical conductivity and $\kappa_e, \kappa_{th}$ are the electronic and phononic contribution to the thermal conductivity, respectively. It is seen that an increase of the figure of merit requires an increase of the Seebeck coefficient as well as the electrical conductivity, and also a reduction of the thermal conductivity. As these parameters are normally interdependent in a material, different strategies have to be taken into account to optimize ZT. In [124], it was shown that the thermal conductivity of phonons was greatly reduced by creating rough surfaces in silicon nanowires. Therefore, the surface morphology of nanowires needs to be characterized in detail to optimize the performance of such devices[125]. Finally, one of the ultimate goals in the synthesis of nanowires is to control the crystal phase

in which they are grown, as there is intermixing between ZB and WZ phases (Section 1.3.2). The surface atomic reconstruction is not usually the one with the lowest surface energy. The study of the different surface reconstructions (or facets) is of paramount importance to understand better the interplay between the growth and the parameters changing the crystal phase as well as the resulting surface structure. Also, nanowires tend to show lateral growth on their surface, which is developed in parallel to the VLS growth at the droplet. This overgrowth can change the properties of the nanowire by inducing new surface reconstructions and defects. As reviewed in section 2.1, one suitable tool from which it is possible to assess at the same time the morphology, atomic structure and electronic properties of the nanowire surfaces is the scanning tunneling microscope (STM).

This chapter covers the most important procedures for the preparation of III-V semiconductor nanowire surfaces in order to study them with STM, as well as what is the main information that can be extracted with this tool. As stated in the previous paragraph, the nanowires are very sensitive to chemical or atomic changes in their surface. Their exposition to oxygen can change the electrical and morphological state of the surfaces. For any reliable STM characterization of the nanowire surface after growth, it is thus necessary to clean the surfaces that might have been exposed to air to recover a surface which is, ideally, as similar as possible, morphologically and electrically, to the ones obtained after the growth. As described in section 3.2, mainly, two surface preparation strategies have been followed by different groups. In the first one, the nanowires are exposed to air when transferred to the STM . The oxide on the surface is removed inside the UHV chamber of the STM by annealing the nanowire substrate at a given temperature (which depends on the type of semiconductor compound) and bombarding it with atomic hydrogen . The other method is realized by covering the as-grown nanowire substrate by a thin, amorphous arsenic capping layer just after the growth. This procedure can be performed when the nanowires are grown by MBE, as a molecular beam of $As_2$ or $As_4$ can be evaporated controllably onto the nanowire substrate at room temperature. The As layer protects the surfaces of the nanowires from reacting with the atmosphere. The As layer is further desorbed with an annealing at moderate temperatures inside the UHV system containing the STM. Then, as III-V semiconductor nanowires are normally grown vertically with respect to the substrate, it is necessary to transfer them to a sample in which they lie horizontally, so that the sidewalls can be accessible within the scanning range of the STM. This is done by cleaving them inside UHV with respect to a suitable substrate, as covered in section 3.3.1. Later, in section 3.3.2, the main surface crystalline structures adopted by the III-V nanowires are summarized. This is supported by a review of STM studies of typical III-V nanowire surfaces. It is seen that both cleaning methods yield reliable and comparable results with respect to the different atomic reconstructions encountered on the surfaces of the nanowires. However, it seems that there are some important morphological and electronic differences between the surfaces of the nanowires cleaned by

atomic hydrogen and by arsenic decapping. As suggested by the STM images, the interaction of the As capping layer with the nanowire sidewalls when the annealing of the layer is performed can produce surfaces with very different morphologies. Furthermore, these morphologies are not encountered by other cleaning methods. The sidewalls of two of the nanowires studied, self-catalyzed InAs and GaAs, show complementary morphologies. In the first case, a large distribution of holes of different sizes appear on the sidewalls while for the second nanowire, there are rounded islands dispersed along the sidewalls. This is further explored by making a study of the atomic structure of the two nanowires as well as the distribution of point defects and the position of their Fermi level. First, for GaAs nanowires, section 3.4.1 describes a possible mechanism in which the most favourable surface point defects produced during the desorption of the As capping layer are dictated by the Fermi level position at the surface of the nanowires. Second, for InAs nanowires, section 3.4 , it is seen that the observed morphology is dictated by the onset of congruent evaporation at the temperature used to desorb the As capping layer, but this morphology can be further tuned by reducing the decapping temperature below the congruent temperature, taking into account what is the position of the Fermi level on the surface of the nanowire. Finally, in the concluding section (3.5), the main results encountered in the chapter are summarized. The surface morphologies observed with the As capping desorption method are put in perspective by comparing them with the resulting morphologies observed with the atomic hydrogen cleaning method.

## 3.2 Surface preparation of Semiconductor Nanowires for STM

When a semiconductor is exposed to air, molecules present in the atmosphere can adsorb or desorb from the surface of the material until the chemical potentials between the surface and the atmosphere are equal, and equilibrium is reached. Even though the surface of a semiconductor is generally reconstructed to reduce the number of dangling bonds to a minimum, it can still be very reactive with adsorbed molecules such as oxygen. This generally leads to the creation of a superficial thin insulating layer. The apparition of such layers prevents the realization of scanning tunneling microscopy in stable conditions.
Indeed, imaging semiconductor surfaces with STM relies on the proper preparation of the surface prior to the measurement. This can be achieved in different ways: First, the use of ultra-high vacuum conditions (UHV), with base pressures down to $10^{-9}$ Torr, allowing to reduce the number of adsorbates in the atmosphere and thus slowing down the adsorption of molecules on the surface; second, the realization of a clean and flat surface, for which it is necessary either to anneal the surface *in-situ* to remove the adsorbates from the surface and/or induce a given surface reconstructions, or to cleave the surface in UHV in order to gain access to unexposed surfaces of the semiconductor.

Any UHV-STM will be prepared to operate in very low vacuum conditions by the combined used of ion-getter pumps and titanium sublimation pumps. But to transfer the nanowires from the growth chamber (being that a MOVPE or MBE chamber) to the STM UHV chambers, they have to be exposed to air. Therefore, the sidewalls of the nanowire can get contaminated. Several approaches have been followed in order to prepare the nanowire sidewalls for a reliable characterization:

The sidewalls of the nanowires can be passivated *ex-situ* using wet chemical methods in order to create nonreactive surfaces and prevent molecular reactions with oxygen[126]. However, atomic characterization with STM can be difficult as the surface often becomes rough and the interaction of the tip with the passivating molecules can lead to unstable or atomically difficult resolved images. In order to inspect the bare surfaces of the nanowires with STM, *in-situ* methods are more suitable.

First, it is possible to anneal the nanowires to induce a desorption of the oxygen complexes on the sidewalls. In [127], a fast and controlled current (Rapid Thermal Annealing) is used to anneal a sample containing Si nanowires. Auger measurements were performed in parallel to the annealing, observing that the oxygen peak disappears after increasing the current in the substrate to heat the nanowires up to 800°C during short periods of time. The morphology of the surface does not change as it is proved by comparing the roughness on the sidewalls of the nanowire before and after the thermal annealing with an electron microscope. Even though this method is easy and fast, it is not suitable for the surface of III-V semiconductor materials, as the temperatures used to desorb the oxygen could induce the evaporation of the group V chemical species as they

are very volatile, resulting in rough surfaces with a high amount of group III clustering [128].

Another approach consists in combining a more moderate annealing with the bombardment of the surface by atomic hydrogen. Such a method is called hydrogen cleaning method. It has been applied to clean and characterize the surface of several nanowires with STM, as InAs[129], GaAs[130] or other III-Vs [131]. In general, an optimization process has to be done for each different material as the decomposition temperatures of the oxide species are different, depending on the kind of group III or V materials. For example: for InAs it was shown that a temperature range and annealing times of $350 - 400°$C, 3-30 min, yield good results to obtain clean and well-resolved surfaces. For GaAs, the temperature has to be slightly higher, 550°C, due to the higher decomposition temperature of gallium oxide. Also, it is known that the exposition of the surface of the nanowire with oxygen can change its morphological and electrical properties due to the high surface-volume ratio of the nanowires. For example, in [132], it was shown that self-catalyzed InAs nanowires exposed to oxygen can induce a high amount of monoatomic steps on the surface, whose shape is influenced by the atomic structure along the nanowire.

Finally, the surfaces of the nanowires can be protected just after the growth is performed. They are capped inside the growth chamber with a protective layer. In the case of III-V semiconductor nanowires and MEB growth, it is very suitable to cover the nanowires with a thin layer of arsenic deposited after growth at room temperature and under high $As_2$ flux. This way, the nanowire sidewalls are homogeneously covered by a thin and amorphous metallic layer which prevents any exposure of the surface to air when transferring the nanowires from the growth chamber to the STM UHV chambers. In the figure 3.1b, a HAADF-STEM image of a Au-catalyzed InAs nanowire coated with an As capping layer is depicted. In the image, it is possible to distinguish the core of the nanowire with the crystallized gold droplet on top, as well as a thin layer of As conformally coating the whole structure of the nanowire.

Once the as-grown nanowire substrate is transported to the STM chamber, the arsenic coating layer is desorbed by passing a electrical current through the nanowires substrate. The arsenic desorption is tracked with an ion-mass spectrometer. A fast and steep increase in the $As_2$ mass peak is detected when the temperature of the substrate is raised above 200°C, as depicted in figure 3.1c. After a certain amount of annealing time, which depends on the thickness of the coating layer, the As peak in the spectrometer disappears, as seen in the figure. This indicates that the arsenic layer capping the nanowire sidewalls has been completely desorbed. Then, the nanowires can be transferred to a suitable substrate in order to study them with STM. This method has been applied to study the surface of GaAs[134], InAs [135] as well as ternary nanowires [62]. In figures 3.1d and e, a comparison of an as-grow InAs nanowire ensemble prior and after As decapping is depicted with cross-sectional SEM images. It is seen that the overall nanowire morphology is not affected by the desorption process of arsenic.

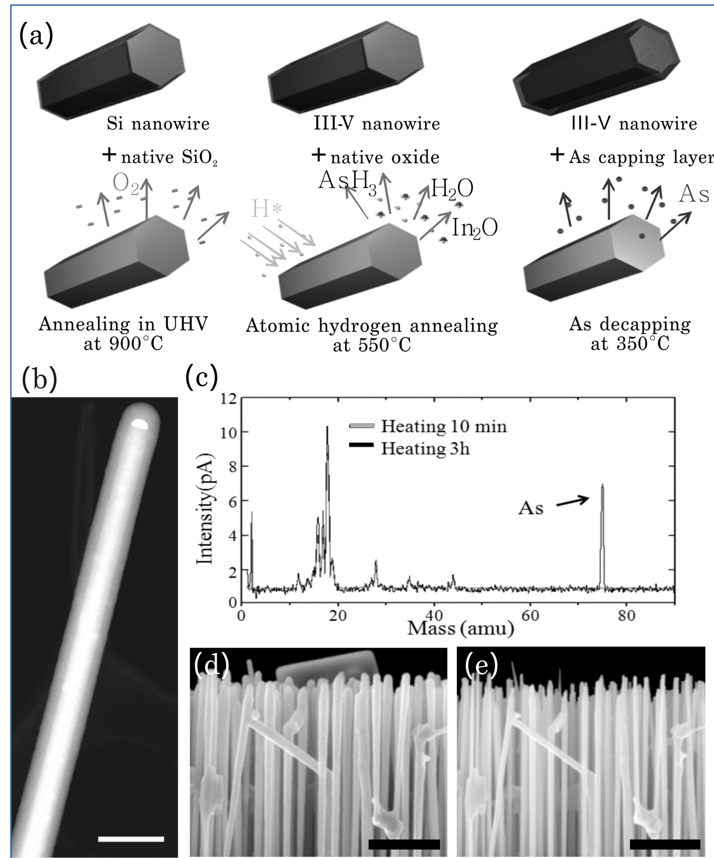


**Figure 3.1:** a) Different surface treatments for the study of semiconductor nanowires with STM. b) HAADF-STEM image of an As-capped InAs nanowire grown by molecular beam epitaxy. c) Real-time mass spectrometry monitoring of As desorption during annealing in the STM preparation chamber at about 350°C, under ultra-high vacuum conditions. (d,e) SEM image, in cross-section mode, of As-capped InAs nanowires before and after the desorption of the capping layer. The scale bar is 200 nm in b), 1 $\mu$m in d) and e). Extracted from [133].

## 3.3 Sidewall morphology of As decapped III-V semiconductor nanowires

### 3.3.1 Transfer of Nanowires in UHV

To characterize the nanowire sidewalls with a STM, it is necessary to be able to place the tip in a stable way along the lateral facets. Such a geometry implies that the nanowires grown vertically along the [111]/[0001] direction must be placed with the growing axis lying parallel to any given substrate. This way, given that the nanowires have a hexagonal cross section with six-equivalent facets on the sidewalls, when one of these facets is facing the substrate, the opposite facet will be parallel to the substrate. If the nanowire diameter does not excess the range of tip retraction accessible with the piezotubes at the

measurement temperature, it is possible to find nanowires on the substrate without crashing the tip, as well as to place the tip on the upper sidewall of the nanowire to inspect its atomic/electronic properties.

As the decapping of arsenic is done in UHV, the procedure used to transfer the nanowires has to ensure that the nanowire surfaces remain clean. Also, the substrates on which the nanowires are being transferred must have a good conductivity as well as very low roughness. One suitable material is highly doped n-type silicon with (111) surfaces reconstructed in the 7x7 configuration. The Si(111) (7x7) surface has been very well characterized with STM and its preparation is simple to achieve, by annealing the Si crystal at high temperatures [136].

Furthermore, the surface of silicon has been coated by evaporating a thin silver layer on top in UHV. This is done to enhance the electrical coupling with the nanowires. The Ag layer has been grown by annealing a small Ag sample in UHV in order to evaporate the material up to the silicon surface. The silicon is held at room temperature during the process. The resulting Ag coating layer for an evaporation time of 1 minute is shown in figure 3.2. The STM picture was acquired over a length of 1$\mu$m, at negative voltage. As seen in the height profile, the Ag layer is formed by a series of regular islands of different heights homogeneously distributed along the surface. The height difference between the deepest island and the highest island is 1.2 nm, as it is seen in the profile of the picture. Such a surface height profile extends over the whole surface. Even though the roughness is higher than the bare Si surface, the waviness of the surface is reduced, so that the cleaved nanowire can land horizontally without any tilting along large distances. Also, the contrast of the image seems to indicate that the silver islands form at preferential heights. This effect has been broadly studied [137][138][139]: the Ag island are stabilized by electronic quantization effects.

The procedure to transfer the nanowires in UHV is schematized in figure 3.3a. First, the nanowire as-grown substrate (figure 3.3b) with the vertically oriented nanowires is placed facing the host Si substrate with the Ag overlayer, as visible in the left part of figure 3.3a. The sample holder in which the nanowire substrate is held has been specifically designed by adding a small metallic soft spring to the back of the substrate as well as a small window in the metallic plate of the holder. When the nanowire substrate touches the host sample the spring is slightly retracted. If the back of the nanowire sample plate is tracked with a camera, it is possible to detect when the mechanical contact has been made to avoid any damage of the Ag/Si substrate. Later, the nanowire substrate is tilted with respect to the Si substrate using the XYZ manipulator described in section 2.1.5 (middle picture of figure 3.3a). As the nanowires are micrometrically long, they are bent against the Ag/Si substrate, eventually promoting the cleavage of the nanowires perpendicularly to the sample. If the tilting is done carefully along the same angle and direction, the distribution of cleaved nanowires on the host substrate will be localized at the contact point between both substrates and with all the nanowires lying almost parallel to each other, as shown in

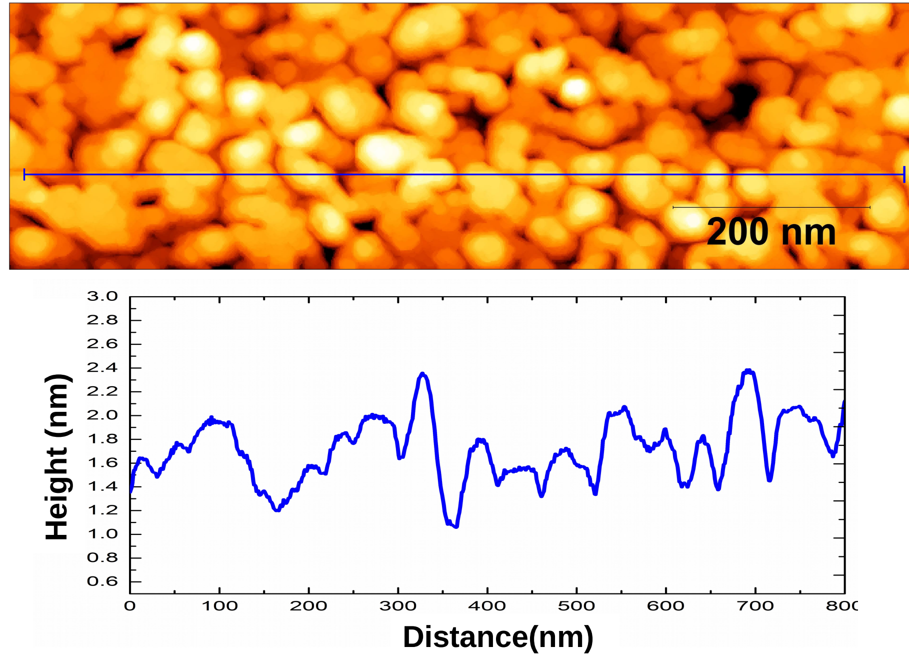


**Figure 3.2:** STM image showing the morphology of the thin silver overlayer grown on top of a Si(111) 7x7 surface. The image was taken at -3V and 1pA. The blue line marks the height profile showed in the graph below the image.

figure 3.3c. The distance between consecutive cleaved nanowires is generally not homogeneous and it is not controlled with this cleavage method. In figure 3.3c, the flat lying individual nanowires are separated by a few micrometers from each other, although it is not rare to find several nanowires stacked together at the same position due to electrostatic interactions. Such bundles of nanowires have been previously described with STM observations [129].

Once the nanowires have been transferred, they must be located by using the STM tip in broad scanning ranges, the procedure to find nanowires and scan the surface with STM is described later in section 4.4.

### 3.3.2 Facets and Surface Morphology in III-V Nanowires

The origin and engineering of the different crystal phases developed during the growth of a III-V semiconductor nanowire is one of the most active areas of research in this field. However, the crystalline facets formed at the surface of the nanowires are not so well treated in the literature and precise information is hard to find. Indeed, the post-growth characterization technique is usually SEM imaging. In this case, even though general morphological aspects of the nanowire are measured, as length and diameter, the crystalline structure of the facets is not distinguishable, and can only be inferred based on the symmetry observed on the sidewalls. Furthermore, none of these techniques is capable of proving nanometric morphological features along the surface, as steps and certain point

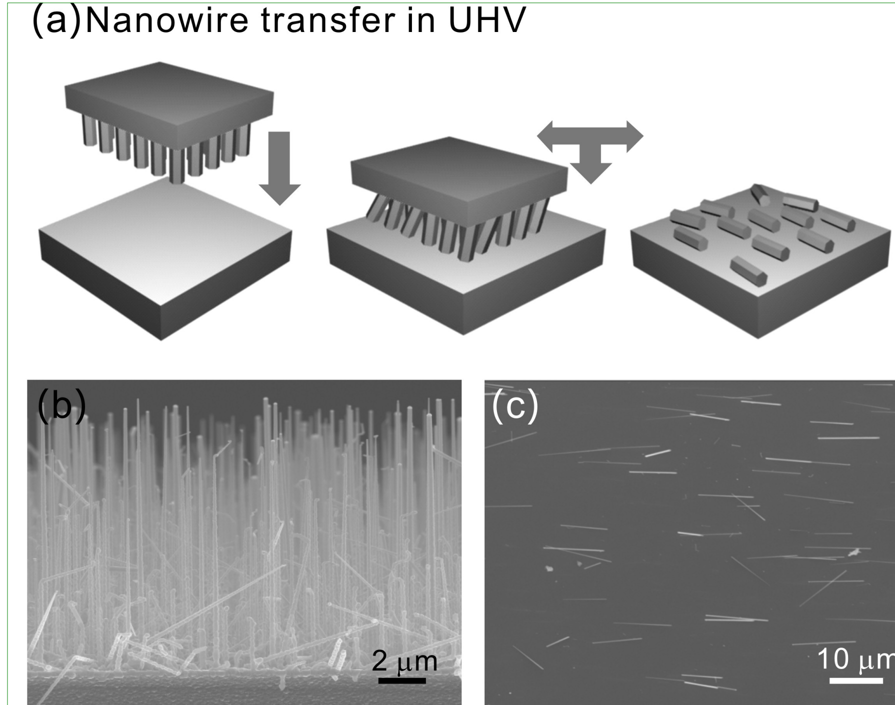


**Figure 3.3:** a) Nanowire transfer procedure in UHV. b) SEM image of <111> oriented Si nanowires grown by chemical vapor deposition before the manipulation of the sample. c) SEM image of Si nanowires deposited on a fresh Si(111) (7x7) surface. Extracted from [133].

defects, that can be very important in determining the surface properties of nanowires. Nonetheless, as stated in section 1.3.2, the crystalline structure in which the nanowires grow is generally not governed by thermodynamics, but rather by kinetics. Its main consequence is the nucleation of WZ phases in otherwise ZB crystals, but also the growth of crystalline surface facets with an atomic reconstruction that does not necessarily has the lowest surface energy.

III-V semiconductor nanowires growing along the [111]/[0001] directions generally adopt a symmetry in which the cross-section is a hexagon with six lateral facets. The commonly observed facets are conformed by crystalline planes with low Miller indexes: in a ZB nanowire, {110} and {112} facets, and its equivalent counterparts in WZ crystals, $\{11\bar{2}0\}$ and $\{10\bar{1}0\}$ facets, respectively. All these facets are depicted schematically in figure 3.4, in which the unreconstructed crystalline structure of the given surface is drawn for the first two surface layers, indicating the unit cell, as well as the orientation of the facet with respect to the growth direction of the nanowire. The {110},$\{11\bar{2}0\}$ and $\{10\bar{1}0\}$ facets are non-polar, while the {112} facet is polar. The {110} facet is formed by stacked rows of anions and cations along the [110] direction in a zig-zag fashion. It is important to note that these rows are not oriented parallel with respect to the growth direction, but making an angle of 35°. This is a consequence of the different stacking sequences of the ZB structure along the [111] direction formed

when the nanowire is growing, as explained in section 1.3.2. The other facets are oriented parallel to the growth direction.

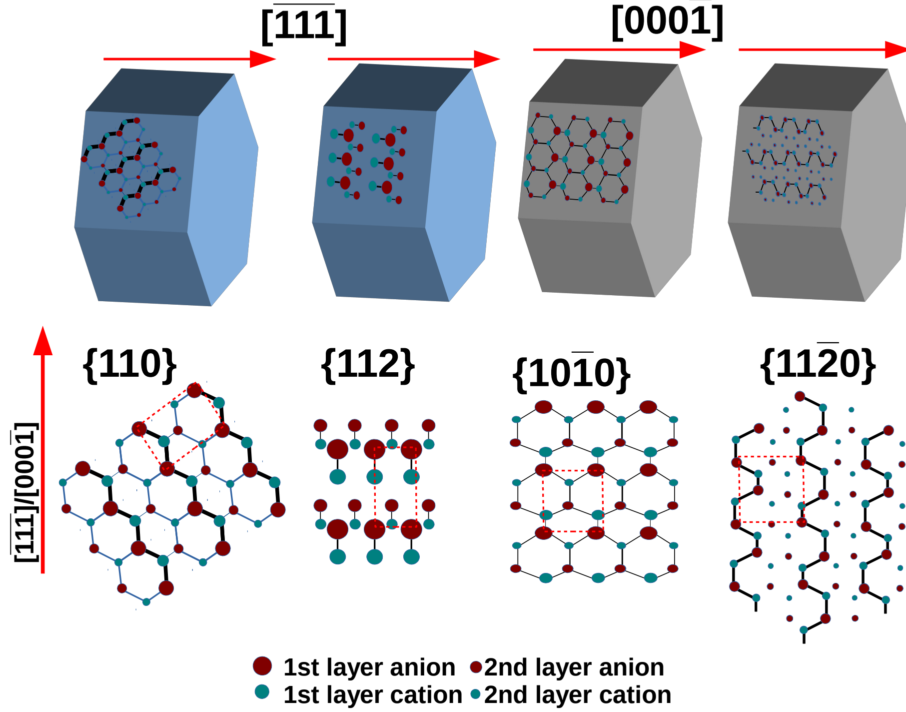


**Figure 3.4:** Schematics of the different crystalline structures forming the facets of III-V semiconductor nanowires, where a hexagonal tube represents a slice of nanowire in which the different atomic structures are drawed overlayed to the sidewalls as well as enlarged in the picture below the nanowire, as viewed from the top with detail from the two topmost layers. From left to right: $\{110\}$, $\{112\}$ type facets of ZB phases (blue hexagons), and $\left\{10\bar{1}0\right\}$, $\left\{11\bar{2}0\right\}$ type facets of WZ phases (grey hexagons). The red arrows mark the growth direction of the nanowire. The red dashed lines mark the unit cell of the different atomic structures.

In [51], Dubrovskii approximated the surface energy of these different facets by calculating the energy necessary to create the unreconstructed surfaces as counted by the number of dangling bonds exposed by sectioning a given atomic plane. He obtained results close to previously calculated values with other methods. For example, the energy of these facets for GaAs is: $\gamma_{110} = 1.543 J/m^2$, $\gamma_{112} = 1.79 J/m^2, \gamma_{10\bar{1}0} = 1.30 J/m^2, \gamma_{11\bar{2}0} = 1.543 J/m^2$. It is noted that the facet with the lowest energy for ZB structure is the $\{110\}$, while for the WZ is the $\left\{10\bar{1}0\right\}$. For InAs, the energy of the facets is: $\gamma_{110} = 1.06 J/m^2$, $\gamma_{112} = 1.19 J/m^2, \gamma_{10\bar{1}0} = 0.91 J/m^2, \gamma_{11\bar{2}0} = 1.06 J/m^2$. Again, the lowest energy facet are the ZB $\{110\}$ and the WZ $\left\{10\bar{1}0\right\}$. Also, there is another kind of facets that develops when the growth of the nanowire proceeds in the coherent twinning regime, as described in section 1.3.2, in which $\{111\}A$ and $\{111\}B$ microfacets are developed in the [112] direction. The orientation of the microfacets changes when a new growing layer is twinned with respect to the previous ones.

In the review of Dick *et.al* [46], the type of facets encountered for different III-V nanowires grown by MOVPE with different conditions are discussed. Some trends regarding the facet distribution are encountered: When the nanowires have a ZB structure, the most common observed facets are $\{11\bar{2}\}$ or $\{111\}$ type facets when twins are formed. In ZB sections of the nanowires, $\{110\}$ facets, even though they have the lowest surface energy for ZB structure, are found less frequently, with some important exceptions: These facets are found when the crystal purity of the nanowire is high, that is, with a few number of stacking faults or twins (as with self-catalyzed GaAs nanowires [54]). Also, $\{110\}$ type facets are frequently observed when the nanowires have a shell, or when there is an important degree of lateral overgrowth [62]. When the growth proceeds creating $\{111\}$ microfacets, as they are not parallel to the growth direction, twins appear along the growth direction, eventually forming twinning superlattices (section 1.3.2). Furthermore, it is observed that sometimes, rather than creating twins to change the orientation of the facets, the crystal adopts $\{110\}$ facets. For WZ structure, the $\{10\bar{1}0\}$ facet is the most frequently observed facet.

A very suitable technique to study the atomic structure of the different facets encountered on the sidewall of III-V semiconductor nanowires is STM. Due to the capabilities of the instrument described in the previous chapter, it is possible to know the atomic structure of the surface in a very precise way, with information not only about the surface atomic structure but also about the morphology of the surface. That is, the roughness and the distribution of point defects, as well as their influence on the electronic properties of the nanowires. The crystalline structure of $\{110\}$ facets of ZB nanowires or nanowire sections as well as the $\{11\bar{2}0\}$ facets and $\{10\bar{1}0\}$ facets of WZ nanowires have been characterized in several works [134][62][129][130][140].

Also, the morphology of the surface has been inspected by STM. As stated in the introduction, a very important feeding mechanism for the liquid droplet driving the growth of the nanowires comes from the diffusion of group III species along the sidewalls of the nanowire while the nanowire is growing. The diffusive species can get stacked along the surface of the nanowires and nucleate new terraces with group V species that get directly attached to the sidewall. This effect is known as lateral overgrowth or tapering, and its signature is generally a larger section of the nanowire across the basis than on the top of the nanowire, where the droplet is. The degree of tapering will be larger for longer nanowires. The lateral growth on the surface of the nanowires can be characterized with STM. Generally, it is found that the transition from diameters of larger section at the bottom of the nanowire to diameters of lower section at the top of it is given by the formation of terraces perpendicular to the growth direction of the nanowire. This kind of terraces have been found for InAs nanowires with WZ structure [132], where a method to infer the degree of tapering is proposed, as well as for other nanowires [131]. Additionally, different types of surface steps are found at the different facets of the nanowires as a result of the incomplete nucleation of an atomic layer along one facet, for example:$\{110\}$ type facets, in

which monoatomic terraces are seen stacked along directions forming 35° with respect to the growth direction. These follow the atomic structure of the facet, as in ZB phases of GaAs nanowires [134]. In [134] and [130], for WZ phases in GaAs nanowires, it is seen that the steps that form on the $\{11\bar{2}0\}$ surface facets have an elongated shape, with rows following the growth direction, while in [130] steps of the $\{10\bar{1}0\}$ facets are perpendicular and parallel to the atomic structure of the facet, forming squared terraces.

As the nanowires are growing, there is intermixing of crystalline phases between ZB and WZ structures. Even though there are ways to cope with this situation in order to reduce the intermixing [46][73], the nanowire crystalline structure at the basis or top of the nanowire will always have some degree of polytypism. This has an impact when lateral overgrowth is produced, as the boundary between facets having different crystalline structure can serve as a nucleation point for the diffusing particles, eventually nucleating new facets with a different orientation than the growth orientation. Such an effect has been seen in [62] and [130], and studied deeply in [141]. The following effects are observed: $\{11\bar{2}0\}$ facets tend to nucleate in the edge between two $\{10\bar{1}0\}$ facets and at the boundary with $\{110\}$ facets, transforming the hexagonal cross-section of the WZ nanowire into a dodecagonal cross-section with the edges of the hexagon being flattened by $\{11\bar{2}0\}$ facets. Also, when the nanowire grows with twinning superlattices of $\{111\}A$ and $\{111\}B$ microfacets, they evolve to $\{110\}$ facets, and the nucleation starts along the trenches of the microfacets, eventually transforming the whole surface of the nanowire to hexagonal cross-sections with $\{110\}$ facets. In [62], strips of $\{110\}$ facets growing at the edges of the twinning superlattices are imaged by STM.

So far, the papers referenced for the description of the surface of the nanowires with STM do not share the same cleaning method. In the group of Lund,[130][140][129][141][132], the method used to prepare the surfaces of the nanowires is done by removing the oxide layer with atomic hydrogen cleaning. In the group of Lille,[62][134][142][135], the method used to clean the surface of the nanowires is through desorption of As capping layers. Even though the observed features along the surface of the nanowires show similar trends between the two research groups with respect to the facet crystalline structure and step morphology, there are additional surface features which are encountered by decapping the nanowires with arsenic, and are not seen for equivalent nanowires cleaned by hydrogen. Also, the electronic properties of the facets as measured by STM spectroscopy are not similar. The origin of these is further investigated.

The sidewall of a series of different III-V semiconductor nanowires after arsenic decapping have been inspected with STM. The differences in surface morphology are presented in figure 3.5 for four different nanowires, with the following morphological characteristics:

- **Figure 3.5a**: The figure shows the sidewall of an InAs nanowire. The nanowire has been grown in MBE using gold aerosol particles as catalyst, and starting the growth from a InP stem, as described in [62]. The sidewall depicted in the STM picture is flat and does not show any particular

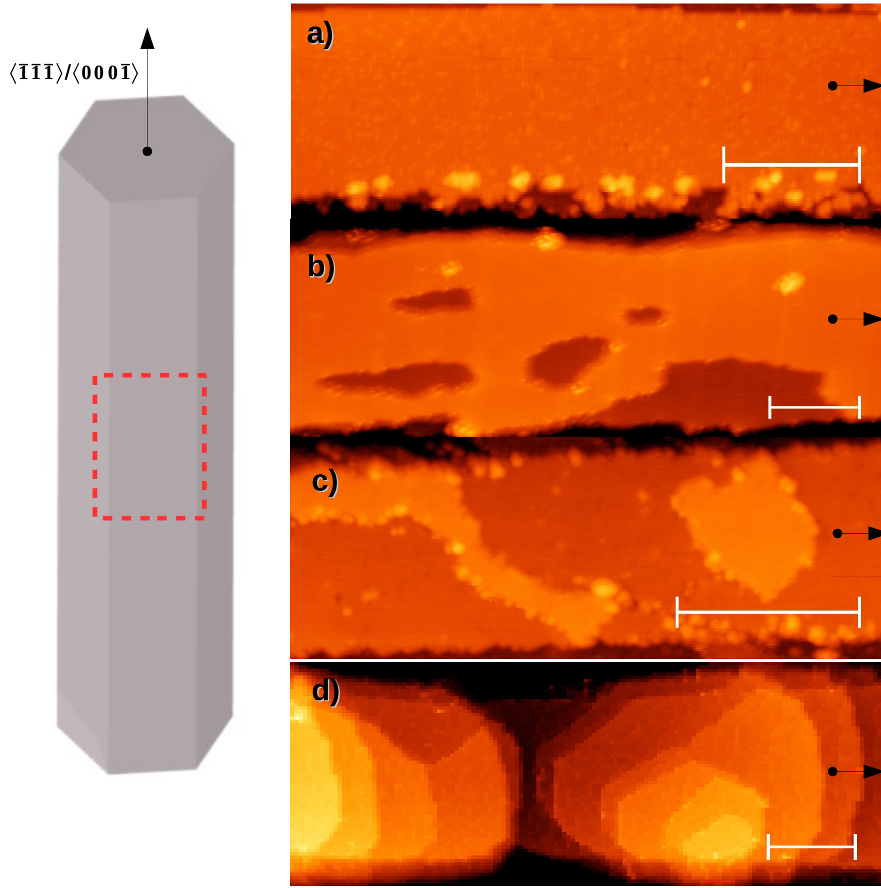


**Figure 3.5:** STM images of the sidewall morphology observed on different As-decapped III-V Nanowires: a) Au-catalyzed InAs nanowires (-3V, 10pA), b) Self-Catalyzed InAs nanowires (2V, 20pA), c) Self-Catalyzed GaAs nanowires (-4V, 17pA), d) Self-catalyzed core-shell GaAs/LT-GaAs nanowires (-3V,10pA). On the left, a schematic representation of a nanowire with a dashed red-line marking the portion of the sidewall that it is imaged with STM. The scale bar for all the images is 20 nm. The black arrow marks the growth direction of the nanowire. All STM images were acquired at 77K.

morphological feature along the growth direction or perpendicular to it. A distribution of small bright protrusions can be observed, dispersed all along the surface. These are individual Sb atoms, and appear as a consequence of the inclusion of Sb in the MBE chamber to grow the ternary compound InAsSb in the latter stage of growth [62]. Additionally, several clusters appear on the bottom part of the STM image. These clusters arise from the segregation of gold atoms from the droplet during the growth of the nanowire, which are distributed close to the edge of the sidewall, and thus can be imaged by STM[62][135]. As there are no particular steps in the terrace, the atomic structure can not be distinguished at this scale. However, the height contrast allows to distinguish a series of rows perpendicular to the growth direction and distributed equally spaced all along

the picture. It is then a WZ section of the nanowire showing a $\{10\bar{1}0\}$ facet.

- **Figure 3.5b**: This is the STM picture of an InAs nanowire. The nanowire has been grown in MBE by the method of self-catalysis described in section 1.3.5. The catalyst particles are In droplets and the nanowires grow following the [111]/[0001] directions, with the substrate being oxidized Si(111). Such nanowires are known to present a high degree of ZB/WZ intermixing[68]. In the picture, depressions of different sizes are observed on the sidewall of the nanowire: two dips of elongated shape are observed at the left, with a more rounded one at the middle, as well as a bigger dip extending from the terrace to the nanowire. These series of dips hold no particular crystallographic direction. Similar dips have been observed all along the sidewall of the nanowire, as well as on the sidewall of all these kind of nanowires studied by STM. The dips have a height of one monoatomic layer. The atomic structure of the nanowire can not be distinguished at this imaging scale.

- **Figure 3.5c**: The figure shows the STM picture of the sidewall of a GaAs nanowire. The nanowire has been grown by self-catalysis from Ga droplets, as described in detail in section 1.3.5. Nanowires grown with this method generally present a very homogeneous ZB structure with {110} facets. In the picture, the sidewall of the nanowire is flat with two monoatomic islands on it. In the left of the picture, the island starts from the edge of the sidewall with rounded shaped steps and a thin strip of steps extending to the opposite sidewall edge. At the right of the picture, a terrace with rounded steps is seen, starting from the edge of the sidewall. These islands do not follow any particular crystallographic direction and are located all along the sidewalls of the nanowire, generally with rounded shapes and starting from the edge of the sidewall. Another picture of the island distribution along a larger portion of the sidewall of the nanowire has been depicted in figure 4.6d. No other assumptions about the facets can be made on these sidewalls at this imaging scale.

- **Figure 3.5d**: The figure shows the STM picture of the sidewall of a core-shell GaAs nanowire. The nanowire has been grown by self-catalysis from Ga droplets, with a shell made of low temperature grown GaAs. The shell has been incorporated after completing the growth of the core. The procedure is detailed in section 4.3. In the picture, the sidewall of these nanowires, unlike the others, has a large degree of roughness. Height profiles acquired along the growth axis on a length of 2 $\mu$m give an average height roughness of 4 nm. It is caused by pyramid like mounds which are confined by the two parallel edges along the sidewalls of the nanowires. They are formed by a series of flat terraces stacked at different heights. The terraces, however, seem to have regular step edges, following crystalline directions with some of the step having angles of 35°C with respect

to the nanowire growth direction. This is a signature of ZB crystal phase with {110} facets[134].

## 3.4 Influence of As decapping in surface morphology

The morphological differences encountered by As decapping III-V semiconductor nanowires in similar conditions suggest that the origin could be ascribed to the interaction between the surface and the capping layer, that is: electronic or thermal effects influenced by the dynamics of the As capping layer when it is desorbed. To further pursue this hypothesis, STM images resolving the atomic structure of the surface as well as the electronic properties from spectroscopy curves have been performed on the sidewall of the self-catalyzed InAs and GaAs nanowires (figure 3.5b and c, respectively). These two nanowires present after cleaning very different surface morphology, the former having a random distribution of rounded holes or pits while the latter presents a series of rounded islands pinned to the edge of the nanowire sidewalls.

### 3.4.1 Self-Catalyzed GaAs Nanowires

To characterize the atomic and electronic structure of self-catalyzed GaAs nanowires, the scanning range is reduced to a small nanometric window in a flat region of the nanowire sidewall and the tunneling current is acquired in the constant current scanning mode at low temperature (77K in the case of these nanowires). The scanning tunneling spectroscopy (STS) is performed by placing the tip on a particular location of the sidewall in which there are no point defects or steps. The tunneling feedback is switched off and the sample voltage is ramped from negative to positive values in order to scan the valence and conduction bands of the nanowire as well as to obtain information about the position of the Fermi level. Furthermore, as explained in section 2.1.3, when the bias voltage magnitude is in the range of energy of the band gap of the material, no tunneling current flows between the tip and the sample. To obtain a measurable tunneling current close to the edges of the band gap, it is necessary to decrease the tip-sample tunneling distance without getting to point contact. Such an operation reduces the barrier height to an extend that a high enough sensitivity is achieved.

The results for the GaAs nanowires are presented in figure 3.6:

Figure 3.6a depicts a STM image, with atomic details, on the sidewall of the GaAs nanowire of figure 3.5b. The image shows a series of rows stacked parallel to each other along the $[0\bar{1}\bar{1}]$ direction and forming and angle of 35° with the growth direction (marked by a green arrow in the picture). This is the signature of a {110} type surface facet. Therefore, the crystal phase present in the scanned area is the ZB structure. The atomic contrast from the image (which is taken at negative voltage) arise, as explained in previous chapter, from the tunneling between the tip and the surface states centered on the As adatoms. However,

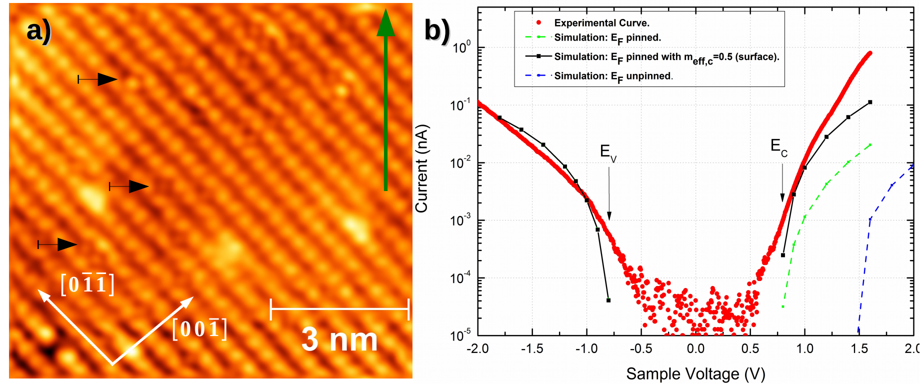


**Figure 3.6:** a) STM image with atomic resolution of a ZB {110} type sidewall of a self-catalyzed GaAs nanowire. Black arrows point to a few of the many As antisites dispersed in the surface. The green vertical arrow marks the orientation of the image with respect to the growth direction. The image was taken at -3.5V and 20pA. b) STS spectroscopy data taken in the nanowire sidewalls of a). The temperature of acquisition was 77K. The setpoint current 200pA. The red line shows the experimental data. The black, green and blue lines correspond to simulated STS curves with different parameters, as detailed in the text.

there is a large distribution of protuberances situated between two rows of As adatoms, in the position where the Ga adatoms lie. Some of the protuberances have been marked by a black arrow in the picture. By counting their number, a very high density is deduced, around $4 \times 10^{13} cm^{-2}$. When such a feature appears, the contrast in the STM image is almost similar to the adjacent As adatoms. Also, the four closest surface As adatoms seem to be slightly strained by their presence.

These point defects have been studied in [143], in which they are described as surface arsenic antisite defects. In [143], STM images of cross-sectional (110) surfaces of different n-type III-V semiconductors such as GaAs, GaP and InP are compared. The same defect appear in all samples, yielding the same atomic contrast as in figure 3.6a. The defect is seen to appear at negative as well as positive voltages with almost the same contrast in tunneling current, indicating that they are not charged [89]. Furthermore, the electronic properties of these defects are studied by STM as well as simulated with DFT to obtain the formation energy and the spatial localization of the wavefunction. The calculated wavefunction of surface antisites obtained from the simulation shows that it is very localized around the antisite lattice site. It has no satellite tails extending to the nearest neighbours, unlike bulk antisites as the ones observed in LT-GaAs ([144] and chapter 4). Also, as they are electrically neutral, as seen by STM and DFT, they do not contribute to the pinning of the Fermi level at the surface.

Figure 3.6b shows the current versus voltage spectroscopy data (in log scale) obtained on the sidewall. The experimental current obtained as a function of voltage is plotted with a red line, in which the position of the edges of the valence and conduction bands are indicated by black arrows. In the region of the band gap, no tunneling current is detected, and the acquired points correspond to

electrical noise. Simulated STS curves with different parameters are overlayed to the experimental curve and represented with thinner lines (black, green, and blue). The simulation of spectroscopic curves has been performed following the same methods presented in section 2.1.4, and references can be found therein. To simulate the experimental data, it is necessary to calculate the degree of band bending occurring at the surface of the semiconductor and determine how it affects the observed band gap. Normally, the exact tip-sample distance as well as the geometrical shape of the tip (radius, angle between the apex and the conical shank) are unknown. These parameters have to be optimized in order to obtain a reasonable fit.

The first thing to notice in the experimental curve is that the Fermi level is positioned at an approximately equal distance from the conduction band edge and from the valence band edge, suggesting that the nanowire is intrinsic. The apparent band-gap width measured at the surface is equal to 1.5 eV, consistent with the bulk band gap of GaAs. It is known that the Fermi level is unpinned for the (110) surfaces of undoped GaAs and the degree of band-bending very large. This is studied in [97]: a large portion of the tip voltage can drop on the surface producing an upward band bending. Then, the onset of the conduction band does not appear until very large voltages, leaving a large apparent band-gap. The blue line in the figure is a simulation of the conduction band current onset if the Fermi level is not pinned. It yields a very large band-gap, with a width close to $2.5eV$. However, this is not what is seen in the experimental data of figure 3.6b. Thus, the Fermi level has to be pinned at the surface of the nanowires. As the surface antisites are neutral, they can not pin the Fermi level. Then, the pinning is likely to be produced by extrinsic states, such as the charged states occurring at the steps of the (110) surface of GaAs, as stated in sections 2.1.4 and 4.4.2, as well as in reference [145] for cleaved (110) surfaces of intrinsic GaAs and in [134] for (110) facets of GaAs nanowires. These states enter in the simulation of the tip-induced band bending being modeled as a distribution of states at the surface of the material. They are distributed at positions in the band gap dictated by the charge transition levels. Their effect is introduced in Poisson's equation as a charged sheet at the interface between the semiconductor and the vacuum [95]. The extrinsic states can pin the Fermi level at the surface by screening the tip voltage and their effect is noticeable even if the spectroscopy is performed at a certain distance from the step edge [100]. Looking at the sidewalls of these GaAs nanowires (figure 3.5c), the steps formed by the nucleation of the aforementioned islands can be responsible for this pinning. In figure 3.6b, the green and black lines simulate the conduction band current when the Fermi level is pinned by a Gaussian distribution of $4 \times 10^{13} cm^{-2}$ surface states centered at a position close to the conduction band onset at 0.75 eV. That alone is enough to reproduce properly the onset of the conduction band edge observed in the experimental curve, taking into account only the effective mass of the lowest conduction band.

To further tune the simulation curve to the experimental one, it is necessary to increase the effective mass of the electrons in the conduction band from

$m_{eff,c} = 0.063m_o$, in which $m_o$ is the free-electron mass, to $m_{eff,c} = 0.5m_o$ (black line in the figure). This is a better estimate for the effective mass of the conduction band close to the band edge, as discussed by Ebert in [146]. The increase in effective mass is produced by the Ga atoms of the surface layer, the surface band of states has a different effective mass and dominates the tunneling current at the conduction band edge. The simulated curve differs from the experimental one at larger voltages because bulk states from the different conduction bands contribute to the tunneling current. However, the current in the conduction band is considered as coming from one band in the simulation, within the parabolic band approximation. As seen in the figure, the experimental curve is better fit with this consideration at low voltages. For the simulation of the valence band (black line), the tunneling current from electronic states arising from the heavy and light hole valence bands is considered. Also, one thing to notice is that there is a small current in the experimental curve for voltage values within the band-gap. This is the current produced by the wave-function tails of these extrinsic states pinning the Fermi-level and it has been also described for nanowires in [134]. However, these states are considered in the model of [95] only through their electric signature in the band-bending but not in the computation of the tunneling current. That is the reason explaining its absence in the simulated curves.

Now it is possible to depict a model for the encountered sidewall morphology based on the electronic properties measured on the sidewalls of the self-catalyzed GaAs nanowires. The GaAs sidewalls exhibit a ZB crystal phase with $\{110\}$ type facets. A series of rounded islands nucleating from the edges between two facets are observed all along the sidewalls (figure 3.5c). A large distribution of point defects in the form of As antisites are observed in the surface. Furthermore, the Fermi level is pinned in the middle of the band-gap, the nanowires being nominally undoped. These nanowires have been protected by an amorphous As capping layer after growth, which has been desorbed in UHV prior to the measurements (section 3.2). It is then possible that this surface morphology might be governed by the different point-defect concentration occurring at the surface. The dynamics of these point defects when the evaporation of the As capping layer is performed drives the formation of the morphology found at the surface of the nanowire.

The equilibrium concentration of point defects in a surface depends on the total formation energy of such defects (the difference in the total energy of the material with and without the defect). If these defects are charged, an electron (hole) is taken from the bulk material in order to negatively (positively) place the charge on the defect so that the formation energy of charged defects also depends on the position of the Fermi level in the material multiplied by the charge state of the defect, $qE_F$. The charge state, q, includes the magnitude and sign of the charges in the defect as: $q = \pm n$, where $n$ is an integer number accounting from the number of charges of the defect. Additionally, the chemical potential of the atomic species involved in the defect formation must be taken into account, as there might be a change in the number of particles of the system

in order to create the defects. Then, the formation energy of a charged defect can be expressed for a III-V semiconductor as [147]:

$$\varepsilon^{form} = E^{Tot}_{def} - E^{Tot}_{ideal} - n_A\mu_A - n_C\mu_C + q(E_F) \tag{3.1}$$

In the equation, $E^{Tot}_{def}$ and $E^{Tot}_{ideal}$ are the energy of formation of a slab of the semiconductor crystal with and without the point defects in its atomic structure, respectively. $\mu_A$ and $\mu_C$ are the chemical potentials of the respective anion and cation species of the III-V semiconductor and $n_A$,$n_C$ are the number of anion or cation species added or removed from the material in order to create the given point defect. $E_F$ is the position of the Fermi level in the semiconductor with respect to the valence band maximum. Regardless of the total formation energy difference, there is a linear dependency between the position of the Fermi level and the formation energy, whose slope is given by the sign and magnitude of the charge of the defect. Then, positively(negatively) charged defects will have a higher equilibrium concentration the more the material is p-type (n-type), whereas for undoped materials, uncharged defects should have the lowest formation energy. However, it should be noticed that in the actual formation of defects in a surface there are different thermodynamical processes involved (atomic diffusion, substitutions, surface reactions...) so that the concentration of defects in the surface is governed by the formation barriers rather than from the initial and final energy of the system. For example, in [148][147], for anion-rich surfaces, the neutral anion antisite is the defect with the lowest formation energy for (110) surfaces at all positions of the Fermi-level. But as the formation of antisites needs more than one atomic process, the most stable point defect encountered experimentally is generally not antisites for p-type(n-type) surfaces, as accounted below.

Several studies of the most stable point defects in the (110) surfaces of various III-V semiconductors have been made in the last years by using cross-sectional STM: It was found that positively charged anion-vacancies (As/P vacancies) are formed on the(110) surface of p-type InP and GaAs semiconductors [149]. Furthermore, the formation barrier of the vacancies is studied by comparing the vacancy concentration change with respect to different annealing times and temperatures. In [150], the formation barrier is studied as a function of the Fermi-level position for p-type (110) InP and GaAs with different doping concentrations, finding that the barrier decreases with increasing p-type doping in both cases, thus increasing the vacancy concentration. No In/Ga vacancies are found on p-type materials, unless they are produced by the STM tip. On the contrary, when the material is n-type, the point defects encountered in the surface in the largest amount are negatively charged defects, as cation vacancies. In [151],Ga vacancies seem to be the dominating surface defect for (110) n-type GaAs. This suggest that in n-type material the energy barrier might also decrease for negatively charged defects when the Fermi-level position moves towards the edge of the conduction band. When the semiconductor is pinned midgap, uncharged point defects have been observed, as neutral Ga vacancies

in (110) GaP [152] as well as neutral antisites in GaP, InP and GaAs (110) surfaces [143].

In view of these results, it is possible to elucidate the most likely point defects to be produced when the As capping layer is evaporated from the nanowire. During the evaporation of the As layer, the conditions at the surface of the nanowires are As-rich, favouring the creation of As related point defects with different charging state depending on the Fermi level. These defects can be As adatoms, being uncharged or negatively charged (depending on Fermi level position), uncharged As antisites or cation vacancies (Ga or In for these nanowires), which are negatively charged. If the Fermi level is pinned midgap, uncharged point defects can also form, like surface As antisites.

For GaAs nanowires, uncharged antisites are created, as detected experimentally. In order to create an antisite, the following model is proposed: A Ga atom is ejected from its lattice site, creating a Ga vacancy. These are negatively charged, even for midgap Fermi level pinning, with a formation energy of approximately 1.2 eV, as shown in [153](figure 4.5 thereof). The charged defects can become uncharged if the vacancy site is replaced by an arsenic atom, creating a surface arsenic antisite, whose formation energy is approximately -0.25 eV for midgap Fermi level pinning [148]. These antisites remain in the surface layer, as the barrier for inward diffusion is very high [153](figure 4.25 thereof). As there is a large supply of As atoms from the capping layer and the nanowire is intrinsic, this process is more effective compensating the surface than the formation of As vacancies. Then, considering that the congruent temperature for GaAs is around 680°C [154], the Ga atoms diffuse along the sidewall of the nanowire but do not evaporate (this has also been shown in nanowire growth publications, as [38]). Therefore, they diffuse on the sidewall until they are pinned at a position with higher energy barrier for diffusion, as the edge between two facets of the nanowire. From there, the Ga atoms act as seed particles to nucleate an island of GaAs in the As-rich conditions, with the excess of As from the cap. This effect is responsible for the distribution of monolayer height islands observed on the sidewalls of these nanowires (figure 3.5c).

The mechanism of island formation driven by the Ga adatoms ejected from the nanowire sidewalls can be further corroborated by studying the distribution of such island on the surface. In figure 3.7, the density distribution of atomic heights is obtained from the STM images of the sidewalls of the GaAs nanowires (as the sidewall portion of the inset). It is seen that the GaAs island occupies approximately 25% of the total surface area of the sidewalls of the nanowire, which stands for a 12.5% of Ga atoms. Such a percentage is in line with the density of surface antisites, which is $4 \times 10^{13} cm^{-2}$, as extracted from figure 3.6a. This density of surface antisites accounts for the 10% of the total number of atoms on a {110}-type surface. Thus, the concentration of Ga atoms ejected from their lattice sites to form the surface antisites roughly matches the concentration of Ga atoms encountered in the islands created along the sidewall of the nanowire.

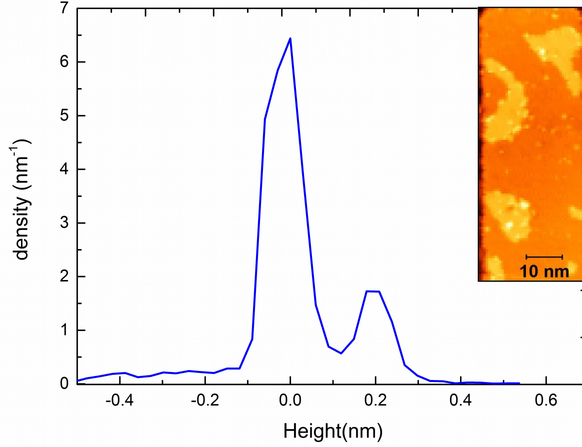


**Figure 3.7:** Histogram showing the distribution of heights extracted from the STM images of the sidewalls of the GaAs nanowires, as the one depicted in the inset. A height of 0 nm marks the atomic plane of the atoms on the sidewall of the nanowire. The height of the atomic plane of the islands is one monolayer of GaAs, 265Å. Approximately one third of the sidewall is occupied by islands. Inset: STM image used to construct the height distribution histogram. It depicts the sidewall of a self-catalyzed GaAs nanowires with the As-layer decapped at 380°C. The image was taken at $V_{bias} = -4V$ and $I_0 = 5pA$.

### 3.4.2 Self-Catalyzed InAs Nanowires

Next, the atomic and electronic characterization of the sidewall of InAs nanowires are presented in figure 3.8. Figure 3.8a depicts an STM image taken in constant current scanning mode with atomic details of a sidewall of the InAs nanowires presented in figure 3.5b. The image has been taken in a reduced area away from the large hole islands observed on the surface. The image shows a series of stacked rows, making an angle with the growth direction (marked by a vertical green arrow in the figure), which corresponds to the ZB crystal phase with {110}-type facets. The sample voltage is negative, with a value equal to -0.7V. At this voltage, the filled surface states of the As adatoms contribute more to the tunneling current and the contrast in the image arises from the filled dangling bond states of As, which are located inside the valence band. Opposite to the GaAs sidewalls, the stacking of the ZB phase gets interrupted every few nanometers. Such a trend is observed on the whole sidewall of these InAs nanowires studied by STM. It is the signature of WZ stacking faults and twins. In the figure, the stacking faults (considered as a single atomic layer of WZ structure intermixed in the ZB crystal phase, section 1.3.2) have been marked by horizontal blue arrows, and the ZB twins have been marked with horizontal green arrows. The image shows that the sidewall presents a very high density of stacking faults and ZB twins, pointing to a very large degree of intermixing, with a preferential ZB structure. Such a density of growth related defects can be linked with experimental observations for InAs nanowires relating morphological aspects with the density of defects. For example: in [7], it has been observed that Au-catalyzed InAs nanowires grown by MOVPE having

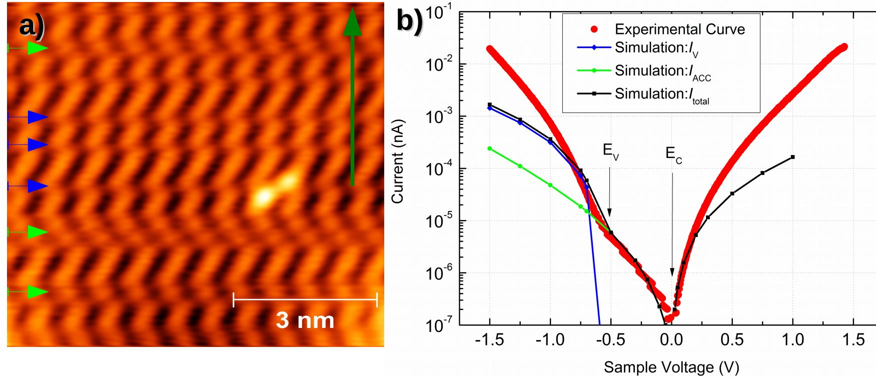


**Figure 3.8:** a) STM image with atomic resolution of a ZB {110} type sidewall of a self-catalyzed InAs nanowire with intermixing of stacking faults (blue arrows) and ZB twins (green arrows). The green vertical arrow marks the orientation of the image with respect to the growth direction. The image was taken at -0.7V and 50pA. b) STS spectroscopy data taken in the nanowire sidewalls of a). The temperature of acquisition was 77K. The setpoint current 20pA. The red line shows the experimental data. The black, green and blue lines correspond to simulated STS curves with different parameters, as detailed in the text.

diameters between 80-90 nanometers exhibit a very high degree of intermixing, with preferable segments of ZB phase interrupted by stacking faults and twins every few nanometers. This is consistent with the diameter of the herein studied nanowires, between 80-100 nm, as measured by the change in tip-sample height when scanning over the nanowire. Furthermore, when the InAs nanowires are grown by MBE and self-catalysis with In droplets, as in [68], a large degree of intermixing is observed by tracking the crystal phase with X-rays at the different stages of growth. It is seen that during the first stages of growth (in which the nanowires are short), the liquid droplet is In-rich, favouring the growth of WZ structure with several stacking fault, while at the latter stages of growth (the nanowires are longer) the In-droplet can be solidified due to the more As-rich conditions. They suggest that in this case the favoured structure is changed to ZB, but with stacking faults, WZ inclusions and twins. The threshold in length for a nanowire having a predominant WZ phase to a ZB phase is measured in [68] to be around 240 nm. In the InAs nanowires studied here by STM, a length larger than 240 nm has been always observed, thus supporting a predominant ZB crystal phase.

The electronic properties of the InAs sidewall have been obtained by placing the STM tip on top of a ZB phase area of the sidewall and performing current versus voltage curves. The results are shown in figure 3.8b. As with the GaAs nanowire, the experimental curve is represented with a broad red line, as well as with the axis in log scale. The simulated curves are represented by thinner lines (green, blue and black). Simulations have been performed using the same methodology as with the GaAs sidewalls.

There is a strong difference between the electronic properties of InAs sidewalls and GaAs sidewalls: First, the position of the Fermi level (Sample voltage

equal to 0 V in the figure) overlaps with the onset of the conduction band edge states contributing to the tunneling current at positive voltage. At negative voltages, the shape of the current is more complex, as there is tunneling current at all voltages, and a change in the curvature of these currents is produced at -0.5 eV. The change in curvature is a consequence of the onset of a different band of states contributing to the tunneling current. The onset of the valence band is marked in the figure and it has been delimited by the method proposed by Feenstra [92]. The measured width of the band-gap is approximately 0.5 eV, which is also consistent with the bulk band-gap of InAs at 77K, so that the degree of tip-induced band-bending is very low.

The Fermi level position indicates a n-type surface, even though the nanowires are nominally undoped. This effect has been studied and it is related to the formation of an accumulation layer on the {110} surfaces of InAs (downward band-bending at the surface), no matter the degree of doping on the bulk InAs [155]. Thus, the surface states of InAs are electron rich, such that the Fermi level crosses the conduction band. The origin of such a phenomenon is related with the electrochemistry of In-adatoms, and can also be produced by extrinsic defects such as unintentional hydrogen impurities adsorbed at the surface during growth, as proposed in [156]. Then, as shown in [157], if tunneling spectroscopy is performed and the sample voltage is ramped down, when the Fermi level of the tip crosses the Fermi level of the sample the accumulation layer is further bent downwards, producing a triangular quantum well between the conduction band and the vacuum (as depicted in figure 2.4b). Electrons in the tip can then tunnel into the conduction band states through localized resonances on the quantum well. The position of such resonances varies dynamically with the degree of band bending, such that several current channels are opened during the voltage ramp, contributing to the current at negative voltages. The resulting tunneling current produced from the accumulation layer states has been simulated and it is plotted with a green line in figure 3.8b, where it perfectly fits the experimental curve in the band-gap region. When the voltage is further ramped down, eventually there are states in the valence band within the bias window that contribute as well to the tunneling current, thus increasing the magnitude of the detected current up to the point in which it is the main contribution to the observed spectra. The current due to the valence band states has been depicted with a blue line in the figure and fits properly to the experiments for voltages larger than the valence band edge onset. It is only when summing up the current from states within the valence band and the accumulation layer states (as marked by a black line in the figure) that the experimental curve is perfectly reproduced, thus confirming the pinning of the Fermi level by an accumulation layer at the surface. The same spectral shape has been observed experimentally and simulated by Feenstra *et.al* for the accumulation layer states on the {110} surface of n-type GaAs. In figure 3.8b, the deviation between the fitted curved (black) and the experimental curve at larger voltages is produced by the underestimation of states contributing to the tunneling current and non-parabolicity effects, because the model only considers states coming from the lowest energy

conduction band in InAs as well as the heavy and light hole valence bands in the parabolic band approximation.

In the InAs nanowires, there is a large intermixing between ZB and WZ crystal phases, but a predominant ZB structure with {110} type facets is found. Vacancy islands with different sizes and shapes are observed distributed all along the sidewalls. No other point defects in a large concentration are observed with STM. The surface is n-type, the Fermi level is pinned on the surface at the conduction band edge position due to an electron accumulation layer.

When the As capping layer is evaporated at approximately 380°C from the nanowire sidewalls, In and As adatoms are evaporated during the decapping process, and InAs has a congruent evaporation temperature (387°C [158]), similar to the decapping temperature. These In and As adatoms are thus evaporated at equal rate from the surface with the rest of the capping layer. This is a thermal effect, and it leads to the creation of this specific pattern produced by holes all along the sidewall of the nanowire. A similar morphology has been recently studied on GaAs-(100) surfaces annealed at low pressure at the congruent temperature of GaAs [159]. When the congruent temperature is reached and Ga and As atoms evaporate at the same rate, the same surface topography, decorated by a random dispersion of holes of different sizes is observed by AFM images. Furthermore, in [132], for In-catalyzed InAs nanowires cleaned by atomic hydrogen, a winding pattern of stripped holes is found along the sidewalls of the nanowire. The formation of the holes could be as well ascribed to the formation of vacancy island during the cleaning, as it is done at a temperature close to the congruent temperature of InAs (380°C).

To further corroborate this hypothesis, another piece of the same substrate with As-capped InAs nanowires has been decapped at a temperature of 325°C, lower than the congruent temperature. The temperature of desorption has been chosen to be high enough to assure that the amorphous As layer is desorbed, even though it occurs at a lower rate. The As desorption has been tracked with a mass spectrometer, as described in section 3.2. The surface morphology on the sidewalls of InAs nanowires decapped at different temperatures (325°C and 380°C) is depicted in figure 3.9. The image at the right shows the sidewall of the InAs nanowire in which the As layer has been evaporated at a temperature close to the congruent temperature of InAs (marked by a red bar in the temperature scale placed above the figure). The observed morphology is the same as the one already described in figure 3.5b. It can be described as a flat facet with rounded and elongated monolayered pits or holes of different sizes dispersed all along the sidewall. As described in the previous paragraph, these depressions arise as a consequence of the congruent evaporation of In and As atoms from the surface of the nanowires. The image in the left of the figure shows the sidewall of the InAs nanowire in which the As layer has been evaporated at 325°C, below the congruent evaporation temperature. As seen in the figure, the surface morphology shows a more complex pattern, with a larger amount of holes of different sizes. Some of these holes have a very irregular shape. Some terraces can be also seen in the lower part of the picture, suggesting a nucleated

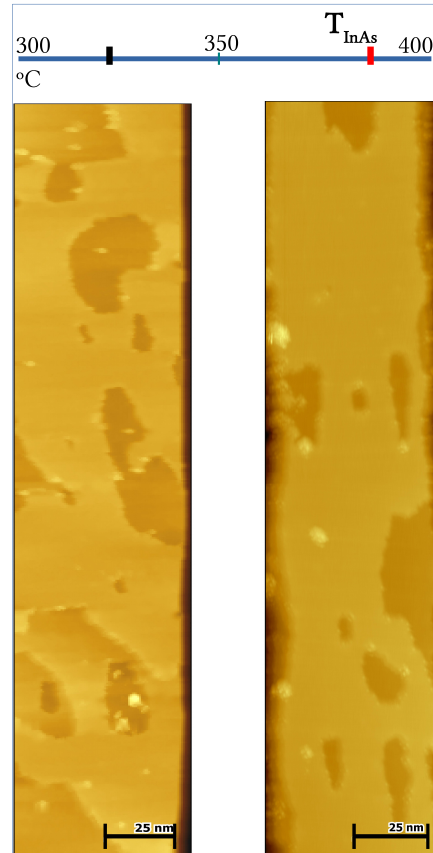


**Figure 3.9:** STM images of the sidewall morphology observed on self-catalyzed InAs nanowires decapped at different temperature. Left: As-decapping temperature of 325°C (2.5V,10pA). Right: As-decapping temperature of 380°C (2V,20pA). The blue line above the two images depicts a temperature scale from 300 to 400 °C. The black bar marks the desorption temperature of the nanowire depicted on the left. The red bar marks the congruent temperature of InAs, $T_{InAs}$, and the desorption temperature of the nanowire depicted on the right. The scale of both STM images is 25 nm.

growth extended from the edges of the sidewalls during the decapping of As. To explain this morphology, it is possible to evoke a similar mechanism of the In adatoms during the desorption of the As capping layer as the one suggested for the GaAs nanowires. Then, when the As layer is desorbed, negatively charged In vacancies are formed. In adatoms are not evaporated and thus can start nucleating island from the edges of the sidewalls or from the edges of previously formed vacancy island. This explain the irregular shape observed on some of the holes, and it is due to the stacking of In adatoms on the hole step edges. To support this claim, it is worth noting that the material, as shown above, is n-type, thus the energy barrier for the formation of In vacancies can be lower than the formation of surface As antisites. Then, the In adatoms ejected from the vacancies contribute to the lateral overgrowth of islands. Indeed, the formation of In vacancies was seen to appear in the surface of cleaved InAs materials

even at room temperature [160]. Also, the creation of such island vacancies in (110) surfaces have been characterized by Kanasaki *et.al* [161][162] from photothermal excitation of surfaces with laser pulses. The same trend is found for (110) GaAs and InP: When the material is p-type, positively charged monovacancies form in the surface after laser irradiation. When the number of laser pulses applied to the surface increases, the number of vacancies does so as well, but only in the form of monovacancies. On the contrary, when the material is n-type, negatively charged monovacancies are created by the laser irradiation. But as the number of laser pulses increases, the vacancies start to aggregate forming vacancy island of different sizes along the exposed surface. As the negatively(positively) monovacancies are equally charged with one electron(hole), the non-aggregation of vacancies at the surface of the materials should be explained by the Coulomb repulsion between the monovacancies. This is the case for p-type materials, as already pointed out by Ebert [149]. The formation of vacancy island in n-type materials is explained by Kanakasi *et al.* as resulting from the role of hole localization in the bond breaking mechanism[162]. On negatively charged monovacancies, there is an upward band bending locally around the vacancy. This increases the probability of hole localization (which is similar to one electron leaving the chemical bonds around the vacancy), the bond strength is weakened at the vacancy position, and the probability that the neighbouring adatoms break their bonds and are expelled then increases. Then, in n-type InAs sidewalls, it is possible to create negatively charged In vacancies during the evaporation of the capping layer at 320°C.

## 3.5 Conclusions

In this chapter, the different cleaning methods of the surfaces of III-V nanowires as well as the influence of these methods on the resulting surface properties have been outlined. As stated in the introduction (section 3.1), controlling the roughness and structure of the surface after the nanowire has been grown is of paramount importance not only for the resulting properties of several nanowire devices, but also to understand better the underlying growth mechanism influencing the surfaces during growth. The study of such surface properties in a precise way can be done with a tool such as STM, which combines the ability to measure very precisely the atomic structure, surface morphology and electronic properties of the sidewalls of the nanowires. To properly characterize the surface, it is therefore necessary to protect the nanowires from oxygen exposition when transferring them from the growth machine to the UHV chamber of the STM. In section 3.2, the two most used cleaning methods for III-V semiconductor nanowires have been reviewed. They deal with either removing the oxide species formed in the surface of the nanowires by bombarding the sidewall of the nanowires with atomic hydrogen at a temperature between $350-400°C$, or avoiding exposure of oxygen to the sidewalls of the nanowire by capping them with a layer of amorphous arsenic in the latter stage of growth in MBE chambers. The As capping layer is easily removed by annealing in the preparation chamber of the STM at temperatures above 200°C. The nanowires need to be put lying parallel to the substrate in order to study them with STM. This is done by cleaving the nanowires to a clean surface, as stated in section 3.3.1, where the convenience of using a Si surface with a thin layer of Ag on top has been explained.

Section 3.3.2 describes the different results obtained with STM on nanowires cleaned by the two methods, allowing to discriminate between the dominant atomic structure of the different crystalline facets on the sidewalls of the nanowires as well as the effects of lateral overgrowth on these facets. The similar conclusions encountered in this regard for differently cleaned nanowires confirm the utility of STM as a very suitable tool for surface structure analysis and to understand the interplay between growth and crystal phase composition of nanowires. However, the morphology and electronic properties of the surfaces seem to be different between apparently equivalent nanowires when the cleaning methods vary from As decapping for InAs and GaAs nanowires (section 3.3.2)[134][135][142], to hydrogen cleaning on InAs and GaAs nanowires [130][140], while in the former case, the surface morphology is decorated by a series of extended defects such as islands for GaAs nanowires or vacancy clusters for InAs nanowires, in the latter case, surfaces do not have any particular accident rather than step nucleation along specific crystalline directions as a result of lateral growth on the surface of the nanowires.

To explore further the possible interplay between the As decapping process and the observed surface morphology, it is necessary to study the distribution of point defects encountered in the surface of these nanowires. Highly resolved

STM images as well as tunneling spectroscopy to study the electronic properties of the surfaces, including the pinning of the Fermi level, is performed on these nanowires. In section 3.4.1, it is found that for As decapped Ga-catalyzed GaAs nanowires, the dominant crystal phase is ZB with {110} type facets. The Fermi level is pinned in the middle of the gap. There is a large distribution of surface As antisites all along the sidewalls. For As decapped In-catalyzed InAs nanowires, the preferred crystal phase is ZB with {110} type facets, but there is a high degree of intermixing also, so that the ZB facets are interrupted every few nanometers by stacking faults and twins. In the InAs nanowires, the Fermi level is pinned in the conduction band as a result of the formation of an electron accumulation layer at the surface of InAs. There is not a particular kind of point defect present in the surface rather than vacancy islands. Finally, in section 3.4.2, the observed STM and STS results are used to describe the mechanism whereby the observed surface morphology is produced during the decapping of the As layer: In the case of GaAs nanowires the material is intrinsic; uncharged defects are favoured, from which the ones of lowest formation energy are surface As antisites given the As-rich conditions. As the formation of an antisite is accompanied by the expulsion of a Ga atom from its lattice site and the Ga adatoms do not evaporate at the decapping temperature, it is suggested that they start nucleating islands of GaAs at the edges of the sidewalls. For InAs nanowires, indium and arsenic adatoms may evaporate from the surface as the decapping temperature is similar to the congruent temperature of InAs. If the decapping temperature is reduced below the congruent temperature, the In adatoms do not evaporate. The n-type surfaces favour the creation of negatively charged defects, mainly in the form of In vacancies, which can increase its size to get stabilized. The In adatoms also form island from the sidewall and step edges much like as the Ga adatoms on GaAs nanowires.

To conclude this chapter, a few points are discussed regarding the validity of this model for the surface morphology by comparing both preparation methods used to image nanowires: First, the growth methods are different. The nanowires cleaned by atomic hydrogen have been grown in MOVPE using gold particles as catalyst. The nanowires capped with As have been grown in MBE using self-catalysis. The InAs nanowire shown in figure 3.5a has been grown using a Au seed particle as well, and it does not present any particular surface accident. The role of Au incorporation in the crystal of the nanowire has been studied before [62][127], and it is seen to diffuse to the atomic layers close the nanowires sidewalls, eventually clustering at the surface when the sidewalls are annealed. This might suggest that the diffusion of gold from the crystallized droplet to the As capping layer during the evaporation of the layer can block the different formation mechanism of extended defects. Although a connection between Au droplets at the sidewalls of the nanowire and a preferred surface morphology is not clear at the moment, given the apparently similar surfaces for both cleaning methods, it might be worth to explore this relation. Second, there are few studies on the cleaning of (110) surfaces of cleaved semiconductors using As capping layers, because these surfaces are usually studied by cross-sectional

STM cleaved in UHV, and therefore no surface preparation is necessary. Despite this, in [163], it was shown, using photo-emission spectroscopy, that this method is “extremely non-intrusive”. It seems to have a minimal influence on the morphology of the surface after decapping. It also respects the Fermi level pinning that the surface had before adding the capping layer. In the opposite to As decapping, studies of hydrogen cleaning in GaAs surfaces showed that the atomic hydrogen interacts very strongly with the surface of the GaAs, producing complex reactions and with different energy barriers to desorb either the arsines complexes or gallium oxides[164], which could eventually affect the surface morphology. Also, atomic hydrogen has been seen to be chemisorbed at the (110) surfaces of GaAs with a $(1 \times 1)$ reconstruction. This affects the electronic properties of the surface [165]. Even though in [129] and [130], it is claimed that hydrogen cleaning does not alter the nanowire sidewalls, it might be interesting to further study, with STM, the sidewall of nanowires produced in the same growth chamber with and without As capping at the end of the growth, and also with and without Au-droplet catalysis. Such a systematic analysis has never been done before, but it could be a large step forward in the understanding of the surface properties of III-V nanowires.

Finally, it is worth mentioning a few results relating the electronic properties and the point defects observed in hydrogen cleaned nanowires: In [130], STM imaging and spectroscopy is performed on GaAs nanowires. On the nanowire sidewalls, there are large sections of ZB $\{110\}$ type facets. On these facets, it is observed that the majority of point defects are positively charged monovacancies. Local STS measurements show that the material is slightly p-type in these ZB sections. This result is in line with the discussion of the previous sections regarding the formation energy for charged defects and the Fermi-level position, in particular the results of Kanasaki *et.al* on p-type surfaces [162] as well as those of Ebert on differently pinned surfaces [89].

In this work, it has been proved that, even though the As capping layer does not seem to change neither the surface reconstruction nor the electronic properties of the surface, it can eventually assist in the formation of extended defects by the combination of thermal activation and Fermi level position when the layer is evaporated. This result can have large consequences for the understanding of the surface properties of III-V semiconductor nanowires and how they are changed by capping them with metallic layers, which might allow to create better electrical contacts with the nanowires.

# Chapter 4

# Structural and electronic characterization of Low-temperature grown GaAs Nanowires

## 4.1 Introduction

The development of ultrafast laser, reaching the femtosecond width pulse regime, has allowed to explore the properties of materials in the THz range of the electromagnetic spectrum. The THz range encompasses the region of the electromagnetic spectrum of the submilimeter wavelength range between 1 and 0.1 mm, lying between the infrared and the microwave regions. The THz waves have encountered many applications in scientific research and technology, a brief summary can be found in chapter 5. In order to detect and emit such waves it is necessary to couple the femtosecond pulses with materials with a very short carrier lifetime that are able to follow the fast electromagnetic transients. Some examples of such materials are III-V semiconductors that have been damaged with radiation or by plastic deformation to create a large amount of defects. These defects act as traps for the photoexcited carriers, thus reducing the lifetime, such as electron irradiated GaAs [166], or $H^+$ bombarded InP [167]. Another way to introduce defects is to epitaxially grow the semiconductors at low temperature. GaAs grown at low temperature is the most investigated material in this regard. When GaAs is grown at low temperature, the growth proceeds in a non-stoichiometric way with an excess of As. This excess of arsenic is incorporated as antisite defects in a large concentration to the GaAs crystalline structure. Also, they are the cause of the very short carrier lifetime encountered in this material. Furthermore, if the material is annealed (at a high temperature) for very short periods of time after growth it becomes semi-insulating.

Even though, the carrier lifetime is still very short. This makes LT-GaAs very suitable for its use as a THz radiation photodetector, normally integrated in photoconductive antenna circuits [123][118]. The origin of the semi-insulating properties of LT-GaAs films and its main structural and electronic properties, as well as the different investigations regarding these characteristics, will be the purpose of the first part of the chapter.

On the other hand, the synthesis of III-V semiconductor nanowires offers a large flexibility to combine different semiconductors in axially or radially extended heterostructures, which have made possible to extend the range of nanowire applications and cover almost all the relevant areas of semiconductor devices technology. Indeed, III-V semiconductor nanowires are usually grown by the VLS method, in which a liquid metallic droplet drives the growth of the nanowire. While this growth procedure has many advantages, the metallic droplet must remain liquid to sustain the growth (at least in self-catalysis schemes), which limits the range of temperatures at which nanowires can grow. This has been the main topic of chapter 1. Then, in the second part of this chapter, a new scheme to integrate a film of LT-GaAs material as a shell of a self-catalyzed GaAs nanowire is described. The core-shell GaAs/LT-GaAs nanowires has been characterized by STM as well as SEM, HR-TEM, Cathodoluminescence and pump-probe reflectivity measurements to assess their structural and electronic properties. The observed structural features as well as the STM spectra performed on the sidewall of the nanowires reveal the incorporation of point defects with similar properties to those found in LT-GaAs films. This work presents a novel way to incorporate unexplored materials such as LT-GaAs as part of nanowires, and this could be relevant as nanowires has been proved to enhance the emission properties of THz radiation due to its geometry and aspect ratio, that reduces the radiation losses commonly observed in conventional thin-film THz emitters.

## 4.2 Low-Temperature Grown GaAs

### 4.2.1 Growth and structural properties

Since the beginning of the eighties, GaAs growth performed with MBE is controlled to a high degree [168]. Usually, MBE growth of GaAs proceeds along the $< 100 >$ direction at a substrate temperature in the range of $580 - 680°C$. Gallium is evaporated from a liquid source and impinges on the growing substrate with an unitary sticking coefficient. At the conventional growth temperature, gallium is liquid and diffuses along the substrate. Furthermore, it is hardly re-evaporated. Arsenic is incorporated through solid or vapor sources and reaches the substrate aggregated as a dimer or tetramer, depending on the type of source. Arsenic sticking coefficient is less than unity for it is know to be very volatile. There is a chemical reaction with gallium involved in the decomposition of arsenic and subsequent incorporation to the GaAs matrix. Therefore, desorption events of arsenic are very common and the growth of a monolayer is limited by the diffusion of gallium. Under these conditions, stoichiometric GaAs is guaranteed as long as there is sufficient excess As in the environment, which is achieved having a high V/III equivalent beam pressure ratio. A good crystalline material is grown with few deep level defects and sometimes a small unintentional impurity addition (mainly Carbon) that tends to give the material p-type character.

In the context of semiconductor devices technology, Low-Temperature grown GaAs (from now on, LT-GaAs) was for the first time presented in 1988 by Smith et al. [169] with the purpose of introducing it as a buffer layer in GaAs MESFET devices between the Semi-Insulating GaAs substrate grown by the liquid encapsulated Czochralski (LEC) method and the active GaAs channel that could prevent undesired backgating effects.

LT-GaAs is grown by MBE on top of (100) SI-GaAs substrates at a temperature range between $200 - 300°C$, and with a high V/III EBP [169][170]. The growth rate is $1\mu$m/h≈1 ML/s . Low-temperature grown means that the growth temperature ($200 - 300°C$) is much lower than the range of temperatures used to grow crystalline GaAs, as described above. The diffusion dynamics of gallium is changed as well as the rate of reactions between gallium atoms and As tetramers. In this way, there is an excess of arsenic incorporated into the GaAs crystalline structure leading to a non-stoichiometric material. The arsenic in excess enters the GaAs by creating different types of point defects in a high concentration. The principal type of point defects created are the arsenic antisite defects ($As_{Ga}$, attachment of an As atom on the Ga atom lattice site of the GaAs ZB crystalline structure, Fig. 4.1a). Additionally, gallium vacancies and arsenic interstitials are produced during the growth of the low-temperature layer.

The creation of arsenic antisites in a high concentration is supported by several characterization techniques. In [170], by using X-Ray diffraction and TEM, LT-GaAs was shown to maintain a crystalline structure with an increase in the relative lattice parameter of 0.001 (Fig. 4.1b), due to the strain induced

by the As antisite tetramers, whose bond length is larger than that between Ga and As. Also, a large quadruplet EPR signal, characteristic of this kind of defects, is observed without any noticeable photoquenching (Fig. 4.1 c). From the amplitude of the EPR signal, a concentration of antisites equal to $N_{As_{Ga}} = 5 \times 10^{18} cm^{-3}$ is extracted , pointing to an excess of arsenic of approximately 0.02% in the material. Finally, LT-GaAs showed semi-insulating properties and the resistivity was further increased upon a post-growth annealing at 600°C for 2 mins. EPR signal was also seen to decrease after annealing as a consequence of a reduction in the concentration of arsenic antisites.

Shortly after the first report of LT-GaAs, the excess As of the post-growth annealed material was shown to be redistributed as arsenic aggregates, as observed by TEM. Their sizes ranged between 2 to 10 nm, with a concentration of $10^{17} - 10^{18} cm^{-3}$ (fig. 4.1 e). [171]. Also, LT-GaAs photoexcited carriers showed a very short lifetime, in the order of picoseconds [119], which, in conjunction with the high dark resistivity of the annealed material has made it a very suitable material for photodetection of very fast optical pulses (optical properties will be extended on section 4.2.3).

However, the nature of the semi-insulating properties and its high resistivity, especially after annealing, were not completely understood and a large amount of research has been devoted to elucidate this point. The arsenic antisite acts as a double donor being in the LT-GaAs material neutral or partially ionized (and thus having two charge transition levels in the band gap: the (0/+) and (+/++) levels) [170]. The electronic states of the antisite lie close to the middle of the band gap forming a band of deep defects (Fig. 4.1 d). The Fermi level is pinned in the middle of the band gap rendering the material semi-insulating[173], which stands for a compensation mechanism mediated by positive charges, as ionized acceptor dopants or positively charged point defects. Gallium vacancies are also produced during growth in a large amount (but not detectable with EPR or near-infrared absorption(NIRA), [174]) and possess an acceptor character. Therefore, they are considered the main compensation agent for the ionized arsenic antisites. After LT-GaAs is annealed at 600°C, the concentration of arsenic antisites is reduced by more than one order of magnitude [174] to form arsenic aggregates [171]. It has been suggested that the aggregation of arsenic is assisted by the gallium vacancies [174] in such a way that their concentration is also greatly reduced. Once annealed, the material has the Fermi level pinned mid-gap again and it is semi-insulating, which led Warren *et.al* to develop a model considering arsenic aggregates responsible for the compensation of the annealed material. This compensation is achieved through the formation of Schottky barriers between the GaAs and the aggregates, enabling a charge transfer that pins the Fermi level at the Schottky barrier height [172]. For other researchers [175][176], even though the concentration of antisites of the annealed material is reduced below detectable limits with EPR or infrared-absorption, the concentration of gallium vacancies is also reduced, most likely reacting with the antisites in such a way that the material is still compensated. Also, it is not clear whether arsenic interstitial are formed, nor what is their concentration

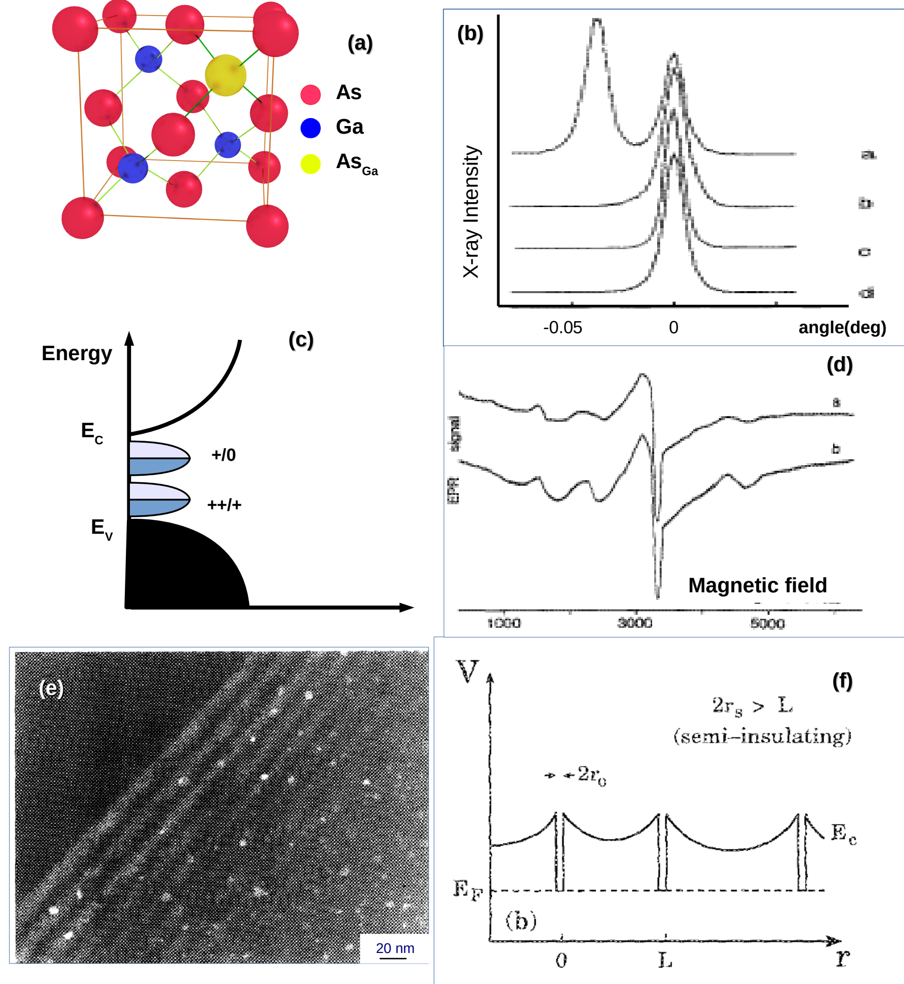


**Figure 4.1:** a) Atomic structure of the cubic cell of Zinc-Blende GaAs with an arsenic antisite, where the arsenic atoms are represented by red spheres, the gallium atoms by blue spheres and the arsenic antisite by a yellow sphere. b) X-ray diffraction spectra of LT-GaAs grown at 200°C for both unannealed and annealed at 600°C for 10 mins. (a to b), and LT-GaAs grown at 270°C kept unannealed as well as grown at 275°C and annealed (c to d). In all cases the resulting material shows crystalline properties. When the growth temperature is very low (curve a), the main diffraction peak is shifted as a result of the strained lattice by the high concentration of As antisites. c) Sketch of the density of states of LT-GaAs. The Fermi level is pinned in the middle of the band gap and a large concentration of As antisites form a deep band in the band gap. The As antisite is a double donor and can be neutral or partially ionized. d) EPR quadruplet spectra of LT-GaAS grown at 200°C and not annealed, measured at 8K. In the upper curve the material was not illuminated during the acquisition and in the lower curve it was illuminated with white light. The EPR quadruplet signal is attributed to the ionized antisite defects. From the intensity of the signal, a concentration of antisites of $5 \times 10^{18} cm^{-}3$ is estimated. Both graphs b) and d) are extracted from [170]. e) TEM dark field image of LT-GaAs buffer layer grown at 220°C and subsequently annealed. The arsenic precipitates are seen as bright sphere-like particles. f) Conduction band diagram of LT-GaAs with As aggregates modeled as potential wells. The Fermi level of the aggregates is pinned in the middle of the GaAs band gap forming a depletion layer around them. According to Warren's model, in the case in which the diameter of the aggregates is in the same order of magnitude as the distance between the aggregates, the material is semi-insulating. Both e) and f) extracted from [172].

and contribution to the charge compensation of the material [177][178] as well as their role in the formation of the As aggregates. For Stellmacher *et.al* [179], the formation of complexes between antisites and interstitials, aside from the antisites, has to be considered during the growth of LT-GaAs in order to understand the dynamics of As aggregation. The aggregates might be produced by the diffusion of the more mobile arsenic interstitials, having intermediate reactions with the vacancies and antisites.
Whatever the compensation mechanism responsible for the Fermi level pinning, annealed LT-GaAs is a semi-insulating material which maintains a very short carrier lifetime. This property can be unidirectionally related with the excess of arsenic incorporated as a band of deep donor antisites or arsenic aggregates after annealing, in both cases, acting as electron traps and enhancing photo-excited carrier recombination.

Both compensations mechanism of annealed LT-GaAs can be summarized as follows:

- **Arsenic aggregates model:** Arsenic in excess was seen to coalesce forming aggregates of various sizes when growing several layers of LT-GaAs in alternance with layers of normal GaAs (which leads to an increase of the grow temperature to 600°C after the LT-GaAs layer is grown)[180]. The LT-GaAs layers were grown at 250°C, 1$\mu$m/h and $V/III_{EBPratio} = 16$. A large amount of clusters of nanometric size in the range from 2 to 10 nm and at a concentration of $10^{17} - 10^{18}$ cm$^{-3}$ was revealed by HRTEM characterization in the region where LT-GaAs was grown (Fig. 4.1 e). Warren et al. [172] proposed, in line with these results, and having a semi-insulating LT-GaAs even if it was highly Si-doped, a mechanism whereby the arsenic aggregates could compensate the excess charges on the material by the formation of buried Schottky barriers with the GaAs. The aggregates could accumulate or deplete charge in n-type (0.8 eV barrier height) or p-type (0.6 eV barrier height) material, depending on the amount of donors or acceptors. In both cases, with the Fermi level pinned at the Schottky barrier height.

  Following [172], if Gauss's equation if solved approximating the arsenic aggregate as a sphere of radius $r_o$ with azimuthal symmetry in the potential, and considering that the potential difference between the aggregate and the semiconductor bulk falls within the depletion region of width $r_s - r_o$, that the charge density in the depletion region arises only from the contribution of ionized antisites with concentration $N_{DD}$ and that there is continuity of the potentials and electric fields in all space, the maximum depletion radius $r_s$ can be calculated with respect to the built-in potential $\phi_b$ and the aggregate radius $r_o$ as:

$$\phi_b = (qN_{DD}/6\epsilon)\left\{2r_s^3/r_o + r_o^2 - 3r_s^2\right\} \tag{4.1}$$

  A sketch of the conduction band profile with three As aggregates is depicted in figure 4.1f. Considering a mean cluster radius of 3 nm, with a

typical Schottky barrier height of $0.8eV$ for GaAs and a density of donors equal to $N_{DD} = 1 \times 10^{18} cm^{-3}$, the depletion region radius obtained using equation 4.1 is 1.9 nm. In [172], they reasoned that under these conditions, and for a cluster density equal or higher than $10^{16} cm^{-3}$, the depletion regions will begin to overlap, as shown in the figure, when the distance between aggregates becomes smaller than their mean diameter, and the material will become semi-insulating, even if it is highly doped. In other words, the amount of charge carriers that an aggregate holds is equal to, considering Laplace's equation:

$$n_m = (4\pi\epsilon/q) r_o \phi_b \tag{4.2}$$

For an average aggregate size of 3 nm, this is equal to $n_{-} = 22$ and $n_{+} = 16$ for n-type and p-type material, respectively. Multiplying this number by the arsenic aggregate density renders the total charge that they are able to compensate in the material. Thus, for a fixed aggregate size, compensation depends on the density of clusters. For LT-GaAs, it is enough if the number of dopants does not exceed $2.2 \times 10^{18} cm^{-3}$ to have a semi-insulating material. This estimated quantity of defects is higher than the detectable density of arsenic antisites after annealing of LT-GaAs.

Shen *et.al* performed photoreflectance measurements on a heterostructure of $n^{+}$-GaAs/Undoped GaAs/LT-GaAs. Either as-grown(unannealed) or annealed for a few seconds at 600°C [173]. By matching the measured carrier density at the LT-GaAs film with the Poisson-Schrodinger solution of the potential under the effective mass approximation, they were able to estimate the position of the Fermi level along the heterostructure, which was pinned in the middle of the gap both for the annealed and unannealed LT-GaAs upper layer. For unannealed LT-GaAs, a concentration of ionized donors of $N_{DD}^{+} = 1 \times 10^{18} cm^{-3}$ is measured and the position of the Fermi level is pinned just above the antisite donor band:$E_C - E_F = 0.47eV$, and $E_C - E_{DD} = 0.57eV$. They argued that compensation is mediated by acceptor defects which can be Ga vacancies or Ga antisites, with an estimated concentration of $N_A^{-} = 1 \times 10^{18} cm^{-3}$. If such concentration of acceptors is not included in the simulation, the Fermi level is not pinned. Then, there must be a large concentration of acceptor defects pinning the Fermi level in LT-GaAs . For the annealed LT-GaAs, the Fermi level position was shifted down to $E_C - E_F = 0.65eV$ and the number of ionized donors was reduced to $N_{DD}^{+} = 1 \times 10^{17} cm^{-3}$. The Fermi level is pinned at the same position no matter how long the annealing time (from 30 s up to 300 s). Such pinning would require a very high amount of acceptor defects that are not likely to be developed as the number of donor defects is seen to be reduced, the number of vacancies being reduced as well. Thus, they argued that the only way to match the result is to fit it to Warren's model. Furthermore, the Fermi level position $E_C - E_F = 0.65eV$ is very close to the Schottky barrier height. Feenstra et

al. [181] studied UHV cleaved $< 110 >$ surfaces of annealed LT-GaAs by STM. They imaged a large amount of arsenic aggregates of various sizes with a depletion region surrounding them. Additionally, local tunneling spectroscopy measurements on the aggregates showed that the Fermi level was pinned on the middle of the LT-GaAs band gap, and a high density of midgap states capable of pinning the Fermi level was observed. Even though compensation by acceptor defects such as vacancies was not ruled out, they were not able to detect any appreciable amount of these kind of defects with STM. Finally, aggregation of arsenic has been theoretically modeled using molecular dynamics and density functional tight binding (DFTB) theory to study the energetic balance of the creation of As antisites [182]. It is found that arsenic antisites can diffuse and the formation of arsenic aggregates of even two arsenic atoms is energetically favourable with respect to the single antisites, as these keep the lattice strained. Also, larger clusters have lower binding energy, thus Ostwald ripening of arsenic aggregates must occur.

- **Point defect model:** It has been also stated that the concentration of ionized antisites as well as gallium vacancies before and after annealing is high enough to firmly pin the Fermi level in the material. According to Liu [174], the arsenic aggregates do not necessarily undergo a charge transfer with the material, what stands for flat-band conditions between the aggregates and LT-GaAs. Such conclusions were reached by comparing magnetic circular dichroism (MCDA) measurements, which gives an estimation of the concentration of ionized antisites with near infrared absorption (NIRA) measurements with and without illumination. Indeed, these techniques yield the concentration of ionized antisites due to the reduction in the absorption of the material which arise as a consequence of photoquenching processes. Comparing both measurements, they showed that the concentration of neutral antisites is approximately twice larger than the one of ionized antisites. From this comparison, and having that the stoichiometry for the formation of arsenic antisites is double in comparison with the single stoichiometry of the gallium vacancies, it is implied that the ionized antisites and the gallium vacancies are in such a concentration that the material is always compensated even after annealing. Thus, without the need of charge transfer with As aggregates. In [183], MCDA and NIRA measurements are put against X-Ray measurements to get an estimation of the relative change in lattice parameter (as well as relative volume change due to volume conservation) as a function of the density of antisites as:

$$\frac{\Delta a}{a_o} = \frac{\Delta V}{V_o} = \frac{r^3_{As_{Ga}-As} - r^3_{Ga-As}}{r^3_{Ga-As}} \frac{1}{2.2 \times 10^{22}} [As_{Ga}] \tag{4.3}$$

Where, $r_{As_{Ga}-As}$ is the interatomic distance between the antisites and the surrounding arsenic atoms and $r_{Ga-As}$ is the interatomic distance

between gallium and arsenic in normal GaAs. The main claim of the point defect model is that the properties of the arsenic antisites can explain structural changes in the material (as bulk volume). Even though the number of antisites is seen to be reduced upon annealing, it does not assign a definite role to the arsenic aggregates, whether they appear or not. Then, structural characterization techniques alone do not give an unified vision about the nature of the defects in the material, further complementary techniques, as electrical and optical characterization have to be performed to solve these issues. This will be developed in the next two sections.

### 4.2.2 Transport models

As stated in the previous section, there is no clear consensus whether the compensation mechanism is due to acceptor defects, as gallium vacancies or even residual carbon impurities or due to the formation of buried Schottky barriers with the arsenic aggregates. Similar discrepancies were found when studying the transport properties of LT-GaAs samples before an after annealing at different temperatures, either by temperature dependent Hall measurements [184][185] or by temperature dependent resistivity measurements, to study activation energies and breakdown voltages [175][176]. Look studied the Hall resistivity of LT-GaAs for as-grown samples [184]. It was shown that the Hall resistivity stays almost constant for LT-GaAs grown between $200-300°C$. Conversely, the carrier concentration follows an anomalous dependence with the temperature as it is reduced at increasing measurement temperatures. For the annealed sample, the tendency was reversed, with the resistivity increasing up to 5 orders of magnitude for 550°C annealed samples and the carrier concentration increasing for higher measurement temperature. In order to fit these results, he proposed a two-band model by which transport is carried out by hopping of holes through the dense band of antisite defects as well as by thermally excited conduction band electrons as:

$$\rho^{-1} = \sigma = \sigma_{CB} + \sigma_{DD} = en_{CB}\mu + \sigma_{DD} \tag{4.4}$$

with $\sigma_{DD}$ being the hopping contribution to the conductivity:

$$\sigma_{DD} = C_{DD}e^{-\gamma/aN_{DD}^{1/3}}e^{-\varepsilon_d/kT} \tag{4.5}$$

where $C_{DD}$ and $\gamma$ are constants, a is the extent of the donor wave function in a hydrogenoid-like model ($a = \hbar/(2m^*E_{DD})^{1/2}$), which is estimated to be $a = 8.67Å$ from a deep donor level position of $E_{DD} = 0.75eV$. $\varepsilon_d$ is the difference in energy between the Fermi energy and the donor energy level. The model fits well from the range of temperatures between 300 and 400 K for both as-grown and annealed LT-GaAs. The increase of resistivity upon annealing is due to the reduction on the concentration of arsenic antisites, which reduces the effective wavefunction overlap necessary to guarantee hopping and keeps

the conduction band electrons as main charge carriers. For temperatures below 300K, it is shown that the dominating transport mechanism is variable-range hopping. As said before, Warren *et.al* suggested in their model [172] that the increase in resistivity for LT-GaAs samples annealed at 600°C is rather due to the overlapping of the depletion regions of the As aggregates with the bulk GaAs. Look [185] calculated that the maximum overlap for their samples, if As aggregates are formed, should fill about 30% of the volume. Also, if the charged aggregates were to completely overlap, the resistivity should be much lower than the measured value, and should show a minimum when the situation of complete overlap is close to be reached due to percolative conductance along the bulk. Both conditions were not observed in resistivity measurements of annealed LT-GaAs. However, the hopping model, assigning the main contribution of conductivity to the point defects, does not explain how the material is compensated. In [185], Look argued that the material must be compensated due to extrinsic defects such as grain boundaries or other extended defects, but without estimating what is the impact of these defects on the resistivity of the material.

Luo et al. [175][176] studied the resistivity and breakdown voltage of both as-grown and annealed LT-GaAs samples at different temperatures and proposed a synthesized transport model. In this model, the arsenic antisite is considered as a monoatomic cluster. As the material is annealed, the number of monoatomic clusters is reduced, but their size increases to form bigger As aggregates. The probability p for electrons hopping from one cluster to another can be expressed by:

$$p = v_{ph} e^{-2\alpha R} \tag{4.6}$$

where $v_{ph}$ is the attempt frequency, $\alpha$ is related to the distance of decay for the cluster wavefunction and R the average jumping distance between cluster, which is linked to the density of clusters $N_T$ (single antisites(monocluster) or aggregates) by:

$$R = [9/(8\pi\alpha N_T)]^{1/4} \tag{4.7}$$

The hopping conductivity is finally written:

$$\sigma = (1/6)e^2 R^2 p N_T / kT \tag{4.8}$$

what results, inserting equations 4.6 and 4.7 in equation 4.8, in a conductivity depending on the density of clusters, similarly to the result obtained by Look for the hopping between antisites. The main assumption of Luo's model is that the hopping is produced between arsenic antisites in the as-grown material, and the As aggregates in the annealed material. As the density of clusters is reduced when the material is annealed (at the expense of increasing their size), the hopping probability is reduced and thus the resistivity increases. Also, they considered a compensation mechanism mediated by the aggregates forming Schottky barriers, the formation of As aggregates having an activation energy of $E_a = 2.1eV$.

### 4.2.3 Optical properties

LT-GaAs presents a very fast carrier recombination time, which, added to the high resistivity of the annealed material and a high enough mobility has allowed the integration of the material as a photodetector of very fast optical pulses, such as the ones in the THz range [186][187]. It can be integrated with photoconductive antenna to produce fast transient pulses in the range of THz [123] as well as coupled with a photomixer setup for detection and emission of THz fields [188].

The lifetime of the photoexcited carriers in LT-GaAs has been studied by several groups using pump-probe techniques with equivalent time-sampling techniques (section 2.2.1). The changes in the relative transmission or reflection of the material impinged by femtosecond laser pulses are tracked as a function of the delay time between pump and probe laser beams. When the pump beam arrives, it generates an electron-hole plasma which is rapidly (in femtoseconds) thermalized through carrier-carrier or carrier-phonon scattering. The photogenerated carriers induce a change in the optical absorption of the material through the mechanism of bandfilling, band-gap renormalization and free carrier absorption. The absorption change can be related to a change in the refractive index of the material, as shown by the Kramers-Kronig relations [118]. As the photogenerated carriers are recombined in the next few picoseconds, the changes in absorption will follow the decay of the excited photocarrier population as a result of trapping and recombination from defects in the material. Several groups have adopted this approach to study carrier recombination in LT-GaAs, either following changes in the transmission [189][190] or the reflection [191][192] of the illuminated material, as well as THz pump-probe [193]. Also, electro-optic sampling and photoconductive Austin switches have been used to characterize the lifetime of the material [119].

Regardless of the technique, similar trends have been encountered with respect to the lifetime of photoexcited carriers in LT-GaAs but with dispute about the nature of the recombination mechanism for the annealed material. In general, the tendencies for the photoexcited carrier lifetimes can be summarized by looking at figure 4.2a. The change of the lifetime is twofold. First, for as-grown LT-GaAs between $200 - 300°C$: as the growth temperature is reduced, the amount of excess As incorporated to the material is increased and as such, the amount of electron and hole traps, thus the recombination probability is increased and the lifetime gets shorter accordingly. However, there is a lower limit for which the material starts to increase its polycristallinity and incorporate large defects due to the extreme non-stoichiometry. Therefore the mobility of the carriers decrease and the lifetime increases. After LT-GaAs is annealed at different temperatures (between $400 - 700°C$), the number of point defects is reduced, most likely to be incorporated as arsenic aggregates. The material becomes highly resistive and the lifetime increases. The larger the annealing temperature, the higher the increase in lifetime.

There is a general remark to be made about the similar growth temperature used by different groups to grow the material, and the dissimilar structural and

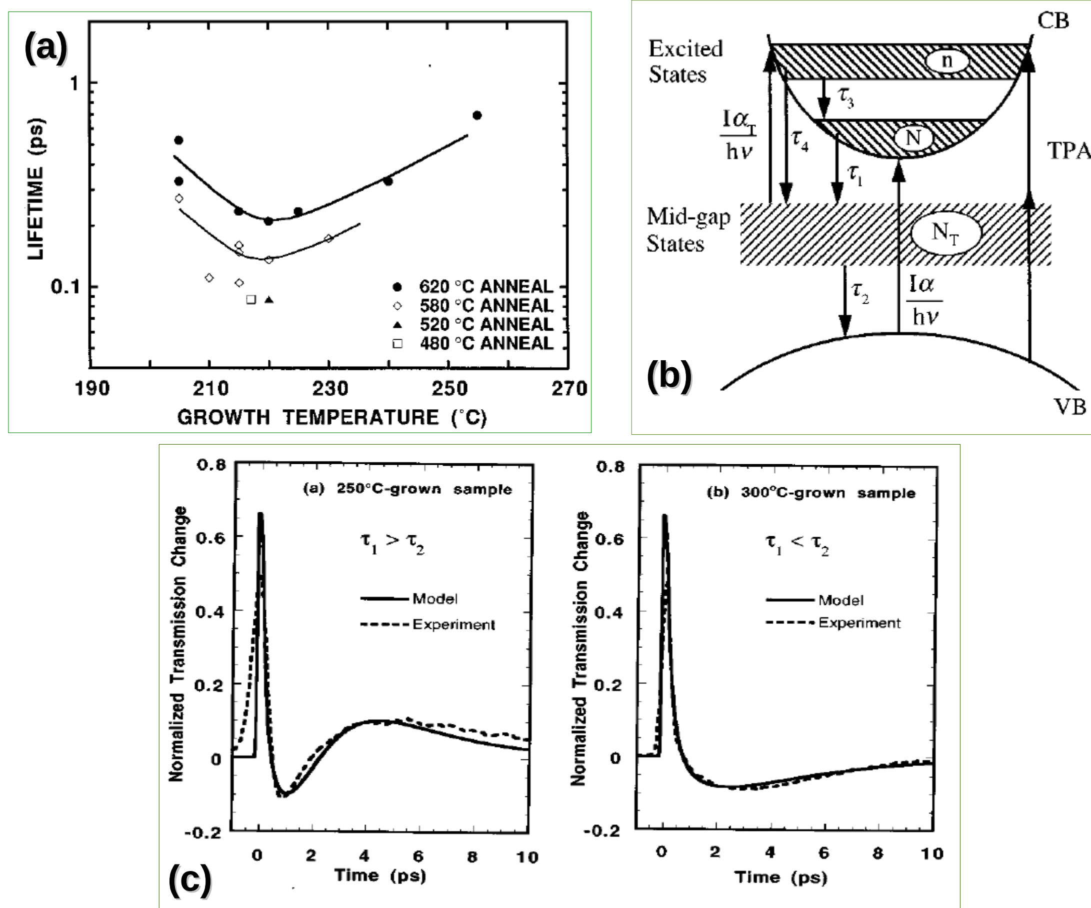


**Figure 4.2:** a) Photocarrier lifetime of LT-GaAs vs growth temperature for several different annealing temperatures. From [191]. b) Band diagram of LT-GaAs showing the main excitation and decay processes with their corresponding lifetime for the model of [190] (described in section 4.2.3). c) Lifetime curves in transmission mode for LT-GaAs as grown at (left) 250 and (right) 300 °C. Dashed lines represent the experimental data and solid lines the simulation of the dynamics predicted in [190]. Both b) and c) extracted from [190].

optical properties encountered. The determination of the growth temperature in the range 200 − 250°C can not be so precisely determined, as the temperature reading in this range is done with the use of thermocouples. The temperature measured by the thermocouple is slower and very sensitive to the thermal contact between the substrate and the thermoresistive material. It is necessary to calibrate them with other temperature measurement instruments such as pyrometers (which are only sensitive above 250°C). Therefore, some dispersion in the values of the growth temperature can be encountered in the range 200 − 300°C between different systems.

By looking at figure 4.2c, a typical transmission change curve for a pump-probe characterization experiment, extracted from [190], of as-grown LT-GaAs is depicted. The samples are grown at two different temperatures. At 0 delay

time, the pump and probe laser beams arrived at the same moment to the sample. The carriers are photoexcited, a very sharp and fast change of the normalized transmission is observed, related to an increase in absorption mainly due to the band-filling processes, as stated by [192][190] [189] and [191]. This is followed by a rapid change in transmission as carriers recombine onto LT-GaAs recombination centers (such as antisites or vacancies) giving rise to the steep falling slope of the curve in a very few picoseconds. The curve is continued by absorption non-linearities, either by a small dip at 2 ps for the 250°C as-grown samples, or by a reduced transmission that is followed by a very slow recovery time (300°C as-grown sample). These features can not be fitted in the transmission curve by a single decreasing exponential as it would be the case if there were a single recombination mechanism (like fast antisite trapping) operating in the as-grown sample, and suggest a more complex recombination dynamics mediated by more than one process. Benjamin *et.al* developed a model to explain this behaviour as produced by the ultrafast recombination dynamic between photoexcited carriers at the deep level defect band up to the conduction band[190] as well as by the production of two-photon absorption (TPA) events. The model can be expressed as follows, with population-balance equations, fig.4.2b:

$$\frac{dN}{dt} = \frac{I\alpha}{h\nu} - \frac{N}{\tau_1} + \frac{n}{\tau_3} \tag{4.9}$$

Equation 4.9 represents the change of population at the bottom of the conduction band: The first term is the absorption of photo excited carriers from the valence band (I:light intensity, $\alpha$:band-to-band absorption coefficient, $h\nu$: photon energy, which is resonant with the energy gap of GaAs), second term stands for recombination with the band of defects in the middle of the gap with a lifetime $\tau_1$, as indicated by the arrows in the figure, and the third term is related to the thermally recombined carriers from the top to the bottom of the conduction band with a lifetime $\tau_3$.
The change of population in the defect band states is expressed as:

$$\frac{dN_T}{dt} = -\frac{I\alpha_T}{h\nu} - \frac{N_T}{\tau_2} + \frac{N}{\tau_1} + \frac{n}{\tau_4} \tag{4.10}$$

The first term is the absorption of photo excited carriers up to the top of the conduction band (I:light intensity, $\alpha_T$: absorption coefficient from traps to excited states, $h\nu$: photon energy, which is resonant with the energy gap of GaAs), the second term stands for recombination with holes of the valence band with a lifetime $\tau_2$, the third term represents the trapping of electrons from the bottom of the conduction band to the defect band states in a time $\tau_1$ and the last term is the trapping of electrons from the top of the conduction band to the defect band states in a time $\tau_4$. Finally, the change of population in the top of the conduction band reads:

$$\frac{dn}{dt} = \frac{I\alpha_T}{h\nu} - \frac{n}{\tau_4} - \frac{n}{\tau_3} + \frac{I^2\beta}{2h\nu} \tag{4.11}$$

Where the three first right-hand terms represent, from left to right: the absorption of light from the defect band to the top of the conduction band with absorption coefficient $\alpha_T$, the trapping of electrons between the top of the conduction band and the defect band states with lifetime $\tau_4$ and finally the thermalization of carriers to the bottom of the conduction band with lifetime $\tau_3$. Also, the last term represents two-photon absorption processes from the valence band with absorption coefficient $\beta$.

The model is fitted with great precision to reproduce the experimental curves shown in figure 4.2c for both, 250 and 300°C as-grown LT-GaAs samples. The lifetimes extracted for the 300°C sample are: $\tau_1 = 1.4ps$, $\tau_2 = 3.0ps$, $\tau_3 = 100ps$, $\tau_4 = 0.3ps$. In light of the different processes considered that can change carrier population, it is possible to explain the non-linearities in the transmission spectra. The recombination time between the upper conduction band and the deep donor band is considered to be extremely fast but the thermalization of photoexcited carriers from the top to the bottom of the conduction band is very slow due to phononic bottleneck. Then, after the initial and fast recombination of carriers from the bottom of the conduction band to the deep donor band in approximately 1.4 ps, there is a very fast excitation to the top of the conduction band from this deep donor defect band that causes a further increase in absorption. The shape of the absorption features will change depending on the interplay between the rates of non-radiative recombination of the conduction band and the band of defect states ($\tau_1$), and the band of defect states and the valence band ($\tau_2$).

For Lochtefeld *et.al* [189], the absorption non-linearities must arise due to the presence of two different traps in the as-grown material, the antisites as electron traps and the vacancies as hole traps. Both traps have different effective cross-sections so that the pump-probe transmission curves can not be fitted by a single exponential as the filling and emptying rates of both donor bands are different. The model developed above can be adapted to this situation by not considering the TPA processes and adding a new band of defect states (representing the vacancies) with its respective population change dynamics. When LT-GaAs is annealed, they find that the transmission spectra can be fitted by a single exponential. They argue that the main recombination mechanism for non-radiative processes comes from the arsenic aggregates acting as electron traps, as the vacancies and antisites reduce its concentrations upon annealing, and there are still very fast recombination times that can not be explained otherwise. [192] and [193] have also found that the transmission curves for the annealed material can be fitted by a single exponential. In [193], using pump-probe THz spectroscopy, they see a single exponential decay in transmission for the as-grown material as well, which allows them to argue that the power used in normal pump-probe experiments creates an excessive amount of photogenerated carriers that cause the measured non-linearities in absorption. Then, the THz pump-probe curves can be fitted in as-grown and annealed LT-GaAs by a simple model considering only one kind of defect (the antisites) capturing electrons by

the Shockley-Read-Hall mechanism:

$$\tau = 1/N_{DD}v_{th}\sigma_{cross} \tag{4.12}$$

Where $N_{DD}$ is the concentration of antisites, $v_{th}$ is the thermal velocity of carriers and $\sigma_{cross}$ is the effective recombination cross-section. The increase in lifetime for the annealed material is simply caused by a decrease in the concentration of antisites defects.

### 4.2.4 Conclusions

In the first part of this chapter; the structural, electrical and optical properties of LT-GaAs films have been reviewed. It is clear that there is not an unified model accounting for all the properties encountered on this material. The principal point of disagreement is related to the compensation mechanism between the defects, as well as what is the dynamic of these defects when the material is annealed. As said before, the origin of all of these differences could be partially accounted for by the uncertainty in the temperature measurement when the material is grown, which makes the measurement between different groups hard to compare. But whatever the model considered, it is clear that there are some common threads: 1) The low temperature growth of the material incorporates arsenic in excess to the crystal lattice, which seems to be mainly in the form of arsenic antisites defects. 2) These defects strain the lattice and deteriorate the crystal quality of the material, but they are efficient electronic traps, conferring the material extremely short lifetimes. 3) When the material is annealed after growth, the concentration of antisites is reduced. They start to aggregate in the form of arsenic clusters, reducing the lattice strain. This have two consequences: the crystal quality is improved (and thus the mobility) and the density of defects (whatever its origin) is still large enough so that the lifetime is very short. This two features makes annealed LT-GaAs an excellent optoelectronic material.

## 4.3 Synthesis of LT-GaAs Nanowires

Low-temperature GaAs nanowires have been synthesized by using a core-shell approach. The core is made up of MBE grown Ga-catalyzed GaAs nanowires (see section 1.3.5) with the low-temperature shell added conformal to it.[1] The main reason to integrate the low-temperature GaAs as a nanowire shell is caused by the impossibility to grow LT-GaAs directly from the well studied Ga-catalyzed approach. At the standard growth temperatures used for LT-GaAs films (between 200 and 300°C), the gallium droplet, with low arsenic concentration, that is necessary to maintain a stable vertical nanowire growth would be below the eutectic point of the binary compound. Thus, producing a solid droplet in which growth is impeded by the lower diffusivity of the chemical species. To date, there is no reported growth of self-catalyzed GaAs nanowires in VSS mode, so this possibility can be ruled out.

The step-by-step route to synthesize the core-shell nanowires is sketched in figure 4.3a, and can be listed by four main consecutive steps (as labeled in the figure):

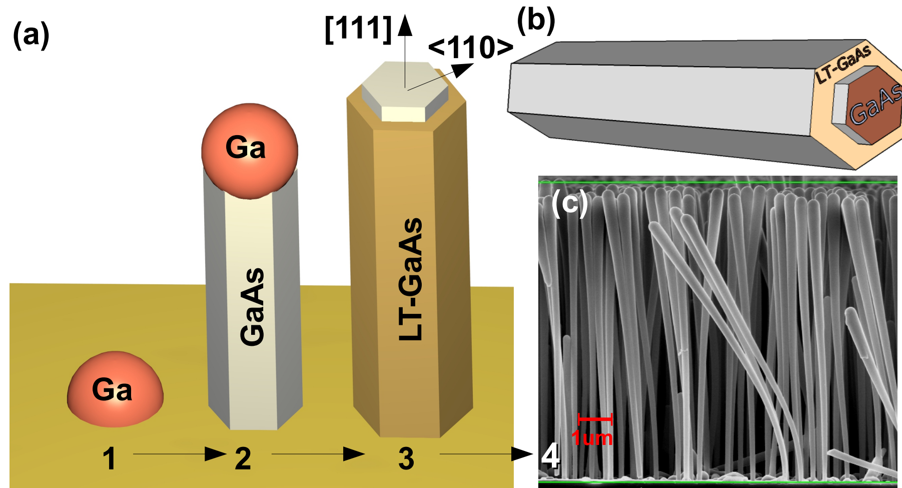


**Figure 4.3:** a) Steps for the growth of core-shell GaAs/LT-GaAs nanowires based on a self-catalyzed scheme using Ga as liquid medium in VLS growth mode. The steps are: (1) formation of Ga seeds droplets on the $SiO_2$ substrate; (2) growth of GaAs NW; (3) crystallization of Ga droplet in As-rich atmosphere and subsequent evaporation of LT-GaAs shell covering the GaAs nanowire sidewalls, (the core-shell structure is represented from another angle in (b)) and finally; (4) evaporation of the amorphous As capping layer on top of the nanowires, resulting in an As encapsulated NW ensemble with an average length of 8.6$\mu$m, as seen in the SEM image of c).

**1** The first step is a pre-deposition of gallium on top of the oxidized Si(111) substrate. The rough, oxidized surface, provides pinholes in which the gallium droplets are nucleated. The nanowire diameter depends on the

[1] LT-GaAs nanowires samples have been grown in the group of Prof. Anna Fontcuberta i Morral at École Polytechnique Fédérale de Lausanne (EPFL), Switzerland, as part of a collaboration between partners of the consortium FP7 EU Nanoembrace.

initial size of the droplet before growth. The density of nanowires depends on the density of droplets formed. It has been studied that the maximum yield of vertical nanowire growth along the $< 111 >$ direction is related to the contact angle of the gallium droplets with the oxide layer before growth of the nanowires starts. This can be tuned by changing the oxide thickness that influences the wetting of gallium [70]. Also, for thin enough oxide layers, the nanowires grow following an epitaxial relation with respect to the Si(111) surface underneath. Optimum conditions in density and size-used in the GaAs/LT-GaAs nanowires- are obtained when the oxide thickness is equal to 0.9 nm, in which case the wetting angle is close to 90 °. Figure 4.3b shows the dense array of nanowires grown under these conditions.

**2** Growth starts by opening the arsenic and gallium shutters at the growth temperature of 640°C. The nanowires grow vertically in the <111>B direction from the gallium droplets following the self-catalyzed growth described in section 1.3.5. The GaAs nanowires are grown at a nominal growth rate of $0.3Å/s$, an $As_4$ partial pressure of $2.5 \times 10^{-6} mbar$, and Ga partial pressure of $1.42 \times 10^{-6} mbar$. The growth time has been 90 mins. Under these conditions, Ga-catalyzed GaAs nanowires are known to predominantly show a ZB structure along their length (section 1.3.2) except on the top and bottom, where the out of steady-state conditions lead to a more defectuous growth. In these regions, the nanowires consist of a dense intermix of ZB twins, WZ insertions and stacking faults. Growth stops when the gallium shutter is switched off. However, the nanowires continue to grow in the As-rich atmosphere until the Ga droplet is consumed and completely crystallized.

**3** After the GaAs core is grown, the LT-GaAs shell is deposited on the lateral facets of the nanowire. Zinc-blende GaAs NWs present six equivalent faceted sidewalls cut by {110} planes. To evaporate the low-temperature shell, temperature was subsequently reduced down to 300°C. Once the temperature has been stabilized, the Ga flux is restored and the low-temperature shell grows at a nominal rate of $1.1Å/s$, with $As_4$ partial pressure of $1.18 \times 10^{-5} mbar$, during approximately 15 minutes. The intended thickness for the shell was 35 nm.

**4** Finally, a thin As capping layer is deposited after growing the shell to protect the surface against atmosphere exposure when the nanowires are transferred from the MBE system to the STM chamber [62]. This is achieved by shutting off the Ga flux in an As-rich atmosphere after the growth of the shell, and by further lowering the substrate temperature down to room temperature. The as-grown GaAs(core)-LT-GaAs(shell) nanowires embedded with the As capping layer have been inspected with SEM. Figure 4.3c shows the high density and aspect ratio of the nanowires, with a mean length of 8.6$\mu$m and a capping thickness varying from 20 nm at the bottom of the nanowires to 60 nm at the top, giving a cotton-bud

shape to the nanowires. This is a known effect occurring upon growth of nanowire arrays called shadowing. It is due to the reduced flux of $As_4$ reaching the nanowire bottom as a consequence of the large density of nanowires impeding an homogeneous redistribution of arsenic along the length of the nanowire during growth.

### 4.3.1 TEM characterization of LT-GaAs nanowires

After cleaving the nanowires onto a lacey carbon film, they have been transferred to a TEM chamber to perform structural and atomic characterization. The resulting images are shown in figure 4.4a and b. The nanowire can be seen encapsulated by the amorphous As layer in the TEM image, a slight roughening of the sidewalls is seeing through the amorphous shell. Using HR-TEM, the observed atomic structure of the LT-GaAs shell is Zinc-Blende. No distinction in lattice parameter is seen between the core and the shell of the nanowire.

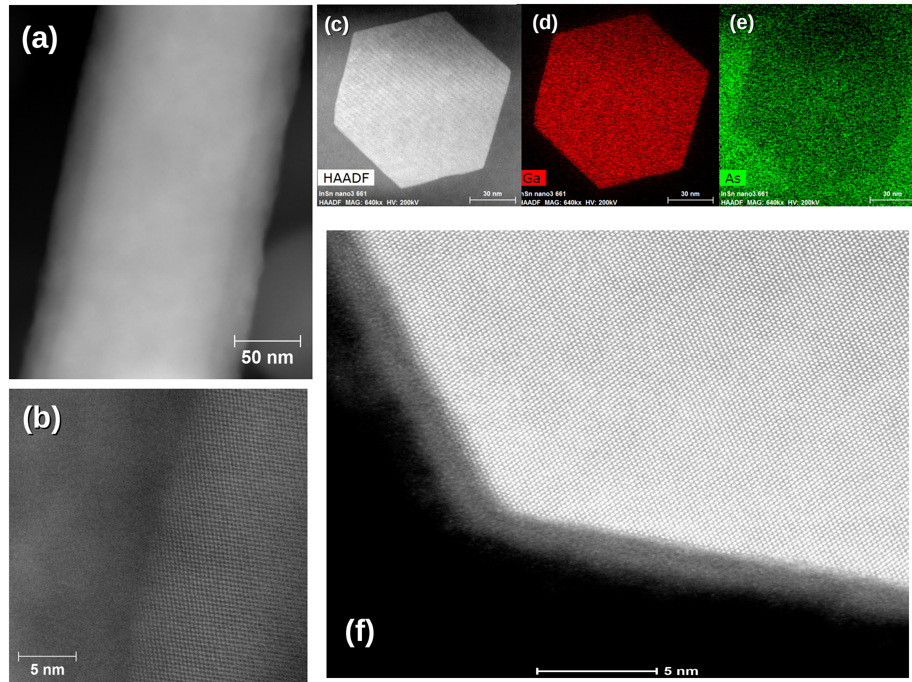


**Figure 4.4:** a) Bright-contrast TEM image of the sidewall of a GaAs/LT-GaAs nanowire encapsulated in the amorphous As capping layer. b) HR-TEM image showing the Zinc-Blende atomic structure found on the sidewalls of the nanowire. c) High angle annular dark field STEM image (HAADF-STEM) of the cross-section of a GaAS/LT-GaAs nanowire. d)e) EDX elemental mappings of gallium and arsenic at the cross-section of the nanowire. f) HR-TEM image of the cross-section of the nanowire showing a 111 plane .

The cross-section of the nanowires was also characterized. To do this: the nanowires were transferred onto a silicon substrate, then encapsulated under a layer of hydrogen silsesquioxane (HSQ) to further cut thin slices perpendicular to the nanowire main axis with the use of a focused ion beam (FIB) machine.

Then, as shown in figure 4.4c-f, HAADF-STEM, chemical mapping by EDX and HR-TEM techniques were applied on the cross-sectional cut of the nanowires. In figure c, the HAADF-STEM image shows the hexagonal structure, signature of a self-catalyzed growth on a $< 111 > B$ direction, with six equivalent and almost regular sidewalls. Some roughening is observed on the sidewalls of the nanowires. Also, there is no contrast between the core and the shell of the nanowire, which is expected given that the shell lattice parameter is almost identical to the core. The elemental mappings of figures d and e show the amount of Ga and As coming from the nanowire as detected by the X-ray elemental mapping, the background of arsenic in figure e comes from the amorphous As capping layer surrounding the nanowires. Even though the shell has been grown at low temperature, the excess of As incorporated to the material, as stated in the last section, is less than 1%. It is therefore not possible to distinguish any chemical contrast between the core and the shell with X-ray elemental mapping. Finally , in figure f, a high resolution TEM image shows the detail of the atomic structure of the $\{111\}$ plane on the cross-section of the nanowire. The interface between the core and the shell is indistinguishable.

## 4.4 STM characterization of LT-GaAs Nanowires

The LT-GaAs nanowires were characterized in an Omicron UHV LT-STM system designed to work at room and low temperature (chapter 2, section 2.1.5). Experiments were conducted at 300 and 77 K. The As capping layer was desorbed from the nanowires by direct contact thermal heating inside the UHV preparation chamber of the microscope. The temperature used to completely desorb the capping layer was around $350 - 380°C$, tracked by the reading of a pyrometer pointing to the nanowire sample. The desorption time was one hour. After desorption, the nanowires were transferred onto a flat Si(111) substrate, with a thin film layer of Ag on top, by direct contact cleaving in UHV (details of this technique can be found in section 3.3.1). This procedure leaves a disperse amount of cleaved flat-lying nanowires across the surface with one lateral facet in contact with the surface of the substrate as sketched in figure 4.5a. After

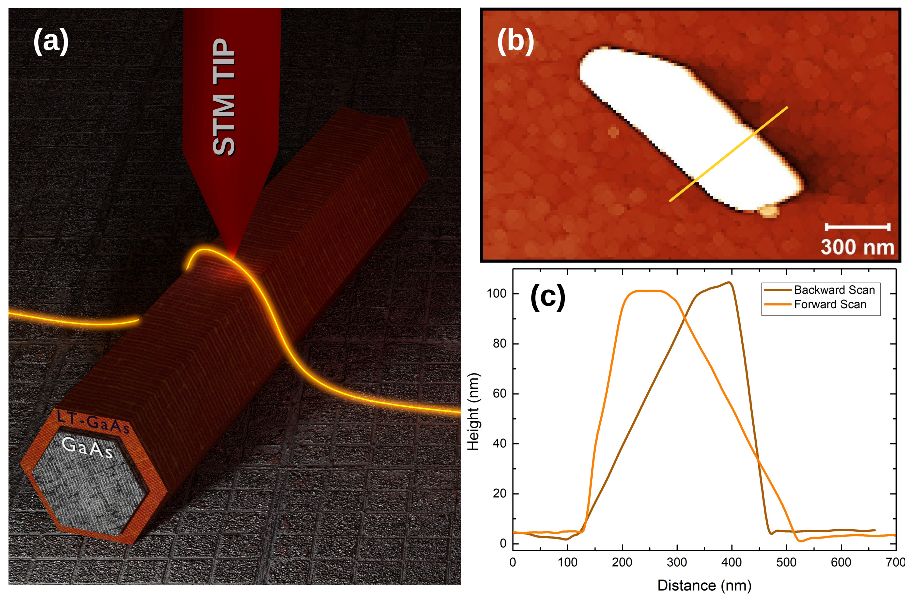


**Figure 4.5:** a) Representation of the STM tip scanning the upper sidewall of a flat-lying nanowire on a substrate. A yellow trace outlines the trajectory of the STM tip when the nanowire is scanned. b) STM image of a GaAs/LT-GaAs nanowire. The rod-like bright protuberance where the contrast is higher marks the boundaries for which the tip scans the nanowire. The image was taken at 77K with $V_{sample} = -3V$ and $I_{tunnel} = 10pA$. Scale bar is 300 nm. The orange line marks the height profile of the STM tip scanning in constant-current mode and it is represented in c), where the tip follows the shape of the lying nanowire, in backward and forward scanning modes.

transferring the nanowires to the substrate, an optical camera is used to locate the places where there are transfer traces as a result of the cleaving. The tungsten STM tip is brought into tunneling close to the position where the transfer traces are observed and the surface is scanned around in constant tunneling current mode. A nanowire is found when the STM tip scans a bright protuberance of much greater height than the surface average, and whose width is approx-

imately equal to its height. If such a height profile is kept when up-scanning a given area for thousand of nanometers, the tip is scanning over a nanowire. This produces a STM image such as the one in figure 4.5b. The image shows a cleaved piece of a LT-GaAs nanowire lying on the substrate. These nanowires are grown along the $< 111 > B$ direction and present six equivalent lateral sidewalls giving them the appearance of an hexagonal tube. Thus, if one facet of the nanowire lies parallel to the substrate, the opposite facet must appear flat when the STM tip surpasses it, as showed in the height profile of figure 4.5c. The height profile followed by the tip when performing a backward and forward scanning over the nanowire is depicted. It is seen that, when the nanowire is detected, the feedback loop reacts with a steep increase in the tip-sample distance, which can give an overestimation of the height of the nanowire. Also, when the tip goes back from the nanowire to the sample, it starts scanning the sloped nanowire sidewalls, as the change in height is softer, giving a longer tail to the height profile. Therefore, the height profile is asymmetric with respect to backward and forward scanning. Nonetheless, the length of the cleaved part and the approximate lateral dimensions of the nanowires can be obtained through the analysis of the height profile. To correctly estimate the dimensions of the nanowire, the feedback loop sensitivity acting on the tip has to be large, so that it reacts rapidly to the sudden change of height occurring when the tip reaches the nanowire, but not so sensitive that the piezotube is over-retracted, giving the tip additional inertia when the nanowire is found, as the tip "jumps" through the sidewall. Once a single nanowire piece is completely scanned and located with respect to the scanning frame, the tip can be put on top of the upper sidewall, as seen in figure 4.5a. The upper surface can be scanned all along the sidewall by moving the tip parallel to it. In this way, the structural properties of the nanowire can be accessed with greater detail and LDOS spectroscopy can be performed, at any selected point on the upper sidewall, to study its electronic properties. In the next two sub-sections, the structural and electronic properties, obtained with the OMICRON STM at 77 and 300K, of the sidewall of the LT-GaAs shell will be described and compared with similar STM measurements for GaAs nanowires, as well as contrasted with the properties of LT-GaAs materials discussed in the previous section.

### 4.4.1 Structural properties

The structural properties of the nanowire surface are accessed by scanning the top sidewall with the STM tip parallel to the growth direction in a frame constrained within the boundaries of the top facet. This way, it is possible to visually inspect the nanowire surface in a single STM image, as showed in figure 4.6b. The scanned part of the sidewall has a lateral dimension of 50 nm, which is consistent with the average diameter measured in the upper part of the as-grown nanowires by SEM and indicates that the cleaved segment must have occurred, as accounted from the shadowing effect, from the middle-up side of the nanowires.

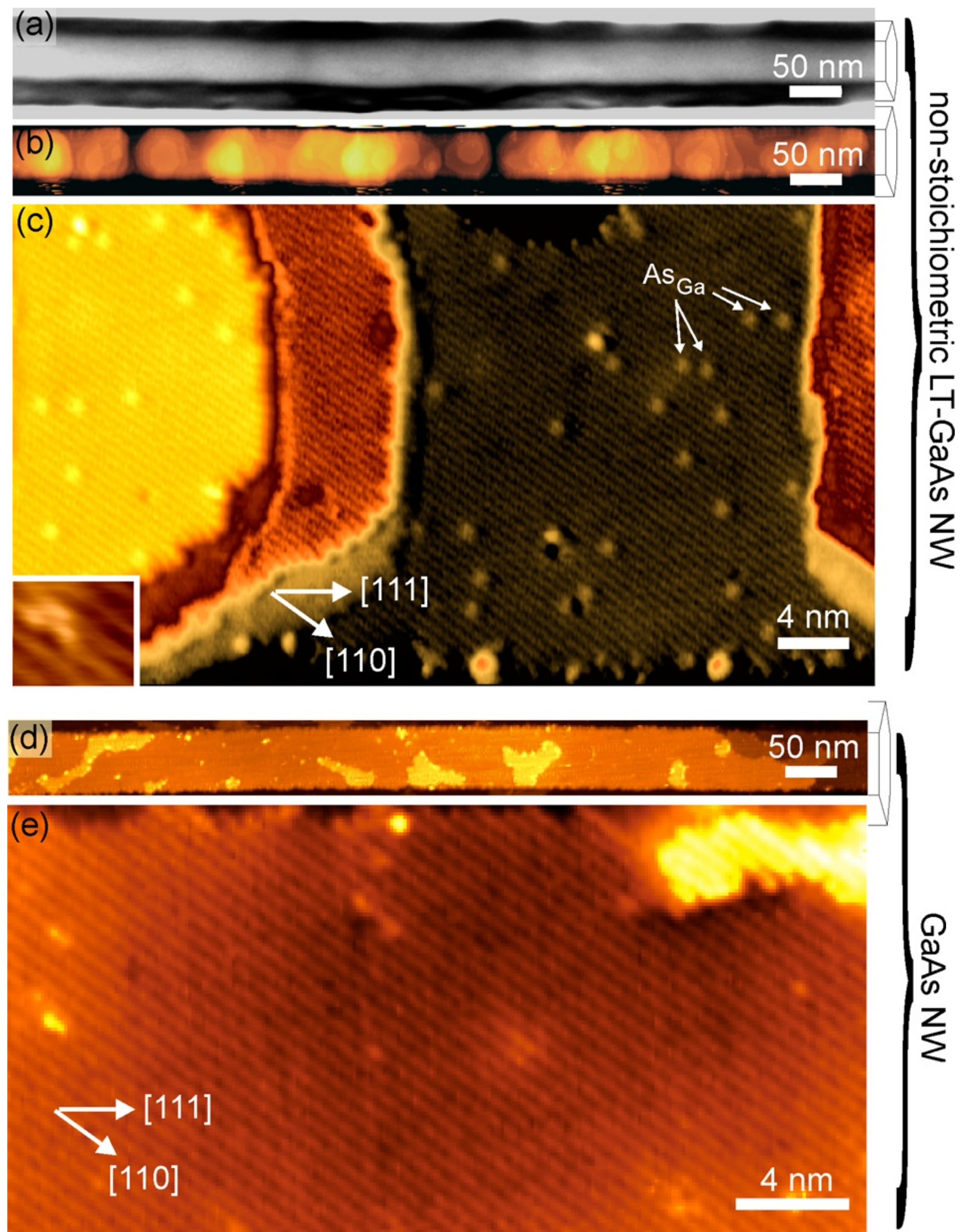


**Figure 4.6:** a) SEM and (b) STM images of a single GaAs/LT-GaAs nanowire transferred onto a Ag/Si(111) surface after decapping the As amorphous layer. In (c), a high-resolution STM image obtained on the {110} sidewall of the LT-GaAs shell is represented. The arrows point to subsurface $As_{Ga}$ arsenic antisites. Inset: STM image of a single antisite defect showing the typical structure for As antisites lying on the second subsurface layer, with the central core and two satellites. d) STM image of a GaAs nanowire sidewall (without LT-GaAs shell) transferred onto a Si(111) surface after the sublimation of the As capping layer. e) High-resolution STM image obtained on the {110} sidewall of the GaAs nanowire. No $As_{Ga}$ antisite defects are present. In (a), the SEM was operated at an accelerating potential of 10 kV, the contrast arise from the detection of secondary electrons. Tunneling conditions in b-c, d-e: $V_{sample} = -3.0, -4.0V$, $I_{tunnel} = 10, 20pA$, respectively. STM images taken at 77K (except inset of c)). The color scales in b),c),d) and e) are 88, 23, 17 and 5 Å, respectively.

The principal feature arising from the STM images is the roughness profile of the nanowire sidewall. It shows faceted flat terraces surrounded by monoatomic steps diagonally oriented along the length of the nanowires. This roughness can be observed in the SEM images of different nanowires from the same sample, as in figure 4.6a, by visually inspecting the changes in bright contrast along the top facet and the dark contrast along the adjacent lateral sidewalls (three sidewalls are seen in the SEM images, consistent with a flat-lying hexagonal nanowire). The roughness is 4 nm, approximately, along the 2$\mu$m length scanned nanowire. This is in contrast with the height profile showed by single GaAs nanowire sidewalls, in which a single atomic layer spans the whole length of the nanowire with small disperse island around its edges, as showed in figure 4.6d. Both nanowires have been grown by the same mechanism of self-catalysis and studied by STM in the same manner. Thus, the difference in roughness must arise from the growth of the low-temperature shell. Homoepitaxial growth with MBE on {110} surfaces of GaAs has been studied in some works[194][195]. When the growth is performed under high As:Ga ratio, it becomes Ga-limited and can lead to instabilities during growth. This instabilities were simulated in [194] under the frame of the Ehrlich-Schwoebel effect, which is caused by large barriers for adatom hopping when growth is performed in Ga-limited regime and under low temperature, as with the nanowire shells. Depending on the As:Ga ratio, 3D features (pyramids or mounds) can appear during the homoepitaxial growth on the surface, forming patterns with characteristic lateral dimensions that increase with the film thickness. The corrugation observed in the nanowire sidewalls is ascribed to the homoepitaxial low-temperature growth on {110} surfaces under high As flux.

The atomic structure of the nanowire surface is highlighted when scanning over a reduced area of the top sidewall, as in the STM image of figure 4.6c. The STM image covers a size of approximately 50 nm, revealing three monoatomic steps separating three flat terraces. Every terrace is conformed by a series of stacked rows along the growth direction but angled with respect to it. In between the rows a numerous and dispersed array of nanometric bright protrusions can be seen. Both features can be analyzed independently:

The series of rows stacked along the length of the nanowire make an angle of $\approx 35°$ with the <111>B growth direction. This is the signature of the Zinc-Blende structure whose stacking direction along the <111> direction is not parallel to it, as discussed in chapter 1, section 1.3.2. The ZB structure is a consequence of the self-catalyzed growth scheme, as the majority of scanned areas of the sidewall of the nanowire shows the same atomic structure. This shows that the cleaved nanowires are being scanned with STM along a portion of the sidewall where the ZB is the dominant crystal phase. Two crossed arrows pointing to the growth and plane direction are placed on the bottom of figure 4.6c to allow a visual identification of the growth direction with respect to the ZB stacking plane. Finally, the constant-current contrast of the STM image at the voltage $V_{sample} = -3V$ indicates that the surface corresponds to the {110} plane of a ZB structure. The {110} plane of the ZB GaAs is known to be

non polar and to show a very small surface reconstruction which is the result of a small vertical buckling of the surface Ga-As dimers with a slight charge transfer between atoms [196]. Otherwise rendering an almost unreconstructed square lattice. Additionally, the surface states associated with the topmost layer lie outside the GaAs band-gap and the HOMO of the surface Ga-As dimers is localized at the As atom while the LUMO is localized at the Ga atom [89]. Thus, imaging the occupied states (negative potential) with STM will give a current in which the contrast will come majoritarily from the localized states on the As atoms while an empty states image will have a larger current when the tip interacts with the states localized on the Ga atom[85](sections 3.4.1 and 2.1.1). Then, the contrast arising from the STM image of figure 4.6c reveals the localization of the As atoms on the ZB GaAs{110} nanowire lateral sidewalls. Same atomic structure can be seen on the GaAs nanowires sidewalls of figure 4.6e.

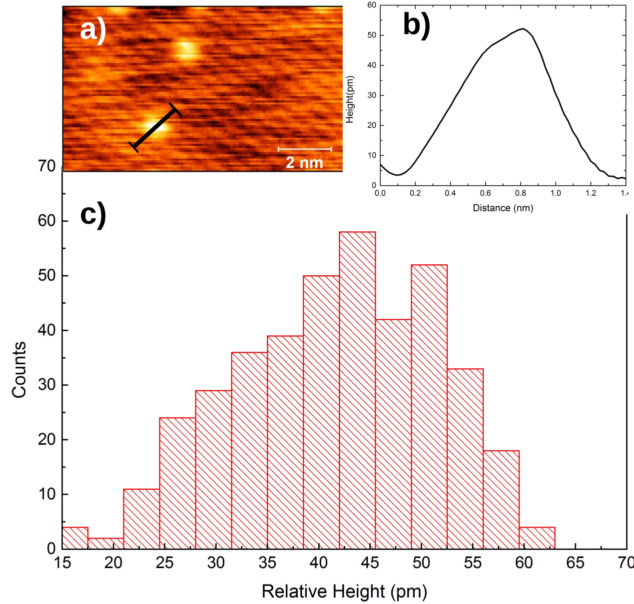


**Figure 4.7:** a) STM image of the sidewall of the GaAs/LT-GaAs nanowire taken at $V_{sample} = -3V$ and $I_{tunnel} = 20pA$ 20, two arsenic antisites defects are distinguishable on the ZB sidewall of the nanowire. The black line marked on the lower antisite traces the length of a height profile taken across it, and shown in b). c) Histogram showing the distribution of relative heights measured over the height profiles of 427 different antisite defects.

The protrusions are identified as subsurface arsenic antisites. They are dispersed on the terraces and superimposed to the As sublattice imaged all along the length of the sidewall as marked in figure 4.6c with the label $As_{Ga}$. The antisites are present in a very high concentration. Arsenic antisites have been investigated previously by STM in {110} planes of UHV cleaved LT-GaAs films by the group of Feenstra [181][144] In their work, the antisites are identified as small bright protrusions with a non-homogeneous aspect. The STM contrast

can change with the scanning voltage as well as with the subsurface layer in which the antisite lies due to the symmetry of {110} planes. Based on these considerations, they identify what is the STM contrast of antisites down to 4 atomic layers below the surface. A distinguishable feature of the antisites is the shape that they show when lying in the second subsurface layer, as shown by Feenstra and collaborators[144][197]. This shape is that of a bright protrusion, apparently extended over several sublattice atoms, with two small satellite features located approximately at the 15th-nearest-neighbour from the antisite position. They arise from the tails of the antisite wavefunction and are related to strain variations of the As tetramer as a consequence of the aforementioned surface buckling. In figure 4.7a, a better resolved STM picture of two antisites on the nanowire sidewall has been depicted. The first thing to notice is that the antisite wavefunction seems to be extended over several lattice sites, without any particular position with respect to the surrounding atoms. This is in contrast with the appearance of surface arsenic antisites presented in section 3.4.1 of the previous chapter, in which the antisite wavefunction occupies only one lattice site, and it is located at the position of Ga adatoms. Furthermore, the apparent height in the STM image of surface antisites is equivalent to the height of the surrounding As adatoms. The antisites of the LT-GaAs nanowires seem to be higher than the surrounding As adatoms. This is an electronic effect rather than a topographical one, and it reveals that the current at the position of the antisites is dominated by the tunneling current from the deep defect states, and thus from more delocalized hydrogenoid type orbitals, suggesting that the antisites are electrically active. This is in contrast with the surface antisites, which are uncharged and do not have defect states within the band gap of the material. Also, as stated by Schwarz [148], the antisites are no longer neutral if they are located just one monolayer below the surface. In the STM image of figure 4.6c, taken at 77K, the contrast on the antisites shows little variation between them. The height profile across one of such antisites has been depicted in figure 4.7b, showing a relative height of 45 picometers. Furthermore, the relative height distribution of 427 different antisites dispersed around the sidewalls of different nanowires has been depicted in figure 4.7c, with the majority of antisites showing a relative height of 45 picometers on the STM images. Thus, looking at the relative height and apparent extension of the antisite from the STM image is not possible to distinguish the subsurface layer in which they are located. Comparing with the results of Feenstra [144], they could be located at least 4 layers below the surface. The reason for the lack of resolution imaging the antisites is twofold: First, the nanowire has to be imaged at larger voltages than the cleaved thin-films due to the additional impedance related with the discrete size of the nanowires, what means that the current comes not only from the antisite state but from a larger amount of valence band states, thus reducing the sensitivity of the tip to image subsurface features. In Feenstra's work, the maximum overlap between tip states and the antisite wavefunction tails is seen at -2V, while LT-GaAs nanowires can not be scanned with stability at less than -2.5V. Second, and added to the lack of sensitivity, the shape of the

tip apex could obscure the exact profile of the antisite wavefunction, so it is not possible to precise the subsurface layer in which they lie. At 300K, the sensitivity is increased and it is possible to image the nanowire at smaller voltages, in some nanometric restrained STM scans, it is possible to observe additional features of the antisites wavefunctions, as showed in the inset of figure 4.6c, where an antisite with two smaller protrusions is superimposed to the As sublattice. Counting the number of antisites per surface layer yields a concentration of $N_{DD} = 5 \pm 2 \times 10^{18} cm^{-3}$. Which is inline with values obtained for LT-GaAs films grown at 300 °C, as shown in section 4.2.1. Finally, no bright protrusions in a large amount are seen on the GaAs nanowire sidewalls (fig.4.6 e), thus we can unambiguously assign the point-defects in the LT-GaAs nanowire shell to result from the dispersion of subsurface arsenic antisites incorporated during the growth of the low-temperature shell.

### 4.4.2 Electronic properties

In order to investigate the electronic properties of the LT-GaAs shell, local tunneling spectroscopy measurements have been performed on selected places of the {110} sidewalls of the nanowire surface. With local spectroscopy, information about the density of states of the sample can be extracted. It allows also to obtain the position of the Fermi level and the width of the GaAs band-gap, as well as the position and charge balance of the antisite levels if the spectroscopy is performed locally on top of them (section 2.1.3).

The STM tip has been brought to the top of the bare {110} sidewall in an area cleared of antisites and steps. The feedback current has been switched off and the voltage has been ramped up in a 5V range, between -2.5V and 2.5V, while the current has been acquired. A Lock-In amplifier has been used to extract the conductance. Also, in order to maximize the sensitivity between the tip and the sample, the tip must be brought sufficiently close to increase the tunneling overlap when the voltage is resonant with the band edges, as there are less charge carriers available in the $eV$ range. At the same time, if the tip-sample distance is too short, there might not be enough charge carriers on the surface to screen the electric field, a space-charge area arises in the semiconductor and a larger apparent band gap is measured. This effect is known as tip induced band bending (TIBB) and has been studied in section 2.1.4. To increase the dynamical range of the measured signal without falling within one of these two extremes, the following approach has been followed: An additional voltage signal added directly to the piezo-electric voltage $V_Z$ (which sets the initial tip-sample distance) has been coupled synchronically with the voltage ramp in order to increase the proximity between the tip and the sample at small voltage, for which the current is reduced and a larger sensitivity is required. This additional voltage signal is a V-shaped pulse centered at 0V and it has been output with a function generator [92] (section 2.1.3). The same procedure has been used to acquire localized spectroscopic measurements on the As antisites.

The resulting spectroscopic measurements, plotted as the normalized con-

ductance versus sample voltage, both for the GaAs surface and the As antisites, are depicted in figure 4.8. The measurements have been performed at 300K and 77K (inset of figure). The normalized conductance amplitude is proportional to the density of states of the sample at any given point for a given energy with respect to the Fermi level. The lower trace, colored brown, represents the LDOS on the LT-GaAs region free of antisites. Two broad humps where the conductance is highly increased are almost symmetrically placed around the Fermi level(0V), the rising slopes in conductance represents the edge of the valence band at negative voltages and of the conduction band at positive voltages, marked in the figure as $E_V$ and $E_C$, respectively, using the method of [92] to delimit the onset of the bands. The central region where the conductance is null is the band gap of the material. At 300K, a band gap width of $\approx 1.42eV$ is measured, inline with the bulk GaAs band gap.

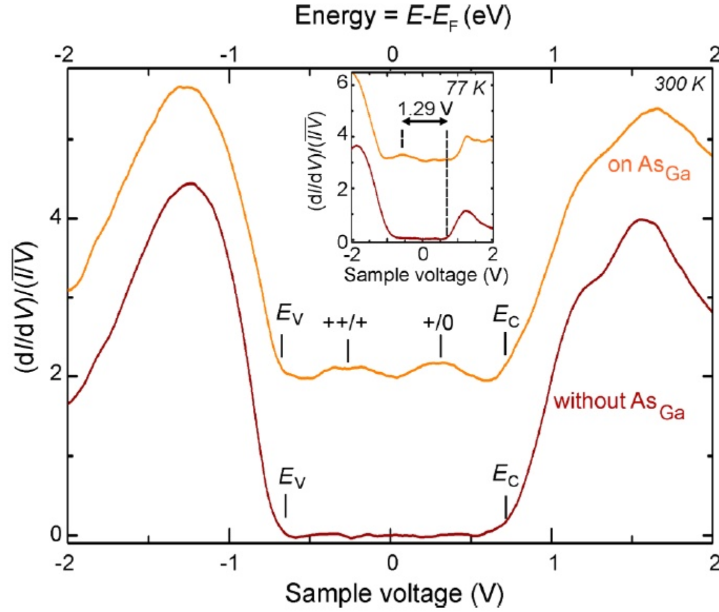


**Figure 4.8:** LDOS tunneling spectroscopy acquired on a subsurface As antisite (upper curve) and in a region free of antisites (lower curve) at the surface of the LT-GaAs shell at a temperature of 300 K (inset:77K). The conduction, valence band edges, and the charge transition levels are indicated by vertical dashed lines, labeled $E_C$, $E_V$, (++/+), (+/0), respectively. The upper curve has been shifted for clarity.

The upper trace, shifted in figure 4.8 for clarity, represents the normalized conductance spectra when the tip is put above an antisite. Similar broad bumps in the conductance can be seen at negative and positive voltages accounting for the valence and conduction band states contributing to the current with the band edges at the same position as well as the Fermi level centered in the middle of the band gap. Moreover, two small peaks appear just above and below the Fermi level. The peaks are the electronic signature of the antisite states representing the two ionization levels (++/+) and (+/0) -as marked in

the figure-, which appear when the Fermi level states of the tip are resonant with the neutral(at negative voltage) and ionized (at positive voltage) bands of antisite states, respectively.

To better understand the shape of the curves and to further corroborate the existence of arsenic antisites, some remarks have to be made:

- First, the Fermi level lies in the middle of the band gap, thus the GaAs/LT-GaAs nanowire is semi-insulating. The measured band gap width is in line with the bulk band gap of GaAs. This suggests that the Fermi level is pinned by surface states in a sufficiently high concentration such that the electric field of the tip that would induce a large band bending in a semi-insulating material is screened by the charge carriers of these states. Films of MBE grown GaAs(100) mechanically cleaved in UHV can produce a very flat (110) surface that is analyzed with STM. In [97], it has been found that in cleaved SI-GaAs (110) surfaces, the Fermi level is unpinned. When the tip-sample voltage is positive (tunneling current into conduction band states) the surface is depleted of electrons. This process is out of equilibrium and the absence of a high concentration of charge carriers in the surface of SI-GaAs impedes any inversion current to screen the electric field. The band bending is large enough so that the Fermi level of the tip can not surpass the conduction band edges. Increasing the voltage widens the depletion layer, thus no current is observed. In general, tip induced band bending in a semiconductor surface produces a large apparent measured band gap. But a careful consideration must be made in every case, as it changes with the type of material and doping. Several works can be found dealing with the simulation of such spectra [93][98][94]. In the case of the LT-GaAs shell, at the surface of the nanowire, the Fermi level is pinned in the middle of the gap and the band edges are well defined even at 77K. Extrinsic defects are thus present to screen the electric field of the tip, impeding a large band bending. The electric signature of such defects has been explored with STM previously: In [145], it is shown by combining spectroscopy with topographic profiles, that the steps of the GaAs(110) surface are able to hold a charge, whose sign depends on the orientation of the step as well as the type of doping of the material. Furthermore, tails of the density of states of such localized states are observed close to the band edge onsets in the spectroscopy data, and the tip apparent height changes when the scanning is performed in very close proximity of the step as a result of the local accumulation or depletion produced by the charged step. For the GaAs/LT-GaAs nanowires, the large amount of extrinsic defects in the surface, accounted by the numerous steps and terraces observed in the topographic image, figure 4.6c, produces the pinning of the Fermi level. Such results are in line with previously observed pinning on surfaces induced by extrinsic defects, both in bulk [198] and in nanowires [134]. In [198], the roughness of cleaved ZnO $(11\bar{2}0)$ surfaces, which are clean and stoichiometric, is compared with the same

surface but sputtered and thermal annealed, that shows a large amount of extrinsic defects. In the first case, there is a strong tip-induced band bending and no indications of intrinsic surface states in the fundamental bandgap, a large apparent band gap is measured. On the contrary, for the defective surface, the Fermi level is pinned and the measured bandgap exhibits an energetic width of the order of the bulk one. Furthermore, Capiod *et al.* [134] have studied the surface of GaAs nanowires with (110) ZB sidewalls which are surrounded by a high amount of monolayered terraces having the same orientation as the LT-GaAs nanowires. The Fermi level is found to be pinned midgap and the measured band gap is also inline with the bulk GaAs bandgap.

- The Fermi level is pinned between both ionization levels of the antisites. A comparison can be traced with the work of Feenstra in the spectroscopy of LT-GaAs antisites [144]: The position of the Fermi level with respect to the band of antisites states was compared with several samples of LT-GaAs films in which shallow dopants were introduced and the material was intentionally changed from $n^{+}$-type to $p^{++}$-type. In the first case, the Fermi level is above the band of antisites states and only the (++/+) ionization level appears on the spectroscopy, which means that they can not be compensated by the dopants. When the doping is changed to $p^{+}$-type and later to $p^{++}$-type, the Fermi level position shifts down to the middle of the donor band, between the (++/+) and (+/0) ionization levels, as in the case of the LT-GaAs nanowires, suggesting that the antisites acts as double donors, and that they are indeed compensated by the intentionally introduced shallow acceptors. Therefore, on the LT-GaAs nanowires, a large amount of antisites must be ionized, their charge being compensated in such a way that the Fermi level is shifted to the middle of the antisite band. As the nanowires are nominally undoped, and no other intrinsic defects or dopants are observed in the topography nor in the spectroscopic graphics, the compensation mechanism for the negative charge of the ionized antisites arises from the contribution of the charged states of the surface steps. Also, the antisite states are deep level defects within the band-gap and there is not enough thermal energy at 77K to hop electrons from the valence/conduction bands to the defect states. The detection of a current coming from the band of antisites in the spectroscopic measurements supports the assistance of extrinsic step states. These act as intermediate hopping levels for the electrons tunneling between the sample and the tip.

### 4.4.3 Arsenic precipitates: Structural and electronic properties

By inspecting, with STM, several pieces of flat-lying LT-GaAs nanowire sidewalls, an additional structural feature to the ones already discussed has been frequently observed. A series of bright, large clusters have been observed. They

have sizes ranging from 1-2 nm to 5-6 nm and, circling their boundaries, an annular region with a darker color.

Such features are depicted in figure 4.9a, that shows a STM image of a sidewall on the nanowire. A series of faint rows are seen, they correspond to the atomic reconstruction of the ZB (110) sidewalls. Also, numerous small protuberances are observed. They can be assigned to be the aforementioned arsenic antisites. Furthermore, larger spots with a dark surrounding annular area are present in the image. In the SEM characterization of the cleaved nanowires on the substrate, the same features can be seen-figure 4.9b- ,predominantly on the upper part of the cleaved nanowires. Several flat-lying nanowires, besides from the one showed in the figure, have been characterized with the SEM and the same features have been detected.

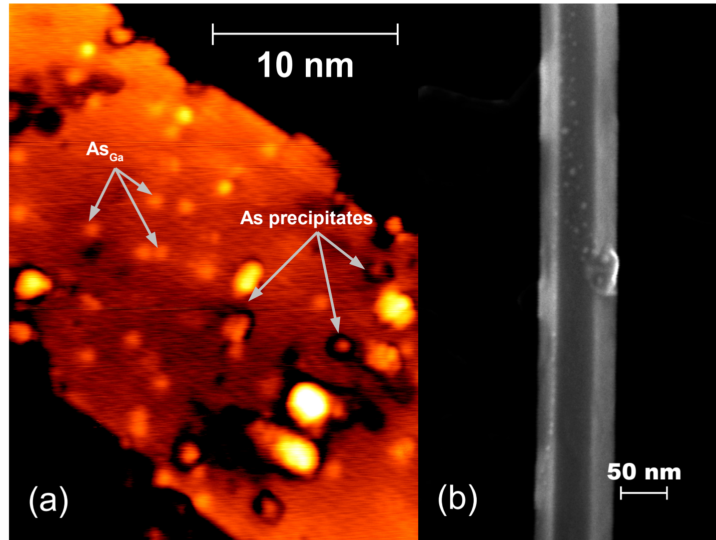


**Figure 4.9:** a) STM image of a terrace on top of the sidewall of the upper part of a GaAs/LT-GaAs nanowire. Several $As_{Ga}$ antisites and As precipitates are observed on the image. Grey arrows highlight some of the defects and precipitates. $V_{sample} = -3V$,$I_{tunnel} = 10pA$,T=77K. Color scale: 15Å. b) SEM image of the top part of a flat-lying GaAs/LT-GaAs nanowire. Bright spots scattered around the sidewall indicate the presence of As aggregates. The accelerating voltage is 10kV. The contrast of the image arise from the detection of secondary electrons.

In order to further study the nature of these larger protrusions, a height profile, as well as LDOS spectroscopy along this profile, has been performed locally on one of them. This is showed in figure 4.10. In the profile, the protrusions have a large apparent height. In the region surrounding them, a lower height than the sidewall is seen, as apparent by the dark contrast in the STM image as well as the lower height in the profile. This is a feature commonly observed when a STM tip scans along a charged defect on a semiconductor surface [89]. The reduced height is thus a consequence of scanning a depleted area around a charged defect. When the tip is put on top of the depletion region on a filled states image, the reduced number of charged carriers in the depletion region re-

duces the tunneling current, thus a darker contrast is observed. Similar results as well as similar profiles have been obtained scanning arsenic aggregates with STM on LT-GaAs films [181]. This observation along with the shape and size of the protuberance allows to identify them as arsenic aggregates. They were produced, most likely, during the annealing step in which the As capping layer was desorbed.

Spectroscopy curves were acquired on one of the As aggregates as well as around it. The spectroscopic measurements have been taken at three points along the profile marked with a blue line, and shown in figure 4.10b. These points are: (I) on the ZB(110) sidewall , (II), on the depletion region surrounding the aggregates and (III), on top of the As aggregates. The results are shown on figure 4.10c, using the same acquisition and normalization methods as with the As antisites described in the previous section.

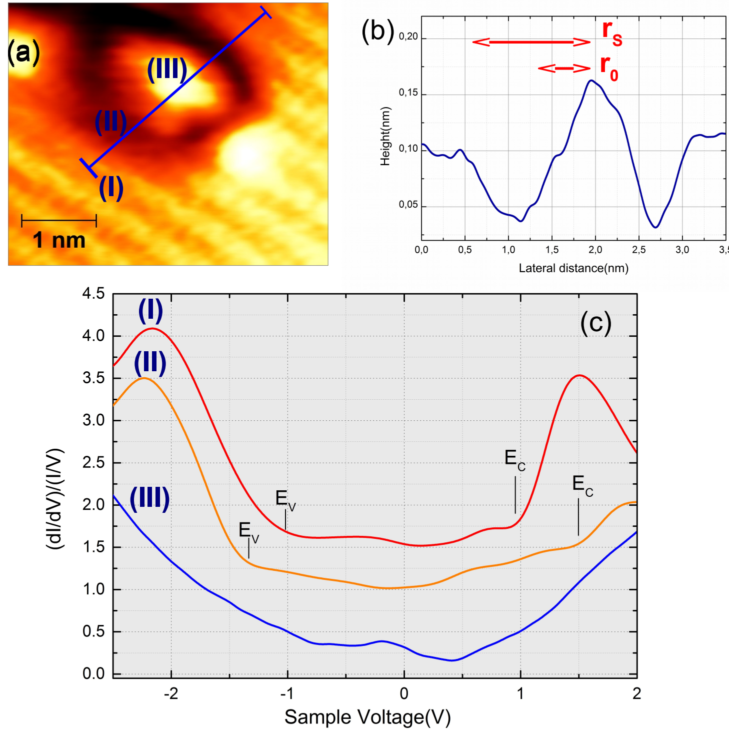


**Figure 4.10:** a) STM image centered on one As aggregate encountered on the {110} sidewall of the upper part of GaAs/LT-GaAs nanowires. The bright protrusion surrounded by a darker contrast represents the As aggregate with the depletion region around. A blue line marks the profile traced in b). $V_{sample} = -3V, I_{tunnel} = 10pA$. Color scale: 14Å. b) Height profile of the STM tip scanning on top of an As aggregate in constant-current mode. $r_0$ delimits the radius of the As aggregate and $r_s$ the radius of the aggregate plus the positively charged depleted region surrounding it. c) LDOS tunneling spectroscopy performed along the three points labeled by roman numerals on (a). (I) On the {110} sidewall, (II) on the depletion region and (III), on top of the As aggregate. The conduction and valence band edges are indicated by vertical dashed lines and labeled $E_C$ and $E_V$, respectively.

Curve (I) in figure 4.10c holds the same shape as the one performed on the LT-GaAs nanowire sidewall at 77K, as seen in the inset of fig 4.8, with the Fermi

level pinned midgap. At the depletion region, curve (II), the observed band gap is wider. This is a consequence of the reduced density of charge carriers on the region, leading to a larger band bending as there are not enough carriers to screen the electric field of the tip. Thus, the onset of electronic states from the valence and conduction bands is seen at larger voltages. Finally, in (III), the overall shape of the curve is smeared out, the metallic aggregate pins the Fermi level in the middle of the gap, and the band edges are not well defined as there are additional states incoming from the arsenic aggregate and contributing to the tunneling current. Also, at lower voltages, the conductance is not completely reduced to zero and an almost constant density of states yield a small current. Such spectroscopic features have been previously described for As aggregates on LT-GaAs by Feenstra [181], where the constant density of states in the GaAs band-gap was also attributed to the metallic nature of the arsenic aggregate.

To further explore the nature of the As precipitates, a comparison with the precipitate model proposed by Warren [172] is followed. In Warren's model, the As precipitates are able to capture electrons or holes. Their number is determined by the barrier height and the size of the precipitate. In the case of the precipitates found on the nanowire sidewalls, as the area surrounding the precipitates is depleted of electrons, it is assumed that the precipitates are negatively charged. Thus the precipitates are able to capture electrons. As explained in section 4.2.1, the maximum number of electrons that a precipitate is able to hold given a built-in potential, follows from Laplace equation and it is equal to:

$$n = (4\pi\epsilon/q)r_o\phi_b \tag{4.13}$$

Given that on the As aggregates, the Fermi level is pinned in the middle of the LT-GaAs band gap -as shown in figure 4.10c, proved theoretically by Tersoff[199] and observed with LT-GaAs precipitates [181]-, and assuming a typical value of $0.8V$ for the Schottky barrier height, a built-in potential of 100 meV is deduced. From figure 4.9b, an average value of $r_o \approx 1.6$ nm is extracted. Using equation 4.13, a rough approximation of one electron captured per precipitate is obtained. The width of the depletion region is estimated using Gauss law, and assuming that the total charge in the region covered by the precipitate and the surrounding depletion region is zero, keeping the material neutral. The resulting total charge is equal to:

$$Q = \frac{4\pi}{3}(r_s^3 - r_0^3)eN_{DD} \tag{4.14}$$

With, $r_0 \approx 1.6$ nm, the charge Q of one electron, and $N_{DD} = 5^{-18}cm^-3$. $r_s = 3.5$ nm is obtained. This radius is consistent with the values observed for the figure 4.10c.

Also, the depletion regions of two close As aggregates are combined into one larger depletion area, as seen in the lower part of the STM image of figure 4.9b. This is a visual identification of one of the assumptions of the arsenic precipitate model as proposed by Warren [172], that the depletion regions of close-enough aggregates are able to overlap between them. This is, to date, the first time that such overlap has been directly observed by microscopy techniques in annealed

LT-GaAs material. However, the concentration and average size of the aggregates as well as the low filling factor seen on the STM image does not justify by itself the semi-insulating properties of the nanowires, and compensation can not be only mediated by the precipitates alone but also by the extrinsic defects found in the nanowire sidewalls, as discussed in the previous section.

Finally, the formation of arsenic precipitates have been precluded during the desorption step of the As capping layer, which have been performed at a temperature of $350-380°$C (as measured by a calibrated pyrometer pointing directly to the as-grown nanowire substrate), during one hour. In the SEM images, the As precipitates are observed to appear in the upper part of the nanowires. This is explained by the inhomogeneous temperature profile that appears in the nanowire when the substrate is heated, as it has been proved analytically by Glas [200]. Generally, the longer the nanowire, the lesser the temperature at the top with respect to the temperature at the bottom for a given ensemble of nanowires vertically growing in a hot substrate. This temperature difference is very small for nanowires of few micrometers height, as the GaAs/LT-GaAs nanowires, but allows to establish a net thermal diffusion path for the mobile As antisites at the desorption temperature which will precipitate the formation of the aggregates at the upper part of the nanowires.

## 4.5 Cathodoluminescence of LT-GaAs nanowires

To test the emission properties and the influence of the low temperature grown shell on them, the nanowires have been investigated by low-temperature cathodoluminescence (CL) experiments.[2] In figure 4.11a the results are shown for the GaAs/LT-GaAs nanowires. Same measurements have been performed on as-grown GaAs nanowires (Fig.4.11 b) as well as GaAs nanowires with a thin AlGaAs passivation shell (Fig. 4.11 c)

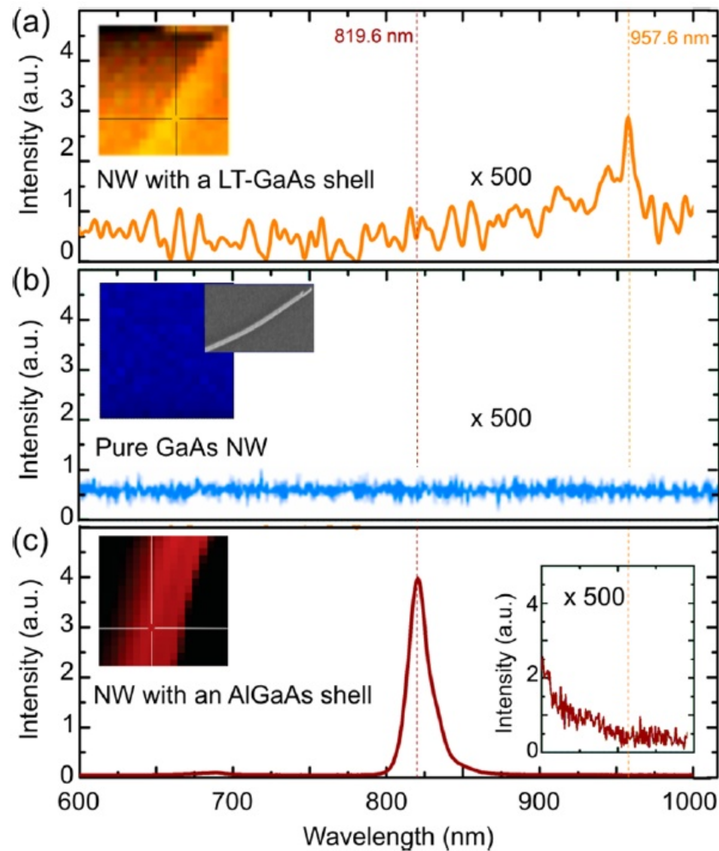


**Figure 4.11:** Low-temperature cathodoluminescence spectra of a GaAs nanowire grown with a LT-GaAs shell (a), (b), a pure GaAs nanowire and (c), a GaAs nanowire grown with an AlGaAs shell. The measurements were performed at 10K with an electron beam of 10 kV and a current of 1nA. Inset: Cathodoluminescence mappings showing the nanowire location. The markers indicate the position where the spectra was acquired on the nanowires. For the pure GaAs nanowires that do not show any CL signal, a SEM image is also shown. The absence of the free-exciton emission at 819.6 nm (1.51 eV, detected only in high-quality GaAs nanowires with AlGaAs shell) indicates a high defect density in the LT-GaAs nanowire. The weak peak at 957.6 nm (1.29eV), not seen in the inset of (c), can be correlated to the energy separation between the ++/+ ionization level and the conduction band measured in LDOS tunneling spectroscopy(Fig. 4.8)

[2]These measurements have been performed at EPFL, Switzerland, by the same team responsible for the growth of the nanowires.

For the passivated GaAs nanowires, a strong CL peak centered at 819.6 nm (1.51 eV) is observed, it is related with the radiative recombination of the free excitons produced when the nanowire electron hole pairs are created by the light. In the unpassivated GaAs nanowires, no peak is observed in the whole wavelength range covered. Finally, in the GaAs nanowires with the LT-GaAs shell, the peak related to radiative recombinations at 819.6 nm is also absent, but a small peak is observed at a higher wavelength (around 957.6 nm) when the CL intensity signal is magnified. The absence of radiative peaks for the unpassivated nanowires (GaAs only and with LT-GaAs shell) is a known effect produced by the high aspect ratio of the GaAs nanowires for which the surface recombination by defects and surface traps overweights the rate of radiative recombination, greatly reducing the intensity of the free exciton signal down to the total absence when the nanowire diameter is further reduced [201]. Passivating with an AlGaAs shell creates a type-I interface for which the concentration of interface traps is greatly reduced and thus the non radiative recombination events. For the GaAs nanowires with the low-temperature grown shell, the defective surface as well as the large concentration of As antisites hinders the cathodoluminescence peak at 819.6 nm. However, the small CL peak observed at 957.6 nm can be directly related to sub-band gap emission between the valence band of the nanowire and the (++/+) ionization levels of the band of As antisites. Furthermore, the energy at which the peak is observed, 1.29 eV, matches with the position of the ionization level peak with respect to the valence band edge observed in the spectroscopy of the LT-GaAs antisites performed at 77K.

## 4.6 Free charge carrier lifetime in LT-GaAs nanowires

The lifetime of free charge carriers in LT-GaAs nanowires has been extracted with optical pump-probe measurements (section 2.2). The transient reflectivity on the nanowire sample has been acquired as a function of the time delay between pump and probe beams. The measurement has also been performed on a LT-GaAs film sample grown on a GaAs substrate at 300° and similar growth conditions [202]. The optical setup is similar to the one described in section 2.2.2, adapted to an optical pump-probe experiment. The results are depicted in figure 4.12. The red line shows the transient reflectivity signal on the nanowire sample, and it is overlayed to the black line, which shows the results for the LT-GaAs film. In the inset of the figure, the same results are presented on a log scale and shifted to each other. Below each experimental curve in the inset, a modeled curve is fit with two exponential decay functions. The transient reflectivity signal has a steep rise at 0 delay, when both pump and probe beams arrive at the same time to the sample: the pump beam creates a distribution of electron-hole pairs on the samples, and the changes in the reflectivity are measured with the probe beam. The reflectivity decreases in a two-step fashion for

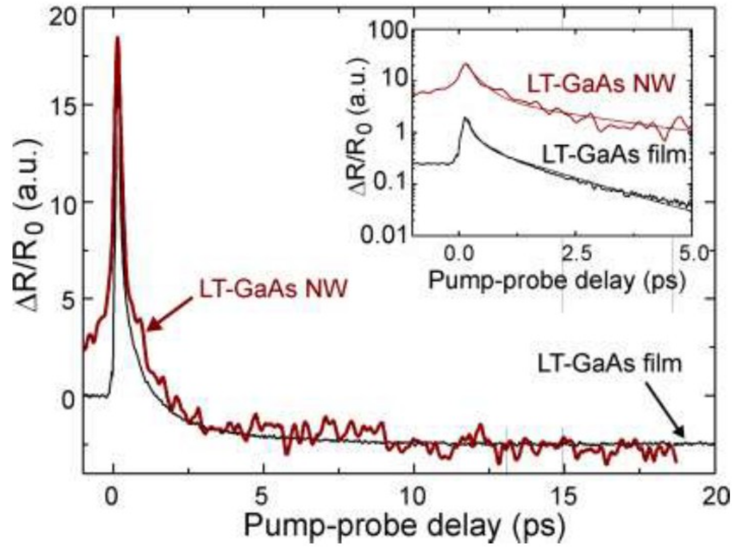


**Figure 4.12:** Transient reflectivity signal (linear scale) measured for the LT-GaAs nanowire sample and for a 1.5 $\mu$m thick film of LT-GaAs grown on a GaAs substrate. Inset: Transient reflectivity signals (log scale) and their respective modeling based on two exponential decay functions.

both samples: First, there is an ultrafast decrease, 300 fs for the nanowires and 180 fs for the thin film, which reflects the relaxation and cooling of the carriers. Then, a longer recombination time, of 2.6ps for the ensemble of nanowires and 1.6 ps for the LT-GaAs film, appears as a consequence of the carrier trapping processes. It is seen that the lifetime of the nanowires is very similar to the one of the LT-GaAs film, supporting the mediation of defects incorporated to the low-temperature grown shell in the non-radiative recombination of carriers. Furthermore, after this decrease, the reflectivity does not recover back to the initial value, but goes to negative ones. The initial reflectivity is only recover after a longer time of few nanoseconds. This effect is a signature of the LT-GaAs material and its possible origin has been discussed in section 4.2.3. Also, its implications for the onset of THz emission from LT-GaAs nanowires will be discussed in the following chapter.

## 4.7 Conclusions

This chapter has been devoted to explain the observed-mainly by STM- structural and electronic properties of a new kind of III-V semiconductor GaAs nanowire in which the shell is made up of GaAs grown at low temperature.

For such, the first part of the chapter has overviewed the main characteristic and the historical development of LT-GaAs thin films. LT-GaAs has become a very suitable material in the emerging field of THz optoelectronic due to its very short carrier lifetime as well as a high enough mobility and resistivity that allows it to follow very fast optical pulses with high detectability. To create such a material, a two-step growth scheme has to be follow: First, the GaAs growth has to proceed in MBE at a much lower temperature than the usual one, that produces stoichiometric, crystalline GaAs. Then, the material is annealed at a higher temperature for very short periods of time to give it its semi-insulating properties. The exact nature whereby the annealed material presents such a high resistivity while maintaining a very short lifetime has not encountered a clear settlement in the field. This has been the main topic of discussion for section 4.2. Later, it has been proposed a scheme to grow a core-shell GaAs/LT-GaAs , which has been studied mainly by STM. Section 4.3 described the main steps followed to grow such nanowires. In Section 4.4 and subsections, the sidewalls of the LT-GaAs shell of the nanowires have been studied by STM, which has allowed the complete characterization of their structural and electronic properties. Finally, in sections 4.5 and 4.6, the cathodoluminescence and the lifetime of carriers of these nanowires has been measured, respectively.

It has been proved that it is possible to incorporate a low-temperature grown GaAs shell to the sidewall of a GaAs nanowire.The properties of the shell resemble those of the equivalent bulk material grown at low-temperature by MBE: a material in which the excess of arsenic is incorporated mainly in the form of point antisite defects. However, as the shell grows at the non-polar {110} surfaces, the role of extrinsic defects becomes a driving force to maintain the electroneutrality in the material. In the case of LT-GaAs nanowires, it is seen that the combination of low-temperature with an As-rich atmosphere during the homoepitaxial growth of the shell leads to the creation of rough surfaces. These surfaces present a high density of steps, which are partially charged and therefore act as extrinsic defect states. These states pin the Fermi level of the surface at the middle of the band gap of GaAs, which otherwise will be unpinned. At the same time, they compensate the charge of the arsenic antisites, which act as double donors and are partially ionized after growth. Therefore, the morphology of the nanowire sidewalls is fundamental for the understanding of the properties of the shell. This interplay between surface and defects has several consequences: 1) It is possible to image the antisite defects at low temperature by creating a hopping channel between the bands and the deep defect levels through the extrinsic step states. 2) The Fermi level is pinned between the two charge transition levels of the antisite, as revealed by the tunneling spectroscopy performed locally on them. This implies that the antisite

population can be partially ionized, and these ionized antisites are primarily responsible for the ultrafast lifetimes encountered in the material, as seen by pump-probe techniques in section 4.6. In conclusion, it has been proved that the growth of low-temperature layers is not restrained to 2D films, as they also can be growth conformally to a nanowire. This result opens the way to the controllable incorporation of point-defects to the structure of a nanowire, which can have important consequences not only to enhance the optoelectronic properties of the nanowires, but also to use these kind of shells as intermediate or buffer layers when the nanowires are contacted to metallic gates.

# Chapter 5

# Terahertz emission from GaAs core-shell nanowires

## 5.1 Introduction

The terahertz radiation is contained in the range of the electromagnetic spectrum for which the frequency of the light waves is of the order of magnitude of $10^{12} Hz$. Equally, the wavelength of light for these frequencies is between $0.1 - 1$ mm, that is why terahertz radiation is also termed as 'sub-millimeter' radiation. This wavelength range lies in the electromagnetic spectrum below the infrared and far-infrared radiation, and above microwave radiation, as depicted in figure 5.1. This zone of the electromagnetic spectrum is also known as the THz gap, as it is situated in a transition region in which it is hard to control the detection and emission of such radiations. It corresponds to signals with a very fast frequency for electronic devices to follow and at the same time very low in energy to be usable as a photonic device.

Nonetheless, radiation in the THz spectrum range has very interesting properties. 1 THz equals to an energy of 4 meV. This radiation is energetically very weak and non-ionizing, of the order of the thermal energy of particles at room temperature (the radiation emitted from electron transitions with energies of the order of kT at room temperature equals 6.2 THz). Terahertz radiation is emitted from black bodies at temperatures in the range 10-60 K, from transition energies between energy levels in the order of meV or from charged bodies whose dynamics change in the sub-picosecond and picosecond time scale. These are the same time scales of molecular rotations and vibrations for several types of molecules and molecular complexes as well as from different kinds of collective motions of phonons and electrons. For its use in research, controlling the emission and detection of THz radiation has many advantages, for example: To perform molecular spectroscopy, as several molecules show an unique absorption spectra in this range [107], as well as time resolved spectroscopy of the ultrafast dynamics of photoexcited particles [105]. Also, being able to detect interste-

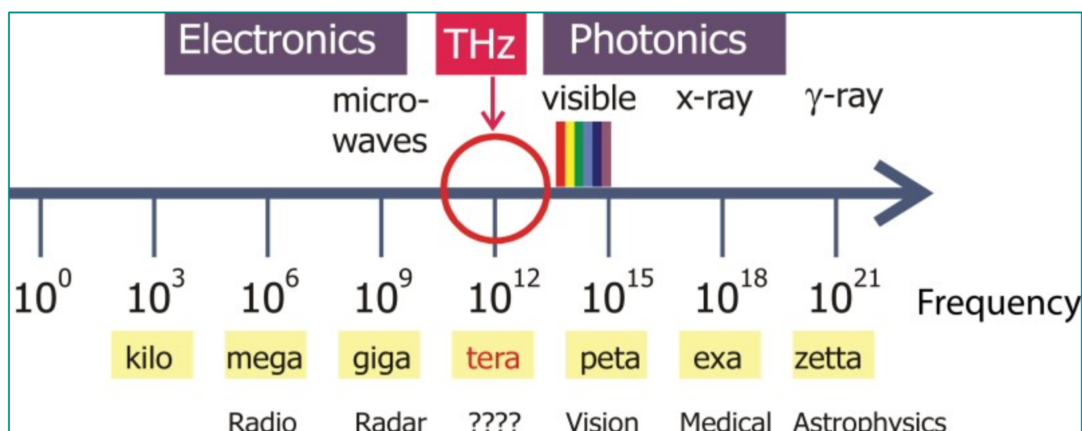


**Figure 5.1:** Electromagnetic radiation spectrum highlighting the position of the THz range above the micro-wave region and below the visible and infrared region. Extracted from [203].

llar radiation in this range of the spectrum allows to gain information about the origin and evolution of interstellar objects at temperatures between 10-60K, such as stellar clouds [204]. THz radiation is highly absorbed by water, as it resonates with several rotovibrational modes of the water molecules [116], and unlike X-rays, it is non-ionizing. It is therefore convenient for its use in medical imaging to detect changes in the water density of the human skin that could be produced by several diseases [205]. Furthermore, some metals and plastics have unique absorption spectra in this frequency range, which can be used to build safe, fast, and non-invasive detectors of weapons and explosives for human security systems [206]. The THz radiation covers a much broader range of potential applications that the ones here described, there are some books detailing the state-of-the-art of the research and application of this radiation [118][207].

The THz gap has been shortened during the past three decades and the development of refined system to emit and detect radiation in this range has been possible thanks to the development of ultrafast lasers, being able to emit radiation pulses with the duration of tenths of femtoseconds on a wide range of different wavelengths. It has then been possible to explore the ultrafast dynamical processes on sub picosecond time scales as well as to use the femtosecond pulses to sample THz radiations transients and convert optical signals to electronic signals, with techniques such as equivalent time sampling, as described in chapter 3, section 2.2.2. In general, with THz devices, there is a tradeoff between the accessible bandwidth, the amount of optical power generated in the THz range in comparison to the optical power needed to excite the pulse, the cost and the usability of the devices. The difficulty to meet all this requirements in a balanced enough way is the factor slowing down the industrialization of such devices. With the advent of nanotechnology, more advanced sources and detectors are available and an increasing amount of research is devoted to this topic.

Detectors of THz radiation can be sorted depending on whether they detect incoherent radiation or not as well as what is the physical mechanism used to detect the radiation. In general, a good detector is characterized by a large bandwidth, a fast responsivity in the detection range and a good noise to equivalent power factor (NEP). Incoherent detectors can generate a signal proportional to the energy of the THz radiation but with no information about the phase, and generally, not time-resolved. Examples of such detectors are based on extrinsic semiconductors such as GeGa or SiAs, for which the THz radiation excites transitions levels in the order of meV between shallow defect states and the conduction or valence bands. Due to the low energy implied, only operation at very low temperatures is possible. Also, bolometers are available for very low temperature operation. These are devices formed by semiconductor crystals such as Ge or Si in which the detection mechanism is based on changes on the thermal resistivity of the material when it is exposed to THz radiation. Additionally, Golay cells are another kind of incoherent detectors, whose detection mechanism is based on the optoacoustic effect. This is related to the changes in volume of a gas subjected to THz radiation. A laser beam detects these small changes in the volume of the gas in the cell. This setup has the advantage of room temperature operation, but at the expense of a lower responsivity. For coherent detection, the most used Thz detectors are semiconductor photoswitches coupled to antennas made from GaAs grown at low temperature as well as electro-optic crystals (such as ZnTe). They convert the THz radiation to an electrical signal (the photocurrent in photoswitches) or optical signal (the change of polarization of a reference laser signal in electro-optic sampling) that is proportional to the energy of the detected radiation and more importantly, that preserves the phase and resolves the signal in the sub-picosecond time scale. Also, they have very high bandwidth of detection and a decent responsivity. These detectors, particularly LT-GaAs photoswitches, have been described in detail in chapter 3, section 2.2.2 and more information can be found in [118][207].

Several sources of THz radiation can be found: THz radiation is naturally emitted from black-bodies at low temperatures (10-50K). The working principle is simple, but the emitted radiation is incoherent and with low power. Several diode-like semiconductor devices are suitable for THz emission, being pulsed or continuous. In general, they are compact devices but perform at low THz frequencies. Some examples are Gunn, Impatt or Tunett RTD diodes [208]. Molecular lasers can be tuned to emit THz radiation [209]. One of the most powerful and complete devices, despite its high cost and size, is the Free Electron Laser [210], which can emit continuous THz radiation in the whole spectrum range. Another kind of very popular (and under strong development) devices are the Quantum Cascade Lasers (QCL) [211], that are compact devices with good enough emitted power at low THz frequencies. Finally, THz radiation can be produced from polarized LT-GaAs antennas in pulsed [186] and continuous regime [212] as well as electro-optical crystals, such as ZnTe [213].

Furthermore, a pulse of THz radiation is generated from the bare surface of several semiconductors when excited by femtosecond laser pulses. The physical

origin of such generation is generally related to the asymmetry created by the surface on the bulk material which alters the spatial distribution of the photogenerated electron-hole pairs and might create a transient current emitting radiation in THz frequencies. Details involving this generation mechanism are extended in the next section.

THz radiation generation was reported from semiconductor nanostructures such as InN nanorods [214] or silicon nanowires [215], as well as other ternary semiconductor nanowires [216]. But the interest of using nanowires as THz emitters was triggered by the reporting in 2011 by Seletskiy *et.al* [14] of an intense THz radiation pulse generated from InAs nanowires, for which it was proved that the emitted power from nanowires was enhanced with respect to the equivalent semiconductor bare surfaces as a consequence of the inherent high aspect-ratio of the nanowires. Since that, such trend has been described for other nanowires, such as GaAs[217] or Ge[218] nanowires, and the interest in terahertz generation and detection with nanowires is rapidly growing in the research field of THz optoelectronic.

The purpose of this chapter is to study the THz emission properties of as-grown samples of GaAs nanowires in which a low-temperature grown GaAs (LT-GaAs) layer has been incorporated as a shell and to compare it to the THz emission from GaAs nanowires. LT-GaAs is a material which presents very suitable optoelectronic properties due to its ultrafast recombination rate combined with high dark resistivity and a good enough mobility (the structural, electrical and optical properties of this material are summarized in chapter 4, section 4.2). It is for this reason, that LT-GaAs is the standardized material for its use as a photoswitch or photoconductor when coupled to metallic antennas to generate or detect THz radiation. Even though LT-GaAs alone is not used for THz emission, it is interesting to study how it performs when it is incorporated to a nanostructure having an inherent antenna geometry such as the nanowires, and how it compares with the emission produced by GaAs nanowires. To this end, time resolved THz-emission spectroscopy has been used and a THz waveform has been detected from GaAs nanowires and GaAs/(LT-GaAs) nanowires. Furthermore, two similar batches of each kind of nanowires but grown in different laboratories have been compared to serve both as a reproducibility test for the experimentally detected THz emission profiles as well as to compare how morphological aspects of nanowire growth such as length, density or orientation can influence the emission of THz radiation.

In the first part of the chapter, section 5.1.1, the mechanism driving THz generation from semiconductor surfaces is detailed, with a focus on the origin of the THz emission from the same semiconductors materials as the nanowires studied in this work, InAs and GaAs. Then, in section 5.1.2, a review of all the reported semiconductor nanowires from which THz radiation has been generated or detected will be described, detailing mostly the results from InAs and GaAs nanowires. For the second part of the chapter: first, in section 5.2.1, the morphological differences for all the core-shell GaAs nanowires studied in this chapter and the growth parameters influencing on them will be described.

Finally, the emission characteristic of the detected THz waveforms from the nanowire samples will be analyzed and the results discussed.

### 5.1.1 THz emission from semiconductor surfaces

When a femtosecond-laser pulse strikes on the surface of many semiconductors, an outgoing THz pulse is produced from the sample. As the bandwidth and emitted power is oftenly limited, the process of THz radiation from semiconductors might not be as technologically relevant as the one obtained with other sources of radiation. However, the emitted radiation arises as a consequence of ultrafast dynamical processes of photoexcited carriers within the material, and it can give important information about physical processes occurring at the nanoscale and contribute to the understanding and realization of novel nanostructures relevant for the THz range. Also, in some cases, as with InAs, the material can be tuned by applying magnetic fields to emit higher power radiation [113], this can be useful to develop simple and versatile THz emitters for use in spectroscopy and imaging at the low THz range.

In this section, two of the most studied effects for THz emission from semiconductor will be described. Emission from surface fields and from photo-Dember effects. Also, other THz emission mechanism will be briefly covered.

**- Surface field.**

In the surface of doped semiconductors, there are localized states resulting from the different surface reconstructions or from the surface morphology. These states can trap electrons from the bulk material. If the material is doped, electrons captured at or release from the surface can alter the electroneutrality with respect to the dopant atoms giving rise to electron accumulation or depletion layers. The electronic band bends at the surface to compensate the charge imbalance and to keep the Fermi level at the same position as the bulk material. As a result a local electric field appears perpendicular to the surface. Then, the creation of depletion or accumulation layers of electrons at the surface depends on the type of doping of the semiconductor (generally, n-type semiconductors produce a depletion region, and p-type an accumulation region). Thus, the magnitude and sign of the electric field will change if the material is p or n-type doped as:

$$E_{surf}(z) = \frac{eN_{eff}}{\varepsilon_0 \varepsilon_r}(W - z) \tag{5.1}$$

Where W is the extent of the depletion or accumulation region, $N_{eff}$ is the effective concentration of carriers in the accumulation or depletion layer arising from the charge balance on the material, $N_{eff} = N_D - N_A$ , where D stand for donors and A for acceptors and $\varepsilon_r$ is the dielectric coefficient of the material. A femtosecond pulse excites electron-hole pairs below the semiconductor surface. The electron and holes are accelerated by the surface field in different directions and splitted, provoking a transient (or surge) current perpendicular to the surface. The THz radiation can be approximated in the far field by the derivative

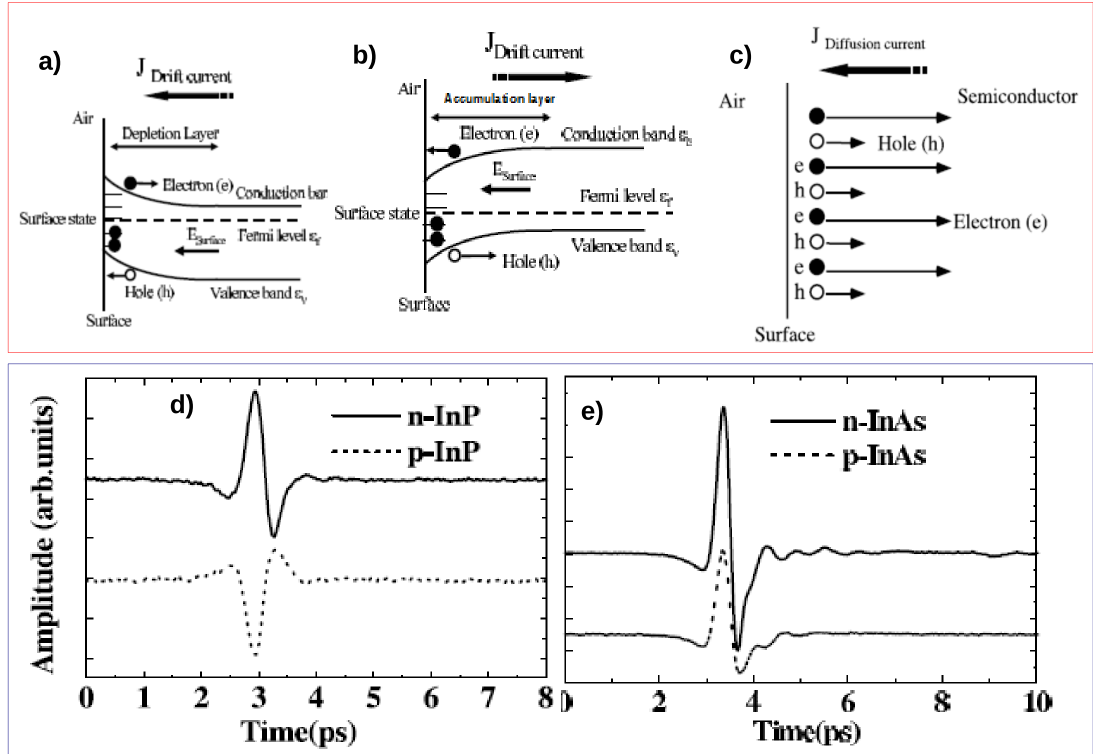


**Figure 5.2:** Band diagram and schematic flow of the drift current in a) n-type and b) p-type semiconductor. c) Schematic diagram with the flow of diffusion current from the photo-Dember effect near the surface of a semiconductor. d) Time-domain waveforms of THz radiation from n- and p-InP. e) Time-domain waveforms of THz radiation from n- and p-InAs. Extracted from [207].

of this current. The electron flux is directed towards the surface or towards the bulk depending on the sign of the electric field (the process is sketched in figure 5.2a-b. Thus, when a semiconductor emitting by this mechanism is switched from p-type to n-type, the polarity of the THz waveform is flipped (as depicted in the graph of figure 5.2d). This effect is proposed as the main THz generation mechanism for several semiconductors such as InP, GaAs or InN [114][219][207].

**- Photo-Dember effect.**

Some narrow band gap semiconductors, such as InAs or InSb, have a very high difference in mobility between the electrons and the holes. After laser pulse excitation, the carriers in excess will diffuse. As the mobility of electrons is higher, they will diffuse faster than the holes. Inside the semiconductor, electrons and holes diffuse equally in all directions. Even if electrons are spatially separated from the holes due to their faster movement, the center of charge is not going to vary and the dipole moments will cancel each other giving no net current. When the absorption is close to the surface, electrons diffusing towards the surface will be trapped or reflected, producing a net electron flux directed

against the surface and separated from the slower holes. Then, a screening electric field perpendicular to the surface is created (sketched in figure 5.2c) . This effect has been termed photo-Dember effect. If the semiconductor doping is changed, the direction of the diffusion current remains the same so the polarity of the emitted THz waveform will not change. This is displayed in figure 5.2e with the emission profile from InAs. The photo-Dember effect is enhanced in semiconductors in which the ratio between mobilities of electrons and holes is very large and when the absorption length is very short. It is important to note that there might be depletion or accumulation fields in the surface of InAs or InSb semiconductors acting on the dynamics of the electron and holes, but as they are narrow band gap semiconductors the magnitude of the field is smaller and the photo-Dember field alone dictates the emission properties from the sample. Nonetheless, in surface field emitters such as GaAs, the mobility of electrons and holes is not the same and a photo-Dember field contribution to the emitted THz radiation does exist, this effect has a smaller influence in this case with respect to the surface field. A simulation of the different contributions from the currents of electrons and holes influencing the onset of THz radiation can be found in [113]. There are other semiconductors that emit THz radiation more predominantly from the photo-Dember effect or from the surface field if the doping is changed. For example, such a behaviour has been found in the emission profile from impurity compensated GaSb[220]. Finally, photo-Dember currents moving parallel to the surface rather than perpendicular to it have been produced by masking the surface of the semiconductor with small metallic stripes[221]. When the laser spot is partially shadowed by the metal pads, there is an induced lateral gradient in the distribution of charge carriers and a diffusion current parallel to the surface. This effect has been termed as lateral photo-Dember. It yields higher bandwidth and power of the THz emission.

**- Other generation mechanisms.**

Another important THz generation mechanism for semiconductor, which is particularly important for high optical fluences, is the optical rectification. When the femtosecond-pulse is very energetic, the material response to light is not linear anymore, resulting in the formation of reflected and transmitted beams with different wavelength with respect to the exciting beam due to frequency mixing. The THz radiation in the far field is approximated by the second derivative with respect to time of the polarization vector of the material. Such a generation mechanism is instantaneous and the emitted beam presents a very high angular profile. Then, the emitted THz radiation from this mechanism can change if the crystalline structure of the surface changes as well as if the sample is rotated. The angular dependence and amplitude of the THz field generated by optical rectification from several semiconductor surfaces can be obtained, such as (111)-InAs, (100)-InAs,(100)-InSb or (100)-InP [207][114]. Although this generation mechanism is the dominant for higher optical fluences, its influence must not be diminished when the power is reduced and the detected THz waveform profile contains the contributions from the processes aforementioned as well as from optical rectifications effects. It is for this reason that some-

times the sample to study is rotated at detection angles in which the radiation emitted from this effect is minimum. Also, collective motions in the semiconductor induced by femtosecond pulses such as plasmons[222] or collective phonon motion[223] can generate THz radiation. For example, in [224], a micrometric layer of n-GaAs was grown above a SI-GaAs substrate, the extrinsic electron distribution in the n-doped material is confined between the barriers formed by the surface and the interface depletion layer. When the femtosecond-laser excites a distribution of electron-hole pairs close to the surface, the ultrafast dynamics of these carriers can dynamically screen the depletion electric field, inducing this way a collective plasma motion of the electrons in the n-GaAs layer that generates THz radiation.

### 5.1.2 Nanowires and THz: Detection and Emission

In the recent years, semiconductor nanowires have entered in the field of THz-optoelectronic being used as THz radiation detectors and emitters. Some advantages is that they have high aspect-ratio and can be integrated into complex heterostructures in a wide range of lengths and diameters.

**- Outcoupling of THz radiation from Semiconductor Nanowires**

As explained in section 5.1.1, when a femtosecond laser pulse is absorbed by a semiconductor surface, an electron-hole plasma of photoexcited carriers appears along the absorption length of the material. A certain physical mechanism separates the electrons from the holes, creating a dipole whose dynamics evolve in the picosecond time scale. This moving dipole emits a THz radiation whose amplitude can be approximated, in the far field regime, as the second derivative with time of its dipole moment (section 2.2.3). In semiconductor surfaces, the orientation of this dipole is perpendicular to the surface. Considering that the angular dependence of the power emitted by a Hertzian dipole is highly directional (as shown in figure 5.3a), more power will be emitted from the sides of the dipole. Then, as depicted in the figure, most of the emitted radiation to air is affected by total internal reflection. Only the radiation whose angular direction lies within the critical angle for total reflection couples outside the semiconductor material. These geometry dampers the emitted power and makes this mechanism ineffective.

In a semiconductor nanowire, the direction of the Hertzian dipole formed by electron-hole pairs is parallel to the axis of the nanowire, thus the limiting effect of total internal reflection is not present and the output power can be greatly enhanced. A sketch of the dipole radiation pattern from a nanowire is shown in figure 5.3b. There are no reflection losses, as the dipole radiation can escape the nanowire without total internal reflection. Seletskiy et al. estimated the magnitude of this effect for the THz emission from InAs nanowires by integrating the ratio of dipole radiation (whose angular dependence is $sin^2(\theta)$) emitted from

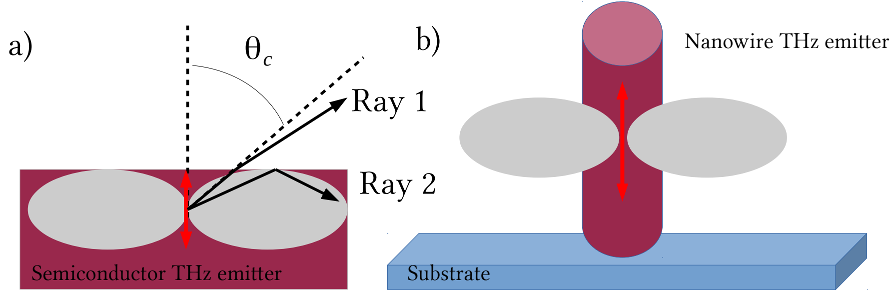


**Figure 5.3:** Radiation pattern from an Hertzian dipole emitter, the direction of the dipole is indicated by a black arrow and the angular dipole radiation pattern as a shaded area formed by two lobes at the sides of the dipole. In a) the dipole is oriented perpendicular to the semiconductor surface, if a ray of light (1) exits the surface of the semiconductor at an angle smaller than the critical angle, it is outcoupled, in the case contrary (ray 2), there is total internal reflection and the radiation does not exit the semiconductor. In b) the dipole is oriented parallel to the axis of the nanowire, the radiation outcoupling is more efficient.

a semiconductor surface and from a nanowire as [14]:

$$\frac{P_{NW}}{P_{bulk}} \propto \frac{\int_0^{\pi} sin^2(\theta) d\Omega}{\int_0^{\theta_c} sin^2(\theta)(1 - R_{||}(\theta)) d\Omega} \tag{5.2}$$

In equation 5.2, the integration range is limited up to the critical angle in the denominator, the $(1 - R_{||}(\theta))$ term accounts for reflective Fresnel losses across the interface of p-polarized dipole radiation, that are not present in the nanowire as the cube of the main THz radiation wavelength emitted is larger than the volume of the nanowire [14]. In [14], an enhancement of emitted radiation of $\sim 20$ was calculated, which was inline with an experimentally observed factor of 15 per InAs nanowire with respect to n-type InAs bulk. Other works have encountered the same trends with respect to the emitted power from nanowires: also with InAs nanowires[225] as well as with GaAs nanowires[217]. It should be noted that this reported emission enhancement is taking into account the nanowire filling factor (which is less than unity), so that the total THz emissivity per nanowire is higher. As nanowires do not fill completely the space, more power is emitted from equivalent areas of the corresponding semiconductor material.

**- Physical mechanism of THz radiation from Semiconductor Nanowires.**

The asymmetry created between the surface and the bulk material allows the effective separation of the electron and holes along one unique direction in space, that is, perpendicular to the surface. In nanowires, the surface has a radial symmetry with respect to the center of the nanowire and due to the nanometric dimension of the nanowire, the absorption of light is homogeneous along its radius. Thus, if a built-in electric field (due to surface depletion/accumulation layers or core-shell engineering) separates the electron or holes radially, the net dipole

moment should be zero or close to zero for angular incident of light, and the emitted THz radiation very small. As THz radiation is emitted from nanowires, the acceleration of the electron-hole plasma must be produced along their axial channel. The mechanism whereby this separation of photoexcited carriers is produced depends very much on the type of materials from which the nanowire is made as well as the surroundings of the nanowire (substrate, catalyst droplet, nanowire morphology). Furthermore, the reduced dimensions of the nanowire and the quasi-1d dimensional geometry can stimulate additional processes of charge carrier generation and separation which are not encountered in bulk materials. To this date, there are few publications reporting THz emission from different III-V or other semiconductor nanowires and the proposed THz generation mechanism in each case does not seem to point to a reproducible physical mechanism but to an ensemble of conditions that change between each batch of nanowires. In this part of the chapter, to set a context for the next section, a review of THz generation from different nanowires (or nanowire-like structures as nanopillars) will be summarized:

- **InAs Nanowires:** In [14], efficient THz emission from InAs nanowires was reported. Nanowires were grown in a MOVPE chamber from a gold catalyst particle on GaAs(111) substrates by the VLS-growth mode. The nanowires presented a length distribution ranging between 15-20 $\mu$m and a broad dispersion in diameter with severe tapering on the top of the nanowires, in which the gold droplet remains crystallized after growth. The THz radiation from the nanowires was detected using a linear autocorrelator setup with a Si-bolometer. The THz emission from the nanowire substrate was compared with respect to n-type InAs bulk, obtaining an enhancement of 15 times. As said in the previous section, emission from n-type InAs is mainly due to the photo-Dember effect. This mechanism is proposed to explain the THz emission from the nanowires: electrons diffuse faster and are separated spatially from the hole distribution. This creates a screening field between e-h which acts as a driving force to recover electroneutrality. If the perturbation occurs on a time scale smaller than the inverse of the plasma frequency, collective plasma motion can take place, leading to a macroscopic dipole which radiates close to the plasma frequency in an Hertzian dipole geometry along the nanowire axis. However, in order to match the main THz frequency components radiated from the nanowire with the plasma frequency for a given number of photoexcited carriers, it was considered that lowest index (acoustic-like) surface plasmons polaritons modes of low frequency are excited within the length of the nanowire as a consequence of its cylindrical geometry. After this publication, at least two more research teams have reported THz generation from InAs nanowires. In [225], the InAs nanowires were grown in a MBE chamber using selective area epitaxial growth as well as catalyst-free growth to obtain a larger control on the length and density of the nanowires. The nanowires thereby growth spanned in length from 1 to 4 $\mu$m and in diameter from 40 to 160 nm. The distance between the

nanowires (pitch) was 250 nm. The THz radiation from the nanowires was detected using a THz-TDS setup with a LT-GaAs photoconductive antenna. An enhancement of up to 3 times was observed in the emitted power from the nanowires with respect to p-InAs. It is claimed that the larger enhancement observed in [14] can arise because of the different reference sample used, as in the former case THz radiation is normalized instead with the n-type InAs reference, which shows less emitted power. In [225], the proposed mechanism for THz generation is discussed to be again the photo-Dember effect created by the charge separation of photoexcited carriers along the axis of the nanowires. In p-type InAs bulk, a third-order nonlinear optical effect, electric field induced optical rectification (EFIOR), contributes as well to the THz radiation. This was not seen in these InAs nanowires because the THz radiation amplitude does not have a dependence on the azimuthal angle. Finally, in [226], the ultrafast dynamics of catalyst-free InAs nanowires was probed by measuring the photocurrent along striplines placed on individually contacted nanowires. Although the symmetry of the nanowire and the experiment is different, it was found that there is a fast photo-current transient in the picosecond scale and all along the length of the nanowire, which is directly related to the generation of THz radiation due to the charge separation by the photo-Dember effect.

- **GaAs Nanowires:** First reporting of THz emission from GaAs nanowires can be found in [227]. In this case, GaAs-AlGaAs core-shell nanowires were grown by MBE with gold as a catalyst particle for the VLS-growth. The nanowires presented a length between 3-8 $\mu$m and diameters of 100-150 nm. Detection of THz radiation was performed with a LT-GaAs photoconductive antenna. The mechanism responsible for THz generation was not discussed. However, the application of a magnetic field parallel to the nanowire surface with different polarities allowed them to infer that the electron-hole pair dipole creating the THz emission must be oriented parallel to the nanowire axis, so that the same enhancement mechanism proposed by [14] should be observed in GaAs nanowires. Shortly after, in [217], THz generation from GaAs nanowire was reported. The effect of the catalyst droplet as well as the doping along the nanowire was studied. To do so, self-catalyzed (Ga droplet) and gold catalyzed vertically oriented GaAs nanowires were grown from a GaAs(111) substrate in MBE. Radiation was detected with an electro-optic sampling setup, using a ZnTe crystal as well as a Golay cell for power measurements. Three kind of nanowires were grown: 1) 1.2 $\mu$m long self-catalyzed p-doped GaAs nanowires (Ga droplet on top) with a 18 nm diameter 2) 300 nm long gold-catalyzed p-doped GaAs nanowires with 20 nm diameter and 3) 300 nm long gold-catalyzed nominally undoped (slightly n-type) GaAs nanowires with 20 nm diameter. In all three cases, it was claimed that the photo-excitation of electron-hole pairs is maximum close to the catalyst droplet due to the formation of surface plasmons in the droplet, as the electrons

posses a higher mobility than the holes, there is a net diffusion flux of electrons from the top of the nanowire to the substrate which creates an ambipolar diffusion current in the opposite direction. Additionally, when the droplet is made out of gold, a Schottky barrier is formed between the nanowire and the metallic droplet which builds up an internal electric field whose direction changes depending if the nanowire is p-doped or undoped. This electric field can additionally separate photoexcited carriers. The polarity and magnitude of the generated THz radiation changed if the drift current arising from this field is opposed to the diffusion current (less efficient), or if it is in the same direction (maximum efficiency). In the best case emitter (diffusion and drift currents parallel), the THz emission can be up to 40 times higher than from bulk GaAs if the fill factor is taken into account. In [228], a selective area growth scheme was used to grow ordered arrays of self-catalyzed GaAs nanowires on top of a GaAs(111) substrate with different pitches in a MOVPE environment. This way, a more homogeneous distribution in the size of the nanowires was obtained, with a higher control in length and diameter by changing the pitch size. The detection scheme was electro-optic sampling. The proposed mechanism for THz emission is the same as in [217], that is, a non-equilibrium distribution in the photo-generated electron-hole plasma due to the different mobilities in GaAs. Additionally, they observed that for very short nanowires (length$<$600 nm), the effect of the contact field between the nanowire and the Si substrate is noticeable in the THz emission amplitude, this drift current opposes the diffusion current and its influence is smaller and only important for very short nanowires.

- **Other Semiconductor Nanowires:** THz emission from silicon and germanium nanowires was reported in [215] and [218]. In the silicon nanowires, the same mechanism of induced surface plasmon (described in [14]) was proposed as the origin of the THz emission. In contrast, the germanium nanowires were coated with an irregular array of gold nanoparticles. The nanoparticles can produce an enhancement of the nanowire surface potential, acting on the separation of electron-hole pairs. There have been also reports of THz emission from ternary semiconductor nanowires, such as Mn-doped InGaAs and GaAsSb [216], as well as undoped InGaAs nanowires [229] and AlGaAs nanowires [230].

**- Detection of THz radiation with Semiconductor Nanowires.**

Detection of THz radiation using Semiconductor Nanowires has been also proved in several works. As stated in chapter 3, section 2.2.3, a semiconductor such as LT-GaAs, used as a photoswitch in an antenna circuit, can either act as an emitter or receiver, depending if the bias field polarizing the antenna is set externally (emitter) or if it is set by the electric THz field impinging on the antenna (detector). To this end, the nanowire inherent high aspect-ratio and the possibility to enhance light absorption within the nanowire [23][22] can be advantageous to scale down a THz radiation detector to one single nanowire

with very high sensitivity. Such a concept has been proposed recently in [231], in which single core-shell GaAS/AlGaAs nanowires have been placed horizontally on a quartz substrate with Au/Ti metallic pads added lithographically to the ends of the nanowires. The metallic pads connecting the nanowire act as antenna and the nanowire as a photoswitch. A detectable photocurrent appears along the nanowires when THz radiation falls on them. However, the sensitivity is low (low pA photocurrent) and the antenna geometry formed by the pads filters out the highest frequencies of the applied THz radiation so that the bandwidth is less than 1THz. The nanowire detector operates in the integration regime (lifetime of tens of picoseconds)[121]. Future research optimizing the antenna geometry as well as reducing the lifetime, with for example defective shells (for instance, the LT-GaAs nanowires presented in this thesis show a lifetime of 2.6 ps, one order of magnitude less), could yield broadband sensitive nanowire photodetectors.

Additionally, single semiconductor nanowires can also be used as incoherent THz detectors for power measurements by integrating the nanowires in a field effect transistor geometry coupled to an antenna, as shown in [232]. The detection of THz radiation from a single nanowire occurs when plasma resonance waves are created by the THz radiation between the gate and the source of the transistor. If there is an asymmetry between the source and the drain, the terahertz signal is rectified, leaving a measurable DC signal between the electrodes that is proportional to the received power. This physical effect is explained by the Dyakonov-Shur plasma wave theory [233]. In [232][234], good responsivity is obtained from single nanowires and noise equivalent power (NEP) values comparable with state-of-the art detection systems. This concept is further extended in [235] to use nanowire FETS as sensors for THz imaging. A raster scan setup is used, the transmitted beam of a quantum cascade laser (QCL) emitting at 2.8THz is passed through a given object (a leaf is used as the object in [235]) and further detected with the nanowire FET. More information about this THz imaging technique can be found in [236].

## 5.2 Characteristic of terahertz emission from GaAs core-shell nanowires

### 5.2.1 GaAs core-shell nanowires: Growth and structural properties

Two different kinds of GaAs nanowires have been studied with THz-emission spectroscopy, the first kind are self-catalyzed GaAs nanowires while the second one are core-shell self-catalyzed GaAs nanowires with a low-temperature grown GaAs shell added to them (the ones studied in chapter 4). For each type of nanowire, two different batches of nanowires grown at different laboratories by the same method have been compared. This serves both as a proof of reproducibility in the results and in the growth method as well as a method to

study the impact of the morphology and density of the nanowires on the final THz-spectra emitted from the samples. In figure 5.4, a sketch of the core-shell structure of the studied nanowires and a SEM picture on a large scale of both batches for each type of nanowire is displayed.

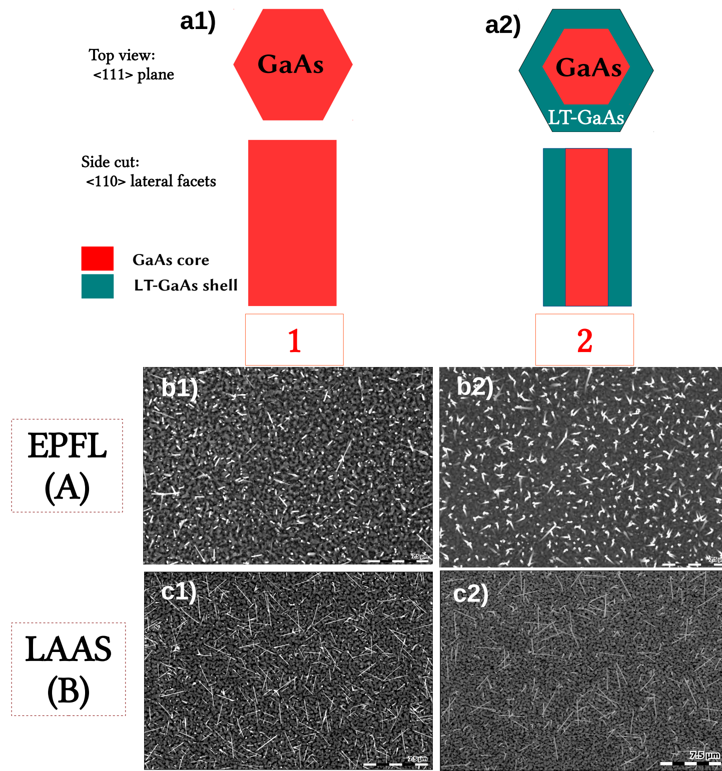


**Figure 5.4:** Comparison of the morphological characteristic of the nanowires studied in this chapter. a1) Sketch of the self-catalyzed GaAs nanowire showing top and side views. b1) SEM image of nanowire sample 1A. Scale bar is 10$\mu$m. c1) SEM image of nanowire sample 1B. Scale bar is 7.5$\mu$m. a2) Sketch of the core-shell GaAs/(LT-GaAs) nanowires showing top and side views. b2) SEM image of the nanowire sample 2A. Scale bar is 10$\mu$m. c2) SEM image of the nanowire sample 2B. Scale bar is 7.5$\mu$m. Electron beam energy is 10kV.

The first column of the figure 5.4(a1,b1,c1) displays the GaAs nanowires. The nanowires have been grown either at EPFL [1] (corresponding SEM picture of the as-grown nanowires in figure 5.4b1) or at LAAS [2] (corresponding SEM picture in figure 5.4c1). The core-shell GaAs/(LT-GaAs) nanowires are displayed in the second column of the figure 5.4(a2,b2,c2). Equally, the SEM picture in the figure b2 corresponds to the nanowires grown at EPFL and the SEM picture in the figure c2 to the nanowires grown at LAAS. From now on, the following labeling will be used to distinguish the type of nanowire and the laboratory in which they have been grown: The GaAs nanowires will be labeled as nanowires

[1]Grown in the group of Prof. Anna Fontcuberta i Morral at *École Polytechnique Fédérale de Lausanne* (EPFL). Lausanne, Switzerland.

[2]Grown in the group of Dr. Sèbastien Plissard at Laboratory for Analysis and Architecture of Systems (LAAS-CNRS). Toulouse, France.

1, while the core-shell GaAs/(LT-GaAs) nanowires will be labeled as nanowires 2. Additionally, the letter A will be used to design the nanowires grown at EPFL and the letter B to design the nanowires grown at LAAS (e.g, nanowires 1A correspond to GaAs nanowires grown at EPFL).

The growth methods for the self-catalyzed GaAs nanowires as well as the GaAs/(LT-GaAs) nanowires have already been outlined in chapters 1 and 4, sections 1.3.5 and 4.3, respectively. The substrate used in every case is p-type silicon (111) substrate with an oxidized layer of $SiO_2$ on top. The main morphological differences and growth parameters between samples A and B are summarized in table 5.1:

| | GaAs (1) | | GaAS / LT-GaAS shell (2) | |
|---|---|---|---|---|
| | **Length ($\mu$m)** | **Density ($\mu$m$^{-2}$)** | **Length ($\mu$m)** | **Density ($\mu$m$^{-2}$)** |
| EPFL (A) | 14-16 | 0.93 | 14-16 | 1.22 |
| LAAS (B) | 5-7 | 1.3 | 5-7 | 0.49 |

**Table 5.1:** Comparison of density and length of the nanowire samples 1A,1B,2A and 2B.

The following differences can be highlighted by inspecting the as-grown nanowire morphologies, as depicted in the SEM pictures of figure 5.4:

- The nanowires grown at EPFL (NW1A, NW2A) present a higher yield of vertical growth than the nanowires grown at LAAS (NW1B,NW2B). The correlation between the different thicknesses of the $SiO_2$ layer and the resulting aspect-ratio, density and length of nanowires have been studied thoroughly in [70]. The thickness of the naturally present silicon oxide layer on Silicon varies with exposition time to air. When the oxide thickness changes, its stoichiometry changes as well (less Si than for very thin oxidized films). This influences the interaction energy between the gallium droplets catalyzed in the openings of the film prior to growth in such a way that the contact angle between the droplet and the substrate changes. In [70], oxide thicknesses between 0.9 and 1.1 nm result in contact angles of approximately 90°C, which gives the highest yield in vertical growth. When the contact angle increases, not all the nanowires grow vertically with respect to the Si(111) substrate, as the creation of kinks can occur in the early stages of growth, tilting the growth direction of the nanowires. In the case of nanowires A, where almost all the nanowires are grown vertically, the oxide thickness must be in the range 0.9-1.1 nm. For the nanowires B, the oxide thickness seems to be slightly larger, in the range of 1.1-1.2 nm.

- The nanowires 1A present a narrower diameter distribution ranging between 70-80 nm, while the nanowires 1B have a diameter distribution between 60-100 nm. This is also a consequence of the different oxide thicknesses, as shown in [70]. When the thickness is in the range 0.9-1.1 nm and the nanowires are grown mostly vertically, the diameter distribution is narrower than in the other case.

- The density of nanowires has been extracted from the SEM images of figure 5.4. The results are presented in table 5.1. The density does not differ significantly between samples except for sample 2B, for which it is approximately reduced by half. The dependency of the density of nanowires with the oxide thickness in the range between 0.9 and 1.2 nm is approximately flat (slightly less density for larger thicknesses) in [70].

- The LT-GaAs shell in nanowires 2A and B has been grown at temperatures between $250 - 300°$C. As the calibration of temperature in the range below 300°C relies on the use of interpolation techniques between the temperature readings of pyrometers and thermocouples, the growth temperature can vary slightly between samples 2A and 2B, which can influence the number of antisites incorporated to the LT-GaAs shell and thus the recombination lifetime. Also, the shell-thickness has been estimated by comparing the time employed to grow the shell with the planar growth time of (100) GaAs thin-films, which was $1.1\text{Å}/s$. Then, the low temperature grown shell thickness of nanowires 2A is approximately 20 nm and in the nanowires 2B, 10 nm.

For every sample studied, a small piece of approximately $100 \times 100$ mm$^2$ of the wafer with the as-grown nanowires has been cut and placed on a mirror with a custom-made holder, so that it is easily integrated into the optical setup.

### 5.2.2 Discussion of results

The THz signal emitted from the nanowires described in the previous section has been characterized using THz-time domain spectroscopy with the setup of chapter 2, section 2.2. A femtosecond-laser pulse operating at a wavelength of 820 nm has been used both as a pump beam, to excite photocarriers in the nanowire sample, and as a sampling beam, to retrieve the THz signal in the detector on the time domain. In all the cases, the average power of the incident pump beam, measured after the beam chopper, was 12mW. The detector is a LT-GaAs photoconductive dipolar antenna. As stated in chapter 3, the detector captures the THz signal emitted from the nanowire sample and generates a nanoampere current whose magnitude is proportional to the magnitude of the THz electric field, and whose sign indicates the phase of the THz waveform.

In order to compare the different THz waveforms captured from the different nanowires samples, a n-type InAs bulk sample has been used as a reference prior to each measurement. The reference sample emits the highest signal of all the here studied samples. The reference signal has been obtained by placing the InAs sample at an angle of 45° with respect to the pump beam, thus forming an angle of 90° between the incident beam and the detection setup which collects the emitted THz beam. The nanowire samples have been placed prior to each measurement with the same orientation as the InAs reference, with only a slight modification of the orientation angle, in order to maximize the signal detected in the antenna. For the analysis and comparison of the results, the peak-to-peak

amplitude of the THz electric field from the reference sample is normalized, the signal captured from the nanowires and depicted in the figures presented in this chapter represents the proportion in which the detected THz radiation is smaller with respect to the InAs reference.

**-GaAs Nanowires.**

The nanowires 1A and 1B were first studied. Their normalized THz signal is depicted in figure 5.5. The shape of the waveform can be described by two

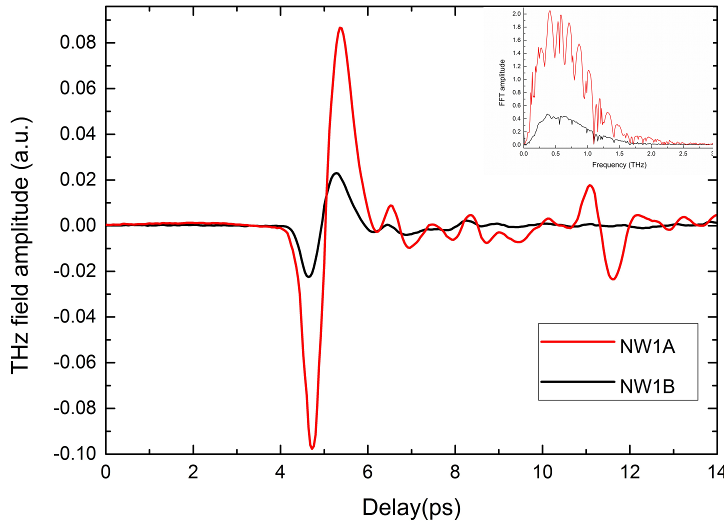


**Figure 5.5:** Time domain waveforms of the emitted THz pulse from GaAs nanowires. Samples 1A(red) and 1B(black). The excitation wavelength of the femtosecond-pulse was 800 nm and the average power 12mW. Inset: Corresponding FFT spectra of the time domain waveforms.

main peaks with different polarity. The polarity of the first(second) peak is negative (positive), respectively. The peak-to-peak amplitude of the signal from the nanowires 1A is approximately 4 times larger than the amplitude from the nanowires 1B. In the inset of the figure, the frequency spectra from the THz signal is displayed. The bandwidth spans approximately 1.5THz with a maximum emission peak centered around 0.4 THz, the frequency profile is similar in both samples. The small peak encountered after a delay of 11 ps can be attributed to an echo of the THz signal reflected in the backside of the nanowire substrate.

Such a polarity has been encountered in studies of THz emission from GaAs nanowires and nanopillars using photoconductive antennas as detectors [227][237]. Direct comparison of the polarity can not be established with other works detecting emission from GaAs nanowires as [238][217][228], because the detection setup was an electro-optic sampling with ZnTe crystals, in which the mechanism involved in the detection of the THz field is different, and generally the captured waveform shape and relative polarity differs from PCA setups [239].

The mechanism of THz generation from GaAs nanowires has been addressed

in [227][237][238][217][228]. In a GaAs nanowire, electron mobility is higher than hole mobility [109]. Also, there is rapid recombination of electrons due to the high density of surface traps that favours non-radiative recombination [201]. Then, the electrons that do not recombine fast are the ones whose momentum distribution lies parallel to the axial channel of the nanowire. Those electrons, diffusing to the nanowire top, either recombine or are reflected at the top facet, leaving an asymmetry in the momentum distribution that produces a diffusion flux of the plasma directed towards the bottom of the nanowire. Thus, the non-equilibrium distribution of diffusing electrons generates a transient ambipolar current directed along the axis of the nanowire, which radiates a pulse of THz frequencies into free space. This effect, similar to the photo-Dember effect (different mobilities plus geometry induced asymmetry in the momentum distribution), has also been termed as a 'reactive electromotive force' [228], for its similarities with a jet-like stream of electrons ballistically moving along the axis of the nanowire. It generates an electromotive force acting against it as the electron-hole pairs are separated. It has also been suggested in [238] that this mechanism can induce the creation of acoustic-like (radially symmetric) surface plasmons modes along the axis of the nanowires -much like as with InAs nanowires [14]-. By using Optical Pump-THz beam spectroscopy, a peak in the real part of the frequency dependent dielectric coefficient measured on GaAs nanowires was found in [109] and [111]. It is attributed to the resonant excitation of a surface plasmon at frequencies lower than 1THz. The surface plasmon resonant frequency should increase quadratically if the optical fluence is linearly varied. However, such an experimental dependence was not observed in [109] and the reason is attributed to charge carrier saturation by surface traps in the nanowire. In THz emission spectroscopy, the main frequency emission peak (maximum of the FFT spectra) should show variations for different optical fluences in order to detect this frequency shift. Such a resonant shift has not been observed with emission from nanowires [217][228][14], because the nanowire radial and axial distribution is not homogeneous, making a broader and smeared out emission spectra. Also, a drastic increase in the optical fluence in the nanowire ensemble could lead to radiation damage if the power applied to a single nanowire is very high.

The differences in the peak-to-peak amplitude of the THz signal between nanowire sample 1A and 1B can be directly attributed to the differences in length between the nanowires. In sample 1A, nanowires are approximately three times longer in average, while the density is almost the same. The same trend between peak amplitude and nanowire length has been encountered in different types of nanowires: InAs nanowires[225], GaAs nanowires[228] and nanopillars[237], InN nanorods[214], Ge nanowires[218] and Si nanowires [215]. Such a dependence can be addressed by considering the absorption of the optical beam within the nanowire ensemble. When the nanowires are shorter, or some percentage of them not vertically oriented (as in sample 1B), the light of the excitation pulse is not completely absorbed in the nanowire ensemble, and a large percentage goes to the silicon substrate. If the nanowires are long

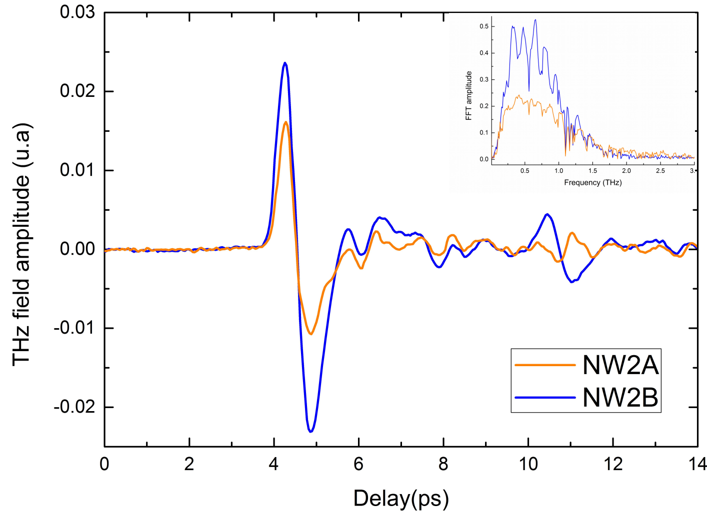


**Figure 5.6:** Time domain waveforms of the emitted THz pulse from GaAs-(LT-GaAs) nanowires. Samples 2A(orange) and 2B(blue). The excitation wavelength of the femtosecond-pulse was 800 nm and the average power 12mW. Inset: Corresponding FFT spectra of the time domain waveforms.

and the density of vertically oriented nanowires very homogeneous, the light of the incident optical beam 'sees' a quasi-continuum nanowire media and it is absorbed preferentially in the nanowire rather than in the substrate. In [217], the effective refraction index of a GaAs nanowire ensemble with very high yield of vertical growth is seen to be similar as the index of refraction of bulk GaAs. Then, even if the nanowires do not fill the space completely, they can absorb light as well as the bulk material. Finally, considering the longer nanowires, if the carrier diffusion flux is triggered by the geometrical asymmetry close to the nanowire top, this radiation effect will be enhanced for longer nanowires if there is a competing effect from other charge recombination pathways.

**- GaAs/LT-GaAs Nanowires.**

The THz emission characteristic from GaAs/(LT-GaAs shell) nanowires (samples 2A and 2B) is depicted in 5.6. The same optical beam power and wavelength as for GaAs nanowires is used. The orientation of the nanowire sample with respect to the beam is also the same. A pulse of THz radiation incoming from the nanowire sample after excitation with the femtosecond-laser pulse has been detected .

There are several aspects to notice in the detected THz waveforms: First, the peak amplitude of the nanowire sample 2B is 2 times higher than in sample 2A. Looking at the FFT spectra in the inset of the figure, it is seen that the bandwidth is similar between both samples and similar to the GaAs nanowires. Second, the peak-to-peak amplitude is smaller than in the sample 1A. Third, the relative polarity of the two main peaks of the THz waveforms is similar between samples 2A and 2B but reversed with respect to the samples 1A and 1B. In figure 5.7, the four signals (1A,1B,2A and 2B) have been displayed overlayed

with different color scales (red for GaAs nanowires and blue for GaAs/(LT-GaAs shell) nanowires). Such a difference in the phase of the electric field radiated between the two kind of nanowires can arise, as explained in section 5.1.1, from the orientation of the dipole formed by the separated electron-hole pairs which can be reversed if the sign of the electric field acting on its separation is changed, as seen, for example, when the doping type of GaAs bulk surfaces is changed from p-type to n-type [113]. Then, if the mechanism generating THz radiation from the samples 2A and 2B is to be similar as from samples 1A and 1B, that is, a fast transient current as a result of the different mobilities of electrons and holes, a different polarity is not expected to arise from the emitted pulse of the LT-GaAs nanowires. This difference in the polarity of the waveforms between

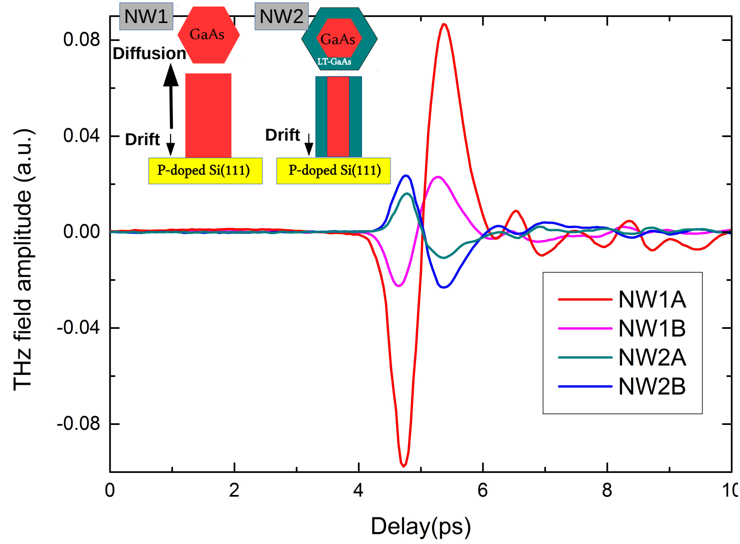


**Figure 5.7:** Time domain waveforms from the nanowires samples 1A,1B (red tones) and 2A,2B (blue tones) overlayed. The inset shows a sketch of the GaAs and GaAS-(LT-GaAs) nanowires as grown on the nanoopenings of the dioxide layer with the p-type Silicon(111) substrate, black arrows mark the corresponding diffusion and drift currents direction generating the THz pulses in the nanowires.

the nanowires must be due to a different charge separation and recombination mechanism within the nanowires. It is likely to be produced by the combined effect of the LT-GaAs shell as well as the nature of the silicon substrate in which the nanowires have been grown, as will be now discussed.

First, the effect of the LT-GaAs shell is addressed. LT-GaAs films have an ultrafast recombination time for the electrons. Since its discovery, there has been different models trying to explain the exact nature of the defects and their trapping mechanism when the material is photoexcited. As explained in chapter 4, section 4.2.3, pump-probe reflectivity experiments performed on LT-GaAs films show unusual features a few picoseconds after the excitation of the probe. Normally, a sharp and large increase in the reflectivity is observed when the pump and probe beams hit the material at the same time. It is

followed by an ultrafast decay of the electron population back to equilibrium that restores the reflectivity to its original value. In LT-GaAs, after the first fast transient and decrease in reflectivity, associated with non-radiative recombination between the photoexcited electrons and the ionized antisites, a dip is generally observed in which the reflectivity is less than in the unexcited materials (negative with respect to reference value). The shape and extend of this dip changes with the annealing and growth time of the material [202]. It has been also shown, in chapter 4, that the pump-probe reflectivity curve obtained with GaAs/(LT-GaAs) nanowires presents a very fast decay time (3 ps) followed by a negative reflectivity which recovers to the reference value in a much longer time (several picoseconds). Some models have been proposed to address this phenomenon [190][189][202][240]. To date, there is not an unified model to fully account for the whole carrier dynamics involved. But it is believed to arise from the different recombination mechanisms followed by electrons and holes in LT-GaAs. The effective cross-section of electron traps is higher than from the hole traps[189]. In [240], all physical mechanisms that change the reflectivity when the electron-hole population is excited as Band-Filling or Band-gap renormalization are compared, and it is concluded that the different recombination lifetimes of electrons and holes in LT-GaAs has to be taken into account to explain this effect. It is proposed that the electron-hole pairs recombine in a two-step process: First, the electrons are trapped in a very short time at the ionized antisites, where they stay until the hole is captured (at a slower rate) by the gallium vacancies or neutral antisites. Second, the electron trapped at the antisite finally decay to the vacancy level to recombine with the hole. The negative dip in reflectivity is ascribed to the excitation of electrons in trapped states up to the conduction band.

In the GaAs/(LT-GaAs) nanowires, there is a large distribution of arsenic antisites at the shell, and the acceptor defects taking part in the electrical compensation of the material are the steps between terraces of the corrugated sidewalls of the nanowire, as shown in chapter 4, section 4.4. It is proposed that when the nanowire is excited by the light, that generates a distribution of electron-hole pairs all along its length, the electrons in the outer LT-GaAs shell will recombine with the antisites and the surface traps in a much shorter time than the electrons in the inner core. This imbalance in electron population between the core and the shell will damp the diffusion of electrons along the nanowires as they will be screened by the transient positive charge sheet distribution arising from the unrecombined holes in the interface. This mechanism has not been proposed before, but LT-GaAs is studied usually from thin-films of micrometric thickness grown on SI-GaAs and as part of photoconductive antenna geometry. Even though it might not be directly comparable to the geometry and dynamic of carriers inside a nanowire, some papers have reported on screening effects created by the different recombination mechanisms [241][242]. In [243], the performance of a LT-GaAs layer as a THz emitter grown on top of n-GaAs is studied with respect to a n-GaAs reference. The different shape of the THz waveform emitted when the LT-GaAs layer is present is related to the trapping

mechanism of electrons and holes by different traps with different time scales that generates a positively charged sheet at the interface between the LT-GaAs layer and the n-GaAs substrate, creating a restoring force for the electronic motion in the n-GaAs material. Furthermore, in [244], the dynamic of the distribution of electrons in a 540 nm thick layer of LT-GaAs grown on top of GaAs and excited by a 800 nm pulse is simulated with respect to time. It is seen that the faster recombination of electrons on the LT-GaAs layer leaves a step-like distribution of electrons at the interface between the LT-GaAs layer and the GaAs material, 1 picosecond after excitation.

Once the possible effect of the LT-GaAs shell on the THz radiation has been proposed, the origin of the observed radiation waveforms in samples 2A,2B is discussed. It has been suggested that the axial diffusion currents in GaAs/(LT-GaAS) nanowires can be disregarded due to the influence of the shell. However, a pulse of THz radiation coming from the nanowires is also detected (figures 5.7). The radiation is now attributed to the electric field existing at the junction between the nanowire (nominally undoped) and the p-doped silicon substrate. The diode-like properties of these kind of heterojunctions have been studied before, even though the lattice strain between silicon and GaAs prevents the formation of high quality interfaces. For example, in [245], a diode ideality factor close to one is observed despite the imperfect interfaces formed with the MBE growth n-GaAs/p-Si heterojunction. Heterojunctions of p-Si and n-GaAs of higher quality have been created recently [246], in which GaAs whisker-like microcrystals are grown on silicon substrates using the same mechanism as self-catalyzed nanowires, thus, taking advantages of the micro-openings between the oxidized surface and the silicon substrate. These heterojunctions have been electrically characterized, showing a well-defined diode behaviour [246]. Therefore,the GaAs and GaAs/LT-GaAs nanowires that grow epitaxially from the oxidized Si(111) surface might as well form heterojunctions with a high-quality interface. Especially because the nanowires can release axial strain very efficiently, as described in chapter 1.

With such a built-in potential at the nanowire-substrate boundary, the injected electron-hole pairs are splitted at the interface between the nanowire and the substrate. This produces a transient drift current of electrons directed from the substrate towards the nanowire, which is opposed in sign to the diffusion current along the axis of the nanowire. In the work of [228], which describes the THz characteristics of undoped self-catalyzed GaAs nanowires , it is observed that the polarity of the THz radiation emitted from the nanowires is reversed in sign when the nanowires have a length shorter than 600 nm. The origin is also ascribed to the drift current of electrons at the interface between the nanowire and the substrate (p-type GaAs(111)). The magnitude of this current is seen to be very low and competes with the diffusion current from the top of the nanowire, thus only becoming important for very short nanowires. Such an effect is not seen in the GaAs nanowires studied in this work (1A,1B). As both nanowires are much longer than 600 nm, the THz radiation is entirely dominated by diffusion currents. However, in the GaAs/(LT-GaAS shell) nanowires

(2A,2B), the diffusion current is suppressed, as explained above, and thus the THz emission originated from the drift current becomes the only contribution to the radiation.

Finally, taking this model for the THz emission from nanowire samples 2A and 2B , it is possible to explain why the emitted power from the sample 2B is larger than from sample 2A. It is related to the difference in density and length, as depicted in table 5.1. Nanowires on sample 2B are three times smaller, less dense, and with a smaller distribution of vertically oriented nanowires. These factors favour the absorption of light close the interface.

## 5.3 Conclusions

This chapter has been devoted to the description of THz emission from nanowires. Especially, THz emission from GaAs nanowires has been characterized. Then, the formation of a low-temperature grown shell to the GaAs and its influence on the emitted radiation has been investigated.

In the first part of the chapter, section 5.1, there was a brief introduction to the field of THz optoelectronic, followed by a description of the main mechanism involved in THz generation from semiconductors surfaces, section 5.1.1. A state-of-the-art in the field of THz emission and detection from semiconductor nanowires is included in section 5.1.2. In section 5.2, the characteristic waveforms of the THz emission from GaAs and (GaAs core/LT-GaAs shell) nanowires detected by a THz-TDS setup has been described. The morphological properties of the nanowires have been reviewed in section 5.2.1: Two GaAs nanowire samples grown at different laboratories, as well as two GaAs/LT-GaAs nanowire samples, also grown at different laboratories. The main morphological differences within each pair of nanowires and their relation with the growth methodology is treated. Although the growth strategy (self-catalyzed nanowires in MBE) is the same for both laboratories, minimal differences in growth parameters can lead to strong variations in the length, density and aspect ratio of the resulting nanowires. In this case, the two kinds of nanowires grown at one laboratory show a larger length (about three times), a slightly larger filling factor and more yield of vertical growth. In section 5.2.2, the impact of these morphological and structural variations on the emitted THz waveform is discussed in a twofold way: First, the difference in length and density between nanowires of the same kind (between the two GaAs nanowire samples and between the two GaAs/LT-GaAs samples) affects the amplitude of the THz waveform, and thus the emitted power. Second, the formation of the low-temperature grown shell to the GaAs nanowire flips the relative polarity of the THz waveform. The possible physical mechanism responsible for this effect is further discussed in the section.

In line with previous research on THz radiation and nanowires, the THz emission from the studied nanowires has been detected and it is found to be very efficient. The emission from the GaAs nanowires grown at EPFL shows the highest yield of power. Although these nanowires are not ordered and therefore the filling factor is not homogeneous, they emit approximately 20 times more efficiently with respect to the reference substrate from equivalent surface areas. For the rest of the nanowires, the emission improvement is around 2-3 times better. These results, taking into account that bulk epitaxial GaAs is not a very efficient THz emitter (for example, in [217], a nanowire efficiency of 40 times is found), draw the potential of nanowires as THz emitters at the nanoscale. Also, it seems that when the nanowire array is too dense, the efficiency of the emission is lowered. This suggests that there might be cooperative effects between different nanowires and light. Such conclusions are also proved in [228], in which it is seen that the power of emitted THz radiation from ordered arrays

of nanowires is not increased when the filling factor increases after a certain threshold. They attribute this effect as resulting from special light resonance modes produced at the nanowires. To further develop this field, it is then necessary to gain more control over the morphology and density of nanowires grown by the different methods as both can affect the interaction between the radiation and the nanowires.

In this chapter, based on the THz-TDS characterization and on previous studies on GaAs and InAs nanowires, it has been suggested that the THz emission from GaAs nanowires arises from a transient diffusive current of electron and holes along the axis of the nanowire, which is an effect similar as the photo-Dember. When the low-temperature grown shell is added, the polarity of the THz waveform is reversed with respect to the GaAs nanowires. It is proposed to arise from the defective nature of the shell, which drastically reduces the lifetime of electrons with respect to the one in the core of the nanowire. This might create a depleted shell in the picosecond timescale, which dampers electronic diffusion along the core. The charge separation at the base of the nanowire is not affected by the shell, a drift current produces an emitted radiation with reversed polarity in comparison with the one in the GaAs nanowires .

To conclude, further modeling and research is necessary to support these results, such as Optical Pump-THz probe experiments, described in chapter 2, which probes directly the mobility and scattering rate of carriers and could help to create a more complete picture of the effect of the defective shells in the THz emission characteristic from nanowires.

# Conclusions

The main purpose of this work is to better understand the relation between the structure of a nanowire and the resulting electronic state of its surface. For this goal, first, it has been necessary to review and understand the main concepts involved in the growth of semiconductor nanowires with the VLS growth mechanism. It is possible to understand the VLS growth mechanism, despite the nanometric section of nanowires, by using classical nucleation theory. In the VLS mechanism, growth is driven by a metallic liquid droplet that incorporates vapor species to it, precluding the nucleation of the different atomic species that grow in a layer-by-layer fashion constrained to the dimensions of the droplet. The role of supersaturation in the liquid droplet, accounting for the crystal phase in the nanowire, has been reviewed in the frame of Glas model. Furthermore, the growth rate is frequently modeled by a balance of material fluxes at the metallic droplet of the nanowire, and depending on the nature of the droplet, different limiting fluxes govern the rate: as surface diffusion of group III atoms for the growth of Au-catalyzed nanowires, or group V vapor flux incorporation for the growth of self-catalyzed nanowires. Finally, a new growth regime is studied. In this regime, the different material fluxes interact during growth in such a way that the liquid droplet size is self-regulated to a given critical value, independent on the initial size of the catalyst droplet. Second, the use of Scanning Tunneling Microscopy (STM) allows for a very complete characterization of the nanowire surfaces. To prove this assertion, the working mechanism of the STM has been reviewed, in chapter 2, with a special focus on the physical effects produced when the polarized metallic tips of STM interact with the semiconductor compounds, locally altering their band structures. This effect, called tip induced band bending (TIBB), can have a strong influence on the measurement of physical features on the surface of nanowires and simulations are required to correctly interpret spectroscopic data.

In chapter 3, the preparation of nanowire surfaces for their study with STM has been treated. It has been shown that, for III-V semiconductor nanowires, there are two main cleaning methods: atomic hydrogen cleaning and the As capping layer method. In the latter, the nanowire is protected after growth with an arsenic amorphous capping layer. This layer is further desorbed in UHV inside the STM system. Then, scanning the surface with STM makes possible to recover a structural nanowire surface which yields valuable information about the crystal phase present in the nanowire. However, it has been shown that

decapping the protective As layer, which implies annealing at a temperature between $200-400°C$, can as well modify the morphology of the nanowire facets. The resulting morphology after decapping consists, respectively, of a distribution of monoatomic island for self-catalyzed GaAs nanowires or vacancy island for self-catalyzed InAs nanowires. In the GaAs nanowire, this morphology appears as a consequence of the relation between the electronic structure of the nanowire and the most probable point defect formation in the As-rich environment present in the surface when the As-layer is decapped. These defects are surface arsenic antisites, that replace Ga atoms ejected from their surface lattice sites. Ga atoms diffuse and start to nucleate islands when pinned at the edges of the nanowires. As to InAs nanowires, the regime of congruent evaporation is achieved during the As decapping, and as such, In and As atoms are evaporated equally from the surface, creating holes all around the sidewalls. Ultimately, this leads to the important conclusion that the morphology of the nanowire surfaces could be, under certain circumstances, anticipated and controlled with the preparation method. To fully develop this claim, possible future experiments are proposed in the concluding section of the chapter.

In chapter 4, surfaces of self-catalyzed GaAs nanowires are functionalized by adding a shell in latter stages of growth. To this end, a low-temperature grown GaAs shell has been grown. This serves to prove that, even though low-temperature grown GaAs nanowires can not be grown with the VLS growth mechanism, they can be added as a shell. With STM and other characterization techniques such as optical pump-probe spectroscopy, it is confirmed that this shell indeed shows the same properties of low-temperature grown GaAs. That is; a very large distribution of subsurface arsenic antisites, partially ionized (yet with a good crystallinity), a very short lifetime of photoexcited carriers and the creation of arsenic aggregates at the top of the nanowire, when these are mildly annealed. Interestingly, the low-temperature used to grow the shell produces rough faceted surfaces stacked as a series of pyramidal mounds which ultimately contribute, thanks to the nanometric dimensions of the shell, to the electrical compensation of the ionized arsenic antisites.

Finally, in chapter 5, the emission properties in the THz range of low-temperature grown GaAs nanowires as well as self-catalyzed GaAs nanowires has been studied, as this material is very used in THz optoelectronic devices. The emitted THz waveform in the time domain shows that all the nanowire substrates can emit radiation in the THz range after excitation with fs-laser pulses. It is confirmed that the emitted power from the nanowires, in terms of emitted power per surface area, is superior with respect to equivalent bulk semiconductor THz emitters. Furthermore, it has been observed that the amplitude of the THz radiation from the GaAs nanowires is higher with respect to the low-temperature GaAs nanowires. The reason is twofold: first, the GaAs nanowires exhibited a very optimized geometry in terms of filling-factor and length, that leads to a more efficient outcoupling of the THz radiation, if we assume that the physical origin of the THz emission is related to the onset of plasmon modes. Second, when using nanowires with the LT-GaAs shell, despite

of its very short carrier lifetime, and precisely because of the large concentration of carrier traps, reduces the coupling of plasmons between the light and the nanowire. However, the physical process whereby the plasmon is damped is not completely understood, and further simulations and experiments need to be realized.

As a concluding remark, this thesis is framed within a FP7 European Framework project called Nanoembrace [247], developed between 2013-2016. In this project, one of the main goals was to improved the interaction between the different areas of the large field of nanowires, to better understand growth and developed new models, to improve the characterization techniques and produce new ideas for effective integration of nanowire as devices. This work has moved along these various dimensions of the field, from the successful creation of a new growth scheme for functionalizing nanowire surfaces, such as low-temperature grown shells, to the development in understanding novel growth regimes as the self-stabilization of the nanowire diameter. Furthermore, using the STM as a powerful surface characterization tool, to get insight into the main physical processes that governs the properties of the nanowire surfaces, it has been possible to investigate how the morphology of the surfaces can be controlled, which can lead ultimately to the better integration of nanowires into devices.

# Bibliography


[1] R. S. Wagner and W. C. Ellis, “Vapor-liquid-solid mechanism of single crystal growth”, *Appl. Phys. Lett.*, vol. 4, no. 5, pp. 89–90, 1964.

[2] B. X. Duan and C. M. Lieber, “General synthesis of compound semiconductor nanowires”, *Advanced Materials*, no. 4, pp. 298–302, 2000.

[3] F. Glas, “Critical dimensions for the plastic relaxation of strained axial heterostructures in free-standing nanowires”, *Phys. Rev. B*, vol. 74, no. 12, pp. 2–5, 2006.

[4] P. Caroff, J. B. Wagner, K. A. Dick, H. A. Nilsson, M. Jeppsson, K. Deppert, L. Samuelson, L. R. Wallenberg, and L. E. Wernersson, “High-quality InAs/InSb nanowire heterostructures grown by metal-organic vapor-phase epitaxy”, *Small*, vol. 4, no. 7, pp. 878–882, 2008.

[5] K. Hiruma, M. Yazawa, T. Katsuyama, K. Ogawa, K. Haraguchi, M. Koguchi, and H. Kakibayashi, “Growth and optical properties of nanometer-scale GaAs and InAs whiskers”, *J. Appl. Phys.*, vol. 77, no. 2, pp. 447–462, 1995.

[6] B. W. Jacobs, V. M. Ayres, M. a. Crimp, and K. McElroy, “Internal structure of multiphase zinc-blende wurtzite gallium nitride nanowires.”, *Nanotechnology*, vol. 19, no. 40, p. 405706, 2008.

[7] C. Thelander, P. Caroff, S. Plissard, A. W. Dey, and K. A. Dick, “Effects of crystal phase mixing on the electrical properties of InAs nanowires”, *Nano Lett.*, vol. 11, no. 6, pp. 2424–2429, 2011.

[8] M. Heiss, S. Conesa-Boj, J. Ren, H. H. Tseng, A. Gali, A. Rudolph, E. Uccelli, F. Peiró, J. R. Morante, D. Schuh, E. Reiger, E. Kaxiras, J. Arbiol, and A. Fontcuberta i Morral, “Direct correlation of crystal structure and optical properties in wurtzite/zinc-blende GaAs nanowire heterostructures”, *Phys. Rev. B*, vol. 83, pp. 1–11, nov 2011.

[9] Y. Cui, X. Duan, J. Hu, and C. M. Lieber, “Doping and Electrical Transport in Silicon Nanowires”, *J. Phys. Chem. B*, vol. 104, no. 22, pp. 5213–5216, 2000.

[10] D. Wang, Q. Wang, A. Javey, R. Tu, H. Dai, H. Kim, P. C. McIntyre, T. Krishnamohan, and K. C. Saraswat, “Germanium nanowire field-effect transistors with SiO2 and high-$\kappa$ HfO2 gate dielectrics”, *Appl. Phys. Lett.*, vol. 83, no. 12, pp. 2432–2434, 2003.

[11] S. A. Dayeh, D. P. R. Aplin, X. Zhou, P. K. L. Yu, E. T. Yu, and D. Wang, “High electron mobility InAs nanowire field-effect transistors”, *Small*, vol. 3, no. 2, pp. 326–332, 2007.

[12] S. A. Dayeh, E. T. Yu, and D. Wang, “III-V nanowire growth mechanism: V/III ratio and temperature effects”, *Nano Lett.*, vol. 7, no. 8, pp. 2486–2490, 2007.

[13] M. Law, “Nanoribbon Waveguides for Subwavelength Photonics Integration”, *Science*, vol. 305, no. 5688, pp. 1269–1273, 2004.

[14] D. V. Seletskiy, M. P. Hasselbeck, J. G. Cederberg, A. Katzenmeyer, M. E. Toimil-Molares, F. Léonard, A. A. Talin, and M. Sheik-Bahae, “Efficient terahertz emission from InAs nanowires”, *Phys. Rev. B*, vol. 84, pp. 1–7, 2011.

[15] X. Duan, Y. Huang, R. Agarwal, C. M. C. Lieber, and C. G. Fast, “Single-nanowire electrically driven lasers”, *Nature*, vol. 421, no. 6920, pp. 241–245, 2003.

[16] F. Qian, Y. Li, S. Gradecak, H.-G. Park, Y. Dong, Y. Ding, Z. L. Wang, and C. M. Lieber, “Multi-quantum-well nanowire heterostructures for wavelength-controlled lasers.”, *Nat. Mater.*, vol. 7, no. 9, pp. 701–706, 2008.

[17] Y. Huang, X. Duan, and C. M. Lieber, “Nanowires for integrated multicolor nanophotonics”, *Small*, vol. 1, no. 1, pp. 142–147, 2005.

[18] Y. Cui, Q. Wei, H. Park, and C. M. Lieber, “Nanowire Nanosensors for Highly Sensitive and Selective Detection of Biological and Chemical Species”, *Science*, vol. 293, no. 5533, pp. 1289–1292, 2001.

[19] A. Kolmakov, Y. Zhang, G. Cheng, and M. Moskovits, “Detection of CO and O2 using tin oxide nanowire sensors”, *Adv. Mater.*, vol. 15, no. 12, pp. 997–1000, 2003.

[20] B. M. Kayes, H. A. Atwater, and N. S. Lewis, “Comparison of the device physics principles of planar and radial p-n junction nanorod solar cells”, *J. Appl. Phys.*, vol. 97, no. 11, pp. 1–11, 2005.

[21] B. Tian, X. Zheng, T. J. Kempa, Y. Fang, N. Yu, G. Yu, J. Huang, and C. M. Lieber, “Coaxial silicon nanowires as solar cells and nanoelectronic power sources”, *Nature*, vol. 449, no. October, pp. 885–889, 2007.

[22] L. Cao, J. S. White, J.-S. Park, J. A. Schuller, B. M. Clemens, and M. L. Brongersma, “Engineering light absorption in semiconductor nanowire devices”, *Nat. Mater.*, vol. 8, no. 8, pp. 643–647, 2009.

[23] P. Krogstrup, H. I. Jørgensen, M. Heiss, O. Demichel, J. V. Holm, M. Aagesen, J. Nygard, and A. Fontcuberta i Morral, “Single-nanowire solar cells beyond the Shockley–Queisser limit”, *Nat. Photonics*, vol. 7, no. March, pp. 1–5, 2013.

[24] J. Moon, J. H. Kim, Z. C. Y. Chen, J. Xiang, and R. Chen, “Gate-modulated thermoelectric power factor of hole gas in Ge-Si core-shell nanowires”, *Nano Lett.*, vol. 13, no. 3, pp. 1196–1202, 2013.

[25] C. K. Chan, H. L. Peng, G. Liu, K. McIlwrath, X. F. Zhang, R. A. Huggins, and Y. Cui, “High-performance lithium battery anodes using silicon nanowires”, *Nat. Nanotechnol.*, vol. 3, no. 1, pp. 31–35, 2008.

[26] X. L. Feng, R. He, P. Yang, and M. L. Roukes, “Very high frequency silicon nanowire electromechanical resonators”, *Nano Lett.*, vol. 7, no. 7, pp. 1953–1959, 2007.

[27] J. Zhou, Y. Gu, P. Fei, W. Mai, Y. Gao, R. Yang, G. Bao, and Z. L. Wang, “Flexible piezotronic strain sensor”, *Nano Lett.*, vol. 8, no. 9, pp. 3035–3040, 2008.

[28] B. P. Timko, T. Cohen-Karni, Q. Qing, B. Tian, and C. M. Lieber, “Design and implementation of functional nanoelectronic interfaces with biomolecules, cells, and tissue using nanowire device arrays”, *IEEE Trans. Nanotechnol.*, vol. 9, no. 3, pp. 269–280, 2010.

[29] V. Mourik, K. Zuo, S. M. Frolov, S. R. Plissard, E. P. a. M. Bakkers, and L. P. Kouwenhoven, “Signatures of Majorana Fermions in Hybrid Superconductor-Semiconductor Nanowire Devices”, *Science*, vol. 336, no. 6084, pp. 1003–1007, 2012.

[30] J. Claudon, J. Bleuse, N. S. Malik, M. Bazin, P. Jaffrennou, N. Gregersen, C. Sauvan, P. Lalanne, and J.-M. Gérard, “A highly efficient single-photon source based on a quantum dot in a photonic nanowire”, *Nat. Photonics*, vol. 4, no. March, pp. 174–177, 2010.

[31] X. Duan and C. M. Lieber, “Laser-Assisted Catalytic Growth of Single Crystal GaN Nanowires”, *JACS*, vol. 122, pp. 188–189, 2000.

[32] P. Yang, H. Yan, S. Mao, R. Russo, J. Johnson, R. Saykally, N. Morris, J. Pham, R. He, and H. J. Choi, “Controlled growth of ZnO nanowires and their optical properties”, *Adv. Funct. Mater.*, vol. 12, no. 5, pp. 323–331, 2002.

[33] E. Givargizov, “Fundamental aspects of VLS growth”, *J. Cryst. Growth*, vol. 31, pp. 20–30, 1975.

[34] K. A. Dick, K. Deppert, T. Mårtensson, B. Mandl, L. Samuelson, and W. Seifert, "Failure of the vapor-liquid-solid mechanism in au-assisted MOVPE growth of InAs nanowires", *Nano Lett.*, vol. 5, no. 4, pp. 761–764, 2005.

[35] F. Wang, A. Dong, J. Sun, R. Tang, H. Yu, and W. E. Buhro, "Solution Liquid Solid Growth of Semiconductor Nanowires", *Inorg. Chem.*, vol. 45, no. 6, pp. 7511–7521, 2006.

[36] J. Johansson, C. P. T. Svensson, T. Mårtensson, L. Samuelson, and W. Seifert, "Mass transport model for semiconductor nanowire growth.", *J. Phys. Chem. B*, vol. 109, no. 28, pp. 13567–13571, 2005.

[37] F. Glas, J. C. Harmand, and G. Patriarche, "Why does wurtzite form in nanowires of III-V zinc blende semiconductors?", *Phys. Rev. Lett.*, vol. 99, no. 14, pp. 3–6, 2007.

[38] V. G. Dubrovskii, N. V. Sibirev, J. C. Harmand, and F. Glas, "Growth kinetics and crystal structure of semiconductor nanowires", *Phys. Rev. B*, vol. 78, no. 23, pp. 1–10, 2008.

[39] F. Glas, M. R. Ramdani, G. Patriarche, and J. C. Harmand, "Predictive modeling of self-catalyzed III-V nanowire growth", *Phys. Rev. B*, vol. 88, no. 19, pp. 1–14, 2013.

[40] P. Krogstrup, H. I. Jørgensen, E. Johnson, M. H. Madsen, C. B. Sørensen, A. Fontcuberta i Morral, M. Aagesen, J. Nygård, and F. Glas, "Advances in the theory of III–V nanowire growth dynamics", *J. Phys. D. Appl. Phys.*, vol. 46, p. 313001, aug 2013.

[41] M.B.Parnish, "Molecular Beam Epitaxy", *Science*, vol. 208, no. May, pp. 916–922, 1980.

[42] V. G. Dubrovskii, N. V. Sibirev, G. E. Cirlin, I. P. Soshnikov, W. H. Chen, R. Larde, E. Cadel, P. Pareige, T. Xu, B. Grandidier, J.-P. Nys, D. Stievenard, M. Moewe, L. C. Chuang, and C. Chang-Hasnain, "Gibbs-Thomson and diffusion-induced contributions to the growth rate of Si, InP, and GaAs nanowires", *Phys. Rev. B*, vol. 79, no. 20, p. 205316, 2009.

[43] A. G. Thompson, "MOCVD technology for semiconductors", *Mater. Lett.*, vol. 30, no. 4, pp. 255–263, 1997.

[44] S. Hofmann, R. Sharma, C. T. Wirth, F. Cervantes-Sodi, C. Ducati, T. Kasama, R. E. Dunin-Borkowski, J. Drucker, P. Bennett, and J. Robertson, "Ledge-flow-controlled catalyst interface dynamics during Si nanowire growth.", *Nat. Mater.*, vol. 7, no. 5, pp. 372–375, 2008.

[45] B. A. Wacaser, K. A. Dick, J. Johansson, M. T. Borgström, K. Deppert, and L. Samuelson, "Preferential interface nucleation: An expansion of the VLS growth mechanism for nanowires", *Adv. Mater.*, vol. 21, no. 2, pp. 153–165, 2009.

[46] K. A. Dick, P. Caroff, J. Bolinsson, M. E. Messing, J. Johansson, K. Deppert, L. R. Wallenberg, and L. Samuelson, “Control of III–V nanowire crystal structure by growth parameter tuning”, *Semicond. Sci. Technol.*, vol. 25, no. 2, p. 024009, 2010.

[47] J. Johansson, L. S. Karlsson, C. P. T. Svensson, T. Mårtensson, B. a. Wacaser, K. Deppert, L. Samuelson, and W. Seifert, “Structural properties of <111>B -oriented III-V nanowires.”, *Nat. Mater.*, vol. 5, no. 7, pp. 574–580, 2006.

[48] R. E. Algra, M. a. Verheijen, M. T. Borgström, L.-F. Feiner, G. Immink, W. J. P. van Enckevort, E. Vlieg, and E. P. A. M. Bakkers, “Twinning superlattices in indium phosphide nanowires.”, *Nature*, vol. 456, no. 7220, pp. 369–372, 2008.

[49] P. Caroff, K. A Dick, J. Johansson, M. E. Messing, K. Deppert, and L. Samuelson, “Controlled polytypic and twin-plane superlattices in III-V nanowires”, *Nat. Nanotechnol.*, vol. 4, no. 1, pp. 50–55, 2009.

[50] M. Tchernycheva, J. C. Harmand, G. Patriarche, L. Travers, and G. E. Cirlin, “Temperature conditions for GaAs nanowire formation by Au-assisted molecular beam epitaxy”, *Nanotechnology*, vol. 17, no. 16, p. 4025, 2006.

[51] N. V. Sibirev, M. a. Timofeeva, a. D. Bol’shakov, M. V. Nazarenko, and V. G. Dubrovskiĭ, “Surface energy and crystal structure of nanowhiskers of III–V semiconductor compounds”, *Phys. Solid State*, vol. 52, no. 7, pp. 1531–1538, 2010.

[52] J. Wallentin, M. Ek, L. R. Wallenberg, L. Samuelson, K. Deppert, and M. T. Borgström, “Changes in contact angle of seed particle correlated with increased zincblende formation in doped InP nanowires”, *Nano Lett.*, vol. 10, no. 12, pp. 4807–4812, 2010.

[53] P. Krogstrup, S. Curiotto, E. Johnson, M. Aagesen, J. Nygård, and D. Chatain, “Impact of the liquid phase shape on the structure of III-V nanowires”, *Phys. Rev. Lett.*, vol. 106, no. 12, pp. 1–4, 2011.

[54] P. Krogstrup, R. Popovitz-Biro, E. Johnson, M. H. Madsen, J. Nygård, and H. Shtrikman, “Structural phase control in self-catalyzed growth of GaAs nanowires on silicon (111)”, *Nano Lett.*, vol. 10, no. 11, pp. 4475–4482, 2010.

[55] X. Yu, H. Wang, J. Lu, J. Zhao, J. Misuraca, P. Xiong, and S. Von Molnár, “Evidence for structural phase transitions induced by the triple phase line shift in self-catalyzed GaAs nanowires”, *Nano Lett.*, vol. 12, no. 10, pp. 5436–5442, 2012.

[56] G. E. Cirlin, V. G. Dubrovskii, Y. B. Samsonenko, a. D. Bouravleuv, K. Durose, Y. Y. Proskuryakov, B. Mendes, L. Bowen, M. a. Kaliteevski, R. a. Abram, and D. Zeze, “Self-catalyzed, pure zincblende GaAs

nanowires grown on Si(111) by molecular beam epitaxy", *Phys. Rev. B*, vol. 82, no. 3, p. 035302, 2010.

[57] L. Schubert, P. Werner, N. D. Zakharov, G. Gerth, F. M. Kolb, L. Long, U. Gösele, and T. Y. Tan, "Silicon nanowhiskers grown on (111)-Si substrates by molecular-beam epitaxy", *Appl. Phys. Lett.*, vol. 84, no. 24, pp. 4968–4970, 2004.

[58] T. Xu, J. P. Nys, A. Addad, O. I. Lebedev, A. Urbieta, B. Salhi, M. Berthe, B. Grandidier, and D. Stievenard, "Faceted sidewalls of silicon nanowires: Au-induced structural reconstructions and electronic properties", *Phys. Rev. B*, vol. 81, no. 11, 2010.

[59] V. G. Dubrovskii and N. V. Sibirev, "Growth rate of a crystal facet of arbitrary size and growth kinetics of vertical nanowires", *Phys. Rev. E - Stat. Nonlinear, Soft Matter Phys.*, vol. 70, no. 3 1, pp. 1–7, 2004.

[60] V. G. Dubrovskii, G. E. Cirlin, I. P. Soshnikov, a. a. Tonkikh, N. V. Sibirev, Y. B. Samsonenko, and V. M. Ustinov, "Diffusion-induced growth of GaAs nanowhiskers during molecular beam epitaxy: Theory and experiment", *Phys. Rev. B*, vol. 71, no. 20, pp. 5–7, 2005.

[61] M. I. den Hertog, J.-l. Rouviere, F. Dhalluin, P. J. Desré, P. Gentile, P. Ferret, F. Oehler, and T. Baron, "Control of gold surface diffusion on si nanowires.", *Nano Lett.*, vol. 8, no. 5, pp. 1544–1550, 2008.

[62] T. Xu, K. A. Dick, S. Plissard, T. H. Nguyen, Y. Makoudi, M. Berthe, J.-P. Nys, X. Wallart, B. Grandidier, and P. Caroff, "Faceting, composition and crystal phase evolution in III-V antimonide nanowire heterostructures revealed by combining microscopy techniques.", *Nanotechnology*, vol. 23, p. 095702, mar 2012.

[63] A. Fontcuberta i Morral, C. Colombo, G. Abstreiter, J. Arbiol, and J. R. Morante, "Nucleation mechanism of gallium-assisted molecular beam epitaxy growth of gallium arsenide nanowires", *Appl. Phys. Lett.*, vol. 92, no. 6, pp. 2008–2010, 2008.

[64] S. Plissard, K. A. Dick, G. Larrieu, S. Godey, A. Addad, X. Wallart, and P. Caroff, "Gold-free growth of GaAs nanowires on silicon: arrays and polytypism", *Nanotechnology*, vol. 21, no. 38, p. 385602, 2010.

[65] S. Plissard, G. Larrieu, X. Wallart, and P. Caroff, "High yield of self-catalyzed GaAs nanowire arrays grown on silicon via gallium droplet positioning", *Nanotechnology*, vol. 22, no. 27, p. 275602, 2011.

[66] Y. J. Kuang, S. Sukrittanon, H. Li, and C. W. Tu, "Growth and photoluminescence of self-catalyzed GaP/GaNP core/shell nanowires on Si(111) by gas source molecular beam epitaxy", *Appl. Phys. Lett.*, vol. 100, no. 5, pp. 2013–2016, 2012.

[67] G. Priante, G. Patriarche, F. Oehler, F. Glas, and J.-C. Harmand, "Abrupt GaP/GaAs Interfaces in Self-Catalyzed Nanowires", *Nano Lett.*, vol. 15, no. 9, pp. 6036–6041, 2015.

[68] A. Biermanns, E. Dimakis, A. Davydok, T. Sasaki, L. Geelhaar, M. Takahasi, and U. Pietsch, "Role of liquid indium in the structural purity of wurtzite InAs nanowires that grow on Si(111)", *Nano Lett.*, vol. 14, no. 12, pp. 6878–6883, 2014.

[69] L. Gao, R. L. Woo, B. Liang, M. Pozuelo, S. Prikhodko, M. Jackson, N. Goel, M. K. Hudait, D. L. Huffaker, M. S. Goorsky, S. Kodambaka, and R. F. Hicks, "Self-Catalyzed Epitaxial Growth of Vertical Indium Phosphide Nanowires on Silicon", *Nano Lett.*, vol. 9, no. 6, pp. 2223–2228, 2009.

[70] F. Matteini, G. Tütüncüoglu, H. Potts, F. Jabeen, and A. Fontcuberta i Morral, "Wetting of Ga on SiOx and Its Impact on GaAs Nanowire Growth", *Cryst. Growth Des.*, vol. 15, no. 7, pp. 3105–3109, 2015.

[71] F. Matteini, V. G. Dubrovskii, D. Rüffer, G. Tütüncüoğlu, Y. Fontana, and A. Fontcuberta i Morral, "Tailoring the diameter and density of self-catalyzed GaAs nanowires on silicon", *Nanotechnology*, vol. 26, no. 10, p. 105603, 2015.

[72] M. R. Ramdani, J. C. Harmand, F. Glas, G. Patriarche, and L. Travers, "Arsenic pathways in self-catalyzed growth of GaAs nanowires", *Cryst. Growth Des.*, vol. 13, no. 1, pp. 91–96, 2013.

[73] S. Lehmann, D. Jacobsson, and K. A. Dick, "Crystal phase control in GaAs nanowires: opposing trends in the Ga- and As-limited growth regimes", *Nanotechnology*, vol. 26, no. 30, p. 301001, 2015.

[74] V. G. Dubrovskii, T. Xu, A. Díaz Álvarez, S. R. Plissard, P. Caroff, F. Glas, and B. Grandidier, "Self-Equilibration of the Diameter of Ga-Catalyzed GaAs Nanowires", *Nano Lett.*, vol. 15, no. 8, pp. 5580–5584, 2015.

[75] J. Tersoff, "Stable Self-Catalyzed Growth of III-V Nanowires", *Nano Lett.*, vol. 15, no. 10, pp. 6609–6613, 2015.

[76] C. Y. Wen, J. Tersoff, K. Hillerich, M. C. Reuter, J. H. Park, S. Kodambaka, E. A. Stach, and F. M. Ross, "Periodically changing morphology of the growth interface in Si, Ge, and GaP nanowires", *Phys. Rev. Lett.*, vol. 107, no. 2, pp. 1–4, 2011.

[77] K. W. Schwarz and J. Tersoff, "From droplets to nanowires: Dynamics of vapor-liquid-solid growth", *Phys. Rev. Lett.*, vol. 102, no. 20, pp. 1–4, 2009.

[78] K. W. Schwarz and J. Tersoff, “Elementary processes in nanowire growth”, *Nano Lett.*, vol. 11, no. 2, pp. 316–320, 2011.

[79] F. Glas, “Statistics of sub-Poissonian nucleation in a nanophase”, *Phys. Rev. B*, vol. 90, no. 12, pp. 1–15, 2014.

[80] G. Priante, J. C. Harmand, G. Patriarche, and F. Glas, “Random stacking sequences in III-V nanowires are correlated”, *Phys. Rev. B*, vol. 89, no. 24, pp. 1–4, 2014.

[81] D. J. Griffiths, *Introduction to Quantum Mechanics.* Cambridge University Press, 2004.

[82] C. J. Chen, *Introduction to Scanning Tunneling Microscopy.* Oxford Science Publications, 2007.

[83] B. Voigtländer, *Scanning Probe Microscopy.* Springer, 2015.

[84] S. Vieira, “The behavior and calibration of some piezoelectric ceramics used in the STM”, *IBM J. Res. Dev.*, vol. 30, no. 5, pp. 553–556, 1986.

[85] R. M. Feenstra, J. A. Stroscio, J. Tersoff, and A. P. Fein, “Atom-selective imaging of the GaAs(110) surface”, *Phys. Rev. Lett.*, vol. 58, no. 12, pp. 1192–1195, 1987.

[86] J. Tersoff and D. R. Hamann, “Theory of the scanning tunneling microscope”, *Phys. Rev. B*, vol. 31, no. 2, pp. 805–813, 1985.

[87] G. Binnig, H. Rohrer, C. Gerber, and E. Weibel, “Tunneling through a controllable vacuum gap”, *Appl. Phys. Lett.*, vol. 40, no. 2, pp. 178–180, 1982.

[88] H. Neddermeyer, “Scanning tunnelling microscopy of semiconductor surfaces”, *Reports Prog. Phys.*, vol. 59, no. 6, pp. 701–769, 1996.

[89] P. Ebert, “Nano-scale properties of defects in compound semiconductor surfaces”, *Surf. Sci. Rep.*, vol. 33, no. 4, pp. 121–303, 1999.

[90] J. Li, W.-D. Schneider, and R. Berndt, “Local density of states from spectroscopic scanning-tunneling-microscope images: Ag(111)”, *Phys. Rev. B*, vol. 56, no. 12, pp. 7656–7659, 1997.

[91] J. Repp, G. Meyer, S. M. Stojković, A. Gourdon, and C. Joachim, “Molecules on insulating films: Scanning-tunneling microscopy imaging of individual molecular orbitals”, *Phys. Rev. Lett.*, vol. 94, no. 2, pp. 1–4, 2005.

[92] R. M. Feenstra, “Tunneling spectroscopy of the (110)surface of direct-gap III-V semiconductors”, *Phys. Rev. B*, vol. 50, no. 7, pp. 4561–4570, 1994.

[93] R. Feenstra, "Electrostatic Potential for a Hyperbolic Probe Tip near a Semiconductor", *J.Vac.Sci.Technol.B 21, 2080 (2003).*, vol. 2080, pp. 1–17, 2003.

[94] N. Ishida, K. Sueoka, and R. M. Feenstra, "Influence of surface states on tunneling spectra of n-type GaAs(110) surfaces", *Phys. Rev. B*, vol. 80, no. 7, p. 075320, 2009.

[95] R. M. Feenstra, S. Gaan, G. Meyer, and K. H. Rieder, "Low-temperature tunneling spectroscopy of Ge(111)c(2x8) surfaces", *Phys. Rev. B*, vol. 71, no. 12, pp. 1–16, 2005.

[96] S. Gaan, R. Feenstra, and P. Ebert, "Structure and electronic spectroscopy of steps on GaAs (110) surfaces", *Surf. Sci.*, vol. 28, pp. 1–14, 2012.

[97] N. Jäger, P. Ebert, K. Urban, R. Krause-Rehberg, and E. Weber, "Scanning tunneling microscopy and spectroscopy of semi-insulating GaAs", *Phys. Rev. B*, vol. 65, no. 19, pp. 1–8, 2002.

[98] R. M. Feenstra, Y. Dong, M. P. Semtsiv, and W. T. Masselink, "Influence of tip-induced band bending on tunnelling spectra of semiconductor surfaces", *Nanotechnology*, vol. 18, p. 044015, 2006.

[99] Y. Dong, R. M. Feenstra, M. P. Semtsiv, and W. T. Masselink, "Band offsets of InGaPGaAs heterojunctions by scanning tunneling spectroscopy", *J. Appl. Phys.*, vol. 103, no. 7, 2008.

[100] S. Gaan, G. He, R. M. Feenstra, J. Walker, and E. Towe, "Size, shape, composition, and electronic properties of InAs/GaAs quantum dots by scanning tunneling microscopy and spectroscopy", *J. Appl. Phys.*, vol. 108, no. 11, 2010.

[101] http://www.scientaomicron.com/en/products/low-temperature-spm/instrument-concept.

[102] A. Díaz Álvarez, T. Zhu, J. Nys, M. Berthe, M. Empis, J. Schreiber, B. Grandidier, and T. Xu, "Scanning tunnelling spectroscopy and raman spectroscopy of monolayer silicene on ag(111)", *Surface Science*, vol. 653, pp. 92 – 96, 2016.

[103] Y. Makoudi, B. Baris, J. Jeannoutot, F. Palmino, B. Grandidier, and F. Cherioux, "Tailored molecular design for supramolecular network engineering on a silicon surface", *ChemPhysChem*, vol. 14, no. 5, pp. 900–904, 2013.

[104] I. Ekvall, E. Wahlström, D. Claesson, H. Olin, and E. Olsson, "Preparation and characterization of electrochemically etched w tips for stm", *Measurement Science and Technology*, vol. 10, no. 1, p. 11, 1999.

[105] R. Ulbricht, E. Hendry, J. Shan, T. F. Heinz, and M. Bonn, "Carrier dynamics in semiconductors studied with time-resolved terahertz spectroscopy", *Rev. Mod. Phys.*, vol. 83, no. 2, pp. 543–586, 2011.

[106] R. P. Prasankumar, P. C. Upadhya, Q. Li, N. Smith, S. G. Choi, a. K. Azad, D. Talbayev, G. T. Wang, a. J. Fischer, J. Hollingsworth, S. a. Trugman, S. T. Picraux, and a. J. Taylor, "Ultrafast carrier dynamics in semiconductor nanowires", *Proc. SPIE*, vol. 7406, no. 9, pp. 74060E–74060E–10, 2009.

[107] J. B. Baxter and G. W. Guglietta, "Terahertz Spectroscopy", *Anal. Chem.*, vol. 83, no. 12, p. 110502124324022, 2011.

[108] H. J. Joyce, P. Parkinson, N. Jiang, C. J. Docherty, Q. Gao, H. H. Tan, C. Jagadish, L. M. Herz, and M. B. Johnston, "Electron mobilities approaching bulk limits in "surface-free" GaAs nanowires", *Nano Lett.*, vol. 14, no. 10, pp. 5989–5994, 2014.

[109] P. Parkinson, J. Lloyd-Hughes, Q. Gao, H. H. Tan, C. Jagadish, M. B. Johnston, and L. M. Herz, "Transient terahertz conductivity of GaAs nanowires", *Nano Lett.*, vol. 7, no. 7, pp. 2162–2165, 2007.

[110] P. Parkinson, C. Dodson, H. J. Joyce, K. A. Bertness, N. A. Sanford, L. M. Herz, and M. B. Johnston, "Noncontact measurement of charge carrier lifetime and mobility in GaN nanowires", *Nano Lett.*, vol. 12, no. 9, pp. 4600–4604, 2012.

[111] H. J. Joyce, C. J. Docherty, Q. Gao, H. H. Tan, C. Jagadish, J. Lloyd-Hughes, L. M. Herz, and M. B. Johnston, "Electronic properties of GaAs, InAs and InP nanowires studied by terahertz spectroscopy.", *Nanotechnology*, vol. 24, no. 21, p. 214006, 2013.

[112] J. L. Boland, A. Casadei, G. Tütüncüoglu, F. Matteini, C. L. Davies, F. Jabeen, H. J. Joyce, L. M. Herz, A. Fontcuberta i Morral, and M. B. Johnston, "Increased Photoconductivity Lifetime in GaAs Nanowires by Controlled n-Type and p-Type Doping", *ACS Nano*, vol. 10, no. 4, pp. 4219–4227, 2016.

[113] M. Johnston, D. Whittaker, a. Corchia, a. Davies, and E. Linfield, "Simulation of terahertz generation at semiconductor surfaces", *Phys. Rev. B*, vol. 65, no. 16, pp. 1–8, 2002.

[114] V. L. Malevich, R. Adomavicius, and A. Krotkus, "THz emission from semiconductor surfaces", *Comptes Rendus Phys.*, vol. 9, no. 2, pp. 130–141, 2008.

[115] A. Reklaitis, "Terahertz emission from InAs induced by photo-Dember effect: Hydrodynamic analysis and Monte Carlo simulations", *J. Appl. Phys.*, vol. 108, no. 5, 2010.

[116] M. Van Exter, C. Fattinger, and D. Grischkowsky, "Terahertz time-domain spectroscopy of water vapor", *Opt. Lett.*, vol. 14, no. 20, pp. 1128–1130, 1989.

[117] L. Duvillaret, F. Garet, J.-F. Roux, and J.-L. Coutaz, "Analytical modeling and optimization of terahertz time-domain spectroscopy experiments, using photoswitches as antennas", *IEEE J. Sel. Top. Quantum Electron.*, vol. 7, no. 4, pp. 615–623, 2001.

[118] J. L. Coutaz, *Optoelectronique Terahertz.* EDP Sciences, 2008.

[119] F. W. Smith, H. Q. Le, V. Diadiuk, M. A. Hollis, A. R. Calawa, S. Gupta, M. Frankel, D. R. Dykaar, G. A. Mourou, and T. Y. Hsiang, "Picosecond GaAs-based photoconductive optoelectronic detectors", *Appl. Phys. Lett.*, vol. 54, no. 10, pp. 890–892, 1989.

[120] J. Shan and T. F. Heinz, "Terahertz radiation from semiconductors", *Ultrafast Dyn. Process. Semicond.*, vol. 59, pp. 1–59, 2004.

[121] E. Castro-Camus, L. Fu, J. Lloyd-Hughes, H. H. Tan, C. Jagadish, and M. B. Johnston, "Photoconductive response correction for detectors of terahertz radiation", *J. Appl. Phys.*, vol. 104, no. 5, pp. 1–7, 2008.

[122] D. H. Auston, "Picosecond optoelectronic switching and gating in silicon", *Appl. Phys. Lett.*, vol. 26, no. 3, pp. 101–103, 1975.

[123] Y. C. Shen, P. C. Upadhya, E. H. Linfield, H. E. Beere, and A. G. Davies, "Ultrabroadband terahertz radiation from low-temperature-grown GaAs photoconductive emitters", *Appl. Phys. Lett.*, vol. 83, no. 15, pp. 3117–3119, 2003.

[124] A. I. Hochbaum, R. Chen, R. D. Delgado, W. Liang, E. C. Garnett, M. Najarian, A. Majumdar, and P. Yang, "Enhanced thermoelectric performance of rough silicon nanowires", *Nature*, vol. 451, no. 7175, pp. 163–167, 2008.

[125] J. Lim, K. Hippalgaonkar, S. C. Andrews, and A. Majumdar, "Quantifying Surface Roughness Effects on Phonon Transport in Silicon Nanowires", *Nano Lett.*, vol. 12, no. 5, pp. 2475–2482, 2012.

[126] F. Seker, K. Meeker, T. Kuech, and A. Ellis, "Surface Chemistry of Prototypical Bulk II VI and III V Semiconductors and Implications for Chemical Sensing", *Chem. Rev*, vol. 100, no. 7, pp. 2505–2536, 2000.

[127] T. Xu, J. P. Nys, A. Addad, O. I. Lebedev, A. Urbieta, B. Salhi, M. Berthe, B. Grandidier, and D. Stievenard, "Faceted sidewalls of silicon nanowires: Au-induced structural reconstructions and electronic properties", *Phys. Rev. B - Condens. Matter Mater. Phys.*, vol. 81, no. 11, pp. 1–10, 2010.

[128] I. M. Vitomirov, A. Raisanen, A. C. Finnefrock, R. E. Viturro, L. J. Brillson, P. D. Kirchner, G. D. Pettit, and J. M. Woodall, "Geometric

ordering, surface chemistry, band bending, and work function at decapped GaAs(100) surfaces", *Phys. Rev. B*, vol. 46, no. 20, pp. 13293–13302, 1992.

[129] E. Hilner, U. Håkanson, L. E. Fröberg, M. Karlsson, P. Kratzer, E. Lundgren, L. Samuelson, and A. Mikkelsen, "Direct atomic scale imaging of III-V nanowire surfaces", *Nano Lett.*, vol. 8, no. 11, pp. 3978–3982, 2008.

[130] M. Hjort, S. Lehmann, J. Knutsson, R. Timm, D. Jacobsson, E. Lundgren, K. A. Dick, and A. Mikkelsen, "Direct imaging of atomic scale structure and electronic properties of GaAs wurtzite and zinc blende nanowire surfaces.", *Nano Lett.*, vol. 13, pp. 4492–8, sep 2013.

[131] J. L. Webb, J. Knutsson, M. Hjort, S. Gorji Ghalamestani, K. A. Dick, R. Timm, and A. Mikkelsen, "Electrical and Surface Properties of InAs/InSb Nanowires Cleaned by Atomic Hydrogen.", *Nano Lett.*, vol. 15, no. 8, pp. 4865–75, 2015.

[132] M. Hjort, J. V. Knutsson, B. Mandl, K. Deppert, E. Lundgren, R. Timm, and A. Mikkelsen, "Surface morphology of Au-free grown nanowires after native oxide removal", *Nanoscale*, vol. 7, no. 22, pp. 9998–10004, 2015.

[133] J. Arbiol and Q. Xiong, *Semiconductor Nanowires: Materials, Synthesis, Characterization and Applications*. Woodhead Publishing Series in Electronic and Optical Materials, Elsevier Science, 2015.

[134] P. Capiod, T. Xu, J. P. Nys, M. Berthe, G. Patriarche, L. Lymperakis, J. Neugebauer, P. Caroff, R. E. Dunin-Borkowski, P. Ebert, and B. Grandidier, "Band offsets at zincblende-wurtzite GaAs nanowire sidewall surfaces", *Appl. Phys. Lett.*, vol. 103, no. 12, p. 122104, 2013.

[135] C. Durand, M. Berthe, Y. Makoudi, J.-P. Nys, R. Leturcq, P. Caroff, and B. Grandidier, "Persistent enhancement of the carrier density in electron irradiated InAs nanowires.", *Nanotechnology*, vol. 24, no. 27, p. 275706, 2013.

[136] R. M. Tromp, R. J. Hamers, and J. E. Demuth, "Atomic and electronic contributions to Si(111)-(7x7) scanning-tunneling-microscopy images", *Phys. Rev. B*, vol. 34, no. 2, pp. 1388–1391, 1986.

[137] D. K. Goswami, K. Bhattacharjee, B. Satpati, S. Roy, P. V. Satyam, and B. N. Dev, "Preferential heights in the growth of Ag islands on Si(1 1 1)-(7 x 7) surfaces", *Surf. Sci.*, vol. 601, no. 3, pp. 603–608, 2007.

[138] M. Miyazaki and H. Hirayama, "Thickness- and deposition temperature-dependent morphological change in electronic growth of ultra-thin Ag films on Si(111) substrates", *Surf. Sci.*, vol. 602, no. 1, pp. 276–282, 2008.

[139] A. Pal, J. C. Mahato, B. N. Dev, and D. K. Goswami, "Roughening in electronic growth of Ag on Si(111)-(7x7) surfaces", *ACS Appl. Mater. Interfaces*, vol. 5, no. 19, pp. 9517–9521, 2013.

[140] M. Hjort, *III – V Nanowire Surfaces.* Department of Physics, Lund University. 2014.

[141] J. V. Knutsson, S. Lehmann, M. Hjort, P. Reinke, E. Lundgren, K. A. Dick, R. Timm, and A. Mikkelsen, "Atomic Scale Surface Structure and Morphology of InAs Nanowire Crystal Superlattices: The Effect of Epitaxial Overgrowth", *ACS Appl. Mater. Interfaces*, vol. 7, no. 10, pp. 5748–5755, 2015.

[142] T. Xu, M. J. Wei, P. Capiod, A. Díaz Álvarez, X. L. Han, D. Troadec, J. P. Nys, M. Berthe, I. Lefebvre, G. Patriarche, S. R. Plissard, P. Caroff, P. Ebert, and B. Grandidier, "Type I band alignment in GaAs81Sb19/GaAs core-shell nanowires", *Appl. Phys. Lett.*, vol. 107, no. 11, p. 112102, 2015.

[143] P. Ebert, P. Quadbeck, K. Urban, B. Henninger, K. Horn, G. Schwarz, J. Neugebauer, and M. Scheffler, "Identification of surface anion antisite defects in (110) surfaces of III-V semiconductors", *Appl. Phys. Lett.*, vol. 79, no. 18, pp. 2877–2879, 2001.

[144] R. Feenstra, J. Woodall, and G. Pettit, "Observation of bulk defects by scanning tunneling microscopy and spectroscopy: Arsenic antisite defects in GaAs", *Phys. Rev. Lett.*, vol. 71, no. 8, 1993.

[145] S. Gaan, R. M. Feenstra, P. Ebert, R. E. Dunin-Borkowski, J. Walker, and E. Towe, "Structure and electronic spectroscopy of steps on GaAs(110) surfaces", *Surf. Sci.*, vol. 606, no. 1-2, pp. 28–33, 2012.

[146] M. Schnedler, Y. Jiang, K. H. Wu, E. G. Wang, R. E. Dunin-Borkowski, and P. Ebert, "Effective mass of a two-dimensional $\sqrt(3) \times \sqrt(3)$ Ga single atomic layer on Si(111)", *Surf. Sci.*, vol. 630, no. September 2016, pp. 225–228, 2014.

[147] A. Höglund, C. W. M. Castleton, M. Göthelid, B. Johansson, and S. Mirbt, "Point defects on the (110) surfaces of InP, InAs, and InSb: A comparison with bulk", *Phys. Rev. B*, vol. 74, no. 7, p. 075332, 2006.

[148] G. Schwarz, J. Neugebauer, and M. Scheffler, "Point defects on III-V semiconductor surfaces", *arXiv preprint cond-mat/0010342.*, 2000.

[149] P. Ebert, M. Heinrich, M. Simon, K. Urban, and M. G. Lagally, "Formation of anion vacancies by Langmuir evaporation from InP and GaAs (110) surfaces at low temperatures", *Phys. Rev. B*, vol. 51, no. 15, pp. 9696–9701, 1995.

[150] U. Semmler, M. Simon, P. Ebert, and K. Urban, "Stoichiometry changes by selective vacancy formation on (110) surfaces of III–V semiconductors: Influence of electronic effects", *J. Chem. Phys.*, vol. 114, no. 1, p. 445, 2001.

[151] C. Domke, P. Ebert, M. Heinrich, and K. Urban, "Microscopic identification of the compensation mechanisms in Si-doped GaAs", *Phys. Rev. B*, vol. 54, no. 15, pp. 10288–10291, 1996.

[152] P. Ebert and K. Urban, "Electronic properties of the Ga vacancy in GaP(110) surfaces determined by scanning tunneling microscopy", *Phys. Rev. B*, vol. 58, no. 3, pp. 1401–1404, 1998.

[153] G. Schwarz, *Untersuchungen zu Defekten auf und nahe der ( 110 )– Oberfläche von GaAs und weiteren III-V-Halbleitern.* PhD thesis, Technischen Universität Berlin, 2002.

[154] C. Chatillon and D. Chatain, "Congruent vaporization of GaAs (s) and stability of Ga (l) droplets at the GaAs (s) surface", *J. Cryst. Growth*, vol. 151, pp. 91–101, 1995.

[155] H. S. Karlsson, R. Viselga, and U. O. Karlsson, "Electron accumulation at the InAs(110) cleavage surface", *Surf. Sci.*, vol. 402-404, no. October 1997, pp. 590–594, 1998.

[156] J. R. Weber, A. Janotti, and C. G. Van De Walle, "Intrinsic and extrinsic causes of electron accumulation layers on InAs surfaces", *Appl. Phys. Lett.*, vol. 97, no. 19, 2010.

[157] R. Dombrowski, C. Steinebach, C. Wittneven, M. Morgenstern, and R. Wiesendanger, "Tip-induced band bending by scanning tunneling spectroscopy of the states of the tip-induced quantum dot on InAs(110)", *Phys. Rev. B*, vol. 59, no. 12, pp. 8043–8048, 1999.

[158] F. Lenrick, M. Ek, K. Deppert, L. Samuelson, and L. Reine Wallenberg, "Straight and kinked InAs nanowire growth observed in situ by transmission electron microscopy", *Nano Res.*, vol. 7, no. 8, pp. 1188–1194, 2014.

[159] C. Heyn and D. E. Jesson, "Congruent evaporation temperature of molecular beam epitaxy grown GaAs (001) determined by local droplet etching", *Appl. Phys. Lett.*, vol. 107, no. 16, 2015.

[160] P. Ebert, "Unpublished".

[161] J. Kanasaki, "Formation and clustering of surface vacancies under electronic excitation on semiconductor surfaces", *Phys. Rev. B*, vol. 376-377, pp. 834–840, apr 2006.

[162] J. Kanasaki, E. Inami, and K. Tanimura, "Fermi-level dependent morphology in photoinduced bond breaking on (110) surfaces of III–V semiconductors", *Surf. Sci.*, vol. 601, pp. 2367–2372, jun 2007.

[163] T. T. Chiang, "Arsenic on GaAs: Fermi-level pinning and thermal desorption studies", *J. Vac. Sci. Technol. A Vacuum, Surfaces, Film.*, vol. 7, no. 3, p. 724, 1989.

[164] T. Kikawa, I. Ochiai, and S. Takatani, "Atomic hydrogen cleaning of GaAs and InP surfaces studied by photoemission spectroscopy", *Surf. Sci.*, vol. 316, no. 3, pp. 238–246, 1994.

[165] O. Hamedi, M. Proix, and F. Sebenne, "Effects of atomic hydrogen on the surface properties of cleaved GaAs(110)", *Semicond. Sci. Technol.*, vol. 418, 1987.

[166] D. Pons and J. C. Bourgoin, "Irradiation-induced defects in GaAs", *J. Phys. C Solid State Phys.*, vol. 18, no. 20, pp. 3839–3871, 2000.

[167] K. F. Lamprecht, S. Juen, L. Palmetshofer, and R. A. Höpfel, "Ultrashort carrier lifetimes in H+ bombarded InP", *Appl. Phys. Lett.*, vol. 59, no. 8, pp. 926–928, 1991.

[168] C. T. Foxon, "MBE growth of GaAs and III-V alloys", *J. Vac. Sci. Technol. B Microelectron. Nanom. Struct.*, vol. 1, no. 2, p. 293, 1983.

[169] F. W. Smith, A. R. Calawa, C. L. Chen, M. J. Manfra, and L. J. Mahoney, "New MBE Buffer Used to Eliminate Backgating in GaAs MESFET's", *IEEE Electron Device Lett.*, vol. 9, no. 2, pp. 77–80, 1988.

[170] M. Kaminska, Z. Liliental-Weber, E. R. Weber, T. George, J. B. Kortright, F. W. Smith, B. Y. Tsaur, and A. R. Calawa, "Structural properties of As-rich GaAs grown by molecular beam epitaxy at low temperatures", *Appl. Phys. Lett.*, vol. 54, no. 19, pp. 1881–1883, 1989.

[171] M. R. Melloch, N. Otsuka, J. M. Woodall, a. C. Warren, and J. L. Freeouf, "Formation of arsenic precipitates in GaAs buffer layers grown by molecular beam epitaxy at low substrate temperatures", *Appl. Phys. Lett.*, vol. 57, no. 15, p. 1531, 1990.

[172] D. T. Mcinturff, "Arsenic precipitates and the semi-insulating properties of GaAs buffer layers grown", *Appl. Phys. Lett.*, vol. 57, no. 13, pp. 1331–1333, 1990.

[173] H. Shen, F. C. Rong, R. Lux, J. Pamulapati, M. Taysing-Lara, M. Dutta, E. H. Poindexter, L. Calderon, and Y. Lu, "Fermi level pinning in low-temperature molecular beam epitaxial GaAs", *Appl. Phys. Lett.*, vol. 61, no. 13, pp. 1585–1587, 1992.

[174] X. Liu, A. Prasad, W. M. Chen, A. Kurpiewski, A. Stoschek, Z. Liliental-Weber, and E. R. Weber, "Mechanism responsible for the semi-insulating properties of low-temperature-grown GaAs", *Appl. Phys. Lett.*, vol. 65, no. 23, p. 3002, 1994.

[175] J. K. Luo, H. Thomas, D. V. Morgan, and D. Westwood, "Thermal annealing effect on low temperature molecular beam epitaxy grown GaAs: Arsenic precipitation and the change of resistivity", *Appl. Phys. Lett.*, vol. 64, no. 26, pp. 3614–3616, 1994.

[176] J. K. Luo, H. Thomas, D. V. Morgan, and D. Westwood, "Transport properties of GaAs layers grown by molecular beam epitaxy at low temperature and the effects of annealing", *J. Appl. Phys.*, vol. 79, no. 1996, p. 3622, 1996.

[177] J. I. Landman, C. G. Morgan, J. T. Schick, P. Papoulias, and A. Kumar, "Arsenic interstitials and interstitial complexes in low-temperature grown GaAs", *Phys. Rev. B*, vol. 55, no. 23, pp. 15581–15586, 1997.

[178] T. Staab, R. Nieminen, J. Gebauer, R. Krause-Rehberg, M. Luysberg, M. Haugk, and T. Frauenheim, "Do Arsenic Interstitials Really Exist in As-Rich GaAs?", *Phys. Rev. Lett.*, vol. 87, no. 4, p. 045504, 2001.

[179] M. Stellmacher, R. Bisaro, P. Galtier, J. Nagle, K. Khirouni, and J. C. Bourgoin, "Defects and defect behaviour in GaAs grown at low temperature", *Semicond. Sci. Technol.*, vol. 16, no. 6, pp. 440–446, 2001.

[180] D. C. Look, D. C. Walters, M. O. Manasreh, J. R. Sizelove, C. E. Stutz, and K. R. Evans, "Anomalous hall-effect results in low-temperature molecular-beam-epitaxial GaAs: Hopping in a dense EL2-like band", *Phys. Rev. B*, vol. 42, no. 6, pp. 3578–3581, 1990.

[181] R. M. Feenstra, a. Vaterlaus, and J. M. Woodall, "Tunneling spectroscopy in low-temperature-grown of midgap states induced GaAs by arsenic precipitates", *Appl. Phys. Lett.*, vol. 63, no. November, pp. 2528–2530, 1993.

[182] T. E. M. Staab, R. M. Nieminen, M. Luysberg, and T. Frauenheim, "Agglomeration of As antisites in as-rich low-temperature GaAs: Nucleation without a critical nucleus size", *Phys. Rev. Lett.*, vol. 95, no. 12, 2005.

[183] X. Liu, a. Prasad, J. Nishio, E. R. Weber, Z. Liliental-Weber, and W. Walukiewicz, "Native point defects in low-temperature-grown GaAs", *Appl. Phys. Lett.*, vol. 67, no. 2, p. 279, 1995.

[184] M. O. Manasreh, D. C. Look, K. R. Evans, and C. E. Stutz, "Infrared-Absorption of Deep Defects in Molecular-Beam-Epitaxial GaAs-Layers Grown at 200°C - Observation of an EL(2)-Like Defect", *Phys. Rev. B*, vol. 41, no. 14, pp. 10272–10275, 1990.

[185] D. C. Look, "Review of Hall Effect and Magnetoresistance Measurements in GaAs Materials and Devices", *J. Electrochem. Soc.*, vol. 137, no. 1, p. 260, 1990.

[186] G. Zhao, R. N. Schouten, N. Van Der Valk, W. T. Wenckebach, and P. C. M. Planken, "Design and performance of a THz emission and detection setup based on a semi-insulating GaAs emitter", *Rev. Sci. Instrum.*, vol. 73, no. 4, p. 1715, 2002.

[187] S. Kono, M. Tani, and K. Sakai, "Detection of up to 60 THz with an LT-GaAs photoconductive antenna", *Tech. Dig. Summ. Pap. Present. Conf.*

*Lasers Electro-Optics. Postconf. Tech. Dig. (IEEE Cat. No.01CH37170)*, vol. 149, no. 3, pp. 102–103, 2001.

[188] S. Matsuura, M. Tani, and K. Sakai, "Generation of coherent terahertz radiation by photomixing in dipole photoconductive antennas", *Appl. Phys. Lett.*, vol. 70, no. 5, p. 559, 1997.

[189] A. Lochtefeld, M. R. Melloch, J. C. P. Chang, and E. S. Harmon, "The role of point defects and arsenic precipitates in carrier trapping and recombination in low-temperature grown GaAs", *Appl. Phys. Lett.*, vol. 69, no. 1996, p. 1465, 1996.

[190] S. D. Benjamin, H. S. Loka, A. Othonos, and P. W. E. Smith, "Ultrafast dynamics of nonlinear absorption in low-temperature-grown GaAs", *Appl. Phys. Lett.*, vol. 68, no. 18, pp. 2544–2546, 1996.

[191] K. A. McIntosh, K. B. Nichols, S. Verghese, and E. R. Brown, "Investigation of ultrashort photocarrier relaxation times in low-temperature-grown GaAs", *Appl. Phys. Lett.*, vol. 70, no. 1997, p. 354, 1997.

[192] S. Gupta, M. Y. Frankel, J. A. Valdmanis, J. F. Whitaker, G. A. Mourou, F. W. Smith, and A. R. Calawa, "Subpicosecond carrier lifetime in GaAs grown by molecular beam epitaxy at low temperatures", *Appl. Phys. Lett.*, vol. 59, no. 25, pp. 3276–3278, 1991.

[193] S. S. Prabhu, S. E. Ralph, M. R. Melloch, and E. S. Harmon, "Carrier dynamics of low-temperature-grown GaAs observed via THz spectroscopy", *Appl. Phys. Lett.*, vol. 70, no. 1997, p. 2419, 1997.

[194] P. Tejedor, P. Šmilauer, C. Roberts, and B. Joyce, "Surface-morphology evolution during unstable homoepitaxial growth of GaAs(110)", *Phys. Rev. B*, vol. 59, no. 3, pp. 2341–2345, 1999.

[195] P. Tejedor, P. Šmilauer, and B. A. Joyce, "Morphological instabilities during homoepitaxy on vicinal GaAs(110) surfaces", *Microelectronics J.*, vol. 30, no. 4, pp. 477–482, 1999.

[196] B. L. A.R. Lubinsky, C.B. Duke and P. Mark, "Semiconductor surface reconstruction: the rippled surface of GaAs(110)", *Phys. Rev. Lett.*, vol. 36, no. 17, pp. 1058–1061, 1976.

[197] B. Grandidier, H. Chen, R. M. Feenstra, D. T. McInturff, P. W. Juodawlkis, and S. E. Ralph, "Scanning tunneling microscopy and spectroscopy of arsenic antisites in low temperature grown InGaAs", *Appl. Phys. Lett.*, vol. 74, no. 1999, p. 1439, 1999.

[198] A. Sabitova, P. Ebert, A. Lenz, S. Schaafhausen, L. Ivanova, M. Dähne, A. Hoffmann, R. E. Dunin-Borkowski, a. Förster, B. Grandidier, and H. Eisele, "Intrinsic bandgap of cleaved ZnO $(11\bar{2}0)$ surfaces", *Appl. Phys. Lett.*, vol. 102, pp. 0–4, 2013.

[199] J. Tersoff, “Schottky barrier heights and the continuum of gap states”, *Phys. Rev. Lett.*, vol. 52, no. 6, pp. 465–468, 1984.

[200] F. Glas and J. C. Harmand, “Calculation of the temperature profile in nanowhiskers growing on a hot substrate”, *Phys. Rev. B*, vol. 73, no. 15, pp. 1–7, 2006.

[201] O. Demichel, M. Heiss, J. Bleuse, H. Mariette, and A. Fontcuberta i Morral, “Impact of surfaces on the optical properties of GaAs nanowires”, *Appl. Phys. Lett.*, vol. 97, no. 20, pp. 2010–2012, 2010.

[202] V. Ortiz, J. Nagle, J. F. Lampin, E. ronne, and A. Alexandrou, “Low-temperature-grown GaAs: Modeling of transient reflectivity experiments”, *J. Appl. Phys.*, vol. 102, no. 4, pp. 1–9, 2007.

[203] http://www.thzscience.nl/THzFAQ.php.

[204] P. Cox and P. G. Mezger, “The galactic infrared/submillimeter dust radiation”, *Astron. Astrophys. Rev.*, vol. 1, no. 1, pp. 49–83, 1989.

[205] P. H. Siegel and V. Pikov, “THz in biology and medicine: toward quantifying and understanding the interaction of millimeter- and submillimeter-waves with cells and cell processes”, *Proc. SPIE*, vol. 7562, pp. 75620H–75620H–13, 2010.

[206] J. F. Federici, B. Schulkin, F. Huang, D. Gary, R. Barat, F. Oliveira, and D. Zimdars, “THz imaging and sensing for security applications—explosives, weapons and drugs”, *Semicond. Sci. Technol.*, vol. 20, no. 7, pp. S266–S280, 2005.

[207] K. Sakai, *Terahertz optoelectronics.* Springer. 2005.

[208] T. W. Crowe, W. L. Bishop, D. W. Porterfield, J. L. Hesler, and R. M. Weikle, “Opening the terahertz window with integrated diode circuits”, *IEEE J. Solid-State Circuits*, vol. 40, no. 10, pp. 2104–2109, 2005.

[209] G. Dodel, “On the history of far-infrared (FIR) gas lasers: Thirty-five years of research and application”, *Infrared Phys. Technol.*, vol. 40, no. 3, pp. 127–139, 1999.

[210] W. t. Ackermann, “Operation of a free-electron laser from the extreme ultraviolet to the water window”, *Nat. Photonics*, vol. 1, no. 6, pp. 336–342, 2007.

[211] B. Williams, S. Kumar, Q. Hu, and J. Reno, “High power terahertz quantum cascade lasers”, *Electron. Lett.*, vol. 42, no. 2, 2006.

[212] S. Matsuura, M. Tani, and K. Sakai, “Generation of coherent terahertz radiation by photomixing in dipole photoconductive antennas”, *Appl. Phys. Lett.*, vol. 70, no. 5, p. 559, 1997.

[213] Q. Guo, Y. Kume, Y. Fukuhara, T. Tanaka, M. Nishio, H. Ogawa, M. Hiratsuka, M. Tani, and M. Hangyo, "Observation of ultra-broadband terahertz emission from ZnTe films grown by metaloganic vapor epitaxy", *Solid State Commun.*, vol. 141, no. 4, pp. 188–191, 2007.

[214] H. Ahn, Y. P. Ku, Y. C. Wang, C. H. Chuang, S. Gwo, and C. L. Pan, "Terahertz emission from vertically aligned InN nanorod arrays", *Appl. Phys. Lett.*, vol. 91, no. 13, pp. 1–4, 2007.

[215] G. B. Jung, Y. J. Cho, Y. Myung, H. S. Kim, Y. S. Seo, J. Park, and C. Kang, "Geometry-dependent terahertz emission of silicon nanowires.", *Opt. Express*, vol. 18, no. 16, pp. 16353–16359, 2010.

[216] K. J. Kong, C. S. Jung, G. B. Jung, Y. J. Cho, H. S. Kim, J. Park, N. E. Yu, and C. Kang, "Room-temperature ferromagnetism and terahertz emission of Mn-doped InGaAs and GaAsSb nanowires.", *Nanotechnology*, vol. 21, no. 43, p. 435703, 2010.

[217] V. N. Trukhin, A. S. Buyskikh, N. A. Kaliteevskaya, A. D. Bourauleuv, L. L. Samoilov, Y. B. Samsonenko, G. E. Cirlin, M. A. Kaliteevski, and A. J. Gallant, "Terahertz generation by GaAs nanowires", *Appl. Phys. Lett.*, vol. 103, no. 7, pp. 1–5, 2013.

[218] W.-J. Lee, J. W. Ma, J. M. Bae, K.-S. Jeong, M.-H. Cho, C. Kang, and J.-S. Wi, "Strongly enhanced THz emission caused by localized surface charges in semiconducting Germanium nanowires.", *Sci. Rep.*, vol. 3, p. 1984, 2013.

[219] R. Ascazubi, *THz emission spectroscopy of narrow bandgap semiconductors*. PhD thesis, Rensselaer Polytechnic Institute, Troy, New York, 2005.

[220] R. Ascázubi, C. Shneider, I. Wilke, R. Pino, and P. S. Dutta, "Enhanced terahertz emission from impurity compensated GaSb", *Phys. Rev. B*, vol. 72, no. 4, pp. 1–5, 2005.

[221] G. Klatt, F. Hilser, W. Qiao, M. Beck, R. Gebs, a. Bartels, K. Huska, U. Lemmer, G. Bastian, M. B. Johnston, M. Fischer, J. Faist, and T. Dekorsy, "Terahertz emission from lateral photo-Dember currents.", *Opt. Express*, vol. 18, no. 5, pp. 4939–4947, 2010.

[222] R. Kersting, K. Unterrainer, G. Strasser, H. Kauffmann, and E. Gornik, "Few-Cycle THz Emission from Cold Plasma Oscillations", *Phys. Rev. Lett.*, vol. 79, pp. 3038–3041, 1997.

[223] M. Tani, R. Fukasawa, H. Abe, S. Matsuura, K. Sakai, and S. Nakashima, "Terahertz radiation from coherent phonons excited in semiconductors", *J. Appl. Phys.*, vol. 83, no. 5, p. 2473, 1998.

[224] R. Kersting, J. N. Heyman, G. Strasser, and K. Unterrainer, "Coherent plasmons in n -doped GaAs", *Phys. Rev. B*, vol. 58, no. 8, pp. 4553–4559, 1998.

[225] A. Arlauskas, J. Treu, K. Saller, I. Beleckaite, G. Koblmüller, and A. Krotkus, “Strong terahertz emission and its origin from catalyst-free InAs nanowire arrays”, *Nano Lett.*, vol. 14, no. 3, pp. 1508–1514, 2014.

[226] N. Erhard, P. Seifert, L. Prechtel, S. Hertenberger, H. Karl, G. Abstreiter, G. Koblmüller, and A. W. Holleitner, “Ultrafast photocurrents and THz generation in single InAs-nanowires”, *Ann. Phys.*, vol. 525, no. 1-2, pp. 180–188, 2013.

[227] J. John Ibanes, M. Herminia Balgos, R. Jaculbia, A. Salvador, A. Somintac, E. Estacio, C. T. Que, S. Tsuzuki, K. Yamamoto, and M. Tani, “Terahertz emission from GaAs-AlGaAs core-shell nanowires on Si (100) substrate: Effects of applied magnetic field and excitation wavelength”, *Appl. Phys. Lett.*, vol. 102, no. 6, pp. 2014–2017, 2013.

[228] V. N. Trukhin, A. D. Bouravleuv, I. A. Mustafin, J. P. Kakko, T. Huhtio, G. E. Cirlin, and H. Lipsanen, “Generation of terahertz radiation in ordered arrays of GaAs nanowires”, *Appl. Phys. Lett.*, vol. 106, no. 25, p. 252104, 2015.

[229] J.-H. Yim, M. Irfan, K.-J. Song, E.-H. Lee, J.-D. Song, and Y.-D. Jho, “Polarized Terahertz Waves Emitted from In0.2/Ga0.8/As Nanowires”, *J. Nanosci. Nanotechnol.*, vol. 15, no. 8, pp. 6024–6027, 2015.

[230] V. N. Trukhin, A. C. Buyskih, A. D. Bouravlev, I. A. Mustafin, Y. B. Samsonenko, A. V. Trukhin, G. E. Cirlin, M. A. Kaliteevski, D. A. Zeze, and A. J. Gallant, “Generation of terahertz radiation by AlGaAs nanowires”, *JETP Lett.*, vol. 102, no. 5, pp. 316–320, 2015.

[231] K. Peng, P. Parkinson, L. Fu, Q. Gao, N. Jiang, Y.-N. Guo, F. Wang, H. J. Joyce, J. L. Boland, H. H. Tan, *et al.*, “Single nanowire photoconductive terahertz detectors”, *Nano letters*, vol. 15, no. 1, pp. 206–210, 2014.

[232] M. S. Vitiello, D. Coquillat, L. Viti, D. Ercolani, F. Teppe, A. Pitanti, F. Beltram, L. Sorba, W. Knap, and A. Tredicucci, “Room-temperature terahertz detectors based on semiconductor nanowire field-effect transistors”, *Nano Lett.*, vol. 12, no. 1, pp. 96–101, 2012.

[233] M. Dyakonov and M. Shur, “Shallow water analogy for a ballistic field effect transistor: New mechanism of plasma wave generation by dc current”, *Phys. Rev. Lett.*, vol. 71, no. 15, pp. 2465–2468, 1993.

[234] M. S. Vitiello, L. Viti, L. Romeo, D. Ercolani, G. Scalari, J. Faist, F. Beltram, L. Sorba, and A. Tredicucci, “Semiconductor nanowires for highly sensitive, room-temperature detection of terahertz quantum cascade laser emission”, *Appl. Phys. Lett.*, vol. 100, no. 24, 2012.

[235] M. Ravaro, M. Locatelli, L. Viti, D. Ercolani, L. Consolino, S. Bartalini, L. Sorba, M. S. Vitiello, and P. De Natale, “Detection of a 2.8 THz quantum cascade laser with a semiconductor nanowire field-effect transistor

coupled to a bow-tie antenna", *Appl. Phys. Lett.*, vol. 104, no. 8, pp. 2–6, 2014.

[236] P. Dean, A. Valavanis, J. Keeley, K. Bertling, Y. L. Lim, R. Alhathlool, A. Burnett, L. H. Li, S. P. Khanna, D. Indjin, T. Taimre, A. Rakić, E. H. Linfield, and A. G. Davies, "Terahertz imaging using quantum cascade lasers—a review of systems and applications", *J. Phys. D. Appl. Phys.*, vol. 47, no. 37, p. 374008, 2014.

[237] C. Kang, J. W. Leem, J. W. Lee, J. S. Yu, and C. S. Kee, "Characteristics of terahertz pulses from antireflective GaAs surfaces with nanopillars", *J. Appl. Phys.*, vol. 113, no. 20, 2013.

[238] A. Koroliov, R. Adomavicius, A. Arlauskas, A. Siusys, J. Sadowski, A. Reszka, and A. Krotkus, "Enhanced terahertz emission from GaAs and GaAs-MnAs nanowires", *Int. Conf. Infrared, Millimeter, Terahertz Waves, IRMMW-THz*, pp. 3–4, 2013.

[239] S. G. Park, M. R. Melloch, and A. M. Weiner, "Analysis of terahertz waveforms measured by photoconductive and electrooptic sampling", *IEEE J. Quantum Electron.*, vol. 35, no. 5, pp. 810–819, 1999.

[240] N. P. Wells, P. M. Belden, J. R. Demers, and W. T. Lotshaw, "Transient reflectivity as a probe of ultrafast carrier dynamics in semiconductors: A revised model for low-temperature grown GaAs", *J. Appl. Phys.*, vol. 116, no. 7, 2014.

[241] G. C. Loata, T. Löffler, and H. G. Roskos, "Evidence for long-living charge carriers in electrically biased low-temperature-grown GaAs photoconductive switches", *Appl. Phys. Lett.*, vol. 90, no. 5, pp. 10–13, 2007.

[242] S. Rihani, R. Faulks, H. Beere, H. Page, I. Gregory, M. Evans, D. A. Ritchie, and M. Pepper, "Effect of defect saturation on terahertz emission and detection properties of low temperature GaAs photoconductive switches", *Appl. Phys. Lett.*, vol. 95, no. 5, pp. 0–3, 2009.

[243] K. Liu, A. Krotkus, K. Bertulis, J. Xu, and X. C. Zhang, "Terahertz radiation from n-type GaAs with Be-doped low-temperature-grown GaAs surface layers", *J. Appl. Phys.*, vol. 94, no. 5, pp. 3651–3653, 2003.

[244] M. C. Beard, G. M. Turner, and C. A. Schmuttenmaer, "Subpicosecond carrier dynamics in low-temperature grown GaAs as measured by time-resolved terahertz spectroscopy", *J. Appl. Phys.*, vol. 90, no. 12, pp. 5915–5923, 2001.

[245] A. Georgakilas, E. Aperathitis, V. Foukaraki, M. Kayambaki, and P. Panayotatos, "Investigation of the GaAs/Si heterojunction band lineup with capacitance and current versus voltage measurements", *Mater. Sci. Eng. B*, vol. 44, no. 1-3, pp. 383–386, 1997.

[246] C. Renard, T. Molière, N. Cherkashin, J. Alvarez, L. Vincent, A. Jaffré, G. Hallais, J. P. Connolly, D. Mencaraglia, and D. Bouchier, “High current density GaAs/Si rectifying heterojunction by defect free Epitaxial Lateral overgrowth on Tunnel Oxide from nano-seed”, *Sci. Rep.*, vol. 6, no. April, p. 25328, 2016.

[247] http://www.nanoembrace.eu.

# Publications

# List of Publications

*A. Díaz Álvarez*, T. Xu, G. Tütüncüoglu, T. Demonchaux, JP.Nys, M.Berthe, F. Matteini, H.A. Potts, D. Troadec, G. Patriarche, JF. Lampin, C. Coinon, A. Fontcuberta i Morral, RE. Dunin-Borkowski, P. Ebert, B.Grandidier **Nonstoichiometric Low-Temperature Grown GaAs Nanowires** *Nano Lett.* **15,** 6440–6445 (2015).

VG Dubrovskii, T. Xu, *A. Díaz Alvarez*, G. Larrieu, SR. Plissard, P. Caroff, F. Glas, B. Grandidier, **Self-Equilibration of the Diameter of Ga-Catalyzed GaAs Nanowires.** *Nano Lett.* ***15,*** *5580–5584 (2015).*

T. Xu, MJ. Wei, P Capiod, *A Díaz Álvarez*, Xiang-Lei Han, D. Troadec, JP Nys, M. Berthe, I. Lefebvre, G. Patriarche, SR Plissard, P. Caroff, Ph Ebert, B. Grandidier ,**Type I band alignment in GaAs81Sb19/GaAs core-shell nanowires** , *Appl. Phys. Lett.* ***107****, 112102 (2015) 107, 112102 (2015)*

*A. Díaz Álvarez*, T. Zhu, J.P. Nys, M. Berthe, M. Empis, J. Schreiber, B. Grandidier, T. Xu, **Scanning tunnelling spectroscopy and Raman spectroscopy of monolayer silicene on Ag(111)**, *Surface Science, 653,92-96 (2016)*

NANO LETTERS

Letter

pubs.acs.org/NanoLett

# Nonstoichiometric Low-Temperature Grown GaAs Nanowires

Adrian Díaz Álvarez,[†] Tao Xu,[†,‡] Gözde Tütüncüoglu,[§] Thomas Demonchaux,[†] Jean-Philippe Nys,[†] Maxime Berthe,[†] Federico Matteini,[§] Heidi A. Potts,[§] David Troadec,[†] Gilles Patriarche,[∥] Jean-François Lampin,[†] Christophe Coinon,[†] Anna Fontcuberta i Morral,[§] Rafal E. Dunin-Borkowski,[⊥] Philipp Ebert,[⊥] and Bruno Grandidier[*,†]

[†]Institut d'Electronique, de Microélectronique et de Nanotechnologies (IEMN), CNRS, UMR 8520, Département ISEN, 41 bd Vauban, 59046 Lille Cedex, France

[‡]Sino-European School of Technology, Shanghai University, 99 Shangda Road, Shanghai, 200444, People's Republic of China

[§]Laboratoire des Matériaux Semiconducteurs, Institut des Matériaux, Ecole Polytechnique Fédérale de Lausanne, CH-1015 Lausanne, Switzerland

[∥]CNRS-Laboratoire de Photonique et de Nanostructures (LPN), Route de Nozay, 91460 Marcoussis, France

[⊥]Peter Grünberg Institut, Forschungszentrum Jülich GmbH, 52425 Jülich, Germany

Supporting Information

**ABSTRACT:** The structural and electronic properties of nonstoichiometric low-temperature grown GaAs nanowire shells have been investigated with scanning tunneling microscopy and spectroscopy, pump−probe reflectivity, and cathodoluminescence measurements. The growth of non-stoichiometric GaAs shells is achieved through the formation of As antisite defects, and to a lower extent, after annealing, As precipitates. Because of the high density of atomic steps on the nanowire sidewalls, the Fermi level is pinned midgap, causing the ionization of the subsurface antisites and the formation of depleted regions around the As precipitates. Controlling their incorporation offers a way to obtain unique electronic and optical properties that depart from the ones found in conventional GaAs nanowires.

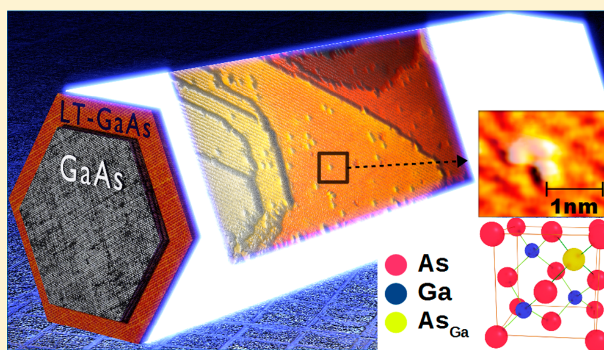


**KEYWORDS:** *Nonstoichiometric GaAs, low-temperature growth, As antisite, As precipitates, nanowires, scanning tunneling microscopy*

The prospect of using semiconductor nanowires (NWs) as building blocks of miniaturized devices has triggered a continuous improvement of the material crystal quality and reproducibility. For instance, gaining control over the phase purity in III−V semiconductor nanowires[1] has led to narrow photoluminescence emission in GaAs/GaAsSb heterostructure nanowires[2] and to ballistic transport of electrons in InAs NW transistors.[3] Similarly, the synthesis of defect-free interfaces in core−shell nanowires was a key achievement in getting higher collection efficiency of the photoexcited charge carriers in solar cells.[4] While defects in semiconductor NWs are generally seen as deleterious, certain applications, however, rely on the intentional incorporation of point defects during growth. A prototypical semiconductor material, where defects matter for resistivity, sub-bandgap optical absorption, and carrier lifetime engineering, is GaAs grown at low temperature. Such a material is crucial for the development of photoconductive devices and, in particular, compact terahertz (THz) sources and detectors with numerous applications in astronomy, communications, sensing, imaging, and medical diagnostics.[5−8]

The growth of GaAs NWs is usually based on the vapor−liquid−solid (VLS) mechanism that involves the continuous supply of precursors into a seed particle maintained above a critical temperature. Whatever the method that is used (Au-assisted or Ga-assisted VLS mechanism),[9,10] the eutectic temperature is higher than the threshold temperature at which nonstochiometric GaAs material can be grown and precludes the direct growth of high-quality nonstoichiometric LT-GaAs NWs. However, there is a great interest to build arrays of LT-GaAs NWs, since nanowires exhibit a significant enhancement of the THz emission with respect to thin films, without the need to insert them into bias photoconductive antenna structures.[11−15] This may help to overcome the limitation of relatively low THz power encountered in thin LT-GaAs layers.[16,17]

Here, we adopt the following core−shell strategy to synthesize a nonstoichiometric LT-GaAs NW: First GaAs

**Received:** May 7, 2015
**Revised:** July 30, 2015
**Published:** September 4, 2015

ACS Publications © 2015 American Chemical Society



DOI: 10.1021/acs.nanolett.5b01802
*Nano Lett.* 2015, 15, 6440−6445

NWs of high quality are grown on Si substrates using the self-assisted VLS mechanism with molecular beam epitaxy.[18] Then the temperature is reduced to grow a nonstoichiometric LT-GaAs shell on the nanowire sidewalls.[19] Here we examine the atomic scale structural and electronic properties of such LT-GaAs NWs. Scanning tunneling microscopy (STM) of the NW sidewalls reveals the existence of point defects. Based on the structural and spectral signature of the defects, they are identified as isolated subsurface arsenic antisites, which are found to affect the optical properties of the NWs. In addition, nanoscale clusters surrounded by narrow space charge layers occur, consistent with the formation of metallic As precipitates in the semiconductor shell. Both features demonstrate the successful growth of nonstoichiometric GaAs NWs with excess arsenic. The here-demonstrated controlled incorporation of arsenic antisites and clusters provides the basis to combine ultrashort carrier lifetimes, high dark resistivity, and large nonlinear optical effects in NWs.

The synthesis of the NWs was achieved by the Ga-assisted method on native oxide-covered Si(111) substrates (step 1 shown in Figure 1). Vertical nanowire growth has been achieved by engineering the native oxide thickness and adjusting the growth conditions.[20] Growth is started by simultaneous opening of gallium and arsenic shutters once the growth temperature is reached. The growth of the NW core was carried out at a nominal growth rate of 0.3 Å/s, an $As_4$ partial pressure of $2.5 \times 10^{-6}$ mbar, Ga partial pressure of $1.42 \times 10^{-7}$ mbar, and a temperature of 640 °C (step 2) for 90 min. The Ga droplet was then consumed by closing the Ga shutter for 30 min under $As_4$ flux. The temperature was subsequently reduced to 300 °C. Once stabilized, a shell was grown at a nominal growth rate of 1.1 Å/s and an $As_4$ partial pressure of $1.18 \times 10^{-5}$ mbar (step 3). At the end of the growth, the Ga flux was stopped, and the temperature was further lowered to room temperature, to cap the NWs with a thin As layer for protection against air exposure (step 4).[21] For comparison, GaAs NWs were also grown using the same conditions (steps 1 and 2), but without the LT-GaAs shell, or were capped with a 4 nm-thick AlGaAs shell grown at a reduced temperature of 465 °C and increased $As_4$ partial pressure of $5 \times 10^{-5}$ mbar.

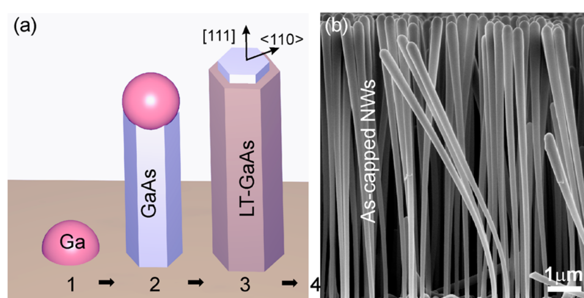


**Figure 1.** (a) Growth steps to obtain a GaAs/LT-GaAs core−shell nanowire structure based on the Ga-assisted vapor−liquid−solid mechanism. (1) Ga seed droplet, (2) growth of a high-quality GaAs NW, (3) followed by the consumption of the Ga droplet and the growth a of low-temperature GaAs shell. In step 3, the top of the nanowire is not shown to better highlight its core−shell structure. (b) SEM of the nanowire array after encapsulation of the wires with a thin amorphous As layer (step 4) for protection against air exposure needed to further perform atomic-scale characterization of the shell.

Figure 1b shows a scanning electron microscopy (SEM) micrograph of the NWs at the end of growth. The As-capped NWs, with an average length of 8.6 $\mu$m, exhibit a cotton-bud shape with a capping thickness decreasing from ∼60 nm in the top region of the NWs to ∼20 nm in the lower part (see Figure S1 and S2e in the Supporting Information). This shape results from the geometrically limited flux of $As_4$ into the dense NW array, which is a known effect in NW array growth called shadowing. After growth, the NWs were transferred to another ultra high vacuum system to be characterized with STM at a temperature $T$ of 77 and 300 K. Prior to the STM measurements, the capping layer was desorbed at 350 °C for 1 h, a temperature much lower than the congruent evaporation temperature of GaAs.[22] Then, the NWs were cleaved off in situ and deposited on a thin Ag film grown on a Si(111) surface.

A flat lying nanowire is shown in the SEM image of Figure 2a. Three sidewalls are visible, consistent with the overall hexagonal shape of the NW indicated schematically at the right end.[23] On the top sidewall, small fluctuations of the bright contrast point to corrugated sidewalls. This roughness is also

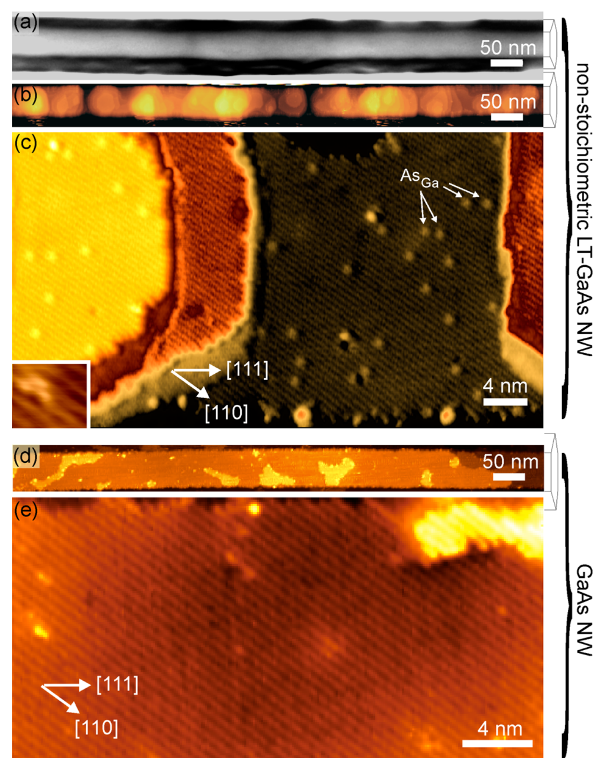


**Figure 2.** (a) SEM and (b) STM images of a single GaAs/LT-GaAs NW transferred onto a Ag/Si(111) surface after the sublimation of the capping layer. (c) High-resolution STM image obtained on the {110} sidewall of a LT-GaAs shell. The arrows point to subsurface $As_{Ga}$ arsenic antisites. Inset: High resolution image of an $As_{Ga}$ defect showing the typical structure consisting of a central core with two satellites. (d) STM image of a GaAs NW (without LT-GaAs shell) transferred onto a Si(111) surface after the sublimation of the capping layer. (e) High-resolution STM image obtained on the {110} sidewall of a GaAs NW. No $As_{Ga}$ antisite defects are present. The SEM was operated at an accelerating potential of 10 kV, and secondary electrons were detected. Tunneling conditions in b−c, d−e: $V_{sample}$ = −3.0, −4.0 V, $I_{tunnel}$ = 10, 20 pA, respectively, $T$ = 77 K. The color scale in b, c, d, and e are 88, 23, 17, and 5 Å, respectively.



DOI: 10.1021/acs.nanolett.5b01802
*Nano Lett.* 2015, 15, 6440−6445

visible for the adjacent sidewalls and clearly resolved in the STM image of the top sidewall (Figure 2b). It strongly differs from the flatness of the sidewalls of GaAs NWs, that are covered with sparse islands with one atomic step height only (see STM image in Figure 2d). As the pure GaAs NWs were grown with similar conditions but without a LT-GaAs shell, we attribute this morphological change to the low growth temperature and, to a lesser extent, to the radial homoepitaxial growth of GaAs on (110) sidewalls, that gives rise, in thin film growth, to very corrugated surfaces.[24,25]

Height profiles acquired along the growth axis on a length of 2 $\mu$m give an average height roughness of 4 nm. It is caused by pyramid like mounds which are confined by the two parallel edges of the sidewalls. The mounds consist of stacked atomically flat layers, separated mostly by single atomic steps, as visible in the high resolution STM image of Figure 2c. All of the layers show well-aligned atomic rows at an angle of ∼35° with respect to the [111] axis of the NW. This is the signature of {110} sidewalls of zinc-blende structure NWs (as confirmed by high resolution transmission electron microscopy, Supporting Information).

Remarkably, on every terrace, a large concentration of small bright protrusions, superimposed on the imaged As sublattice, are visible. We attribute these protrusions to point defects, which are only present in the LT-GaAs shell. Comparison with the sidewall of GaAs NWs that were similarly capped but grown without the LT-GaAs shell reveals the absence of this type of features (Figure 2e). At the atomic scale (inset of Figure 2c), these defects always exhibit a shape with a central core and two satellites. This is consistent with the features observed for subsurface arsenic antisites $As_{Ga}$ in bulk LT III−V compounds.[26,27] The absence of subsurface antisites in the GaAs NWs without a LT-GaAs shell rules out the creation of antisites during the sublimation of the capping layer. Hence the antisites are incorporated during the growth of the shell at low temperature. Counting the number of antisites per surface layer yields a concentration $N_{DD}$ of $(5 \pm 2) \times 10^{18}$ cm$^{-3}$. Considering the growth temperature used here, the concentration is inline with LT-grown bulk materials[26,27] and is consistent with a concentration below the detection limit of energy-dispersive X-ray spectroscopy (EDX) performed concomitantly with TEM analyses of the NW cross sections (Supporting Information).

In order to highlight the electronic structure of these defects in the shell, spatially resolved scanning tunneling spectroscopic measurements were performed on the sidewalls with a variation of the tip−sample separation during the voltage ramp. Such a technique ensures a large dynamic range of the conductance.[28] In areas where no antisite is visible, measurements reveal the typical spectrum of a GaAs(110) NW sidewall[29] (lower curve in Figure 3) with the valence band at negative voltages and the conduction band at positive voltages. Both bands are separated by a zero-conductance region that has the width of GaAs bulk band gap at 300 K. Note, the Fermi level $E_F$ at the surface of the sidewalls is positioned at midgap.

On the antisites, the spectrum also gives a value of the band gap comparable to that of bulk GaAs, and the band edges show a similar shape (upper curve in Figure 3). But, two additional peaks are now visible in the band gap region. We attribute their existence to the tunneling of electrons into or out of the band of midgap donor states induced by the antisites. In undoped LT-GaAs thick films, the Fermi level is not pinned inside the film[30] and should be positioned above both the 0/+ and +/++

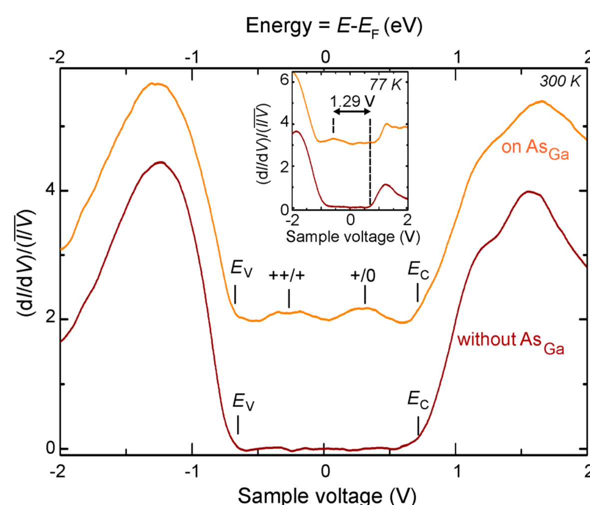


**Figure 3.** Tunneling spectra acquired on a subsurface antisite (upper curve) and in a region free of antisites (lower curve) at the surface of the LT-GaAs shell at a temperature of 300 K (inset: 77 K). Tunneling conditions: $V_{sample}$ = −2.5 V, $I_{tunnel}$ = 10 pA. The conduction, valence band edges, and the charge transition levels are indicated by vertical dashes, labeled $E_C$ and $E_V$, ++/+, and +/0, respectively. The upper curve has been shifted for clarity.

ionization levels of the antisite, leaving the donor states completely filled, the antisite being neutral. However, the high density of steps on the {110} sidewalls of GaAs NWs leads to a pinning of the Fermi level midgap.[29] As a result, the donor states associated with subsurface antisites are partially filled to compensate the charged defect states induced by the step. The Fermi level is thus positioned midgap between both ionization levels 0/+ and +/++, and this position accounts for the occurrence of two peaks in the tunneling spectra.[31] Thus, we expect that most arsenic antisites are single positively ionized in the LT-GaAs shell over a significant thickness of the shell due the strong corrugation of the sidewalls (∼half of the shell thickness, see Figure S3 in the Supporting Information). This is in analogy with previous spectroscopic measurements on subsurface As antisites in LT grown bulk materials,[26,27,32] where acceptors were used to shift the Fermi level. Thus, we can unambiguously assign the defects seen on the sidewalls of the LT-GaAs shell to subsurface arsenic antisites.

The physical impact of the antisites on the electronic and optical properties of the NWs were further investigated with pump−probe reflectivity and low-temperature cathodoluminescence (CL) experiments. The pump−probe reflectivity measurements performed at a wavelength of 820 nm revealed a carrier lifetime of 2.6 ps, much shorter than the typical lifetime of a few nanosecond found in GaAs/AlGaAs core−shell NWs.[33] While it is consistent with the short carrier lifetime that is found for pure unpassivated GaAs NWs,[34,35] we have performed similar experiments for a 1.5 $\mu$m thick LT-GaAs film grown on a GaAs substrate at 300 °C (see Supporting Information). The measured carrier lifetime is 1.6 ps and results from trapping at the antisites in such thin films,[36] suggesting that both surface states at the NW sidewalls and antisite defects contribute to the short lifetime in the LT-GaAs NWs.

The short lifetime due to a subsurface high recombination rate in the LT-GaAs NWs is further corroborated by the very weak signal observed in the cathodoluminescence (CL) spectrum of the As-capped LT-GaAs NWs: Figure 4 illustrates


DOI: 10.1021/acs.nanolett.5b01802
Nano Lett. 2015, 15, 6440−6445

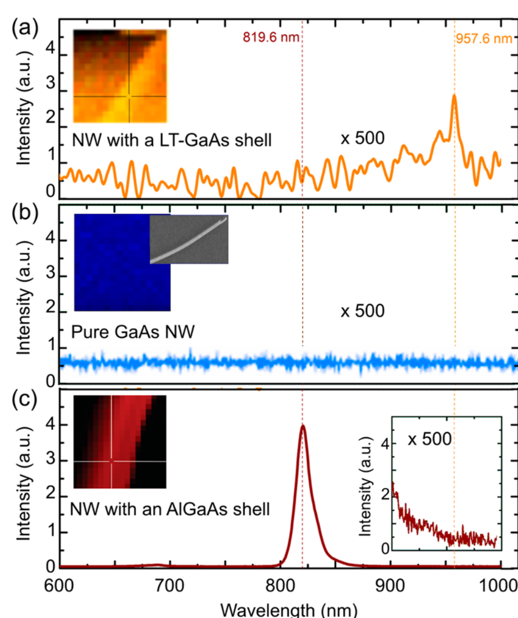


**Figure 4.** Low-temperature cathodoluminescence spectra of (a) a GaAs NW grown with a LT-GaAs shell, (b) a pure GaAs NW, and (c) a GaAs NW grown with an AlGaAs shell. The measurements were performed at 10 K with an electron beam of 10 kV and a current of 1 nA. Inset: Cathodoluminescence mappings showing the NW location. The markers indicate the position where the spectra were acquired on the NWs. For the pure GaAs NWs that do not show any CL signal, a SEM image is also shown. The absence of the free-exiton emission at 819.6 nm (1.51 eV, detected only in high-quality GaAs NW with AlGaAs shell) indicates a high defect density in the LT-GaAs NW. The weak peak at 957.6 nm (1.29 eV), not seen in the inset of (c), can be correlated to the energy separation between the ++/+ ionization level and the conduction band measured in STS (inset Figure 3).

that the peak at 819.6 nm (1.51 eV) related to the free-exciton emission of GaAs, seen in the CL spectrum of a high-quality GaAs/AlGaAs core−shell NW, is absent in the CL spectrum of the LT-GaAs NW. Instead a new but small peak appears at 957.6 nm (1.29 eV), that is not found in pure GaAs NWs. Comparison with tunneling spectroscopic measurements performed at 77 K (inset of Figure 3) shows that this transition corresponds to the energy between the conduction band edge of GaAs and the +/++ ionization level, allowing to assign this sub-bandgap emission to the antisites. Hence, the LT-GaAs NW contain a high defect concentration assignable to $As_{Ga}$ antisites in good agreement with short carrier lifetimes and the STM results.

In addition to arsenic antisites, small clusters occur in the highest part of the NWs as visible in the SEM image of Figure 5a (inset). The filled-state STM images reveal that the clusters (protrusions in Figure 5a) are surrounded by a dark area. The observation of a dark layer around the clusters implies the existence of a depleted zone.[37] This interpretation is confirmed by the tunneling spectra acquired on a well-ordered region of the sidewall and on the dark layer (spectra i and ii in Figure 5b). The apparent bandgap observed on the dark layer is wider, due to a smaller free carrier concentration in the depleted material.[38] The clusters themselves are found to exhibit a small but steadily decrease of the conductivity in the tunneling spectrum (iii) in Figure 5b. This is a signature of a metallic behavior. Therefore, we attribute the dark zone surrounding the clusters to a depletion zone arising from the formation of a Schottky barrier between a metallic cluster and the GaAs matrix, in agreement with arsenic precipitates in bulk GaAs.[37] As the presence of Ga clusters can be ruled out, these clusters are identified as arsenic precipitates.

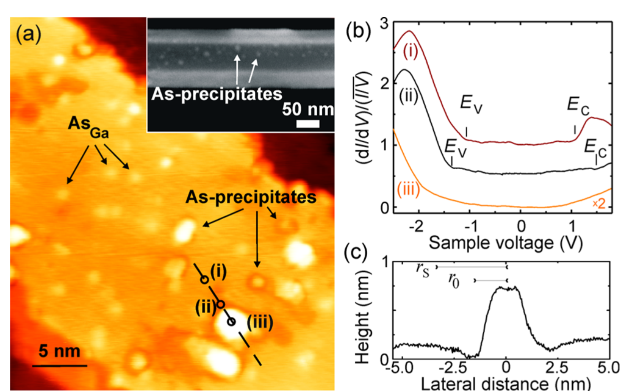


**Figure 5.** (a) STM and SEM (shown as inset) images of the top part of a NW transferred onto a Ag/Si(111) surface after the sublimation of the capping layer. Several As precipitates and three $As_{Ga}$ arsenic antisites are highlighted. Color scale of the STM image: 15 Å. (b) Tunneling spectra acquired at the positions indicated in (a) by circles numbered i−iii. The conduction and valence band edges are indicated by vertical dashes and labeled $E_C$ and $E_V$, respectively. (c) Height profile measured along the dashed line shown in a. $r_0$ and $r_s$ correspond to the radius of the precipitate and of the positively charged sphere surrounding the precipitate. Tunneling conditions: $V_{sample}$ = −3.0 V, $I_{tunnel}$ = 10 pA, $T$ = 77 K.

The As precipitates are able to capture electrons. The number $n$ of electrons stored in a precipitate of radius $r_0$ corresponds to $n = (4\pi\varepsilon/q)\, r_0\phi_b$, with $\varepsilon$ the permittivity of GaAs, $q$ the elementary charge, and $\phi_b$ the built-in potential.[39] In the STM image of Figure 5a, the precipitate that is analyzed in the line profile has a radius $r_0$ of 1.6 nm. Assuming a typical barrier height of 0.8 V[39] and taking into account the observed midgap pinning of the Fermi level (Figure 5b), a built-in potential $\phi_b$ of 100 mV is deduced, corresponding to the capture of roughly one electron per precipitate. Based on the concentration of ionized arsenic antisites $N_{DD}$ that appears similar in Figure 5 and Figure 2, we can then estimate the width of the depletion zone around the precipitates. The condition of charge balance implies the formation of a positively charged sphere with radius $r_s$ around a precipitate. As a result, the negative charge Q found in the precipitate is related to $r_s$ by

$$Q = \frac{4\pi}{3}(r_s^3 - r_0^3)eN_{DD} \tag{1}$$

yielding $r_s$ = 3.5 nm. Subtracting $r_0$ from $r_s$ leads to a depleted zone, consistent with the height profile of Figure 5c. Remarkably, when the precipitates are close enough, the depletion spheres overlap, allowing the direct visualization of the As precipitate model to account for the semi-insulating character of annealed LT-GaAs layers.[39]

Finally, the As precipitates were only observed on the top part of the NWs. They are known to result from the accretion of arsenic point defects upon annealing, predominantly As interstitials that are much more mobile than $As_{Ga}$ and can thus form precipitates at much lower temperature.[40] As this incorporation of excess of arsenic is directly related to the growth temperature,[41] we suspect that it is caused by an


DOI: 10.1021/acs.nanolett.5b01802
*Nano Lett.* 2015, 15, 6440−6445

inhomogeneous temperature profile along the NW during the growth. Such a lower temperature at the top of the NW can be explained by heat losses that are expected to be the highest at the top part of the NW, since it is surrounded by "cold" vacuum, in contrast to the bottom that sees the hot surfaces of the surrounding NWs. Hence by a suitable choice of the growth temperature, the NW electronic properties could be tuned by point defects or precipitates leading to hopping via localized states or to a semi-insulating state, respectively.

In conclusion, we have investigated the structural, electronic, and optical properties of a LT-GaAs shell grown around GaAs NWs. Although the radial growth of the shell gives rise to rough sidewalls, the low temperature growth does not preclude the formation of a shell with a good crystallinity as deduced by the crystallographic characterization of the NW surface. It further allows the successful incorporation of excess arsenic in the GaAs matrix in the form of arsenic antisites. Depending on the annealing, the shell can also contain As precipitates. All of these defects introduce midgap states that are key elements to simultaneously obtain a short carrier lifetime and a low electrical conductivity, suggesting that the shell has the required properties for terahertz and photoconductive applications.

## ■ ASSOCIATED CONTENT

### Ⓢ Supporting Information

The Supporting Information is available free of charge on the ACS Publications website at DOI: 10.1021/acs.nanolett.5b01802.

TEM analysis of the nanowires, pump−probe reflectivity experiments (PDF)

## ■ AUTHOR INFORMATION

### Corresponding Author

*E-mail: bruno.grandidier@isen.iemn.univ-lille1.fr.

### Notes

The authors declare no competing financial interest.

## ■ ACKNOWLEDGMENTS

This study was financially supported by the European Community's Seventh Framework Program (Grant No. PITN-GA-2012-316751, "Nanoembrace" Project), the EQUIPEX program Excelsior, the RENATECH network, and the Impuls und Vernetzungsfond of the Helmholtz-Gemeinschaft Deutscher Forschungszentren (Grant No. HIRG-0014). T.X. acknowledges the support of the Region Nord-Pas-de-Calais and of the National Natural Science Foundation of China (Grant No. 61204014). T.D. acknowledges funding by DGA. F.M. and A.F.iM. thank SNF (Grant No. 143908). G.T., H.A.P. and A.F.iM. thank funding through the NCCR QSIT. A.F.iM. thanks the DAR of EPFL for funding the CL set-up. The authors thank X. Wallart for fruitful discussions.

## ■ REFERENCES

(1) Caroff, P.; Dick, K. A.; Johansson, J.; Messing, M. E.; Deppert, K.; Samuelson, L. *Nat. Nanotechnol.* **2009**, *4*, 50−55.

(2) Dheeraj, D. L.; Patriarche, G.; Zhou, H.; Hoang, T. B.; Moses, A. F.; Grønsberg, S.; Van Helvoort, A. T. J.; Fimland, B.-O.; Weman, H. *Nano Lett.* **2008**, *8*, 4459−4463.

(3) Kretinin, A. V.; Popovitz-Biro, R.; Mahalu, D.; Shtrikman, H. *Nano Lett.* **2010**, *10*, 3439−3445.

(4) Tang, J.; Huo, Z.; Brittman, S.; Gao, H.; Yang, P. *Nat. Nanotechnol.* **2011**, *6*, 568−572.

(5) Ferguson, B.; Zhang, X. C. *Nat. Mater.* **2002**, *1*, 26−33.

(6) Nagel, M.; Först, M.; Kurz, H. *J. Phys.: Condens. Matter* **2006**, *18*, S601.

(7) Liu, H. B.; Zhong, H.; Karpowicz, N.; Chen, Y.; Zhang, X.-C. *Proc. IEEE* **2007**, *95*, 1514−1527.

(8) Jepsen, P. U.; Cooke, D. G.; Koch, M. *Laser Photon. Rev.* **2011**, *5*, 124−166.

(9) Tchernycheva, M.; Harmand, J. C.; Patriarche, G.; Travers, L.; Cirlin, G. E. *Nanotechnology* **2006**, *17*, 4025.

(10) Plissard, S.; Dick, K. A.; Larrieu, G.; Godey, S.; Addad, A.; Wallart, X.; Caroff, P. *Nanotechnology* **2010**, *21*, 385602.

(11) Ahn, H.; Ku, Y.-P.; Wang, Y.-C.; Chuang, C.-H.; Gwo, S.; Pan, C. L. *Appl. Phys. Lett.* **2007**, *91*, 132108.

(12) Seletskiy, D. V.; Hasselbeck, M. P.; Cederberg, J. G.; Katzenmeyer, A.; Toimil-Molares, M. E.; Léonard, F.; Talin, A. A.; Sheik-Bahae, M. *Phys. Rev. B: Condens. Matter Mater. Phys.* **2011**, *84*, 115421.

(13) Trukhin, V. N.; Buyskikh, A. S.; Kaliteevskaya, N. A.; Bourauleuv, A. D.; Samoilov, L. L.; Samsonenko, Y. B.; Cirlin, G. E.; Kaliteevski, M. A.; Gallant, A. J. *Appl. Phys. Lett.* **2013**, *103*, 072108.

(14) Lee, W. J.; Ma, J. W.; Bae, J. M.; Jeong, K. S.; Cho, M. H.; Kang, C.; Wi, J. S. *Sci. Rep.* **2013**, *3*, 3.

(15) Arlauskas, A.; Treu, J.; Saller, K.; Beleckaitė, I.; Koblmüller, G.; Krotkus, A. *Nano Lett.* **2014**, *14*, 1508−1514.

(16) Peytavit, E.; Arscott, S.; Lippens, D.; Mouret, G.; Matton, S.; Masselin, P.; Bocquet, R.; Lampin, J. F.; Desplanque, L.; Mollot, F. *Appl. Phys. Lett.* **2002**, *81*, 1174−1176.

(17) Mikulics, M.; Michael, E. A.; Schieder, R.; Stutzki, J.; Güsten, R.; Marso, M.; Van der Hart, A.; Bochem, H. P.; Lüth, H.; Kordoš, P. *Appl. Phys. Lett.* **2006**, *88*, 041118.

(18) Dufouleur, J.; Colombo, C.; Garma, T.; Ketterer, B.; Uccelli, E.; Nicotra, M.; Fontcuberta i Morral, A. *Nano Lett.* **2010**, *10*, 1734−1740.

(19) Heigoldt, M.; Arbiol, J.; Spirkoska, D.; Rebled, J. M.; Conesa-Boj, S.; Abstreiter, G.; Peiro, F.; Morante, J. R.; Fontcuberta i Morral, A. *J. Mater. Chem.* **2009**, *19*, 840−848.

(20) Matteini, F.; Tütüncüoglu, G.; Potts, H.; Jabeen, F.; Fontcuberta i Morral, A. *Cryst. Growth Des.* **2015**, *15*, 3105−3109.

(21) Xu, T.; Dick, K. A.; Plissard, S.; Nguyen, T. H.; Makoudi, Y.; Berthe, M.; Nys, J.-P.; Wallart, X.; Grandidier, B.; Caroff, P. *Nanotechnology* **2012**, *23*, 095702.

(22) Zhou, Z. Y.; Zheng, C. X.; Tang, W. X.; Jesson, D. E.; Tersoff, J. *Appl. Phys. Lett.* **2010**, *97*, 121912.

(23) Heiss, M.; et al. *Phys. Rev. B: Condens. Matter Mater. Phys.* **2011**, *83*, 045303.

(24) Tejedor, P.; Šmilauer, P.; Roberts, C.; Joyce, B. A. *Phys. Rev. B: Condens. Matter Mater. Phys.* **1999**, *59*, 2341.

(25) Tejedor, P.; Šmilauer, P.; Joyce, B. A. *Surf. Sci.* **1999**, *424*, L309−L313.

(26) Feenstra, R. M.; Woodall, J. M.; Pettit, G. D. *Phys. Rev. Lett.* **1993**, *71*, 1176.

(27) Grandidier, B.; Chen, H.; Feenstra, R. M.; McInturff, D. T.; Juodawlkis, P. W.; Ralph, S. E. *Appl. Phys. Lett.* **1999**, *74*, 1439−1441.

(28) Feenstra, R. M. *Phys. Rev. B: Condens. Matter Mater. Phys.* **1994**, *50*, 4561−4570.

(29) Capiod, P.; Xu, T.; Nys, J. P.; Berthe, M.; Patriarche, G.; Lymperakis, L.; Neugebauer, J.; Caroff, P.; Dunin-Borkowski, R. E.; Ebert, Ph.; Grandidier, B. *Appl. Phys. Lett.* **2013**, *103*, 122104.

(30) Warren, A. C.; Woodall, J. M.; Kirchner, P. D.; Yin, X.; Pollak, F.; Melloch, M. R.; Otsuka, N.; Mahalingam, K. *Phys. Rev. B: Condens. Matter Mater. Phys.* **1992**, *46*, 4617.

(31) De La Broise, X.; Delerue, C.; Lannoo, M.; Grandidier, B.; Stiévenard, D. *Phys. Rev. B: Condens. Matter Mater. Phys.* **2000**, *61*, 2138.

(32) Grandidier, B.; Nys, J. P.; Delerue, C.; Stievenard, D.; Higo, Y.; Tanaka, M. *Appl. Phys. Lett.* **2000**, *77*, 4001−4003.

(33) Demichel, O.; Heiss, M.; Bleuse, J.; Mariette, H.; Fontcuberta I Morral, A. *Appl. Phys. Lett.* **2010**, *97*, 201907.

(34) Parkinson, P.; Lloyd-Hughes, J.; Gao, Q.; Tan, H. H.; Jagadish, C.; Johnston, M. B.; Herz, L. M. *Nano Lett.* **2007**, *7*, 2162−2165.

(35) Chang, C. C.; Chi, C. Y.; Yao, M.; Huang, N.; Chen, C. C.; Theiss, J.; Bushmaker, A. W.; LaLumondiere, S.; Yeh, T.-W.; Povinelli, M. L.; Zhou, C.; Dapkus, P. D.; Cronin, S. B. *Nano Lett.* **2012**, *12*, 4484−4489.

(36) Adomavičius, R.; Krotkus, A.; Bertulis, V.; Sirutkaitis, V.; Butkus, R.; Piskarskas, A. *Appl. Phys. Lett.* **2003**, *83*, 5304−5306.

(37) Feenstra, R. M.; Vaterlaus, A.; Woodall, J. M.; Pettit, G. D. *Appl. Phys. Lett.* **1993**, *63*, 2528−2530.

(38) Jäger, N. D.; Ebert, P.; Urban, K.; Krause-Rehberg, R.; Weber, E. R. *Phys. Rev. B: Condens. Matter Mater. Phys.* **2002**, *65*, 195318.

(39) Warren, A. C.; Woodall, J. M.; Freeouf, J. L.; Grischkowsky, D.; McInturff, D. T.; Melloch, M. R.; Otsuka, N. *Appl. Phys. Lett.* **1990**, *57*, 1331−1333.

(40) Melloch, M. R.; Otsuka, N.; Mahalingam, K.; Chang, C. L.; Woodall, J. M.; Pettit, G. D.; Kirchner, P. D.; Cardone, F.; Warren, A. C.; Nolte, D. D. *J. Appl. Phys.* **1992**, *72*, 3509−3513.

(41) Luysberg, M.; Sohn, H.; Prasad, A.; Specht, P.; Liliental-Weber, Z.; Weber, E. R.; Gebauer, J.; Krause-Rehberg, R. *J. Appl. Phys.* **1998**, *83*, 561−566.



DOI: 10.1021/acs.nanolett.5b01802
*Nano Lett.* 2015, 15, 6440−6445

NANO LETTERS

Letter

pubs.acs.org/NanoLett

# Self-Equilibration of the Diameter of Ga-Catalyzed GaAs Nanowires

V. G. Dubrovskii,[†,‡,§] T. Xu,[∥,⊥] A. Díaz Álvarez,[∥] S. R. Plissard,[∥,#] P. Caroff,[∥,∇] F. Glas,[○] and B. Grandidier*[,∥]

[†]St. Petersburg Academic University, Khlopina 8/3, 194021, St. Petersburg, Russia

[‡]Ioffe Physical Technical Institute RAS, Politekhnicheskaya 26, 194021, St. Petersburg, Russia

[§]ITMO University, Kronverkskiy pr. 49, 197101 St. Petersburg, Russia

[∥]Institut d'Electronique, de Microélectronique et de Nanotechnologies (IEMN), CNRS, UMR 8520, Département ISEN, 41 bd Vauban, 59046 Lille Cedex, France

[⊥]Sino-European School of Technology, Shanghai University, 99 Shangda Road, Shanghai, 200444, People's Republic of China

[#]CNRS-Laboratoire d'Analyse et d'Architecture des Systèmes (LAAS), Université de Toulouse, 7 avenue du colonel Roche, 31400 Toulouse, France

[∇]Department of Electronic Materials Engineering, Research School of Physics and Engineering, The Australian National University, Canberra, ACT 0200, Australia

[○]CNRS-Laboratoire de Photonique et de Nanostructures (LPN), Route de Nozay, 91460 Marcoussis, France

**ABSTRACT:** Designing strategies to reach monodispersity in fabrication of semiconductor nanowire ensembles is essential for numerous applications. When Ga-catalyzed GaAs nanowire arrays are grown by molecular beam epitaxy with help of droplet-engineering, we observe a significant narrowing of the diameter distribution of the final nanowire array with respect to the size distribution of the initial Ga droplets. Considering that the droplet serves as a nonequilibrium reservoir of a group III metal, we develop a model that demonstrates a self-equilibration effect on the droplet size in self-catalyzed III–V nanowires. This effect leads to arrays of nanowires with a high degree of uniformity regardless of the initial conditions, while the stationary diameter can be further finely tuned by varying the spacing of the array pitch on patterned Si substrates.

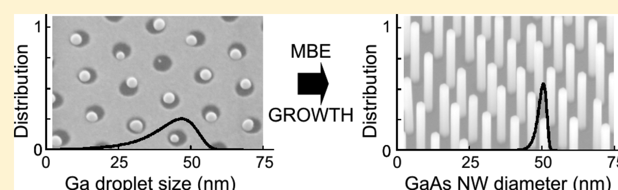


**KEYWORDS:** *III–V nanowires, silicon integration, self-catalyzed growth, growth kinetics, size distribution, focusing effect*

Growing semiconductor materials with high precision at the nanoscale is essential to improve the efficiencies of ongoing technologies.[1−4] Among the existing growth methods for compound semiconductor nanostructures, a few rely on the use of a tiny reservoir consisting of one of the element composing the nanostructure. A prototypical case is a reservoir of the group III metal during growth of III–V coumpound semiconductors. Such a reservoir initiates or fuels epitaxial growth leading to the formation of nanostructures with specific geometries such as rings and wires.[5−7] For nanowires (NWs), the so-called self-catalyzed growth is based on the vapor–liquid–solid (VLS) mechanism assisted by a group III metal droplet and has been successfully demonstrated with Ga droplets and also In droplets.[8−13] In contrast to the other common Si-compatible growth technique, namely the catalyst-free selective-area epitaxy,[14,15] self-seeded NWs have been shown to easily reach crystal phase purity.[9,16,17]

In the self-catalyzed VLS growth, the NW elongation rate is controlled entirely by the kinetics of group V species,[6,18] while the catalyst particle undergoes a significant and unavoidable attachment and detachment of group III metal atoms. The incoming atoms can either directly impinge from vapor or diffuse from the NW sidewalls to feed the droplet. Changing the different fluxes can thus result in a significant modification of the NW morphology including the NW diameter, because the latter is known to be governed by the size of the droplet.[18−20] As homogeneity of the NW diameter and shape is essential for making reproducible devices[21,22] and crucial for improving the collective properties of NW arrays,[23,24] there is a strong demand to control the behavior of the droplet size in the self-catalyzed VLS growth.

Here, we examine the diameter evolution of Ga-catalyzed GaAs NWs grown by droplet-engineered molecular beam epitaxy (MBE). Such a method has been shown to give a high yield of vertical GaAs NWs when a Ga predeposition step is added prior to growth initiation and when a good control over the surface properties of the patterned material exposed to growth is achieved.[25−27] As a new milestone, we show that under appropriate growth conditions the NW diameters converge toward a critical value that is directly related to the size evolution of the droplet during the self-catalyzed growth. By theoretically investigating the dynamical change of the

**Received:** June 5, 2015
**Revised:** June 29, 2015


© XXXX American Chemical Society

DOI: 10.1021/acs.nanolett.5b02226
*Nano Lett.* XXXX, XXX, XXX–XXX

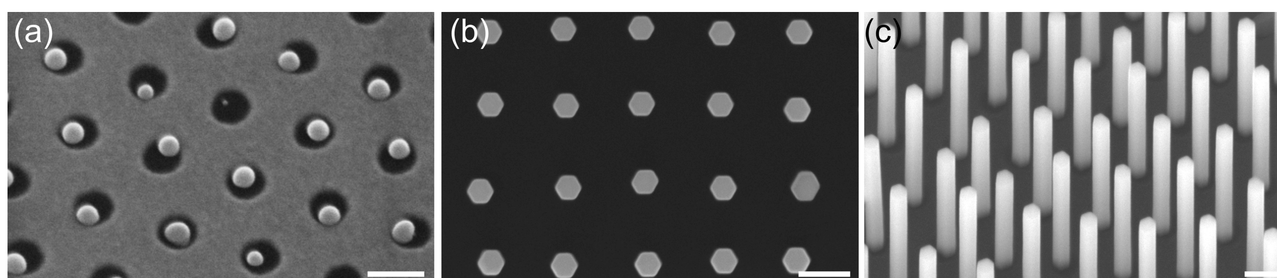


Figure 1. (a) A 30° tilted SEM image of Ga droplets obtained after predeposition of Ga onto a hole array defined in a $SiO_2$ native oxide on a Si(111) substrate using electron beam lithography and etching. The diameter of the holes is 60 nm and the pitch between the holes is 100 nm. (b,c) Top view and 30° tilted SEM images of self-catalyzed GaAs NWs grown from the array of Ga droplets shown in (a). The scale bar corresponds to 100 nm.

droplet size as a function of the incoming flux and the crystallization rate of the NW, we demonstrate the key role of the diffusion-induced contribution of Ga adatoms in focusing the droplet size distribution. This self-equilibration of the droplet size in self-catalyzed III–V NWs enables the formation of unique NW arrays with very narrow distribution of the NW diameters despite being initially grown from differently sized droplets. The critical diameter can be further finely tuned by the wire-to-wire spacing.

In our experiments, the growth of GaAs NW on Si(111) substrates was achieved through three steps, as described previously:[28] (i) patterning of a hole array in a thin silicon dioxide layer to allow the precise positioning of the NWs on a silicon substrate, (ii) predeposition of Ga to form droplets in the etched holes and (iii) MBE growth of NWs. The NW growth was performed at a temperature of 630 °C, an As/Ga growth rate equivalent ratio of 1.8 and a two-dimensional equivalent growth rate of GaAs of one monolayer per second. Figure 1 shows scanning electron microscopy (SEM) images obtained after steps (ii) and (iii) for an array of holes with a diameter of 60 nm and a pitch of 100 nm. It is seen that the Ga predeposition leads to the formation of Ga droplets in the oxide-free openings only, resulting in the growth of NWs at the position of the holes. While the diameter of the Ga droplets varies significantly from hole to hole (the droplet diameter distribution may depend on the droplet preparation process but is never uniform), we notice a high degree of uniformity of the NW diameters with minimal tapering effect due to the low V/III ratio.

This difference between the droplet size distribution and the NW diameter distribution was reproducible, whatever the initial size and the pitch between the holes in the array were. For example, Figure 2 compares the size distribution of the Ga droplets with the distribution of the NW diameters for an array with a hole size of 60 nm and a pitch of 250 nm. Again, the NWs in the array are quite uniform and the NW diameter distribution appears clearly much narrower than the hole size distribution. Remarkably, the Ga-catalyzed growth of NWs leads to a focusing effect toward a diameter of ~50 nm, slightly bigger than the peak value of the droplet size distribution, but still smaller than the hole size. In order to understand this striking difference, we establish the following model.

As mentioned above, the elongation rate of Ga-catalyzed GaAs NWs is limited by the kinetics of As species that arrive at and desorb from the droplet surface but do not diffuse from the sidewalls.[6,18,29,30] Because of a known low solubility of As in liquid Ga, the catalyst droplet consists of almost pure Ga and serves as a Ga reservoir for arriving As species. Therefore, the

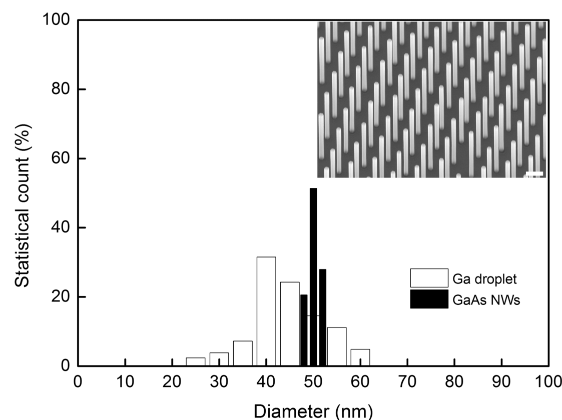


Figure 2. Histograms of the Ga droplet size distribution and the NW diameter distribution. Inset: 30° tilted SEM images of the corresponding array of GaAs NWs. For this array, the hole size and pitch are 60 and 250 nm, respectively. Scale bar in the inset corresponds to 100 nm.

droplet can either inflate or shrink with time depending on the balance of Ga species.[18] Indeed, the total number of Ga atoms in the droplet $N$ changes in time according to

$$\frac{dN}{dt} = \chi I \pi R^2 + 2I\lambda R \sin \alpha - \frac{\pi R^2}{\Omega_{GaAs}} \frac{dL}{dt} \quad (1)$$

Here, $I$ is the direct atomic flux of Ga, $\chi$ is the geometrical function that depends on the contact angle $\beta$ of the droplet and the incident angle $\alpha$ of the Ga beam and equals $1/\sin^2 \beta$ when $\beta \geq \pi/2 + \alpha$,[31] $R$ is the radius of cylindrical NW, $\lambda$ is the effective diffusion length of Ga adatoms on the NW sidewalls, $\Omega_{GaAs}$ = 0.0452 $nm^3$ is the volume per GaAs pair in the solid and $dL/dt$ is the NW elongation rate. The first term stands for the direct impingement of Ga, the second gives the diffusion-induced contribution of Ga adatoms from the length $\lambda$ beneath the droplet (more complex scenarios of the diffusion fluxes are given, for example, in refs 32 and 33) and the third describes the sink due to the NW elongation.

The droplet volume equals $V = \Omega_{Ga} N = (\pi R^3/3) f(\beta)$, where $\Omega_{Ga}$ = 0.02 $nm^3$ is the Ga atomic volume in liquid[34] and $f(\beta) = (1-\cos \beta)(2 + \cos \beta)/[(1 + \cos \beta)\sin \beta]$ is the geometrical function relating the volume of a spherical cap to the radius of its base. Assuming $\beta$ as being independent of radius and using eq 1, we arrive at


DOI: 10.1021/acs.nanolett.5b02226
Nano Lett. XXXX, XXX, XXX–XXX

$$\frac{dR}{dt} = -A + \frac{B}{R} \tag{2}$$

with

$$A = \frac{\Omega_{Ga}}{\Omega_{GaAs} f(\beta)}\left(\frac{dL}{dt} - \chi\nu\right); \quad B = \frac{2\Omega_{Ga}}{\pi \Omega_{GaAs} f(\beta)}\nu\lambda \sin\alpha \tag{3}$$

and $\nu = I\Omega_{GaAs}$ as the Ga deposition rate in nm/s. Obviously, the behavior of the NW radius is very different at $A > 0$ and $A < 0$. When the effective Ga imbalance is positive ($A < 0$), that is, more Ga atoms are brought from vapor to the droplet than removed from it to grow a NW, the droplet will inflate with the help of surface diffusion ($B$) and consequently the NW will extend radially regardless of its initial dimension (the regime of radial growth).[18] This situation corresponds to low As influx which yields small elongation rates such that $dL/dt < \chi\nu$. Whenever $A > 0$, that is, more Ga atoms are removed from the droplet due to crystallization than brought from vapor, the situation becomes completely different. An additional diffusion flux of sidewall Ga adatoms will have a focusing effect on the diameter, that is, small NWs with $R < R_c$ will extend and large NWs with $R > R_c$ shrink to reach the critical radius $R_c = B/A$ (the regime of diameter self-equilibration).

The radius distribution $f(R,t)$ of NWs at time $t$ obeys the following first order equation[35,36]

$$\frac{\partial f(R,t)}{\partial t} = -\frac{\partial}{\partial R}\left[\frac{dR}{dt} f(R,t)\right] \tag{4}$$

where the initial condition is determined by the size distribution of Ga droplets prior to growth. Introducing the scaled size $r = R/R_c$ and scaled time $x = t/\tau$ with $\tau = R_c/A = B/A^2$ as the characteristic relaxation time, solutions to eqs 2 and 4 can be put in the universal form with the minimized number of parameters. The time-dependent radius of individual NW that has emerged from the droplet of radius $r_0 = R_0/R_c$ at $t = 0$ is given by

$$x = r_0 - r + \ln\left(\frac{r_0 - 1}{r - 1}\right) \tag{5}$$

In particular, this equation applies to the most representative NW radius $r_*(x)$ which corresponds to the most representative size of the initial droplets $r_*^0$ at $t = 0$. The size distribution is obtained in the form:

$$f(r,x) = \frac{cr}{|r-1|} g\left[r_*(x) - r + \ln\left|\frac{r_*(x) - 1}{r - 1}\right|\right] \tag{6}$$

where the time dependence $r_*(x)$ is determined by eq 5 with $r_0 = r_*^0$. The shape of the function $g(y)$ is time-invariant and is defined by the initial size distribution of the Ga droplets, while the time evolution of the NW diameter distribution is described by the time dependence of the most representative size $r_*(x)$. The combination of variables in the argument of $g$ is the first integral of eq 4, while the prefactor $c$ ensures the correct normalization of the distribution.

Figure 3 shows the narrowing effect in the scaled variables for an ensemble of droplets described by the Gaussian distribution $g(y) = (1/\Delta r\sqrt{\pi} \exp(-y^2/\Delta r^2)$ with the initial distribution width $\Delta r = 0.5$ and the initial mean size $r_*^0 = 1.5$. It is seen that our nonlinear system features quite unique behavior where the mean size self-equilibrates to $R_c$ and this process gradually decreases the effective width of the size distribution.

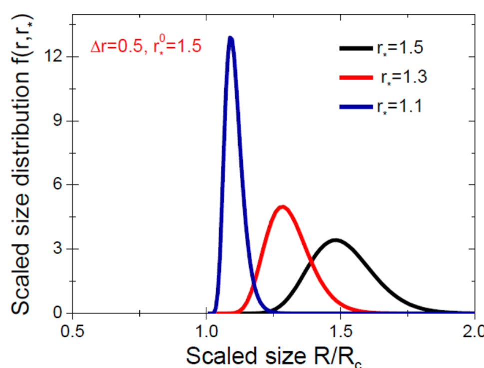


**Figure 3.** Evolution of the initial radius distribution with the width $\Delta r = 0.5$ to a much narrower distribution as the scaled mean size tends to one.

To observe this focusing effect on the diameters of Ga-catalyzed NWs, one needs to fulfill the condition $dL/dt > \chi\nu$, which requires high enough As influx. In our case, the GaAs NWs reach ~1 $\mu$m length after 300 s of growth, therefore the average elongation rate equals $dL/dt$ = 3.33 nm/s. The equivalent two-dimensional growth rate $\nu \cos\alpha$ equals 0.326 nm/s, yielding $\nu = 0.360$ nm/s at $\alpha = 25°$. Taking the average value of the contact angle $\beta = 115°$, we obtain the Ga flux impinging the droplet at $\chi\nu$ = 0.438 nm/s. Therefore, the difference $dL/dt - \chi\nu$ = 2.89 nm/s in our case is positive and large, which definitely favors the self-equilibration regime. With these plausible parameters, we obtain $A$ = 0.300 nm/s. Using the value of $R_c$ of 25 nm (because the critical diameter is close to 50 nm from Figure 2), we arrive at $B = 7.50$ nm$^2$/s. On the basis of eq 3, we deduce a reasonable estimate for the effective diffusion length of Ga adatoms at the NW sidewalls of $\lambda = 750$ nm. Indeed, with the effective distance between the neighboring NWs of approximately 250 nm the collection length limited by the shadow effect in this array[37,38] would be about 540 nm. Larger $\lambda$ obtained from our fits should be due to the simplified form of the Ga diffusion flux in eq 1 that does not precisely describe the initial growth stage at $L < \lambda$.[31,32] Finally, the relaxation time $\tau$ equals 83 s, which is noticeably shorter than the total growth time of 300 s. The distribution of the NW top diameters is therefore expected to be almost completely equilibrated after stopping the growth.

Figure 4 shows the plots of NW diameters $D = 2R$ versus time obtained from eq 5 with the above parameters and at different initial droplet diameters ranging from 25 to 60 nm. The effect of self-equilibration is clearly seen and correlates with the experimental histograms at $t_g$ = 300 s. The size distribution is narrowed from 25 to 60 nm to ~50 nm, as observed in Figure 2, while thinner and thicker NWs are no longer present in the histograms. The described effect is very important because it will transform an arbitrary broad diameter distribution of the initial Ga droplets to the asymptotically uniform distribution provided that the growth time is long enough to allow for the complete size relaxation. After reaching this size-uniform state, the NWs will continue to elongate with stationary diameter and at almost diameter-independent rate that also yields the uniform length. This explains why the ensembles of Ga-catalyzed GaAs NWs usually have more uniform dimensions compared to Au-catalyzed ones.[39]

According to the quantitative nucleation-based model of Glas et al.,[30] the growth rate of a self-catalyzed NW under steady


DOI: 10.1021/acs.nanolett.5b02226
Nano Lett. XXXX, XXX, XXX−XXX

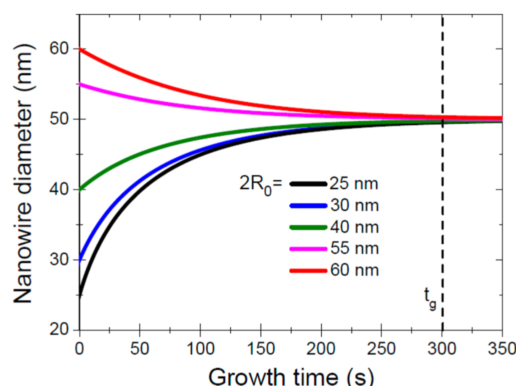


**Figure 4.** Theoretical time-dependent variations of the NW diameters obtained from eq 5 with different $R_0$. The vertical dash segment indicates the experimental growth time $t_g$ of 300 s.

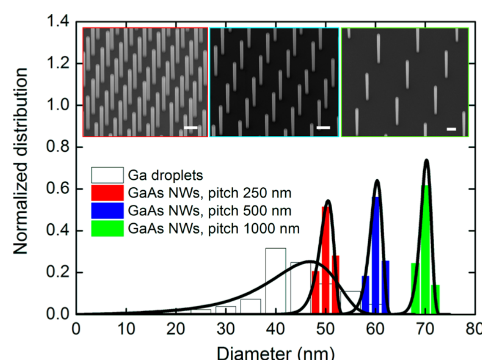


**Figure 5.** Histograms showing the distribution of the Ga droplet size and NW diameter for arrays with a hole size of 60 nm and three different pitches (left, 250 nm; middle: 500 nm; right, 1000 nm). Inset: 30° tilted SEM images of the corresponding GaAs NW arrays. The scale bar is 200 nm. The solid lines show the theoretical fits obtained from eqs 5 and 6.

state fluxes depends on the NW radius (this is partly due to the different areas available for nucleation at the liquid–solid interface of differently sized NWs). The fact that narrow NWs may grow very slowly should effectively produce some reduction of NW radius distribution with respect to an initial droplet diameter distribution. However, the same does not hold for large NW radii and the expected narrowing is much less marked than in the present model. Moreover, the analysis of ref 30, assumes a constant radius for each NW and therefore ignores the self-equilibration mediated by radius changes that is described here. In this sense, the diameter self-equilibration in self-catalyzed III–V NWs resembles the height equilibration of self-induced GaN NWs.[40] This effect is caused by completely different physical reasons but also leads to stable asymptotic size-uniformity, while narrowing the length distribution of Ge NWs described in ref 33 could be reached only at a certain moment of time. We also note that a diameter self-regulation in array of NWs has recently been reported for catalyst-free, spontaneously formed GaN NWs.[41] However, the mechanism of the diameter self-equilibration in our case is different and is associated with the reservoir effect of nonequilibrium Ga droplet while no such droplet is present on top of any self-induced NWs.

Furthermore, Figure 5 shows that the stationary diameter of NWs can be tuned by the pitch of the Ga droplet array. The normalized histograms of the diameter distributions show the large dispersion of the Ga droplet sizes that equilibrate to regular arrays of 50, 60, and 70 nm diameter NWs in the course of growth for the pitch of 250, 500, and 1000 nm, respectively. The diameter distributions are fitted by eqs 5 and 6 with the same parameter as before but with different $2R_c \sim 50$, 60, and 70 nm depending on the pitch. The increase of the stationary diameter is well-understood through the shadowing effect,[37,38] which is important for the smallest pitch but vanishes for the large pitches. Thus, the effective collection length of Ga increases for larger pitches and finally becomes limited by the Ga incorporation to the growing shells around the NW (this process is necessary to maintain a uniform NW diameter from base to top). The increase of $\lambda$ raises the $B$ value in eq 3 and therefore results in the larger stationary diameter that is proportional to $B$. In other words, the Ga transport into the droplet can be regulated by the wire-to-wire spacing and the resulting NW diameter can be finely tuned to the desired value.

In conclusion, we have demonstrated experimentally and described theoretically the effect of the diameter self-equilibration in Ga-catalyzed GaAs NWs that produces regular arrays of NWs regardless of the initial droplet size distribution. This effect is not at all restricted to particular epitaxy technique or deposition conditions and should be observed in all self-catalyzed VLS systems where the low vapor flux of a group III metal is compensated by diffusion of surface adatoms. The resulting NW arrays show a very high degree of the diameter uniformity while the stationary diameter can be tuned by the growth conditions or geometrical parameters such as the array pitch on patterned Si substrates. The described self-equilibration effect is important from the fundamental view-point and should be useful for applications that require the controlled fabrication of regular NW arrays with tunable diameters.

## AUTHOR INFORMATION

### Corresponding Author

*E-mail: bruno.grandidier@isen.iemn.univ-lille1.fr.

### Notes

The authors declare no competing financial interest.

## ACKNOWLEDGMENTS

This study was supported by the European Community's Seventh Framework Program (Grant PITN-GA-2012-316751, "Nanoembrace" Project), the EQUIPEX program Excelsior, the RENATECH network. T.X. acknowledges the supports of the Region Nord-Pas-de-Calais and of the National Natural Science Foundation of China (Grant 61204014). V.G.D. thanks the Russian Science Foundation for the financial support received under the Grant 14-22-00018.

## REFERENCES

(1) Tian, B.; Zheng, X.; Kempa, T. J.; Fang, Y.; Yu, N.; Yu, G.; Huang, J.; Lieber, C. M. *Nature* **2007**, *449*, 885–890.

(2) Dousse, A.; Suffczyński, J.; Beveratos, A.; Krebs, O.; Lemaître, A.; Sagnes, I.; Bloch, J.; Voisin, P.; Senellart, P. *Nature* **2010**, *466*, 217–220.

(3) Bulgarini, G.; Reimer, M. E.; Hocevar, M.; Bakkers, E. P. A. M.; Kouwenhoven, L. P.; Zwiller, V. *Nat. Photonics* **2012**, *6*, 455–458.

(4) Schneider, C.; et al. *Nature* **2013**, *497*, 348–352.

(5) Mano, T.; Kuroda, T.; Sanguinetti, S.; Ochiai, T.; Tateno, T.; Kim, J.; Noda, T.; Kawabe, M.; Sakoda, K.; Kido, G.; Koguchi, N. *Nano Lett.* **2005**, *5*, 425–428.



DOI: 10.1021/acs.nanolett.5b02226
*Nano Lett.* XXXX, XXX, XXX–XXX

(6) Colombo, C.; Spirkoska, D.; Frimmer, M.; Abstreiter, G.; Fontcuberta i Morral, A. *Phys. Rev. B: Condens. Matter Mater. Phys.* **2008**, *77*, 155326.
(7) Zhou, Z. Y.; Zheng, C. X.; Tang, W. X.; Tersoff, J.; Jesson, D. E. *Phys. Rev. Lett.* **2013**, *111*, 036102.
(8) Jabeen, F.; Grillo, V.; Rubini, S.; Martelli, F. *Nanotechnology* **2008**, *19*, 275711.
(9) Krogstrup, P.; Popovitz-Biro, R.; Johnson, E.; Madsen, M. H.; Nygård, J.; Shtrikman, H. *Nano Lett.* **2010**, *10*, 4475−4482.
(10) Plissard, S.; Dick, K. A.; Larrieu, G.; Godey, S.; Addad, A.; Wallart, X.; Caroff, P. *Nanotechnology* **2010**, *21*, 385602.
(11) Dimakis, E.; Lähnemann, J.; Jahn, U.; Breuer, S.; Hilse, M.; Geelhaar, L.; Riechert, H. *Cryst. Growth Des.* **2011**, *11*, 4001−4008.
(12) Grap, T.; Rieger, T.; Blömers, C.; Schäpers, T.; Grützmacher, D.; Lepsa, M. I. *Nanotechnology* **2013**, *24*, 335601.
(13) Biermanns, A.; Dimakis, E.; Davydok, A.; Sasaki, T.; Geelhaar, L.; Takahasi, M.; Pietsch, U. *Nano Lett.* **2014**, *14*, 6878−6883.
(14) Tomioka, K.; Kobayashi, Y.; Motohisa, J.; Hara, S.; Fukui, T. *Nanotechnology* **2009**, *20*, 145302.
(15) Björk, M. T.; Schmid, H.; Breslin, C. M.; Gignac, L.; Riel, H. *J. Cryst. Growth* **2012**, *344*, 31−37.
(16) Cirlin, G. E.; Dubrovskii, V. G.; Samsonenko, Y. B.; Bouravleuv, A. D.; Durose, K.; Proskuryakov, Y. Y.; Mendes, B.; Bowen, L.; Kaliteevski, M. A.; Abram, R. A.; Zeze, D. *Phys. Rev. B: Condens. Matter Mater. Phys.* **2010**, *82*, 035302.
(17) Conesa-Boj, S.; Kriegner, D.; Han, X.-L.; Plissard, S.; Wallart, X.; Stangl, J.; Fontcuberta i Morral, A.; Caroff, P. *Nano Lett.* **2014**, *14*, 326−332.
(18) Priante, G.; Ambrosini, S.; Dubrovskii, V. G.; Franciosi, A.; Rubini, S. *Cryst. Growth Des.* **2013**, *13*, 3976−3984.
(19) Cui, Y.; Lauhon, L. J.; Gudiksen, M. S.; Wang, J.; Lieber, C. M. *Appl. Phys. Lett.* **2001**, *78*, 2214−2216.
(20) Somaschini, C.; Bietti, S.; Trampert, A.; Jahn, U.; Hauswald, C.; Riechert, H.; Sanguinetti, S.; Geelhaar, L. *Nano Lett.* **2013**, *13*, 3607−3613.
(21) Fan, Z.; Ho, J. C.; Jacobson, Z. A.; Razavi, H.; Javey, A. *Proc. Natl. Acad. Sci. U. S. A.* **2008**, *105*, 11066−11070.
(22) Tomioka, K.; Yoshimura, M.; Fukui, T. *Nature* **2012**, *488*, 189−192.
(23) Wang, Z. K.; Lim, H. S.; Zhang, V. L.; Goh, J. L.; Ng, S. C.; Kuok, M. H.; Su, H. L.; Tang, S. L. *Nano Lett.* **2006**, *6*, 1083−1086.
(24) Kelzenberg, M. D.; Boettcher, S. W.; Petykiewicz, J. A.; Turner-Evans, D. B.; Putnam, M. C.; Warren, E. L.; Spurgeon, J. M.; Briggs, R. M.; Lewis, N.; Atwater, H. A. *Nat. Mater.* **2010**, *9*, 239−244.
(25) Russo-Averchi, E.; Vukajlovic Plestina, J.; Tütüncüoglu, G.; Matteini, F.; Dalmau Mallorqui, A.; de la Mata, M.; Rüffer, D.; Potts, H. A.; Arbiol, J.; Conesa-Boj, S.; Fontcuberta i Morral, A. *Nano Lett.* **2015**, *15*, 2869−2874.
(26) Matteini, F.; Tütüncüoglu, G.; Potts, H. A.; Jabeen, F.; Fontcuberta i Morral, A. *Cryst. Growth Des.* **2015**, *15*, 3105.
(27) Munshi, A. M.; Dheeraj, D. L.; Fauske, V. T.; Kim, D. C.; Huh, J.; Reinertsen, J. F.; Ahtapodov, L.; Lee, K. D.; Heidari, B.; van Helvoort, A. T.; Fimland, B. O.; Weman, H. *Nano Lett.* **2014**, *14*, 960−966.
(28) Plissard, S.; Larrieu, G.; Wallart, W.; Caroff, P. *Nanotechnology* **2011**, *22*, 275602.
(29) Ramdani, M. R.; Harmand, J. C.; Glas, F.; Patriarche, G.; Travers, L. *Cryst. Growth Des.* **2013**, *13*, 91−96.
(30) Glas, F.; Ramdani, M. R.; Patriarche, G.; Harmand, J. C. *Phys. Rev. B: Condens. Matter Mater. Phys.* **2013**, *88*, 195304.
(31) Glas, F. *Phys. Status Solidi B* **2010**, *247*, 254−258.
(32) Dubrovskii, V. G.; Sibirev, N. V.; Cirlin, G. E.; Soshnikov, I. P.; Chen, W. H.; Larde, R.; Cadel, E.; Pareige, P.; Xu, T.; Grandidier, B.; Nys, J.-P.; Stievenard, D.; Moewe, M.; Chuang, L. C.; Chang-Hasnain, C. *Phys. Rev. B: Condens. Matter Mater. Phys.* **2009**, *79*, 205316.
(33) Dubrovskii, V. G.; Xu, T.; Lambert, Y.; Nys, J.-P.; Grandidier, B.; Stievenard, D.; Chen, W.; Pareige, P. *Phys. Rev. Lett.* **2012**, *108*, 105501.
(34) Hoather, W. H. *Proceedings of the Physical Society* **1936**, *48*, 699−707.
(35) Dubrovskii, V. G. *J. Chem. Phys.* **2009**, *131*, 164514.
(36) Dubrovskii, V. G.; Nazarenko, M. V. *J. Chem. Phys.* **2010**, *132*, 114507.
(37) Dubrovskii, V. G.; Consonni, V.; Geelhaar, L.; Trampert, A.; Riechert, H. *Appl. Phys. Lett.* **2012**, *100*, 153101.
(38) Sibirev, N. V.; Tchernycheva, M.; Timofeeva, M. A.; Harmand, J. C.; Cirlin, G. E.; Dubrovskii, V. G. *J. Appl. Phys.* **2012**, *111*, 104317.
(39) Wu, Z. H.; Mei, X. Y.; Kim, D.; Blumin, M.; Ruda, H. E. *Appl. Phys. Lett.* **2002**, *81*, 5177−5179.
(40) Sabelfeld, K. K.; Kaganer, V. M.; Limbach, F.; Dogan, P.; Brandt, O.; Geelhaar, L.; Riechert, H. *Appl. Phys. Lett.* **2013**, *103*, 133105.
(41) Fernández-Garrido, S.; Kaganer, V. M.; Sabelfeld, K. K.; Gotschke, T.; Grandal, J.; Calleja, E.; Geelhaar, L.; Brandt, O. *Nano Lett.* **2013**, *13*, 3274−3280.



DOI: 10.1021/acs.nanolett.5b02226
*Nano Lett.* XXXX, XXX, XXX−XXX

APPLIED PHYSICS LETTERS **107**, 112102 (2015)

# Type I band alignment in $GaAs_{81}Sb_{19}$/GaAs core-shell nanowires

T. Xu,[1,2] M. J. Wei,[2] P. Capiod,[1] A. Díaz Álvarez,[1] X. L. Han,[1] D. Troadec,[1] J. P. Nys,[1] M. Berthe,[1] I. Lefebvre,[1] G. Patriarche,[3] S. R. Plissard,[1,4] P. Caroff,[1,5] Ph. Ebert,[6] and B. Grandidier[1,a)]

[1]*Institut d'Electronique, de Microélectronique et de Nanotechnologies (IEMN), CNRS, UMR 8520, Département ISEN, 41 bd Vauban, 59046 Lille Cedex, France*
[2]*Key Laboratory of Advanced Display and System Application, Shanghai University, 149 Yanchang Road, Shanghai 200072, People's Republic of China*
[3]*CNRS-Laboratoire de Photonique et de Nanostructures (LPN), Route de Nozay, 91460 Marcoussis, France*
[4]*CNRS-Laboratoire d'Analyse et d'Architecture des Systèmes (LAAS), Univ. de Toulouse, 7 Avenue du Colonel Roche, F-31400 Toulouse, France*
[5]*Department of Electronic Materials Engineering, Research School of Physics and Engineering, The Australian National University, Canberra, Australian Capital Territory 0200, Australia*
[6]*Peter Grünberg Institut, Forschungszentrum Jülich GmbH, 52425 Jülich, Germany*

(Received 10 July 2015; accepted 2 September 2015; published online 15 September 2015)

The composition and band gap of the shell that formed during the growth of axial GaAs/$GaAs_{81}Sb_{19}$/GaAs heterostructure nanowires have been investigated by transmission electron microscopy combined with energy dispersion spectroscopy, scanning tunneling spectroscopy, and density functional theory calculations. On the $GaAs_{81}Sb_{19}$ intermediate segment, the shell is found to be free of Sb (pure GaAs shell) and transparent to the tunneling electrons, despite the (110) biaxial strain that affects its band gap. As a result, a direct measurement of the core band gap allows the quantitative determination of the band offset between the $GaAs_{81}Sb_{19}$ core and the GaAs shell and identifies it as a type I band alignment. © *2015 AIP Publishing LLC*. [http://dx.doi.org/10.1063/1.4930991]

Narrow band gap antimonide-based III-V semiconductors are promising materials for the fabrication of photonic and electronic devices with high tunability and enhanced performances.[1,2] They can cover a wide infrared wavelength range and allow great flexibility in engineering different types of band alignment as well as refractive index. This is particularly the case for the $GaAs_{1-x}Sb_x$ system, that has been used as the active layer of infrared lasers.[3,4] While the two-dimensional growth of such a ternary compound has proven to suffer from low miscibility,[5] compositional broadening at the interfaces,[6] and misfit dislocations,[7] high quality material has been recently obtained in the nanowire (NW) form.[8–11] Indeed, axial heterostructure NWs are known to sustain higher lattice mismatch, due to a more efficient lateral strain relaxation.[12–14]

However, the growth of axial heterostructure NWs is not solely axial but usually involves radial growth, i.e., the deposition of materials on the sidewall facets.[15–18] Such a small lateral overgrowth by a thin layer of GaAs is expected during the growth of axial $GaAs_{1-x}Sb_x$/GaAs heterostructure NWs. Recently, it was even found that the Sb content on the periphery of $GaAs_{1-x}Sb_x$ segments is reduced, due to an enhanced exchange of Sb atoms by As atoms at the surface of the NWs,[19] suggesting the existence of a pure GaAs shell around the $GaAs_{1-x}Sb_x$ segment. Because the lattice parameters of zinc blende (ZB) $GaAs_{1-x}Sb_x$ and GaAs are different, strain should affect the bang gap of the GaAs shell, due to the interplay between the bond strength in crystals and the band structure.[20] Such an effect has been advantageously used in optoelectronics to extend the wavelength range in optical emission and absorption spectra of semiconductor heterostructures.[21,22] Questions thus arise regarding the contribution of the GaAs shell to the electrostatic potential profile and band offsets along the NW radial direction in order to tailor the confinement of the charge carriers in axial $GaAs_{1-x}Sb_x$ /GaAs heterostructure NWs.

In this work, we investigate axial $GaAs_{81}Sb_{19}$/GaAs heterostructure NWs that have been grown by molecular beam epitaxy. Analysis of the Sb distribution across the $GaAs_{81}Sb_{19}$ segment by means of transmission electron microscopy (TEM) combined with energy-dispersive X-ray spectroscopy (EDX) reveals the existence of a thin shell around the $GaAs_{81}Sb_{19}$ segment. Although this shell is essentially free of Sb atoms at the surface, scanning tunneling spectroscopy (STS) indicates an apparent band gap that is much smaller than the band gap of pure GaAs. *Ab-initio* calculations of the evolution of GaAs band gap under (110) biaxial strain are unable to account for the band gap narrowing. Conversely, the measured band gap fits well with the band gap of a $GaAs_{81}Sb_{19}$ alloy, demonstrating a type I heterostructure with a shell thin enough to leave that barrier transparent to tunneling electrons.

The growth of the axial heterostructure NWs was achieved with Ga seed particles using the vapor-liquid-solid mechanism, as described previously.[23,24] The NW structure shown in Fig. 1(a) consists of a ZB GaAs bottom segment, a ZB $GaAs_{1-x}Sb_x$ intermediate segment with a nominal Sb concentration $x$ of 0.19 (labelled $GaAs_{81}Sb_{19}$), and a GaAs top segment with intended lengths of 800 nm, 400 nm, and 400 nm, respectively. $GaAs_{1-x}Sb_x$ NWs with a nominal composition $x$ of 0.5 were also grown with the same growth conditions (labelled $GaAs_{0.5}Sb_{0.5}$) and used as reference samples for STS measurements. At the end of the growth, all the NWs were capped with a thin As layer, deposited at

a)E-mail: bruno.grandidier@isen.iemn.univ-lille1.fr

 © 2015 AIP Publishing LLC

Reuse of AIP Publishing content is subject to the terms at: https://publishing.aip.org/authors/rights-and-permissions. Download to IP: 193.49.225.10 On: Fri, 09 Sep 2016 11:05:32

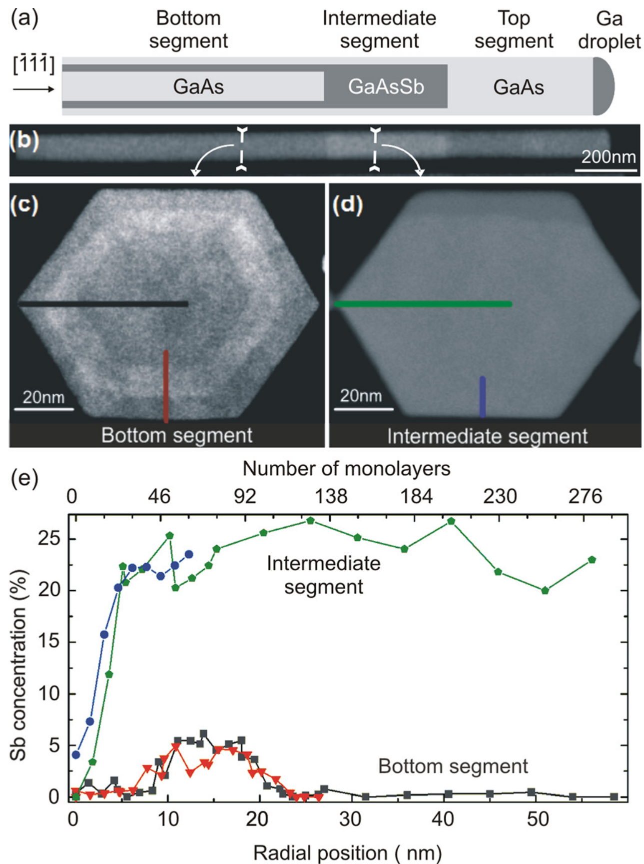


FIG. 1. (a) Schematic of the GaAs/GaAsSb heterostructure nanowire. (b) HAADF STEM image of GaAs/$GaAs_{0.81}Sb_{0.19}$ nanowire heterostructure. (c) HAADF STEM cross-sectional view of the bottom segment. (d) HAADF STEM cross-sectional view of the intermediate segment. (e) Sb concentration profile deduced from EDX point scan analyses performed along the colored segments defined in the cross-sectional views. The origins of the radial profiles start at the NW sidewall.

room temperature for 50 min under high $As_4$ flux to protect the NWs from air exposure (oxidation).[17]

The NWs were first analysed using TEM. For that purpose, the NWs were transferred onto a silicon substrate with a good control over the orientation of the NWs.[25] Then, they were buried under a 120 nm-thick layer of hydrogen silsesquioxane (HSQ) and thin slices, perpendicular to the NW main axis, were extracted using a focused ion beam. Scanning transmission electron microscopy (STEM) was performed on an aberration-corrected microscope (Jeol 2200FS) with EDX capacity. The EDX point analyses used a probe size of about 1 nm and a probe current of about 150 pA (half-convergence of 30 mrad). The NWs were also characterized by low-temperature (77 K) scanning tunneling microscopy (STM) in ultrahigh vacuum, after the complete desorption of the As capping layer and the subsequent cleavage of the NWs onto a silver terminated Si(111) substrate.[17]

Figure 1(b) shows a typical high angle annular dark field (HAADF) STEM micrograph of two axial GaAs/$GaAs_{81}Sb_{19}$/GaAs heterostructure NWs. The $GaAs_{81}Sb_{19}$ segment is identified from its bright contrast with respect to the GaAs segments. Its position as well as its length are consistent with the intended structure of the NWs. From high resolution TEM images (not shown), interface abruptnesses of 4.5 +/− 0.5 and 17.0 +/− 0.5 nm were, respectively, found for the GaAs bottom segment/GaAsSb and GaAsSb/GaAs top segment interfaces. The cross-sectional HAADF-STEM view of the bottom segment in Fig. 1(c) shows a hexagonal shape with the existence of a double shell, indicating radial overgrowth each time a new segment is grown along the main axis of the NW. This observation suggests the existence of a shell around the $GaAs_{81}Sb_{19}$ segment. The shell is however not resolved in Fig. 1(d), but detected in the quantitative EDX analysis shown below. Note that the dark contrast seen parallel with the top sidewall of the hexagonal cross-section in Fig. 1(d) is an artefact from the sample preparation.

Quantitative concentration profiles extracted from the EDX analyses are displayed in Fig. 1(e). In the bottom segment, the profile of the Sb content is consistent with the contrast variations visible in the HAADF-STEM image. It outlines the existence of a hexagonally shaped $GaAs_{1-x}Sb_x$ quantum well with $x = 0.04 \pm 0.02$, that is surrounded by two GaAs potential barriers. In the intermediate segment, the profile of the Sb content indicates a $GaAs_{81}Sb_{19}$ core with a slightly higher Sb content than the nominal one. Remarkably, the Sb concentration is reduced close to the sidewalls, and this drop is even more acute at the vertices of the NWs. As seven NWs were investigated in this way and all showed the same profile, such a result demonstrates the existence of a few nm thin Sb-poor shell around the $GaAs_{81}Sb_{19}$ segment, in agreement with Ref. 19.

In order to corroborate the absence of Sb at the surface of the $GaAs_{81}Sb_{19}$ segment, the sidewalls were imaged with STM.[17] The $GaAs_{81}Sb_{19}$ segment can be identified from its bright contrast in the STM image of Fig. 2(a). This contrast, corresponding to a topographic change of 2–3 nm, indicates a slight difference in diameter. The difference in diameters for these two sections is attributed mainly to a change of the wetting configuration/volume of the droplet during growth of the GaAsSb segment[26] and also to a lattice relaxation. The sidewall of the $GaAs_{81}Sb_{19}$ segment is atomically flat and sprinkled with single atomic layer terraces that have nucleated at the border of the sidewalls. High resolution STM images obtained on the sidewall, such as the one seen in Fig. 2(b), exhibit the atomic sublattice of a ZB {110} face, without significant contrast variation between the atoms. This observation differs from the corrugation seen on the sidewall of a ZB GaAsSb NW with 50% Sb nominal composition (see Fig. 2(d)), where numerous bright protrusions, typical of antimony atoms are clearly resolved.[17] Therefore, the STM characterization of the sidewalls supports the formation of a Sb-free shell around the $GaAs_{81}Sb_{19}$ segment of the heterostructure NWs.

Tunneling spectroscopic measurements were further performed to determine the electronic structure of the shell. Spectrum (i) of Fig. 3 obtained on the pure ZB GaAs segment, far from the interface, shows a width of the voltage region without current that is in agreement with the band gap of ZB GaAs (~1.50 eV). Similarly, spectrum (iii) obtained on the ZB GaAsSb NW reveals a smaller band gap of 0.75 eV, which is close to the theoretical band gap of $GaAs_{50}Sb_{50}$.[5,27] Finally, spectrum (ii), measured in the center of the $GaAs_{81}Sb_{19}$ segment, yields a band gap of 1.1 eV, that is between the band gap of GaAs and $GaAs_{50}Sb_{50}$. As

Reuse of AIP Publishing content is subject to the terms at: https://publishing.aip.org/authors/rights-and-permissions. Download to IP: 193.49.225.10 On: Fri, 09 Sep 2016 11:05:32

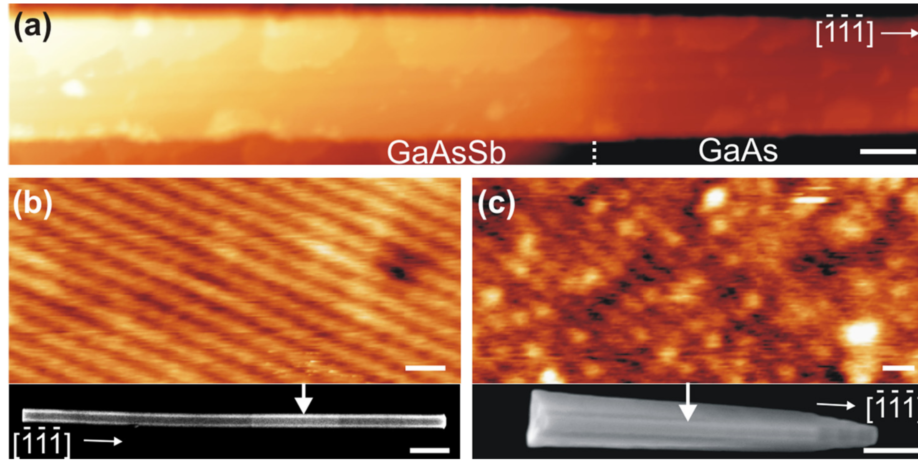


FIG. 2. (a) STM image of the interface between the intermediate segment and the top segment of a $GaAs/GaAs_{81}Sb_{19}$ NW sidewall. Experimental parameters: tunneling current of 10 pA, sample voltage of +2.8 V, and temperature of 77 K. Scale bar: 25 nm. (b) and (c) High resolution occupied state STM images obtained on the {110} sidewall of the intermediate segment of the heterostructure NW and on the {110} sidewall of the $GaAs_{50}Sb_{50}$ NW, respectively. Experimental parameters: tunneling current of 100/20 pA, sample voltage of −2.0 V/−3.5 V, and temperature of 77 K. Scale bar: 0.4 nm. Insets: SEM images of a $GaAs/GaAs_{81}Sb_{19}/GaAs$ NW and a $GaAs_{50}Sb_{50}$ NW, respectively. Scale bars: 200 nm. The arrows point at the position where the STM images have been acquired.

the shell is almost pure GaAs (strong Sb depletion, see above), the effect of the strain on the band gap of a GaAs shell was investigated first. A thin GaAs shell is expected to be tensile (110) biaxial strained when grown on a $GaAs_{81}Sb_{19}$ substrate. For that purpose, we studied the evolution of the GaAs band gap as a function of the in-plane strain by means of electronic structure computations, in the Density Functional Theory (DFT) Framework. All total energy calculations were performed with the Vienna *ab initio* simulation program [VASP, version 5.2.11],[28] using all electron projector augmented wave (PAW) pseudopotentials,[29] with the Ceperley and Alder approximation,[30] parameterized by Perdew and Zunger for exchange and correlation energies (i.e., the As, Ga_d, H1.25 and H.75 PAW potentials). To account for the band splittings,

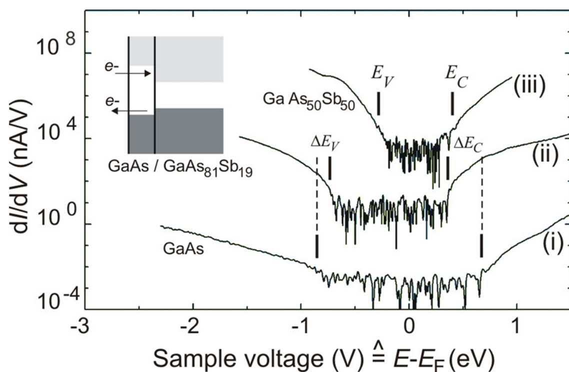


FIG. 3. Tunneling spectra acquired on (i) the pure GaAs top segment and (ii) the shell surrounding the $GaAs_{81}Sb_{19}$ segment of a $GaAs/GaAs_{81}Sb_{19}/GaAs$ heterostructure NW, as well as (iii) a $GaAs_{50}Sb_{50}$ NW. All spectra were acquired at 77 K with tunneling conditions of (i) 1.6 V, 0.8 nA, (ii) 1.6 V, 0.8 nA, and (iii) −1.0 V, 0.5 nA. Spectra (ii) and (iii) have been shifted for clarity. The conduction $E_C$ and valence $E_V$ band edges are indicated by vertical segments, while $\Delta E_C$ and $\Delta E_V$ correspond to the band offsets between GaAs and the $GaAs_{81}Sb_{19}$ core. Inset: Energy band diagram of the radial $GaAs/GaAs_{81}Sb_{19}$ heterostructure, the arrows indicating the tunneling of electrons from or into the $GaAs_{81}Sb_{19}$ core through the GaAs shell.

we included spin-orbit (SO) coupling explicitly in the calculations. All calculations were done using a kinetic energy cutoff of 456.28 eV. The lattice constant of the GaAs unit cell was calculated to be 5.6102 Å, in good agreement with an experimental value of 5.6533 Å (the relative discrepancy is about 0.77%).

We first considered a bulk-like GaAs unit cell corresponding to GaAs(110) under the biaxial strain due to growth on the $GaAs_{1-x}Sb_x$. The in-plane $a_x$ parameter has been estimated by mean of a Vegard's law (relative to the optimized GaAs parameter). The $c_x/a_x$ parameter was optimized for different Sb content (see Table I). To take into account the (110) surface, supercells containing six GaAs layers were constructed with the lower surface of the slab saturated by H atoms and the two first layers fixed to the bulk-like optimized positions. The six layer-thick slabs were separated by a vacuum region equivalent to a distance of seven layers which has been demonstrated to be sufficient.[31] All structures were optimized with respect to the ionic positions, using a quasi-Newton-method for relaxation, until the forces on all atoms were less than 1 meV/Å. A (3 × 3 × 1) Monkhorst-Pack $k$-point grid was used for the relaxation of surface structures. The local density of states was computed on the supercells in order to discriminate surface from "bulk-like" contributions. The tetrahedron method with Blöchl corrections was used to determine how the partial occupancies are set. Computations were done on a (10 × 10) Monkhorst-Pack $k$-point meshes of the surface Brillouin zone.

TABLE I. Lattice parameters and in-plane strain as a function of the Sb content.

| Sb content | $a_x$ | Optimized $c_x$ | In-plane strain |
|---|---|---|---|
| 0 | 5.6102 | 3.9670 | 0 |
| 0.2 | 5.6987 | 3.9470 | 0.0158 |
| 0.4 | 5.7872 | 3.9323 | 0.0316 |
| 0.8 | 5.9643 | 3.8900 | 0.0631 |

Reuse of AIP Publishing content is subject to the terms at: https://publishing.aip.org/authors/rights-and-permissions. Download to IP: 193.49.225.10 On: Fri, 09 Sep 2016 11:05:32

Figure 4 summarizes the evolution of the bulk and surface band gap for strained GaAs(110): the band gap decreases with strain. Previous calculations for biaxially strained GaAs(001) and (111) corroborate this trend.[32,33] However, such a decrease is clearly not enough when the biaxial strain is caused by a core corresponding to a Sb content $x$ of $\sim$0.2 only. Therefore, strain is unable to account for the measured band gap narrowing.

In contrast, if we consider unstrained $GaAs_{1-x}Sb_x$ material, the evolution of the measured band gap as a function of the Sb content fits well with the theoretical band gap calculated from the linear interpolation between the parameters of GaAs and GaSb according to the Vegard's law[5] drawn as a solid line in Fig. 4. This indicates that tunneling spectroscopy reveals the band edge position of the $GaAs_{81}Sb_{19}$ core in the intermediate segment. The shell acts as a potential barrier and is transparent to the tunneling electrons transferred in the energy range corresponding to the shell band gap. This is consistent with the observed shell thickness of a few nanometers only, as deduced from the compositional analysis of the core-shell NWs in cross-section. Hence, the radial band alignment between the GaAs shell and the $GaAs_{81}Sb_{19}$ core is of type I as indicated by the inset in Fig. 3. The values of the band offsets can be determined from the spectra on the pure GaAs and the $GaAs_{81}Sb_{19}$ segments: The top surface is in both cases GaAs with the Fermi energy pinned by extrinsic midgap surface states arising from steps.[24] Their energy position is essentially unaffected by a quantum confinement in the thin GaAs shell and can serve as reference energy. Therefore, the valence ($\Delta E_V$) and conduction ($\Delta E_C$) band offsets are directly measured in Fig. 3 to be 0.1 and 0.3 eV, respectively.

In conclusion, axial $GaAs_{81}Sb_{19}$/GaAs heterostructure NWs grown by molecular beam epitaxy are found to exhibit a thin pure GaAs shell around the core. This shell is transparent to tunneling electrons allowing the direct determination of the nature of the band alignment between the $GaAs_{81}Sb_{19}$ core and the GaAs shell of the NWs. Due to

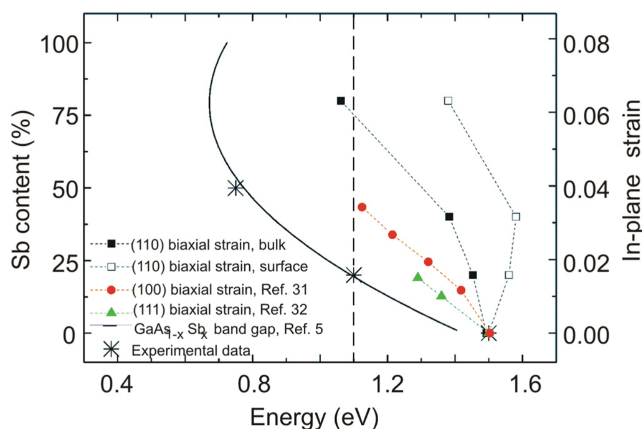


FIG. 4. Evolution of the band gap of differently oriented biaxially strained GaAs layers as a function of the in-plane strain, right axis (or in terms of the Sb content for $GaAs_{1-x}Sb_x$, left axis). The vertical dashed line indicates the experimental value of the band gap measured on the shell. The calculated data for pure unstrained GaAs are shifted to match the experimental bulk band gap. Similarly, the calculated surface band gap is matched to the measured one of about 1.5 eV.[24]

the lack of intrinsic surfaces states on the (110) surfaces of most III–V semiconductor materials, we expect tunneling spectroscopic experiments to be relevant to a large variety of other core-shell nanowires grown along a ⟨111⟩ direction in order to gain insight into the band discontinuities of those heterostructures.

This study was financially supported by the European Community's Seventh Framework Program (Grant No. PITN-GA-2012-316751, "Nanoembrace" Project), the EQUIPEX program Excelsior, the RENATECH network, and the Impuls- und Vernetzungsfonds of the Helmholtz-Gemeinschaft Deutscher Forschungszentren (Grant No. HIRG-0014). T. Xu acknowledges the support of the Region Nord-Pas-de-Calais and of the National Natural Science Foundation of China (Grant No. 61204014). The authors thank X. Wallart for fruitful discussions.

[1]B. R. Bennett, R. Magno, J. B. Boos, W. Kruppa, and M. G. Ancona, Solid-State Electron. **49**, 1875 (2005).
[2]C. Liu, Y. Li, and Y. Zeng, Engineering **2**, 617 (2010).
[3]F. Quochi, D. C. Kilper, J. E. Cunningham, M. Dinu, and J. Shah, IEEE Photonics Technol. Lett. **13**, 921 (2001).
[4]E. Gesrter, I. Ecker, S. Lorch, C. Hahn, S. Menzel, and P. Unger, J. Appl. Phys. **94**, 7397 (2003).
[5]R. E. Nahory, M. A. Pollack, J. C. DeWinter, and K. M. Williams, J. Appl. Phys. **48**, 1607 (1977).
[6]R. Kaspi and K. R. Evans, J. Cryst. Growth **175/176**, 838 (1997).
[7]T. Wosiński, A. Makosa, T. Figielski, and J. Raczyńka, Appl. Phys. Lett. **67**, 1131 (1995).
[8]D. L. Dheeraj, G. Patriarche, L. Largeau, H. L. Zhou, A. T. J. van Helvoort, F. Glas, J. C. Harmand, B. O. Fimland, and H. Weman, Nanotechnology **19**, 275605 (2008).
[9]D. L. Dheeraj, G. Patriarche, H. L. Zhou, T. B. Hoang, A. F. Moses, S. Gronsberg, A. T. J. Van Helvoort, B. O. Fimland, and H. Weman, Nano Lett. **8**, 4459 (2008).
[10]S. Plissard, K. A. Dick, X. Wallart, and P. Caroff, Appl. Phys. Lett. **96**, 121901 (2010).
[11]X. Yuan, P. Caroff, J. Wong-Leung, H. H. Tan, and C. Jagadish, Nanoscale **7**, 4995 (2015).
[12]F. Glas, Phys. Rev. **74**, 121302 (2006).
[13]M. W. Larsson, J. B. Wagner, M. Wallin, P. Håkansson, L. E. Fröberg, L. Samuelson, and L. R. Wallenberg, Nanotechnology **18**, 015504 (2007).
[14]M. de la Mata, C. Magén, P. Caroff, and J. Arbiol, Nano Lett. **14**, 6614 (2014).
[15]M. A. Verheijen, G. Immink, T. de Smet, M. T. Borgström, and E. P. A. M. Bakkers, J. Am. Chem. Soc. **128**, 1353 (2006).
[16]P. K. Mohseni, C. Maunders, G. A. Botton, and R. R. LaPierre, Nanotechnology **18**, 445304 (2007).
[17]T. Xu, K. A. Dick, S. Plissard, T. H. Nguyen, Y. Makoudi, M. Berthe, J.-P. Nys, X. Wallart, B. Grandidier, and P. Caroff, Nanotechnology **23**, 095702 (2012).
[18]J. V. Knutsson, S. Lehmann, M. Hjort, P. Reinke, E. Lundgren, K. A. Dick, R. Timm, and A. Mikkelsen, ACS Appl. Mater. Interfaces **7**, 5748 (2015).
[19]H. Kauto, B. O. Fimland, T. Grieb, A. M. Munshi, K. Müller, A. Rosenauer, and A. T. J. Van Helvoort, J. Appl. Phys. **116**, 144303 (2014).
[20]F. H. Pollak and M. Cardona, Phys. Rev. **172**, 816 (1968).
[21]K. Ozasa, M. Yuri, S. Tanaka, and H. Matsunami, J. Appl. Phys. **68**, 107 (1990).
[22]A. M. Smith, A. M. Mohs, and S. Nie, Nat. Nanotechnol. **4**, 56 (2009).
[23]C. Colombo, D. Spirkoska, M. Frimmer, G. Abstreiter, and A. Fontcuberta i Morral, Phys. Rev. B **77**, 155326 (2008).
[24]P. Capiod, T. Xu, J. P. Nys, M. Berthe, G. Patriarche, L. Lymperakis, J. Neugebauer, P. Caroff, R. E. Dunin-Borkowski, Ph. Ebert, and B. Grandidier, Appl. Phys. Lett. **103**, 122104 (2013).
[25]T. Xu, J.-P. Nys, A. Addad, O. I. Lebedev, A. Urbieta, B. Salhi, M. Berthe, B. Grandidier, and D. Stiévenard, Phys. Rev. B **81**, 115403 (2010).

Reuse of AIP Publishing content is subject to the terms at: https://publishing.aip.org/authors/rights-and-permissions. Download to IP: 193.49.225.10 On: Fri, 09 Sep 2016 11:05:32

[26] S. R. Plissard, D. R. Slapak, M. A. Verheijen, M. Hocevar, G. W. G. Immink, I. van Weperen, S. Nadj-Perge, S. M. Frolov, L. P. Kouwenhoven, and E. P. A. M. Bakkers, Nano Lett. **12**, 1794 (2012).
[27] K. Alberi, J. Wu, W. Walukiewicz, K. M. Yu, O. D. Dubon, S. P. Watkins, X. Liu, Y.-J. Cho, and J. Furdyna, Phys. Rev. B **75**, 045203 (2007).
[28] G. Kresse and J. Furthmüller, Phys. Rev. B **54**, 11169 (1996).
[29] P. E. Blöchl, Phys. Rev. B **50**, 17953 (1994).
[30] D. M. Ceperley and B. J. Alder, Phys. Rev. Lett. **45**, 566 (1980).
[31] Ph. Ebert, B. Engels, P. Richard, K. Schroeder, S. Blügel, C. Domke, M. Heinrich, and K. Urban, Phys. Rev. Lett. **77**, 2997 (1996).
[32] P. R. C. Kent, G. L W. Hart, and A. Zunger, Appl. Phys. Lett. **81**, 4377 (2002).
[33] E. S. Kadantsev, M. Zieliński, and P. Hawrylak, Phys. Rev. B **86**, 085411 (2012).

Reuse of AIP Publishing content is subject to the terms at: https://publishing.aip.org/authors/rights-and-permissions. Download to IP: 193.49.225.10 On: Fri, 09 Sep 2016 11:05:32

Surface Science 653 (2016) 92–96

Contents lists available at ScienceDirect

Surface Science

journal homepage: www.elsevier.com/locate/susc

# Scanning tunnelling spectroscopy and Raman spectroscopy of monolayer silicene on Ag(111)

A. Díaz Álvarez [a], T. Zhu [a], J.P. Nys [a], M. Berthe [a], M. Empis [b], J. Schreiber [b], B. Grandidier [a,*], T. Xu [a,c,**]

[a] Institut d'Electronique, de Microélectronique et de Nanotechnologie (IEMN), CNRS, UMR 8520, Département ISEN, 41 bd Vauban, 59046 Lille Cedex, France
[b] HORIBA Jobin Yvon SAS, Raman Division, 231 rue de Lille, 59650 Villeneuve d'Ascq, France
[c] Sino-European School of Technology, Shanghai University, 99 Shangda Road, Shanghai 200444, People's Republic of China

ARTICLE INFO

*Article history:*
Received 2 March 2016
Received in revised form 14 May 2016
Accepted 14 June 2016
Available online 15 June 2016

*Keywords:*
Silicene
Scanning tunnelling spectroscopy
Raman spectroscopy

ABSTRACT

Low temperature scanning tunnelling spectroscopy and Raman spectroscopy were used to study the electronic and vibrational properties of silicene formed on the Ag(111) surface for coverage up to one monolayer in the temperature range 230–250 °C. The tunnelling spectra reveal the strong contribution of silver states in the measured density of states around the Fermi level. The Raman spectra are found to evolve as a function of the submonolayer coverages, giving rise at one monolayer coverage to peaks that are characteristic of chemical bonds with distorted $sp^3$ hybrid orbitals. Such properties account for the electronic transparency of the silicene/Ag(111) interface.

© 2016 Elsevier B.V. All rights reserved.

## 1. Introduction

The epitaxial growth of ultra-thin films with atomic-layer precision offers an interesting way to produce materials with electronic properties that depart from the bulk ones. Such a quest has led to the successful formation of two-dimensional silicon crystals on a silver surface [1–4]. Based on the comparison of diffraction patterns, real space imaging and first principles density functional theory (DFT), several atomic phases have been identified, that all have in common a honeycomb structure [5]. In analogy to graphene, these crystals have been coined the name of "silicene". While it was first thought that the band structure of silicene supported on silver could be similar to graphene with the existence of Dirac cones, the absence of Landau levels and thus the lack of anomalous quantum Hall effect demonstrated that these atomic crystals bound to silver did not behave like graphene [4]. Instead, theoretical calculations of their electronic properties and structural analyses have revealed a strong hybridization of the silicon orbitals with the silver atoms underneath [6–10]. Although the calculations were able to reproduce some features observed around the Fermi level with angle-resolved photoemission spectroscopy, they clearly showed a loss of the two-dimensional nature of the π-symmetry states.

These findings point to a subtle arrangement of the surface atoms not only in the Si crystal but also at the surface of the Ag(111) crystal. While the Si atoms have a honeycomb structure with part of the Si atoms buckled, Ag atoms located under the buckled Si atoms have been shown to undergo a vertical displacement. This interplay leads to peculiar electronic and vibrational couplings that make the physical properties of the Si atoms different from the ones obtained for the Si adatoms on the Si (111) or (100) surfaces. Hints of this difference have been found when the surface is overgrown with Si and has raised unsettled controversies about the physical nature of this silicon multilayer [11–14]. These properties that deviate from the one of Si atoms in bulk crystal or thin films were also highlighted through chemical reactions such as hydrogenation or oxidation. Indeed, exposure to hydrogen led to a modification of the buckling configuration of Si atoms, showing unexpected asymmetric sections in the surface reconstruction unit cell [15], while monolayer and multilayer silicenes were found to show a good resistance to air exposure opposite to the surface of Si crystals [16,17].

All these results question the real nature of the Si–Si bonds and the interplay between Si and Ag atoms. To gain further insight into the properties of silicene grown on the Ag(111) surface, we have first investigated the electronic density of states near the Fermi level for the (4 × 4) and (√13 × √13) silicene phases by means of scanning tunnelling spectroscopy (STS). The unalterability of the spectra with increasing electric field and the similarity of their features with the ones observed on the bare silver surface reveal the strong contribution of the silver states in the vicinity of the Fermi level. Then, the vibrational properties of the silicene phases have been studied as a function of the surface coverage. A change in peak intensity and position of in-situ

* Corresponding author.
** Correspondence to: T. Xu, Institut d'Electronique, de Microélectronique et de Nanotechnologie (IEMN), CNRS, UMR 8520, Département ISEN, 41 bd Vauban, 59046 Lille Cedex, France.
*E-mail addresses:* bruno.grandidier@isen.iemn.univ-lille1.fr (B. Grandidier), xtld@shu.edu.cn (T. Xu).

http://dx.doi.org/10.1016/j.susc.2016.06.005
0039-6028/© 2016 Elsevier B.V. All rights reserved.

Raman spectroscopy measurements correlates with the proportion of the three observed phases, the (4 × 4), ($\sqrt{13} \times \sqrt{13} - \alpha$) and ($\sqrt{13} \times \sqrt{13} - \beta$) silicene phases, allowing to assign the lowest Raman peak to the more or less disordered ($\sqrt{13} \times \sqrt{13} - \beta$) silicene phase. At coverage of 1 ML, the Raman spectrum resembles the one of Si crystal with an additional tail at frequencies lower than the first-order optical phonon peak, departing thus from pure $sp^3$ orbitals. Taking into account the results obtained with both techniques, we suggest that the states related to the hybridized orbitals in the vicinity of the Fermi level correspond to the coupling of the Si $p_z$ states with the Ag surface states. Such a coupling reduces the chemical reactivity of the Si atoms bound to silver, enabling silicene to act as a protective and electronic transparent monolayer for the silver surface.

## 2. Experimental

Sample preparation and most experiments were performed under ultra-high-vacuum conditions, allowing the contamination free epitaxial growth of silicon on single crystal Ag(111) substrates. Clean and well-ordered Ag(111) surfaces were prepared by several cycles of Ar ion sputtering (1.5 kV, $5 \times 10^{-5}$ mbar) and subsequent annealing at ~530 °C for 30 min. The synthesis of silicon adlayers was carried out by evaporating atomic Si onto the Ag(111) surface at a deposition rate of 0.02 ML·min$^{-1}$ with the silver surface held at 230–250 °C, where 1 ML of silicene corresponds to $1.56 \times 10^{15}$ Si atoms/cm$^2$. The whole growth process and the evolution of the Si-adlayer were monitored by low energy electron diffraction (LEED). Scanning tunnelling microscopy (STM) and STS measurements were performed with two systems: a low temperature microscope (5 and 77 K) and a room temperature microscope that is combined with Raman spectroscopy. Tunnelling spectroscopic measurements were performed with the first system to benefit from the higher energy resolution due to the use of low temperatures. The differential conductivity ($dI/dV$) was measured at a given setpoint sample bias $V_s$ by superimposing a sinusoidal voltage modulation (9 $mV_{rms}$, 480 Hz) on the tunnelling voltage and measuring the current response by a lock-in amplifier.

In the second system, the sample fixed on the STM stage was excited with a laser source ($\lambda = 532$ nm) from a SuperHead Raman fiber probe (Horiba Scientific). The SuperHead probe was mounted on an x,y,z-table located outside the STM chamber and was equipped with a video camera for observation of the STM tip position on the sample. The beam made an angle of 38° with the normal of the sample and was focused into a 10 μm spot with a 0.15 numerical aperture (NA), the lens being positioned 25 mm away from the sample. The power was adjusted to 7 mW in front of the viewport of the STM chamber. The same optical path was used to collect the scattered light, the SuperHead probe being coupled to an iHR 550 spectrometer (Horiba Scientific). Single crystalline silicon, annealed in UHV to obtain a surface with the (7 × 7) reconstruction, was used to calibrate the Raman shift frequency during every run resulting in an uncertainty in the peak frequency of <2 cm$^{-1}$.

## 3. Results and discussion

Fig. 1 shows the evolution of the surface as the Si coverage increases. At low coverage, the surface consists of strips that form at step edges, consistent with the literature for similar growth temperatures [18]. The baseline of the strips is lower than the upper silver terrace. The strips are filled with Si domains that show either a structure of similar height than the upper silver terraces or, protrusions that appear higher than the upper silver terraces. As the Si coverage increases (Fig. 1(b)), the Si domains grow at the expense of the silver terraces. The bright protrusions show some ordering that give rise to the ($\sqrt{13} \times \sqrt{13} - \beta$) phase at a coverage of 1 ML (Fig. 1(c)). The two other structures that also grow at the same time are identified as the (4 × 4) and ($\sqrt{13} \times \sqrt{13} - \alpha$) silicene phases in agreement with the structures observed in the temperature range of 230–250 °C [5,18,19]. We note that the proportion of the ($\sqrt{13} \times \sqrt{13} - \beta$) phase with respect to the two other phases decreases as the coverage approaches 1 ML.

Prior to tunnelling spectroscopic measurements performed on the different silicene phases, the electronic properties of the tungsten STM tips were analysed by recording tunnelling spectra on bare Ag islands, such as the one visible in Fig. 1(b). A typical $dI/dV$ curve shows step-shaped onset at a voltage of −100 mV (Fig. 2(a)). The step is usually followed by undulations that vary in number, intensity and separation depending on the size of the Ag islands and also on the setpoint current. Such a sharp rise is caused by the Shockley surface states. The one seen in Fig. 2(a) is consistent with the position usually obtained for the edge of the energy band of the Ag(111) surface state, as long as lateral quantum confinement is negligible in the island [20,21]. Additional tip-surface separation curves were acquired along with $dI/dV$ spectra with an active feedback loop [Fig. 2(b)]. As the sample bias is positively ramped, maintaining the tunnelling current constant requires a smooth withdrawal of the tip, followed by a sharp rise above 4 V. At such an onset, the $dI/dV$ curve shows a peak, signature of a field emission resonance [22]. This peak appears for a voltage of 4.2 V. Therefore it yields a work function that is close to the typical work function obtained for silver and tungsten [23,24]. This result as well as the correct position of the onset of the Shockley surface states ensure that the STM tip does not suffer from any electronic artefact.

Fig. 3(a) shows typical STS curves obtained on the three different phases. Small and broad peaks are observed when the occupied states are probed at negative bias, while a featureless increase is visible at positive bias when empty states are filled up with electrons. Such variations, that show a small signal in the region between −0.5 and 0.5 V and then an increase of the signal from either side of the Fermi level

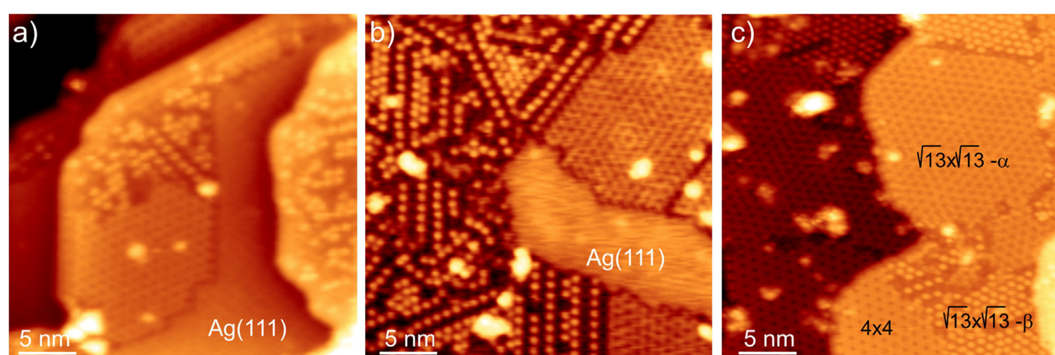


**Fig. 1.** Sequence of STM images showing the evolution of the Ag(111) surface upon deposition of Si up to 1 ML at a temperature of 230 °C. Coverage of (a) 0.4 ML, (b) 0.7 ML, and (c) 1.0 ML. Experimental parameters: tunnelling current of (a) 50 pA, (b) 20 pA and (c) 50 pA, sample voltage of −1.0 V, and temperature of 77 K.

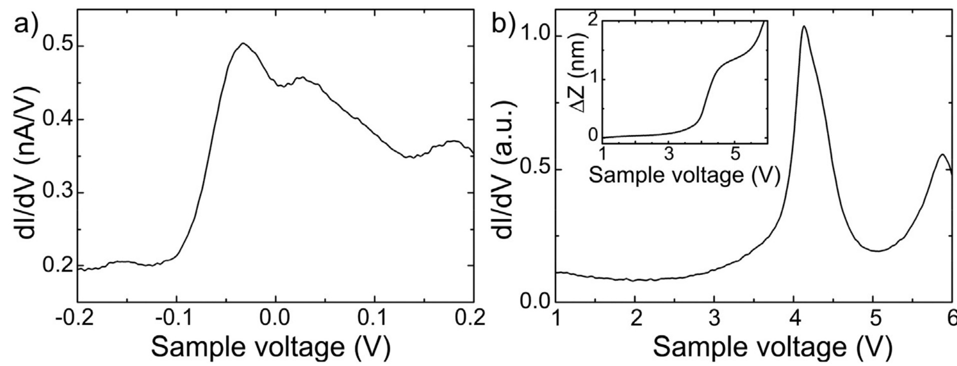


**Fig. 2.** (a) Differential conductance acquired on a bare Ag island in the voltage range that shows a steplike onset due to tunnelling into the Shockley surface states. (b) Differential conductance acquired on a bare Ag island in the voltage range that shows field emission resonances. Inset: Tip displacement curve acquired simultaneously with the feedback loop on. Experimental parameters: tunnelling current of 60 pA, sample voltage of (a) −0.2 V and (b) +1.0 V, and temperature of 77 K.

($V_s = 0$ V) are consistent with previous tunnelling spectroscopic studies [25,26]. We note that the *dI*/*dV* curve of the (4 × 4) phase is not zero at $V_s = 0$ V, indicative of a finite density of states at the Fermi level. Although variations in the magnitude of the different spectra are clearly seen, we attribute them to different tip-surface separations prior to the opening of the feedback loop, as shown below. When spectroscopic measurements were performed with increasing setpoint currents at 5 K, the small and broad peaks become stronger and new features are resolved [Fig. 3(b) and (c)]. Remarkably, the increase of the electric field in the junction due to the tip proximity does not change the position of the features, suggesting the absence of sizable Stark effect. The importance of a charge screening at the surface supports a strong electronic coupling between the silicene phase and the Ag surface. In addition, no V shaped density of states that vanishes at the Dirac point is measured in the vicinity of the Fermi level [27], whatever the phase is characterized. Both results are in agreement with the hybridization of the silicon orbitals with the silver atoms underneath [6,7,8], causing a substantial modification of the silicene electronic structure.

However we note that our experimental *dI*/*dV* curves do not match the simulated local density of states for the different observed phases [9]. Therefore to get deeper insight into the states contributing to the tunnelling current, spatially resolved spectroscopic measurements were further performed. In the middle of a domain, the states near the Fermi level are found to be rather delocalized, since there is no spatial dependence between spectra acquired at different positions in the unit cell, as shown in the inset of Fig. 3(b). Close to the boundary between a (4 × 4) domain and an adjacent Ag island (Fig. 4), the *dI*/*dV* curves measured at negative bias exhibit similar features as the ones visible in Fig. 3(b). Interestingly, these features occur in silver too and the variation of their amplitude looks stronger. As those occupied states lie 100 meV below the Fermi level in the silver region, we attribute them to surface states that are degenerated with bulk states. Upon adsorption of silicene, these states still retain a large amplitude close to the surface.

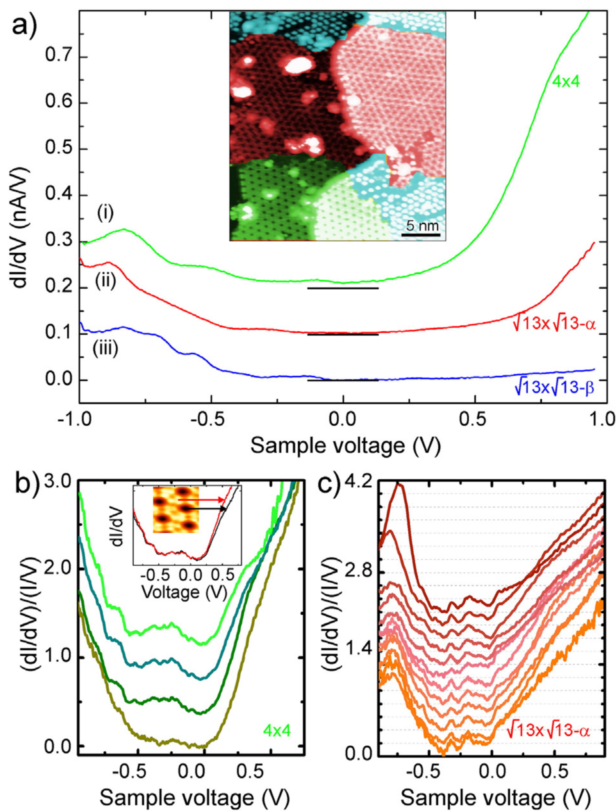


**Fig. 3.** (a) Spatially resolved tunnelling spectra measured on the different phases of silicene. The horizontal lines show the zero level of each spectrum, which are shifted for clarity. Experimental parameters: tunnelling current of 50 pA, sample voltage of −1.0 V, and temperature of 77 K. (b) Set of normalized differential conductance curves measured on the (4 × 4) phase at setpoint currents of 0.05/0.10/0.50/1.00 nA from bottom to top, a sample voltage of −1.0 V and a temperature of 5 K. Inset: differential conductance measured on a hole and on a top Si atom (0.5 nA, −1.0 V, 5 K). (c) Set of normalized differential conductance curves measured on the ($\sqrt{13} \times \sqrt{13} - \alpha$) phase at different setpoint currents of 2, 4, 6, 8, 10, 15, 20, 25, 30, 35, 40, and 50 nA from bottom to top, a sample voltage of −1.0 V, and a temperature of 5 K. The spectra are shifted for clarity.

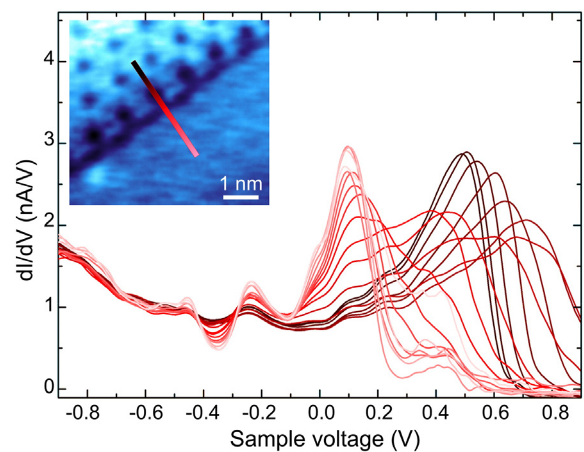


**Fig. 4.** Spatially resolved differential conductance measured across the boundary between a domain with a (4 × 4) phase and an Ag island. Experimental parameters: tunnelling current of 1 nA, sample voltage of −1.0 V, and temperature of 5 K.

As their position in energy is not altered by the silicon atoms, they correspond to surface resonances that decay smoothly through the silicene adlayer.

At sample voltages higher than −100 mV, a strong peak, centred at 100 mV, is visible in the silver island. The peak energy position and magnitude vary as the tip approaches the boundary between the silver island and silicene. This observation is consistent with the scattering of electrons occupying Shockley-type surface states [28]. The lower binding energy of the Shockley surface state band as the tip approaches the island edge is explained by the faster decline of the image potential outside the Ag surface due to the dielectric constant of the neighbour silicene adlayer. It is consistent with the shift measured when the (111) surface of noble metals is covered with weakly bound adsorbates [29–32]. In silicene, the Shockley surface state band has almost disappeared, in agreement with the disappearance of the bottom of the parabolic dispersion of the Shockley surface states in angle-resolved photoemission maps upon adsorption of silicene on Ag(111) [8]. A new peak, found around +0.5 V, that corresponds to the plateau observed in Fig. 3(b) at high setpoint currents, emerges. We attribute its origin to the hybridization of the silicon orbitals with silver atoms and believe that it involves the Si $p_z$ states, based on the theoretical results described in Ref. [9]. Therefore the formation of monolayer silicene suppresses the Shockley surface states, but leaves the bulk Ag states unaltered below the Fermi level, in agreement with the absence of occupied Si derived bands around the Γ point of the Brillouin zone in an energy range of 500 meV as found by several first-principle calculations [7–9].

In order to further understand how the orbitals of the Si atoms hybridize, Raman spectroscopy was performed. Fig. 5 shows the evolution of the Raman spectra as a function of the Si coverage up to the formation of the ($\sqrt{3} \times \sqrt{3}$) phase that occurs after the completion of the first monolayer silicene at a temperature of 250 °C [12]. While the Raman spectrum of the bare Ag(111) crystal does not show any peak, the Raman spectrum acquired on the ($\sqrt{3} \times \sqrt{3}$) phase exhibits a strong peak at 518.7 cm$^{-1}$. This peak is slightly shifted with respect to the transverse optical (TO) mode of the pristine diamond cubic phase of silicon measured in a Si(111) crystal, as seen in the inset of Fig. 5. The peak shows a tail toward lower frequencies, that is similar to the one found in microcrystalline silicon due to amorphous/small grain regions [33]. Such a result is in agreement with a previous Raman analysis of the same phase [11].

At 1 ML, that corresponds to the full coverage of the Ag(111) surface with the (4 × 4) and ($\sqrt{13} \times \sqrt{13} - \alpha$) silicene phases, the same line shape appears, but with a much smaller amplitude. We note that the peak is still centred at the same wave number than the one measured on the ($\sqrt{3} \times \sqrt{3}$) phase. It is thus shifted by 2 cm$^{-1}$ toward lower frequency with respect to the TO mode of silicon crystal, this shift being however smaller than the redshift found in Ref. [34]. The shape of the peak agrees also with the one found in Ref. [35]. We note a difference in energy in this case, due to the different temperature of the samples [36], 300 K versus 77 K. Although the surface is sprinkled with small clusters and the terraces have limited sizes, we believe that the tail at lower frequencies is predominantly caused by vibrational modes related to the particular hybridization of the Si orbitals in the (4 × 4) and ($\sqrt{13} \times \sqrt{13} - \alpha$) silicene phases [34]. At smaller coverage (0.7 ML), the line shape changes, the major peak vanishes. Also, a new peak appears at ~246 cm$^{-1}$. At even smaller coverage (0.4 ML), there is no detectable scattering of the first-order optical phonon of silicene, whereas the peak at low frequency, that has undergone a slight shift of 4 cm$^{-1}$, is still seen.

This peak was previously found to be affected by the amount of boundary defects in the (4 × 4) and ($\sqrt{13} \times \sqrt{13} - \alpha$) silicene phases [35]. However our study shows that the peak is absent when the surface is saturated with domains consisting of the (4 × 4) and ($\sqrt{13} \times \sqrt{13} - \alpha$) silicene phases with many boundary defects. From the comparison of the Raman spectra with the STM images of Fig. 1, we rather attribute the occurrence of the peak measured at low frequency to the concentration of domains filled with the bright protrusions. This hypothesis is supported by the slight shift of the peak that takes along with the ordering of the bright protrusions at increasing coverage. As suggested recently [37], the silicon atoms in these domains do not form complete rings and might strongly interact with the silver atoms, giving rise to new vibrational modes.

As mentioned above, at full monolayer coverage, where the surface predominantly consists of the (4 × 4) and ($\sqrt{13} \times \sqrt{13} - \alpha$) silicene phases, the strongest Raman peak is centred at 518.7 cm$^{-1}$, as better seen in Fig. 6. Exposure to ambient for 20 min and measurement of the Raman spectrum in air with the same system where the lens has been replaced by a long working distance objective (50×, NA = 0.45) to allow higher backscattering collection, shows the same characteristic band between 450 and 530 cm$^{-1}$. In addition, due to the higher collection efficiency, two small and broad peaks at 300 and 970 cm$^{-1}$, respectively, are now visible. They are respectively attributed to the scattering of two transverse acoustic (2TA) phonons and two transverse optical (2TO) phonons in the pristine diamond cubic phase of silicon. The observation of these features is in clear contrast with the typical spectra obtained for silicon oxide materials, that are characterized by a broad and diffuse band centred at 440 cm$^{-1}$ and a sharp but not too intense peak at 492 cm$^{-1}$ [38,39]. Such a peak, that was also observed in the spectra of silicene monolayer and layers obtained for higher Si coverages when the samples were measured in air [11], is clearly absent in Fig. 6, suggesting some resistance to air of monolayer silicene in agreement with a previous work [40]. However a recent study of the oxidation of the (4 × 4), ($\sqrt{13} \times \sqrt{13} - \alpha$) and ($2\sqrt{3} \times 2\sqrt{3}$) silicene phases revealed the loss of the peak at 520 cm$^{-1}$ [41]. A possible scenario to account for this difference between this work and our result is based on the sparse occurrence of bulk-like Si(111) areas on our surface [11,12, 42], since the LEED pattern in Fig. 6 indicates the presence of domains with the ($\sqrt{3} \times \sqrt{3}$) phase. In these domains, the few Si layers below the surface would keep the diamond cubic structure and would contribute predominantly to Raman scattering. A second alternative is related to the partial coverage of the silver surface with silicene. In Ref. [41], the authors showed that the Ag(111) surface is not completely covered with silicene, what could enhance the oxidation rates of monolayer

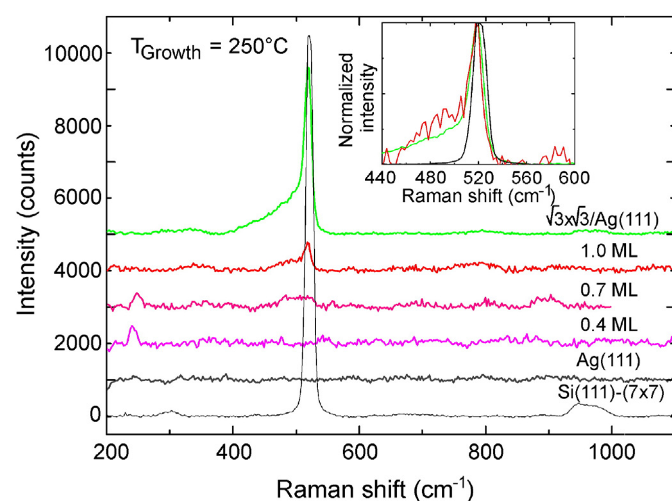


**Fig. 5.** Raman spectra of a Si(111) crystal terminated with the (7 × 7) reconstruction, a Ag(111) crystal, a 0.4 ML-thick silicene adlayer on the Ag(111) crystal, a 0.7 ML-thick silicene adlayer on the Ag(111) crystal, a 1.0 ML-thick silicene adlayer on the Ag(111) crystal, a 2.5 ML-thick multilayer silicene on the Ag (111) crystal showing the ($\sqrt{3} \times \sqrt{3}$) surface reconstruction. The spectra measured for the silicene samples were recorded for 300 s per 1000 cm$^{-1}$ wave number window. Inset: Comparison of the position of the strongest Raman peak between a Si(111) crystal terminated with the (7 × 7) reconstruction, a 1.0 ML-thick silicene adlayer on the Ag(111) crystal and a ($\sqrt{3} \times \sqrt{3}$) multilayer silicene on the Ag (111) crystal.

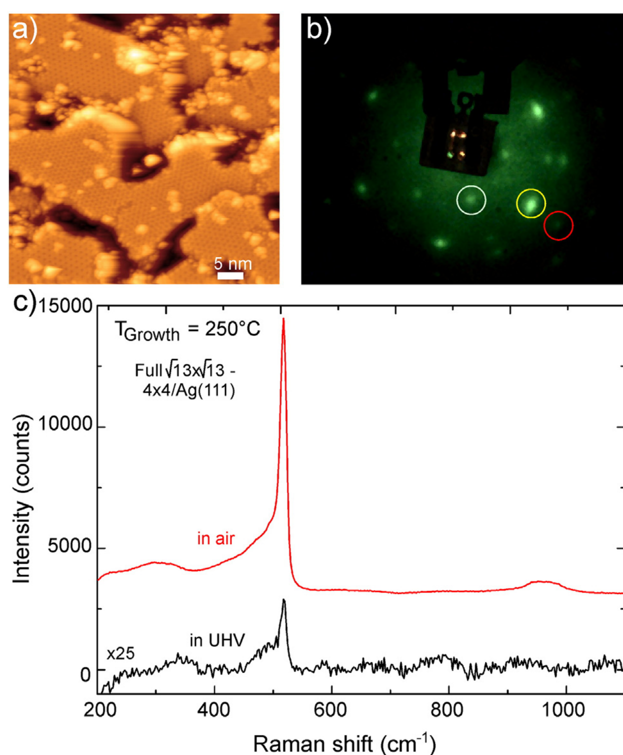


**Fig. 6.** (a) STM image of monolayer silicene showing the full coverage of the surface with the (4 × 4) and ($\sqrt{13} \times \sqrt{13} - \alpha$) silicene phases. (b) Corresponding LEED pattern (red circle: silver integer order spot; yellow circle: silicene integer order spot, blue circles: (1/3,1/3) type superstructure spots of the ($\sqrt{3} \times \sqrt{3}$)R30° silicene). (c) Raman spectra of a monolayer silicene adlayer on the Ag(111) acquired in UHV (lower curve) and in air (upper curve) respectively. The spectrum measured in UHV was recorded for 100 s per 1000 $cm^{-1}$ wave number window, whereas the spectrum measured in air, 20 min after being taken out of UHV, was recorded for 10s per 1000 $cm^{-1}$ wave number window.

silicene. Although we are not able to identify the physical reason for the lack of a clear oxidation of our sample, the characteristic peaks of the Raman spectra point to the existence of chemical bonds in monolayer silicene that consist of distorted $sp^3$ hybrid orbitals, behaving differently from pure Si dangling bonds. Due to their negligible contribution to the density of states near the Fermi level, as found in the STS measurements, full monolayer silicene shows a lower chemical reactivity than standard Si crystal surfaces and therefore prevent silver underneath from getting quickly oxidized.

## 4. Conclusion

In summary, we have studied the electronic and vibrational properties of monolayer silicene in the temperature range of 230–250 °C. Three phases have been observed, that all show a complex density of states near the Fermi level. Comparison with the tunnelling spectra measured on the Ag(111) surface reveals that tunnelling spectroscopy probes states slowly decaying from silver through the silicene adlayer into the vacuum at negative bias, while the Shockley surface states disappear at positive bias, due to the hybridization of Si states with the Ag(111) surface. Similarly, the vibrational modes of monolayer silicene shows the characteristic Raman peaks of pristine diamond cubic phase plus an additional broad band, indicating that the silicene orbitals rather behave as distorted $sp^3$ hybrid orbitals. However, opposite to most of the silicon surfaces, the orbitals give rise to surface resonances and not localized surface states, what significantly reduces the chemical reactivity of the silicene/Ag interface.

## Acknowledgment

This study was financially supported by the European Community's Seventh Framework Programme (Grant No. PITN-GA-2012-316751, “Nanoembrace” Project), the EQUIPEX (ANR-11-EQPX-0015) program Excelsior, and the RENATECH network. T. Xu acknowledges the support of the “Chenguang” project (13CG42) supported by Shanghai Municipal Education Commission and Shanghai Education Development Foundation and of the Region Nord-Pas-de-Calais. Conversations with Guy Le Lay are gratefully acknowledged.

## References

[1] P. Vogt, P. De Padova, C. Quaresima, J. Avila, E. Frantzeskakis, M.C. Asensio, A. Resta, B. Ealet, G. Le Lay, Phys. Rev. Lett. 108 (2012) 155501.
[2] B. Feng, Z. Ding, S. Meng, Y. Yao, X. He, P. Cheng, L. Chen, K. Wu, Nano Lett. 12 (2012) 3507.
[3] L. Chen, C.-C. Liu, B. Feng, X. He, P. Cheng, Z. Ding, S. Meng, Y. Yao, K. Wu, Phys. Rev. Lett. 109 (2012) 056804.
[4] C.-L. Lin, R. Arafune, K. Kawahara, M. Kanno, N. Tsukahara, E. Minamitani, Y. Kim, M. Kawai, N. Takagi, Phys. Rev. Lett. 110 (2013) 076801.
[5] N. Takagi, C.-L. Lin, K. Kawahara, E. Minamitani, N. Tsukahara, M. Kawai, R. Arafune, Prog. Surf. Sci. 90 (2015) 1.
[6] Z.-X. Guo, S. Furuya, J.-I. Iwata, A. Oshiyama, Phys. Rev. B 87 (2013) 235435.
[7] S. Cahangirov, M. Audiffred, P. Tang, A. Iacomino, W. Duan, G. Merino, A. Rubio, Phys. Rev. B 88 (2013) 035432.
[8] S.K. Mahatha, P. Moras, V. Bellini, P.M. Sheverdyaeva, C. Struzzi, L. Petaccia, C. Carbone, Phys. Rev. B 89 (2014) 201416(R).
[9] P. Pflugradt, L. Matthes, F. Bechstedt, Phys. Rev. B 89 (2014) 035403.
[10] K. Kawahara, T. Shirasawa, R. Arafune, C.-L. Lin, T. Takahashi, M. Kawai, N. Takagi, Surf. Sci. 623 (2014) 25.
[11] A.J. Mannix, B. Kiraly, B.L. Fisher, M.C. Hersam, N.P. Guisinger, ACS Nano 8 (2014) 7538.
[12] P. Vogt, P. Capiod, M. Berthe, A. Resta, P. De Padova, T. Bruhn, G. Le Lay, B. Grandidier, Appl. Phys. Lett. 104 (2014) 021602.
[13] H. Fu, L. Chen, J. Chen, J. Qiu, Z. Ding, J. Zhang, K. Wu, H. Li, S. Meng, Nanoscale 7 (2015) 15880.
[14] Y. Borensztein, A. Curcella, S. Royer, G. Prévot, Phys. Rev. B 92 (2015) 155407.
[15] J. Qiu, H. Fu, Y. Xu, A.I. Oreshkin, T. Shao, H. Li, S. Meng, L. Chen, K. Wu, Phys. Rev. Lett. 114 (2015) 126101.
[16] Y. Du, et al., ACS Nano 8 (2014) 056804.
[17] P. De Padova, et al., 2D Materials 1, 2014 1003.
[18] R. Bernard, Y. Borensztein, H. Cruguel, M. Lazzeri, G. Prévot, Phys. Rev. B 92 (2015) 045415.
[19] Z.-L. Liu, M.-X. Wang, J.-P. Xu, J.-F. Ge, G. Le Lay, P. Vogt, D. Qian, C.-L. Gao, C. Liu, J.-F. Jia, New J. Phys. 16 (2014) 075006.
[20] J. Li, W.-D. Schneider, R. Berndt, O.R. Bryant, S. Crampin, Phys. Rev. Lett. 81 (1998) 4464.
[21] L. Limot, T. Maroutian, P. Johansson, Phys. Rev. Lett. 91 (2003) 196801.
[22] R.S. Becker, J.A. Golovchenko, B.S. Swartzentruber, Phys. Rev. Lett. 55 (1985) 987.
[23] M. Chelvayohan, C.H.B. Mee, J. Phys. C 15 (1982) 2305.
[24] E.W. Müller, J. Appl. Phys. 26 (1955) 732.
[25] D. Chiappe, C. Grazianetti, G. Tallarida, M. Fanciulli, A. Molle, Adv. Mater. 24 (2012) 5088.
[26] C.-L. Lin, R. Arafune, M. Kawai, N. Takagi, Chin. Phys. B 24 (2015) 087307.
[27] E.Y. Andrei, G. Li, X. Du, Rep. Prog. Phys. 75 (2012) 056501.
[28] P. Avouris, I.-W. Lyo, R.E. Walkup, Y. Hasegawa, J. Vac. Sci. Technol. 12 (1994) 1447.
[29] H. Hövel, B. Grimm, B. Reihl, Surf. Sci. 477 (2001) 43.
[30] F. Foster, A. Bendounan, J. Ziroff, F. Reinert, Surf. Sci. 600 (2006) 3870.
[31] N. Nicoara, E. Román, J.M. Gómez-Rodríguez, J.A. Martín-Gago, J. Méndez, Org. Electron. 7 (2006) 28.
[32] Y. Pan, S. Benedetti, N. Nilius, H.-J. Freund, Phys. Rev. B 84 (2011) 075456.
[33] D. Han, J.D. Lorentzen, J. Weinberg-Wolf, L.E. McNeil, Q. Wang, J. Appl. Phys. 94 (2003) 2930.
[34] E. Cinquenta, E. Scalise, D. Chiappe, C. Grazianetti, B. van den Broek, M. Houssa, M. Fanciulli, A. Molle, J. Phys. Chem. 117 (2013) 16719.
[35] J. Zhuang, X. Xu, Y. Du, K. Wu, L. Chen, W. Hao, J. Wang, W.K. Yeoh, X. Wang, S.X. Dou, Phys. Rev. B 91 (2015) 161409(R).
[36] T.R. Hart, R.L. Aggarval, B. Lax, Phys. Rev. B 1 (1970) 638.
[37] K. Wu, Chin. Phys. B 24 (2015) 086802.
[38] R.J. Hemley, H.K. Mao, P.M. Bell, B.O. Mysen, Phys. Rev. Lett. 57 (1986) 747.
[39] B. Li, D. Yu, S.-L. Zhang, Phys. Rev. B 59 (1999) 1645.
[40] A. Molle, C. Grazianetti, D. Chiappe, E. Cinquenta, E. Cianci, G. Tallarida, M. Fanciulli, Adv. Funct. Mater. 23 (2013) 4340.
[41] J. Chen, Y. Du, Z. Li, W. Li, B. Feng, J. Qui, P. Cheng, S.X. Dou, L. Chen, K. Wu, Sci. Report. (2015) 5.
[42] Y. Du, J. Zhuang, H. Liu, X. Xu, S. Eilers, K. Wu, P. Cheng, J. Zhao, X. Pi, K.W. See, G. Peleckis, X. Wang, S.X. Dou, ACS Nano 8 (2014) 10019.

# Acknowledgments

This thesis has been framed within a FP7 European Framework project called Nanoembrace. I acknowledge not only their financial support, but also the possibility to interact and learn with all the people taking part in this project. It is a tremendous opportunity to start a thesis in the nanowire field and be able to personally learn from and interact with some of the main researchers on this field. Furthermore, I have met and enjoyed fruitful collaborations with other PhD students of the same project from all across Europe.

I would like to thank the jury that has evaluated my thesis; the president, Gilles Dambrine, the examiners, Michel Gendry and Damien Riedel, which have carefully review the manuscript and offered very valuable suggestions to improve it and the opponents, Silvia Rubini and Sébastien Plissard, for their acute observations and questions, which have contributed to further improve this work.

But this thesis would not have been possible without the confidence of my supervisor, Prof. Bruno Grandidier, who granted me with the possibility to come to Lille and embark myself in the Nanoembrace project. From day one, he hosted me with the utmost attention and understanding. He has offered me trust, a complete availability and a great sense of pedagogy above research goals or deadlines. Also, he has given me a great deal of freedom to pursue my own ideas. I have not only learn a lot of science from him, but also a lot about how science gets done, how to work in large research projects and how to interact with other people to maximize the quality of the final work. Merci, Bruno.

During these past three years, I have been part of the physics group at IEMN as well as the deparment of physics at ISEN. I wish to express my sincere gratitude to Maxime Berthe, the engineer in charge of the LT-STM at ISEN as well as the Nanoprobe at IEMN, for devoting his time to show me every inch of both instruments with precision, patience and a good mood. Thanks to his great expertise as instrumentation and research engineer, I have been able to truly deepen my knowledge about scientific instrumentation, in every aspect of it. Also, he has even had the courage to speak French with me, from time to time. I want to thank Jean-Philippe Nys, the engineer in charge of the RT-STM at IEMN, whose kind disposition and large experience with sample preparations have always come at hand to solve any issue that I might have found along the way. My work with nanowires and STM has not started from scratch, thanks to the methodology settled years ago by Tao Xu, and with his collaboration and company within some of these experiments, I have been able to

handle the characterization of nanowires surfaces with a lot more confidence and guarantee of success. Furthermore, the THz characterization of nanowires would not have been possible without the collaboration of Prof. Jean-François Lampin, his profound knowledge about optoelectronics, clear explanations and precise experimental methodology have been critically important for the completion of the last part of this work. I want to thank some other excellent researchers, engineers and students that I have worked with at IEMN as well as ISEN, that have thoroughly enriched my daily experience: Christophe, Didier, François, Isabelle, Sergio, Sylvie, Thomas, Yannick. In particular, I owe a big thanks to Sergio, whose unselfish help and friendship within the first months of my project eased a lot to tackle some not so easy procedures with the French administration. And Thomas, whose company in the office during the denser parts of the writing this last year has been a great support.

Finally, I want to express my profound gratitude to Claire Dehondt, Laetitia Perquin and Florence Senez, for their excellent work and help dealing with all the administrative paperwork.

Outside Lille, I want to thank the scientific exchange of ideas and material with different researchers: Anna Fontcuberta and Gözde Tütüncuoglü, from EPFL, for growing and providing with various III-V and the LT-GaAs Nanowires as well as for performing the cathodoluminescence characterizations. Sébastien Plissard, from LAAS, for growing and providing as well with different III-V nanowires. Gilles Patriarche, from LPN, for hosting me at his institution in Paris and help me to perform the TEM characterization of the LT-GaAs nanowires. And Philipp Ebert, from Peter Grünberg Institut, whose great insight into surface science and semiconductors has been very valuable for the understanding of the surface morphology of III-V nanowires.

Since I moved out from the small town to the city of Madrid some many years ago to pursue my studies in Physics, many people has crossed along my way; some of them bringing their friendship, helping to solve my problems, shaping my view of the world and sharing with me a part of their lives. If this work is in some degree a complete and sound scientific production, it is in part thanks to them: Abhishek, Antonio, Belén, Chara, Dani, Giorgos, Jero, Moni, Rafa, Richi, Samu, Siya, Teresa.

My last words and deepest gratitude and love belong to all my family, specially my parents, and to Alba. My choices, better or worse, are only mine. But in every step of the way, in every career or life choice, they have been there to support me.